

EXPERIMENTAL CONTROL OF INSTABILITIES AND CHAOS IN FAST DYNAMICAL SYSTEMS

TECHNICAL REPORT

DAVID W. SUKOW

June 1997

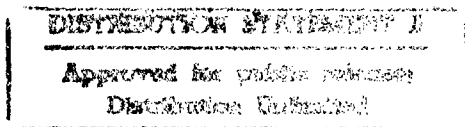
Department of Physics
Duke University

Approved for public release;
Distribution Unlimited

The views, opinions, and/or findings contained in this report are those of the author and should not be construed as an official Department of the Army position, policy, or decision, unless so designated by other documentation.

Prepared for:

U.S. Army Research Office
ATTN: AMXRO-ICA-I (Hall)
P.O. Box 12211
Research Triangle Park, NC 27709-2211



19970818 036

Copyright © 1997 by David Wayne Sukow
All rights reserved

REPORT DOCUMENTATION PAGE

Form Approved
OMB NO. 0704-0188

Public reporting burden for this collection of information is estimated to average 1 hour per response, including the time for reviewing instructions, searching existing data sources, gathering and maintaining the data needed, and completing and reviewing the collection of information. Send comment regarding this burden estimate or any other aspect of this collection of information, including suggestions for reducing this burden, to Washington Headquarters Services, Directorate for Information Operations and Reports, 1215 Jefferson Davis Highway, Suite 1204, Arlington, VA 22202-4302, and to the Office of Management and Budget, Paperwork Reduction Project (0704-0188), Washington, DC 20503

AGENCY USE ONLY (Leave blank)		2. REPORT DATE June 1997	3. REPORT TYPE AND DATES COVERED Technical	
TITLE AND SUBTITLE Experimental control of instabilities and chaos in fast dynamical systems			5. FUNDING NUMBERS DAAH04-95-1-1-0529	
AUTHOR(S) David W. Sukow				
PERFORMING ORGANIZATION NAME(S) AND ADDRESS(ES) Duke University Department of Physics Box 90305 Durham, NC 27708			8. PERFORMING ORGANIZATION REPORT NUMBER	
SPONSORING / MONITORING AGENCY NAME(S) AND ADDRESS(ES) U.S. Army Research Office P.O. Box 12211 Research Triangle Park, NC 27709-2211			10. SPONSORING / MONITORING AGENCY REPORT NUMBER ARO 34611.6-PH	
11. SUPPLEMENTARY NOTES The views, opinions and/or findings contained in this report are those of the author(s) and should not be construed as an official Department of the Army position, policy or decision, unless so designated by other documentation.				
2a. DISTRIBUTION / AVAILABILITY STATEMENT Approved for public release; distribution unlimited.			12 b. DISTRIBUTION CODE	
13. ABSTRACT (Maximum 200 words) Please see pages iv-v.				
14. SUBJECT TERMS nonlinear optics, nonlinear dynamics, chaos, controlling chaos, semiconductor lasers, unstable periodic orbits			15. NUMBER OF PAGES 229	
			16. PRICE CODE	
17. SECURITY CLASSIFICATION OR REPORT UNCLASSIFIED	18. SECURITY CLASSIFICATION OF THIS PAGE UNCLASSIFIED	19. SECURITY CLASSIFICATION OF ABSTRACT UNCLASSIFIED	20. LIMITATION OF ABSTRACT UL	

GENERAL INSTRUCTIONS FOR COMPLETING SF 298

The Report Documentation Page (RDP) is used in announcing and cataloging reports. It is important that this information be consistent with the rest of the report, particularly the cover and title page. Instructions for filling in each block of the form follow. It is important to *stay within the lines* to meet *optical scanning requirements*.

Block 1. Agency Use Only (Leave blank)

Block 2. Report Date. Full publication date including day, month, and year, if available (e.g. 1 Jan 88). Must cite at least year.

Block 3. Type of Report and Dates Covered. State whether report is interim, final, etc. If applicable, enter inclusive report dates (e.g. 10 Jun 87 - 30 Jun 88).

Block 4. Title and Subtitle. A title is taken from the part of the report that provides the most meaningful and complete information. When a report is prepared in more than one volume, repeat the primary title, add volume number, and include subtitle for the specific volume. On classified documents enter the title classification in parentheses.

Block 5. Funding Numbers. To include contract and grant numbers; may include program element number(s), project number(s), task number(s), and work unit number(s). Use the following labels:

C - Contract	PR - Project
G - Grant	TA - Task
PE - Program Element	WU - Work Unit Accession No.

Block 6. Author(s). Name(s) of person(s) responsible for writing the report, performing the research, or credited with the content of the report. If editor or compiler, this should follow the name(s).

Block 7. Performing Organization Name(s) and Address(es). Self-explanatory.

Block 8. Performing Organization Report Number. Enter the unique alphanumeric report number(s) assigned by the organization performing the report.

Block 9. Sponsoring/Monitoring Agency Name(s) and Address(es). Self-explanatory.

Block 10. Sponsoring/Monitoring Agency Report Number. (If known)

Block 11. Supplementary Notes. Enter information not included elsewhere such as; prepared in cooperation with...; Trans. of...; To be published in.... When a report is revised, include a statement whether the new report supersedes or supplements the older report.

Block 12a. Distribution/Availability Statement. Denotes public availability or limitations. Cite any availability to the public. Enter additional limitations or special markings in all capitals (e.g. NORFORN, REL, ITAR).

DOD - See DoDD 4230.25, "Distribution Statements on Technical Documents."
DOE - See authorities.
NASA - See Handbook NHB 2200.2.
NTIS - Leave blank.

Block 12b. Distribution Code.

DOD - Leave blank
DOE - Enter DOE distribution categories from the Standard Distribution for Unclassified Scientific and Technical Reports
NASA - Leave blank.
NTIS - Leave blank.

Block 13. Abstract. Include a brief (*Maximum 200 words*) factual summary of the most significant information contained in the report.

Block 14. Subject Terms. Keywords or phrases identifying major subjects in the report.

Block 15. Number of Pages. Enter the total number of pages.

Block 16. Price Code. Enter appropriate price code (*NTIS only*).

Block 17. - 19. Security Classifications. Self-explanatory. Enter U.S. Security Classification in accordance with U.S. Security Regulations (i.e., UNCLASSIFIED). If form contains classified information, stamp classification on the top and bottom of the page.

Block 20. Limitation of Abstract. This block must be completed to assign a limitation to the abstract. Enter either UL (unlimited) or SAR (same as report). An entry in this block is necessary if the abstract is to be limited. If blank, the abstract is assumed to be unlimited.

EXPERIMENTAL CONTROL OF INSTABILITIES AND CHAOS IN FAST DYNAMICAL SYSTEMS

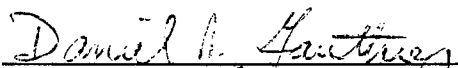
by

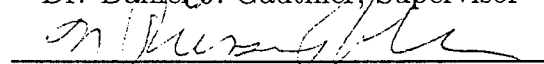
David Wayne Sukow

Department of Physics
Duke University

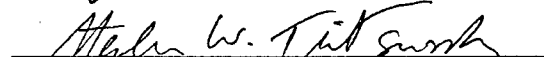
Date: 6 June 1997

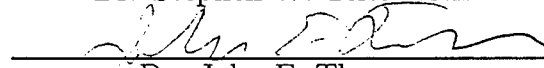
Approved:


Dr. Daniel J. Gauthier, Supervisor


Dr. N. Russell Roberson


Dr. Joshua E. S. Socolar


Dr. Stephen W. Teitsworth


Dr. John E. Thomas

Dissertation submitted in partial fulfillment of the
requirements for the degree of Doctor of Philosophy
in the Department of Physics
in the Graduate School of
Duke University

1997

ABSTRACT

(Physics)

EXPERIMENTAL CONTROL OF INSTABILITIES AND
CHAOS IN FAST DYNAMICAL SYSTEMS

by

David Wayne Sukow

Department of Physics
Duke University

Date: 6 June 1997

Approved:

Daniel J. Gauthier

Dr. Daniel J. Gauthier, Supervisor

N. Russell Roberson

Dr. N. Russell Roberson

Joshua E. S. Socolar

Dr. Joshua E. S. Socolar

Stephen W. Teitsworth

Dr. Stephen W. Teitsworth

John E. Thomas

Dr. John E. Thomas

An abstract of a dissertation submitted in partial
fulfillment of the requirements for the degree
of Doctor of Philosophy in the Department of
Physics in the Graduate School of
Duke University

1997

Abstract

I investigate experimentally and theoretically the application of control techniques in systems that display temporal instabilities, including chaos, on very short timescales. My study includes two distinct systems: a fast chaotic electronic circuit called the diode resonator, and a compound-cavity semiconductor laser system that exhibits an instability called low-frequency fluctuations. Control of fast unstable systems presents several experimental challenges. It is also a topic of broad interest, since it requires the development of new control techniques, and addresses technologically important devices such as the semiconductor laser.

The diode resonator is a well-understood system, and when modified for 10 MHz operation serves as a good testbed for the application of novel control techniques. I develop a new high-speed time-delay feedback control technique that is based on the comparison of the present value of a system variable with a series of its past values. The principles of operation of this technique are studied in both time and frequency domains, as well as possible methods for its implementation. I develop a detailed analog electronic implementation that addresses the experimental needs of rapid processing and faithful reproduction of the feedback signal. This control system successfully stabilizes unstable periodic orbits in the diode resonator, the fastest experimental instability controlled to date. This technique also increases significantly the regions of parameter space in which control is effective, in comparison with previous methods. The improvement is gained by incorporating more information from further in the system's past.

I study the dynamics of the external cavity semiconductor laser system in the regime where low-frequency fluctuations occur, seeking to improve our understanding of the system before attempting to control its behavior. This system is not com-

pletely understood, as it exhibits extremely complex, high-speed, potentially infinite-dimensional dynamics in which spontaneous emission noise plays an important part. The dominant feature of the instability is the probabilistic occurrence of spontaneous, rapid dropouts in the laser power that occur on the nanosecond time scale, although much faster picosecond dynamics are also present in the system. I perform new measurements of the probability distributions for the time between power dropouts, showing that the data can be modeled approximately as a first-passage time problem. However, the simple theory does not capture accurately my experimental results under certain circumstances; I suggest possible explanations for the discrepancies.

I apply open-loop and closed-loop control perturbations to the laser system in the form of perturbations to the drive current, in an attempt to regulate or stabilize the complex dynamics. I entrain the power dropouts using a 19 MHz sinusoidal modulation, such that the power dropouts occur periodically rather than irregularly, thereby eliminating much of the associated low-frequency noise. In addition, higher frequency modulation (hundreds of MHz) can produce multiple effects, inducing new dynamics in certain cases yet doing nothing in others. Finally, I study a closed-loop feedback technique, finding that it changes the shape of the power dropouts but does not suppress them, and I consider means of improving the feedback's effectiveness.

Acknowledgments

As a student of how little influences can produce desirable results in complicated systems, I am grateful for the influences of many people who have helped bring this dissertation into existence. I would like to take a moment to thank those people.

It is hard to imagine how to adequately express my love and gratitude to Mom and Dad, my own Initial Conditions. They have made this entire enterprise possible. All through my life they encouraged my interests and endeavors, they gave me a love of knowledge, and they provided the tools and opportunities to learn. Through the last six years they proudly celebrated the successes, they held me up when things got bad, they funneled a little green stuff to me to supplement the stipend, and they helped me to maintain my sense of perspective and remember the important things. They are my heroes, and I hope to follow their examples. Thanks also to my sister and brother-in-law, Cathy and Jaap, for their unconditional love, support, and empathy as they too have worked through graduate physics and biophysics programs.

I am grateful to many people in the physics department here at Duke. Thanks to my advisor, Dan Gauthier, for being an ethical, knowledgable, and demanding scientist, for sharpening my writing skills, and for relentlessly seeking ways to make students in his group more marketable and prepared for life beyond graduate school. I have benefitted in a tangible way from his skills at schmoozing for research grants, and I gratefully acknowledge several sources of support: the National Science Foundation, the Army Research Office, and the Air Force Office of Scientific Research. Thanks to the 105th Congress for not cutting *all* federal support for basic research.

Thanks to all my committee members, especially Joshua Socolar, who has been a major collaborator in this effort. Thanks to Mike Bleich, who provided good code, theoretical support, and shared enthusiasm. Thanks to the members of the Quan-

tum Electronics group in its current incarnation, Martin Hall, Bill Brown, and Jeff Gardner, for making the daily office culture the amusing and peculiarly supportive environment it was, and for keeping the refrigerator stocked with nice refreshing beverages when my generic soda supplies ran low. Hope Concannon deserves special recognition as the other charter member of the QE group, the ultimate colleage, and a dear friend. I am appreciative of the other members of my incoming graduate class who endured for the duration, for their good company and camaraderie through these years: Michael John Bergmann, Linda Blue, Tom Savard, and Daniel Patrick Cronin-Hennessy.

I am greatly indebted to all the secretaries, librarians, and support staff who helped things run smoothly while all this research was going on. Special thanks to Judy Bailey and Mary Ann Southern, the librarians who helped me locate references despite the library renovations that scattered the stacks throughout the building in my last month of writing. To Donna Ruger, honorary Duke Mom for my incoming graduate class, thanks for welcoming us to Duke, looking out for us, and remembering us on holidays. And thanks to Dick Poole in the machine shop, who had endless patience and good humor for my fledgling machinist skills. He pointed out my errors by deadpanning 'I've never seen anyone use a milling machine *that* way before,' and he generously did not kill me during the month I spent in the shop noisily cutting several large holes in a 1/4" thick stainless steel beam line.

I owe thanks to many physicists and educators whom I've known prior to and during graduate school. Milo Opegard, Sue Popelka, Steve Mellema, DC Henry, Chuck Niederriter, Richard Fuller, and Mitchell Feigenbaum were all important influences and role models. Thanks to Tim Newell, Vassilios Kovanis, Tom Gavrielides, and Chris Clayton at the Phillips Labs in Albuquerque, for an excellent summer's work in an environment that was simultaneously challenging and supportive, spark-

ing both my enthusiasm and confidence. I'm glad there's more to come! Thanks to Cyrus Dastur at the North Carolina Museum of Life and Science, for his friendship and for letting me work in *Scientifica*.

There are many people who contributed not to the scientific content of this thesis but rather to the well-being of its author. Thanks to Rodney Wynkoop and the Duke Chorale, for helping me keep the liberal arts flame burning and for letting me explore my tenor range. I have also had the pleasure of training and performing with several dancers in the past years. It was always good to be reminded that many people in the world value you based not on what you *know* but rather on what you can *do*. Thanks to Jon Paul and Sharon McClellan for teaching me the ways of ballroom dance, especially the tango. Thanks to Barbara Dickinson, Jill and Michael Eng, Laura Thomasson, and Thaddeus Bennett of the Ways and Means dance company, for letting me work with them on 'Trilogy' and a children's performance. Special thanks to the members of that group who have been my teachers at the Durham Arts Council, Rebecca Hutchins and Betsy Romer. Thanks to Clay Taliaferro, who made me do floor barre for the entire first month of class, portentiously explaining 'You must first learn control. Then, when you have your freedom, you can control your freedom.'

Thanks to all my other good friends here, for making the whole graduate experience more enjoyable. Thanks especially to Sean Hinton, Sonia Cavigelli, and Jef Lamoureaux, who started out as volleyball friends but quickly assumed much broader responsibilities. Thanks for all the good sets, for an endless source of lemur jokes, for all the excellent dinner parties with cheap Italian wine, and for the unforgettable Hurricane Fran 'it's spoiling so let's grill the living daylight out of it' meat-eating extravaganza. On a somewhat different note, thanks to William Hunt and the cheery students at the Cafe for providing the daily cup of Sumatra, Colombia, Yukon, or

Kenya. Thanks to BW3's in Chapel Hill for Tuesday night hot wings specials. And, thanks to the rest of the Friday Volleyball regulars for helping me work off the effects of those indulgences.

And finally, I want to thank Gretchen, my wife and companion. Her love has kept me grounded and happy all through the writing of this thesis. She has believed in me, made me laugh, heard my worries, and fed me plenty of vegetables. Her willingness and even excitement to pick up and move has made it possible for me to accept a great postdoc opportunity. She has given me the very best incentives to complete this thesis and move on to the next adventures. For all these things and the promise of everything in the years to come, I thank her with all my heart. This thesis is dedicated to you, Gretchen, and to Lillian, Samuel, Julia, Carl, or whatever their names may be.

Contents

Abstract	iv
Acknowledgments	vi
List of Figures	xiv
List of Tables	xxii
1 Introduction	1
1.1 Nonlinear dynamics and predictability	1
1.2 Overview of thesis	7
2 Fundamentals of nonlinear dynamics and control	14
2.1 Motivation	14
2.2 Fundamentals of control	17
2.2.1 Open-loop vs. closed-loop control	17
2.2.2 Feedback control in a simple system	19
2.2.3 Stabilizing the damped pendulum	20
2.3 The Ott, Grebogi, and Yorke concept	25
2.3.1 Control in fast systems	27
3 Extended Time-Delay Autosynchronization	32
3.1 Understanding ETDAS	32
3.1.1 The ETDAS feedback form	34
3.1.2 Linear stability analysis	36
3.1.3 Frequency domain analysis	38
3.2 Implementing ETDAS	40

3.2.1	General implementation	40
3.2.2	All-optical implementation	42
3.3	Implementation for the diode resonator	43
3.3.1	Electronic circuit layout	43
3.3.2	Selection of components	46
3.3.3	Adjustment of circuit parameters	48
3.3.4	Compensating for nonideal circuit behavior	50
4	ETDAS Control of the Fast Chaotic Diode Resonator	54
4.1	Experimental system: the fast diode resonator	55
4.1.1	Model of system	56
4.1.2	Characterization of uncontrolled system	57
4.2	Experimental observation of control	59
4.3	Domain of control	63
4.4	Transient behavior	65
4.5	Average time to attain control	67
4.6	Theoretical analysis	69
4.7	Effects of control-loop latency	74
4.8	Dynamics of the system outside the domain of control	76
5	Power Dropout Events in an External-Cavity Semiconductor Laser	82
5.1	Introduction to semiconductor lasers in external cavities	83
5.1.1	The semiconductor laser	84
5.1.2	External cavity effects	86
5.2	Model of the system	88
5.2.1	The Lang-Kobayashi equations	88

5.2.2	Steady states of the laser with optical feedback	93
5.3	Experimental apparatus	96
5.3.1	External cavity configuration	96
5.3.2	Stabilized semiconductor laser	97
5.4	Characterization of low-frequency fluctuations	103
5.4.1	Power dropout events	104
5.4.2	Dynamics on the attractor	112
5.5	Distribution of interspike intervals	113
5.5.1	Theoretical analysis	115
5.5.2	Comparison with experimental results	120
6	Open-Loop Regulation and Entrainment of Power Dropout Events	129
6.1	Open-loop control	131
6.2	Low-frequency modulation	133
6.2.1	Sensitivity to weak driving	133
6.2.2	Entrainment of dropouts	136
6.3	High-frequency modulation	141
7	Attempts to Stabilize an Unstable Steady State of an External-Cavity Semiconductor Laser	149
7.1	High-pass filter control	150
7.2	Experimental effects of high-pass filter feedback	153
7.3	Discussion	158
8	Conclusion and Future Directions	160
A	The Diode Resonator	166
A.1	Circuit model	167

A.1.1	Dimensionless form	168
A.2	Measurement of real circuit parameters	169
B	The Lang-Kobayashi Equations	172
B.1	Derivation of the equations	172
B.1.1	Semiclassical foundations	172
B.1.2	Phenomenological description	175
B.1.3	Rate equation for electric field	177
B.1.4	Rate equation for carrier density	181
B.2	Dimensionless form	182
C	The Henry and Kazarinov Theory and First-Passage Time Problems	184
C.1	The first-passage time problem	184
C.2	Approximate solution for Henry and Kazarinov model	187
	Bibliography	192
	Biography	206

List of Figures

1.1	Phase space projections of the chaotic Lorenz attractor. The single trajectory shown is complex and aperiodic.	3
1.2	Sensitive dependence on initial conditions on the chaotic Lorenz attractor. The chaotic dynamics cause rapid decorrelation of a cluster of closely spaced initial conditions.	4
1.3	Unstable periodic orbits of the Lorenz attractor. Graphs (b) and (c) are two of the simplest unstable periodic orbits embedded in the chaotic attractor shown in graph (a).	6
1.4	The diode resonator.	9
1.5	External cavity semiconductor laser. A portion of the emitted field is reflected back into the solitary laser after traversing an external cavity of length L	11
2.1	Block diagram illustrating open-loop (a) and closed-loop (b) control. .	18
2.2	The damped pendulum (a) and its stable (b) and unstable (c) steady states.	21
2.3	Linearized dynamics of the damped pendulum. The graphs show the trajectory without control (a) and when control is added (b), starting from the same initial conditions near the fixed point at $(0,0)$	24
3.1	Evidence of unstable periodic orbits in the chaotic diode resonator. Three regions of approximately periodic behavior indicate the system is near an UPO.	33
3.2	Illustration of ETDAS. The system is initially near an UPO, but then diverges from it. The dots indicate the values of $\xi(t)$ at various times, separated by the period τ of the UPO.	35
3.3	Transfer function of ETDAS. The "notches" at multiples of f_* indicate that no feedback is generated if the system is on the UPO.	39

3.4	Logical design for an ETDAS system. The signal $\xi(t)$ from the dynamical system is processed to generate $\delta p(t)$. The components in the dashed box generate the infinite series of time-delay terms using a single delay line.	41
3.5	All-optical implementation of ETDAS. The interferometer in the dashed box creates the time-delay series, with τ equal to the roundtrip time of light in the cavity.	42
3.6	Electronic implementation of ETDAS for control of the fast diode resonator. See text of Sec. 6.3.2 for a description.	44
3.7	Experimental ETDAS transfer functions. They are very similar in shape to the ideal transfer functions in Fig. 6.3, indicating that the circuitry faithfully reproduces the form of the ETDAS feedback signal.	51
3.8	Experimental ETDAS transfer functions without predistortion filters. Performance of the circuit is severely degraded, as the notches no longer go to zero and the peak heights are not uniform.	52
4.1	The high-speed diode resonator. The signal conditioner isolates the drive from the circuit and adds to it the ETDAS feedback. The behavior of the system is sensed with a high-impedance buffer.	55
4.2	Experimental and numerically generated bifurcation diagrams of the uncontrolled diode resonator. All major features are reproduced by the model.	58
4.3	Experimental and numerically generated first-return maps of the uncontrolled diode resonator.	60
4.4	Time series data and first return maps illustrating successful ETDAS control. Temporal evolution (solid line, scale on left) is shown for the stabilized period-1 (a) and period-4 (b) UPOs, along with their associated ETDAS error signals (dashed line, scale on right). Similar data are shown as first-return maps for the controlled period-1 (c) and period-4 (d) trajectories. The controlled maps are highlighted by dark dots indicated by arrows, superimposed on lighter dots representing the uncontrolled system. Parameter values are given in the text.	62

4.5	Experimental domains of control as a function of drive amplitude for period-1 and period-4 UPOs for two different values of R . The shaded regions indicate period-1 domains for $R = 0$ (a) and $R = 0.68$ (b), and period-4 domains for $R = 0$ (c) and $R = 0.65$ (d). The dashed lines mark the points at which the orbit becomes unstable in the absence of feedback.	64
4.6	Transient dynamics of the diode resonator following initiation of ET-DAS control. The dots represent the peak values V_n of $V(t)$, and the dashed vertical lines mark the points at which control is initiated. Graphs (a) and (b) show convergence to the period-1 UPO, and (c) and (d) show approaches to the period-4 UPO. Note that the transients have brief sections of decaying period behavior. Parameter values are given in the text.	66
4.7	Average transient times $\langle t_r \rangle$ as functions of feedback gain γ for the period-1 UPO for $R = 0$ (a) and $R = 0.68$ (b), and the period-4 UPO for $R = 0$ (c) and $R = 0.65$ (d). The error bars indicate the standard deviation of $\langle t_r \rangle$, and the hashed regions indicate the range of γ for which control is not achieved.	68
4.8	Comparison of experimental and theoretical domains of control. Period-1 domains (a) and (b) have $R = 0.68$, and period-4 domains (c) and (d) have $R = 0.65$. The vertical lines indicate the points at which the orbits become unstable in the absence of feedback. The theoretically predicted domains assume $t_\ell = 0$	71
4.9	Comparison of experimental and numerically simulated domains of control. The numerical simulations include control-loop latency equal to that of the experiment, $t_\ell = 10$ ns. Other parameter values are the same as Fig. 7.8. Note that inclusion of nonzero t_ℓ improves the quantitative agreement of the domains.	73
4.10	Effects of control-loop latency on the domain of control for the period-1 UPO. The dashed vertical line at $t_\ell = 10$ ns indicates the minimum latency of the ETDAS circuitry. Note that the larger R value has a much larger domain of control at large t_ℓ	75
4.11	Effects of control-loop latency on the domain of control for the period-4 UPO. The vertical dashed line again indicates the minimum t_ℓ for the ETDAS circuitry. Note the region of intermittency for $\gamma < 0$ at large t_ℓ in (b).	77

4.12	Intermittent chaotic bursts away from period-4 UPO. The dots represent peaks V_n of $V(t)$. Note that control is regained abruptly (a), but the system destabilizes gradually through higher-periodic behavior (b).	78
4.13	First return maps illustrating the dynamics of the system outside the period-1 domain of control. In (a), the system displays period-2 behavior (two dark dots indicated by arrows) when the feedback gain γ is too weak. These dots do not fall on the return map of the unperturbed system (lighter dots), indicating this period-2 orbit is not a true UPO of the original system. In (b), the system undergoes quasi-periodic dynamics (the dark oval centered on the period-1 fixed point) when the feedback gain is too large.	79
4.14	Power spectra of $V(t)$ outside the domain of control for the period-1 UPO. The cases shown are similar to those in Fig. 7.13. In (a) the spectrum has features at multiples of 5 MHz, indicating period-2 behavior when the feedback gain is too weak. In (b) the spectrum displays sidebands displaced by ~ 2 MHz, indicating low-frequency modulation of the fundamental frequency when the feedback gain is too strong.	80
5.1	External-cavity semiconductor laser. The active region of the solitary laser is sandwiched between p-type and n-type cladding layers that provide electron-hole pairs generated by the current J . The solitary laser cavity is formed by the mirrors r_1 and r_2 , whereas the external cavity is formed by r_1 and the reflector R located a distance L from the right facet of the laser.	87
5.2	Phase space ellipse indicating possible locations of fixed points. Unstable antimodes occur on the branch of the ellipse above the dashed line, and modes occur below. The dominant mode is the fixed point at which the output power is maximized. The operating point of the solitary laser is at the origin. The linewidth enhancement parameter is taken to be $\alpha = 5$.	94
5.3	Experimental layout of the external cavity semiconductor laser.	98

5.4	Temperature control system for semiconductor laser. The system is designed to force the resistance of the thermistor in the laser mount to match the sum of the resistances S1 and P1. The difference of these resistances is measured by an instrumentation amplifier and fed to an integrator. The integrator drives the base of a Darlington transistor, which generates the current that drives the thermoelectric cooler in the laser mount.	100
5.5	Rear (a) and front (b) views of laser mount assembly. The thermoelectric cooler (TEC) cools the small piece that contains the laser diode LD, and the temperature is sensed with a thermistor T. The copper block at the base acts as a heat sink. The screw S dictates the distance from the collimating lens and the laser diode.	102
5.6	Experimental time series showing a typical power dropout. Note the small scale structure, evidence of faster dynamics hidden by bandwidth limitations of the digitizing oscilloscope.	105
5.7	Experimental time series data illustrating the dependence of power dropout behavior on drive current level. Increasing the current increases the average rate at which the dropouts appear, and also changes their shape.	106
5.8	Simulated time series of LFF dynamics illustrating the influence of noise. Compared with the purely deterministic time series (a), the inclusion of noise (b) decreases the maximum intensity peaks, alters the shape of the dropouts, and changes the distribution of interspike intervals.	108
5.9	Simulated fast pulsing dynamics of LFF near the beginning of a dropout event. The pulses are short (50-200 ps wide) and have irregular spacing and height.	110
5.10	Typical experimental power spectrum of a system undergoing LFF. The low-frequency noise results from the irregular power dropouts. The regularly-spaced peaks are at harmonics of the external cavity, and are related to the fast pulsing dynamics of the laser.	111

5.11	Trajectory of a power dropout event in phase space. Graph (a) shows one full dropout cycle. Following the dropout (<i>A</i>), the system is reinjected onto the ellipse near the solitary laser operating point (<i>B</i>), after which it traverses the external cavity mode structure (<i>C</i>) as the average intensity rebuilds. Graph (b) is a close-up of the region near the dropout, making the destabilized cavity mode structure apparent. . .	114
5.12	Average times between power dropout events as a function of drive current. The error bars represent only statistical errors. The dashed line is a fit to the experimental data using the functional form of Henry and Kazarinov (Eq. 5.32).	122
5.13	Comparison of experimental interspike interval probability distribution and theoretical first-passage time distributions.	123
5.14	Overlay of multiple power dropouts, illustrating the relevance of the reinjection time t_r . The average laser intensity has essentially recovered to its level prior to the dropout after $t_r = 260$ ns.	125
5.15	Experimental and theoretical interspike interval probability distributions, for increasing power levels with the optical feedback level held constant. The dashed lines represent $\zeta(n, t - t_r)$. The agreement is clearly best at lower powers.	127
6.1	Frequency response of solitary laser to external modulation applied through the bias-tee. The laser response is normalized to one at 40 MHz.	132
6.2	The effect of weak 19 MHz modulation on power dropouts. The dropouts still occur and have the same general shape for both the (a) unperturbed and (b) modulated behavior.	133
6.3	Probability distributions $\eta(t)$ for interspike intervals when a 19 MHz modulation is applied for various amplitudes. Weak modulation shifts the distribution and causes a comb to appear with peaks occurring at multiples of the drive period. At sufficiently large amplitudes, $\eta(t)$ is collapsed to a single peak, indicating a regular appearance of dropout events.	135

6.4	Experimental time series of the laser intensity illustrating entrainment of power dropouts. Graph (a) shows dynamics of the unperturbed system, while (b) and (c) illustrate entrained dynamics. The current modulation amplitudes for (b) and (c) are 8% and 14% of the dc level, respectively.	137
6.5	Simulated phase space trajectories of the unperturbed (a) and entrained dynamics (b) of the LFF system. Graph (a) shows a single typical dropout event, and (b) shows four dropouts in sequence. The entrained dynamics occupy a limited region of phase space.	139
6.6	Experimental power spectra of the unperturbed and entrained dynamics. Graphs (a) and (d) show the spectra of the unperturbed system, (b) and (e) show 1:2 entrainment, and (c) and (f) show 1:1 entrainment. The entrained dynamics exhibit reduced low-frequency noise, but the high-frequency features are not suppressed.	140
6.7	Experimental time series of laser intensity comparing the (a) unperturbed system with the system when a 1.9% current modulation is applied at (b) 230 MHz and (c) 120 MHz. The high-frequency modulation increases the average dropout rate, and can induce rapid sequences of dropouts (c).	142
6.8	Experimental probability distributions $\eta(t)$ of interspike intervals under high-frequency modulation of fixed amplitude (1.9% of dc current) and varying frequency. The modulation induces a comb in $\eta(t)$ except when the frequency corresponds to the external cavity resonance (d). In some cases (b), (f) a feature appears at small interspike times, indicating a significant probability of power dropouts occurring in rapid succession.	144
6.9	Simulated time series of laser intensity showing unperturbed behavior (a) and increased dropout rates when a 230 MHz modulation is applied to the pump current (b).	145
6.10	Phase space representation of simulated time series from Fig. 6.8. The 230 MHz modulation (b) restricts the region in which the dynamics occur, forcing dropouts to occur before the maximum gain mode is reached and reinjecting the dynamics onto the ellipse before the roundtrip phase difference reaches zero.	146

7.1	Transfer function of the high-pass filter. The corner frequency is the point at which the response of the filter has fallen off by 3 dB. This is equivalent to the ETDAS transfer function with the first notch at infinity.	151
7.2	Experimental layout for implementation of high-pass filter control in the external cavity semiconductor laser system.	152
7.3	Experimental time series of laser intensity with high-pass filter feedback. The shape of the dropout is dependent on the feedback gain.	155
7.4	The effect of feedback with the wrong sign of the gain on power dropout shape. The dropout when (b) feedback is applied has a much longer duration, compared with the (a) unperturbed dropout.	156
7.5	Experimentally measured probability distributions $\eta(t)$ of the interspike intervals when high-pass filter feedback is introduced. The unperturbed dynamics are represented in graph (a).	157
A.1	Schematic of the diode resonator and its model using ideal components.	166
B.1	Schematic of a semiconductor laser with external feedback. The rectangle between $z = -\ell$ and $z = 0$ represents a Fabry-Perot laser diode with facet reflectivities of r_1 and r_2 . The external cavity is formed by a flat mirror of reflectivity r_3 located at $z = L$. Effective reflectivities r_R and r_L are defined for right and leftgoing fields E^+ and E^-	177

List of Tables

3.1	Component values for electronic implementation of ETDAS.	45
A.1	Parameters for the diode resonator model	171
B.1	Parameter values for the Lang-Kobayashi equations	182

Chapter 1

Introduction

1.1 Nonlinear dynamics and predictability

Dynamics is an old and venerable field of physics, with its origins in Newton's discovery of differential equations and his solution for the motion of two bodies under mutual gravitational attraction. Dynamics, most broadly, concerns the behavior of systems as they evolve in time. Today, the multidisciplinary field known as nonlinear dynamics contains an extraordinary range of problems, including those from physics, chemistry, engineering, population ecology, biology, epidemiology, and economics. In fact, it has been quipped that the breadth of nonlinear dynamics is analogous to that of nonelephant zoology.

The modern field of nonlinear dynamics has grown from the insightful work of Poincaré in the late 1800s. He was aware that certain apparently simple problems could not be solved analytically, such as the three-body problem. So he instead developed new geometric methods to address dynamics problems from the standpoint of *stability*, rather than seeking precise analytical solutions valid for all time.

Poincaré also foresaw the possibility of sensitive dependence on initial conditions, a hallmark of deterministic chaos. Chaotic systems display unpredictable long-term aperiodic behavior that depends critically on its initial state. Unpredictable behavior might be expected if a system is driven by random processes, yet the dynamics of chaotic systems are governed by deterministic laws. Poincaré described this paradoxical situation in *The Foundation of Science*:

If we could know exactly the laws of nature and the situation of the

universe at the initial instant, we should be able to predict exactly the situation of this same universe at a subsequent instant. But even when the natural laws have no further secret for us, we could know the initial situation only *approximately*. If that permits us to foresee the subsequent situation *with the same degree of approximation*, this is all we require, we say the phenomenon has been predicted, that it is ruled by laws. But this is not always the case; it may happen that slight differences in the initial conditions produce very great differences in the final phenomena; a slight error in the former would make an enormous error in the latter. Prediction becomes impossible, and we have the fortuitous phenomenon [1].

In 1963, after the dawn of the computer, Lorenz accidentally rediscovered this important feature when he numerically integrated equations for a greatly simplified model of convection in the atmosphere [2]. He also found, however, that there was a deep structure lurking beneath the unpredictable dynamics, that the trajectories were not truly random, despite their unpredictability. Lorenz visualized his system in *phase space*, a geometric construct in which the coordinate axes represent the dynamical variables needed to specify the instantaneous state of the system, and found the chaotic trajectories fell onto an “infinite complex of surfaces,” a fractal object we now call a strange attractor.

The Lorenz system serves as a useful instructional example to illustrate the concepts of phase space and sensitive dependence on initial conditions. Figure 1.1 shows projections in phase space of the Lorenz attractor, with only two variables per graph for ease of visualization. The dynamical variables of the system form the axes of the

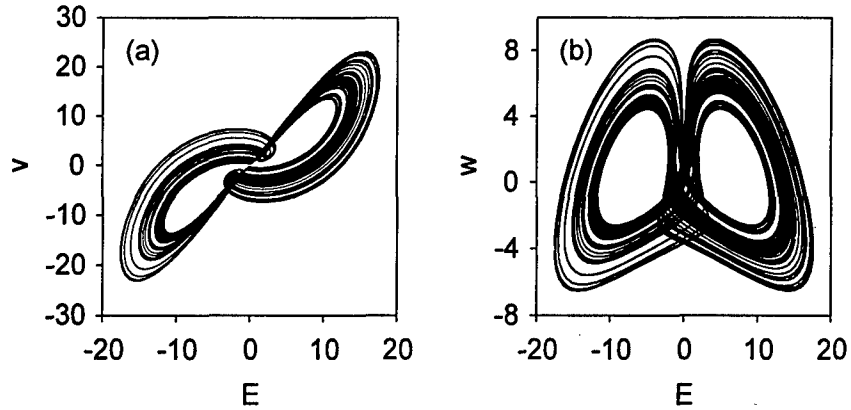


Figure 1.1: Phase space projections of the chaotic Lorenz attractor. The single trajectory shown is complex and aperiodic.

graphs, and their evolution is described by

$$\begin{aligned}
 \dot{E} &= -\kappa(E - v), \\
 \dot{v} &= Ew - v, \\
 \dot{w} &= -b(w + Ev - r).
 \end{aligned}
 \tag{1.1}$$

This form of the equations actually represents a laser system, but is equivalent to Lorenz's convection model equations [3]; E , v , and w represent a normalized electric field, polarization, and population inversion, respectively. I use normalized pump ($r = 40$) and decay ($\kappa = 4$, $b = 0.4$) parameters to generate the single phase-space trajectory (a record of the time evolution of the dynamical variables) shown in Fig. 1.1. To generate it I select an arbitrary initial condition, numerically integrate for a period of time to eliminate transients, and then record the trajectory from $t = 100$ to 375. Note that the trajectory is complex and aperiodic, but is not random (if it were random, the trajectory would fill phase space [4]).

The same Lorenz system can be used to illustrate sensitive dependence on initial

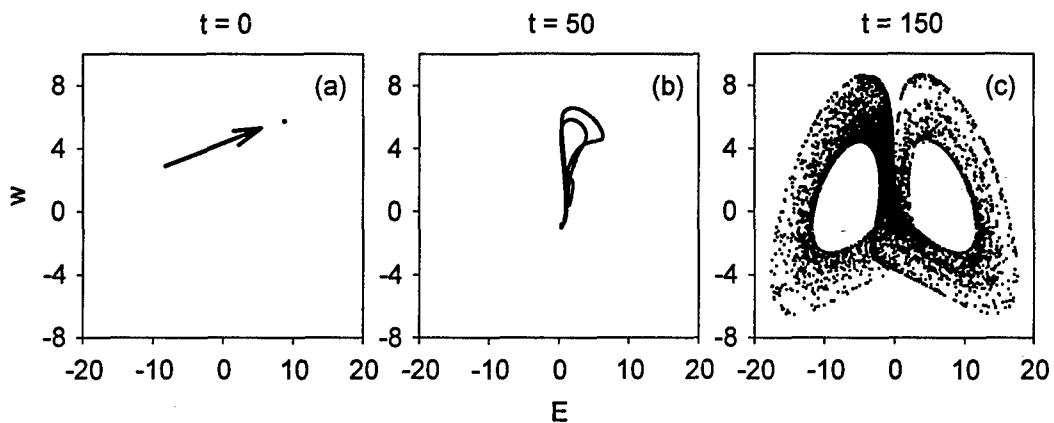


Figure 1.2: Sensitive dependence on initial conditions on the chaotic Lorenz attractor. The chaotic dynamics cause rapid decorrelation of a cluster of closely spaced initial conditions.

conditions, as shown by the sequence of graphs in Figure 1.2. To generate this figure I choose a point on the attractor from the trajectory of Figure 1.1 for an initial condition, and then define a cluster of 8000 additional points located no more than 0.01 in any direction from the central point. The location of this cluster is indicated by the arrow in Fig. 1.2a. I then use these points as initial conditions for the Lorenz equations, and the subsequent plots show their corresponding positions after increasing periods of time. The dot is stretched and folded (1.2b) and quickly fills the attractor (1.2c), losing all correlation with nearby initial states.

The sequence of graphs in Fig. 1.2 demonstrates that having a good model does not result in the ability to predict the behavior of the system when the system is chaotic. However, it is exactly this predictive capability that the scientific community has historically sought from its models of the natural world. Although chaotic systems are beautiful and interesting in their own right to nonlinear dynamicists, their *inherent* unpredictability has also naturally led to the development of techniques to alter their behavior using perturbations to the system, forcing it to be stable or

regular. This is the study of *control*, and it is a growing field within the nonlinear dynamics community. Although control theory is new to this community, it has been and continues to be an active area of research in applied mathematics and engineering [5, 6]. There is a vast, well-developed literature on the subject, and this wealth of expertise has fueled the efforts of nonlinear dynamicists. However, these control techniques have been adapted for *chaotic* systems only recently, perhaps because it seemed so unlikely that they would work. As Freeman Dyson said in 1985,

A chaotic motion is generally neither predictable nor controllable. It is unpredictable because a small disturbance will produce exponentially growing perturbation of the motion. It is uncontrollable because small disturbances lead only to other chaotic motions and not to any stable and predictable alternative [7].

This viewpoint changed in 1990 with the publication of the seminal paper *Controlling Chaos* by Ott, Grebogi, and Yorke (OGY) [8]. They demonstrated that a chaotic system can be stabilized using only small, carefully chosen perturbations by taking advantage of the fact that such systems have unstable solutions called *unstable periodic orbits* (UPO's) that have special characteristics. If the system is placed precisely on any one of the UPO's, it will stay there indefinitely in the absence of noise. However, the slightest perturbation will drive the dynamics off the orbit since it is unstable. As an analogy, consider a marble rolling along the ridge of a saddle: it will oscillate back and forth along the ridge indefinitely, but any disturbance from this trajectory, no matter how small, will make the marble fall off the saddle.

To illustrate, I plot two UPO's of the chaotic Lorenz system in Fig. 1.3, where the chaotic attractor is shown for reference in graph (a). I generate the plot of each orbit by starting the system from initial conditions that are essentially on the UPO

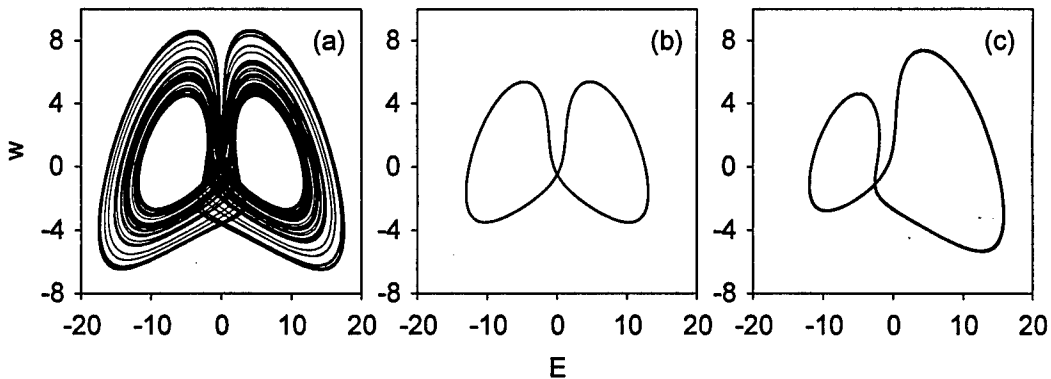


Figure 1.3: Unstable periodic orbits of the Lorenz attractor. Graphs (b) and (c) are two of the simplest unstable periodic orbits embedded in the chaotic attractor shown in graph (a).

and then numerically integrating for at least fifteen cycles around each orbit. The system follows the orbit for the entire time, despite the instability of the UPO. This demonstrates that a system placed very close to an UPO will remain there for a significant period of time, before noise and the orbit's natural instability ultimately drive it away. There are an infinite number of UPO's embedded in a given chaotic attractor [9].

It is possible to stabilize these UPO's using only small perturbations. In simple terms, the outline of the procedure is as follows. The unperturbed system will eventually come sufficiently close to an UPO to remain nearby for a short period of time, since chaotic systems are ergodic. Small perturbations can then be applied to place the system essentially on the UPO and to counteract the destabilizing effects of noise, thereby rendering the orbit stable. For example, suppose a chaotic laser system were near one of the UPO's illustrated in Fig. 1.3. We can measure the laser intensity to detect if the system begins to diverge from the orbit. If it does, we can apply a small perturbation to an accessible system parameter (such as the pump parameter)

in such a way that the system is placed back on the UPO.

Following the OGY concept of stabilizing UPO's, researchers have successfully stabilized a wide variety of systems, including physical, chemical, and biological systems [10]. The first experiments were on relatively simple chaotic systems, involving only temporal instabilities occurring on frequency scales from 10^{-2} to 10^5 Hz. Some current topics in the field now include control and synchronization of systems that are noisy [11, 12, 13], high dimensional or hyperchaotic [14, 15, 16], display spatio-temporal instabilities [17, 18, 19], or have instabilities that occur on very fast time scales [20, 21].

My contribution to this field is primarily in the area of controlling *fast* systems. Specifically, I study systems which exhibit only temporal instabilities on very short time scales. This is an exciting new area; it requires the development of novel control techniques, addresses technologically important systems such as the semiconductor laser, and is still relatively unexplored. There are also particular experimental challenges associated with fast systems. For example, chaotic trajectories rapidly become uncorrelated with their past behavior, so any control perturbations based on information measured from the system must be applied while the information still relates to the current state of the system. This is quantified as *latency*, the time t_ℓ between measuring the system and applying feedback based on that measurement. A second consideration is that it may be difficult to accurately measure the state of the system at discrete times, making some control protocols unworkable such as map-based algorithms.

1.2 Overview of thesis

This dissertation documents my study of controlling instabilities and chaos in fast nonlinear systems. It is organized in eight chapters, covering two major experimental

systems. Chapter 2 is pedagogical in nature, introducing important concepts needed to understand the experiments. Chapters 3 and 4 present my work on a new feedback technique and its application to a fast chaotic electrical circuit. Chapters 5 through 7 describe my study of the characterization and control of an external cavity semiconductor laser. I conclude in Chapter 8 by reviewing the major results obtained and considering further work to be done.

In Chapter 2 I begin by motivating this work more thoroughly, explaining the scientific and technological relevance of the problem of control in nonlinear systems, and fast systems in particular. I then develop the basic concepts needed to understand this work, particularly those of control and linear stability, and show how these ideas can be applied in a simple physical example, the pendulum. I also review some of the research that has preceded my work, including the OGY technique for controlling unstable periodic orbits [22] and Pyragas's time-delay feedback protocol [23].

Following this introduction, in Chapter 3 I begin a thorough study of a new continuous time-delay feedback technique called "extended time-delay autosynchronization" (ETDAS) [20] that is well-suited for control of UPO's in fast systems. It is a completely analog technique based on feedback that is proportional to the difference between the current value of a system variable and an infinite series of past values. Specifically, the form of ETDAS feedback is

$$\delta p(t) = -\gamma \left[\xi(t) - (1 - R) \sum_{k=1}^{\infty} R^{k-1} \xi(t - k\tau) \right], \quad (1.2)$$

where $\delta p(t)$ represents the continuous adjustment of an accessible system parameter p about a nominal value, ξ represents a measured quantity from the system, R determines the relative weight of information from past cycles, τ is the period of the UPO to be stabilized, and γ is the feedback gain. One section of this chapter is intended to develop our understanding of the technique using time- and frequency-domain analy-

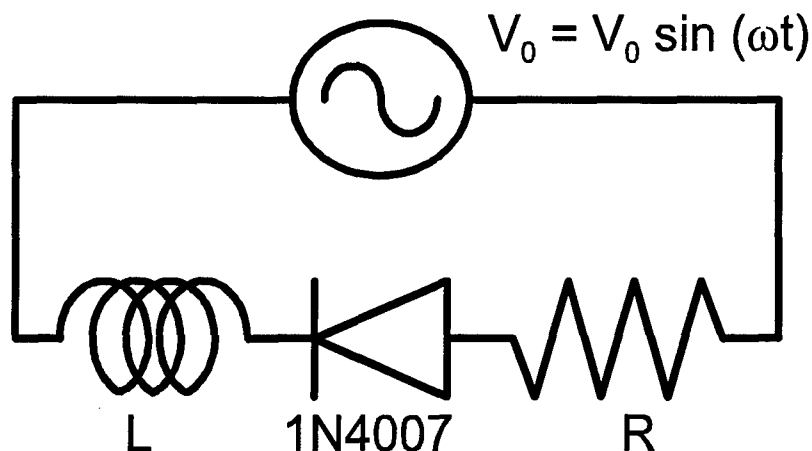


Figure 1.4: The diode resonator.

ses. A subsequent section presents methods for implementing ETDAS, including an all-optical version which holds promise for controlling fast optical systems such as the semiconductor laser. The last section of Chapter 3 presents a detailed electronic implementation of ETDAS, in which I explore some practical issues of developing a feedback system that faithfully reproduces the form of Eq. 1.2. I apply this electronic implementation of ETDAS control in a chaotic circuit, and the results are described in Chapter 4.

I choose the diode resonator [24] as the experimental chaotic system on which to test the efficacy and operation of ETDAS, because it displays a wide range of nonlinear behaviors, is easy to build and customize, and is well-characterized on slow time scales [24]-[31]. As shown schematically in Figure 1.4, it consists of a rectifier diode in series with an inductor L and a resistor R , all driven by a leveled sinusoidal voltage V_0 at a frequency of 10.1 MHz (this experiment represents the fastest instability controlled by feedback to date [21, 32]). I operate this circuit in a regime for which it displays a period-doubling route to chaos. I briefly describe the circuit system in Chapter 4 (more detail is given in Appendix A), and explain my data

acquisition methods. I enumerate the criteria for successful control and demonstrate that ETDAS is significantly more effective than previous time-delay feedback protocols. These results are compared with numerical and theoretical predictions, with good agreement. This study also demonstrates the importance of latency, the time t_ℓ between measuring the system and applying feedback based on that measurement, showing that control becomes impossible when t_ℓ becomes too large. I conclude my work on control of the diode resonator system by investigating the transient behavior and dynamics of the system outside the domain of control, shedding light on the mechanisms by which control may be lost.

In Chapter 5 I introduce and characterize my second experimental system, the unstable external cavity semiconductor laser system. Its dynamics are fast and highly complex, and thus careful characterization is a necessary step before attempting control. This system has been widely studied, both because of the basic scientific interest in the semiconductor laser and because instabilities can degrade the performance of the laser in practical situations (see review articles Refs. [33, 34]). In addition, these instabilities occur on fast time scales; typical relaxation frequencies in laser diodes have been measured to be a few GHz [35]. Thus, semiconductor laser instabilities provide great motivation to devise techniques for control of fast systems.

The origin of instabilities in this system is optical feedback due to weak or moderate reflections from a partial reflector such as an optical disc or a junction in fiber-optic communication lines. Such a system is shown schematically in Fig. 1.5. The output beam from the solitary laser is collimated and directed into a cavity of length L , it strikes a partially reflecting mirror R , and the reflected portion of the incident beam is reinjected back into the solitary laser. The Lang-Kobayashi equations [36] describe the time evolution of the complex field variable E and the carrier density N

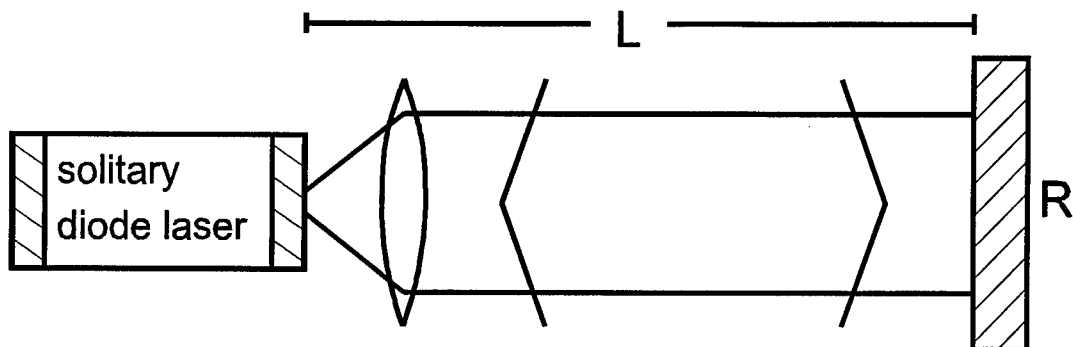


Figure 1.5: External cavity semiconductor laser. A portion of the emitted field is reflected back into the solitary laser after traversing an external cavity of length L .

in this system as

$$\begin{aligned} \frac{dE}{dt} &= \frac{1}{2} (1 + i\alpha) G_N (N - N_{th}) E + \frac{\kappa}{\tau_{in}} e^{-i\omega_0 t} E(t - \tau), \\ \frac{dN}{dt} &= J - \frac{N}{\tau_s} - \left[\frac{1}{\tau_p} + G_N (N - N_{th}) \right] |E|^2. \end{aligned} \quad (1.3)$$

One important feature of these equations is the delay term $E(t - \tau)$ representing the reinjected field. This term causes the otherwise simple system to become infinite-dimensional, and is the source of the instabilities. Chapter 5 will include a discussion of the Lang-Kobayashi equations in greater detail, and a detailed derivation is given in Appendix B.

Several types of instabilities may arise from the injection of the delayed field; the particular manifestation depends on the length of the cavity and the strength of the optical feedback. The instability I study is “low-frequency fluctuations” (LFF), also known as “power dropout events,” which occurs for the case of a long cavity with weak to moderate levels of optical feedback. Its highly complex dynamics occur on a very wide range of timescales, from milliseconds to picoseconds, and its dominant feature is spontaneous, rapid decreases in the laser intensity. It has created much interest since its discovery by Risch and Voumard in 1977 [37], yet questions remain regarding the

physical mechanism of LFF despite two decades of study. For example, it is unclear to what extent the dropouts are caused by quantum fluctuations or by deterministic chaos [38]. Only recently has it been predicted and experimentally confirmed that picosecond pulse dynamics are hidden beneath the slower, nanosecond-scale dropouts [39, 40]. I conclude Chapter 5 by extending these theoretical studies to a first-passage time theory to predict the distribution of interspike intervals (the time between power dropouts), and compare experimental data with these predictions. Details of the first-passage time problem are given in Appendix C.

Chapter 6 describes my first efforts to stabilize this laser system, using open-loop control in the form of a sinusoidal perturbation added to the drive current. Unlike closed-loop feedback schemes such as ETDAS, open-loop control does not suffer from problems with latency and therefore is a natural technique to choose, given that the dynamics of the LFF instability are known to be extremely fast (Section 2.2.1 describes the differences between open- and closed-loop control in greater detail). In addition, this approach has had success in previous laser studies [41]-[44] and is easy to implement. In Chapter 6 I demonstrate that the LFF power dropouts can be entrained with a comparatively slow (~ 20 MHz) modulation in 1:1 and 1:2 ratios, such that one dropout occurs every (or every other) drive cycle. When the frequency of the modulation is higher (hundreds of MHz), I show that the interspike intervals occur preferentially at times that are multiples of the drive period, except when the frequency corresponds to a harmonic of the external cavity. These results are elucidated by numerical simulations.

After this study of open-loop control, Chapter 7 continues the investigation of the laser with the application of a true closed-loop feedback signal to attempt stabilization of an unstable steady state of the system. The control protocol is quite simple, and feeds back only the time-varying component from a measurement of the system.

Specifically, I generate the feedback by detecting the laser intensity, converting it to a voltage, and applying it to the drive current after passing it through a high-pass filter. A similar feedback protocol has been successful in stabilizing an electronic circuit [45], and is actually a limiting case of the ETDAS method discussed in Chapter 3. I find that the feedback control changes the shape of individual power dropouts and changes the distribution of interspike intervals, but is unsuccessful at stabilizing an unstable steady state of the system.

The high-speed, high-dimensional dynamics of LFF make feedback control in this system challenging. There is more work to be done to control this system; we and other groups have proposed all-optical control techniques [32, 46, 47] for control of UPO's that may yet be fruitful in such circumstances. I consider possible future efforts that build on these experiments in Chapter 8, my Conclusion, as I review the major results of this work. There are three appendices following the conclusion. Appendix A contains details of the diode resonator model, including how the parameters that represent my circuit are determined. Appendix B contains the derivation of the Lang-Kobayashi equations, and Appendix C describes the details of the first-passage time theory.

Chapter 2

Fundamentals of nonlinear dynamics and control

This chapter is intended to motivate the importance of studying control in unstable nonlinear systems, and to introduce the tools and concepts needed to understand the results of my investigations. I explain the relevance of this work from the points of view of both fundamental inquiry as well as technological benefit. I review the concepts of control and linear stability, illustrating these points by stabilizing the unstable steady state of a damped pendulum system. Following this example I discuss various feedback control methods and review the development of control of unstable periodic orbits in fast chaotic systems. This review includes the OGY technique and Pyragas' technique, leading to our method of "extended time delay autosynchronization" which is an extension of Pyragas' scheme.

2.1 Motivation

Control systems are all around us, both natural and man-made. For example, the human body has many regulatory systems, such as elevating the heart rate in response to danger and maintaining a constant body temperature. Control mechanisms are also pervasive in technology, ranging from thermostats and engines to electronics and guidance systems. Knowledge of control is therefore necessary both to understand the functioning of natural systems, as well as to design new technological applications.

Control theory has a long history of mathematical analysis and engineering application. Modern control theory remains a very active field, with current topics including optimal control [48] to minimize the "cost" of the controller, adaptive [49, 50] and

robust control [51] in systems where the model or the controller may be imperfect, stochastic control [52], and control of systems with “aftereffect” in which the current behavior is influenced by previous history [53].

Controlling nonlinear dynamics is a particularly important topic because of the overwhelming abundance of systems that display nonlinear and complex behavior. The task is complicated because the dynamics of such systems are challenging to accurately model, understand, and predict. Nonlinear systems near to equilibrium can be described approximately by more tractable linear differential equations, but this severely restricts the regime in which the model is useful. Such simplified models generally give little insight into complex and interesting far-from-equilibrium dynamics such as chaos and turbulence. Furthermore, many analytical techniques that are useful for linear problems (e.g. Laplace transforms, Fourier decomposition) generally cannot be applied if the problem is nonlinear. Finally, the dynamical essence of many systems simply cannot be captured with a linear model, since nonlinear terms necessarily are present in systems for which various elements cooperate, compete, interfere, or otherwise interact.

Additional mathematical complexity is introduced when the system incorporates time delays. The study of delay-differential equations is itself currently an active area of research [54, 55], and it has been shown that time-delay systems have analogies with spatially extended systems [56]. Furthermore, it has been recognized that many natural systems involve time-delays. As examples, some predator-prey population models incorporate a lag between the moment a prey is killed and the earliest time the predator population may increase as a result [57], and a model for controlling blood-sugar levels accounts for the time needed to produce insulin [58]. There is an emphasis on time-delay systems in this thesis; the external cavity generates a delay in the laser system, and the “extended time-delay autosynchronization” feedback

technique relies on information from the past.

In this context, the study of control provides an unique tool to develop our understanding of such systems. We must carefully model a system to design a good control protocol, and the response of the system to control perturbations can in turn probe the model's validity. In a different vein, a control algorithm that is successful at stabilizing unstable periodic orbits or unstable steady states provides a simple empirical method to easily find those states and investigate the dynamical structure of the system.

Beyond the basic scientific value present in studying control of instabilities and chaos, many dynamical systems in applications rely on smooth and predictable behavior for optimum performance. Examples abound in lasers, circuits, aerodynamics, and fluids, to name a few. My emphasis on fast dynamical systems in this thesis is driven by the technological importance of the semiconductor laser, which can display instabilities with GHz frequencies. These instabilities lead to diminished performance of the laser in such applications as fiber-optic communications or CD players. As a more dramatic example, chaotic dynamics can lead to catastrophic failure in biological systems such as the heart, in which regular beating is crucial and the onset of irregular cardiac behavior leads to fibrillation and death of the organism.

In such examples, it is easy to understand why chaos traditionally has been regarded as something to be avoided or eliminated. However, in recent years there has been a growing realization that controllable chaos itself could be put to use. An entire chaotic circuit has been placed on a single integrated circuit, its large number of UPO's providing a rich and flexible signal source [59]. Chaos also has applications for secure communications [60, 61], since information can be masked in a wideband chaotic spectrum. This application relies on *synchronization* of chaos [62], a field intimately related to control. Finally, it is desirable to *maintain* chaotic dynam-

ics in some situations, rather than stabilize them. This process, sometimes called “anti-control,” may play a role in preventing epileptic seizures [63].

2.2 Fundamentals of control

This central issue of this thesis is the problem of control in systems that exhibit unstable dynamics. One key feature of such systems is the presence of unstable states, which allows particular types of control schemes to be applied. I use these control techniques in my research to stabilize or regulate unstable states such as unstable fixed points and unstable periodic orbits by means of perturbations to accessible parameters of the system [64], although one can in principle induce any kind of behavior using an appropriate controller. It is instructive to review these concepts of control and instability to aid in the understanding of the experiments I discuss in later chapters. I use the damped pendulum as an example to help make these concepts more clear.

2.2.1 Open-loop vs. closed-loop control

Techniques for controlling unstable states in nonlinear systems using small perturbations can be divided into two general categories: feedback and nonfeedback approaches. Both are used in this thesis, so it is important to understand their main features and differences. I note that these two methods can be applied individually or in combination for a given system. Figure 2.1 illustrates the generic building blocks needed for the two types. I consider the applicability of both methods to systems with unstable states (although either can be applied to systems which do *not* exhibit chaos or dynamical instabilities).

The open-loop (nonfeedback) scheme is shown in Figure 2.1a. The control perturbation is generated and applied to the system without regard for the current state of

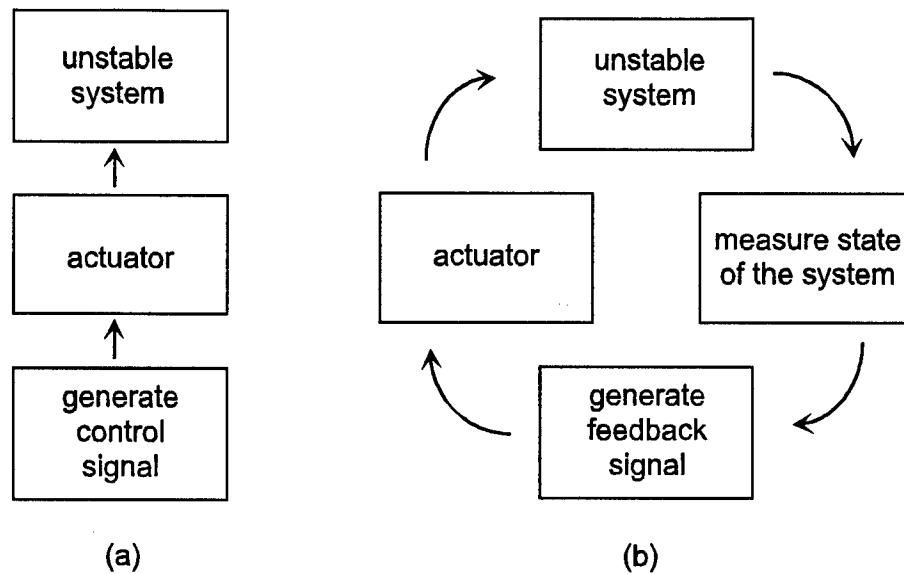


Figure 2.1: Block diagram illustrating open-loop (a) and closed-loop (b) control.

the system. This is accomplished by adjusting an accessible system parameter about its nominal value by a weak periodic signal, usually in the form of a continuous sinusoidal modulation. An orbit is *entrained* when such a scheme [65, 66] is successful, whereby the system is forced into an orbit similar, but not identical, to an unstable state of the unperturbed system. Open-loop schemes have the advantage of being comparatively easy to implement, as they do not require real-time measurement of the state of the system and processing of a feedback signal. Latency is also not a consideration in open-loop methods since the perturbation is predetermined and is applied regardless of the state of the system. Unfortunately, nonfeedback controls are generally less flexible and they fail in many cases to entrain the orbit (success or failure is highly dependent on the specific form of the dynamical system [67]).

In comparison, closed-loop feedback control techniques have the capability to stabilize true unstable states of the system. Figure 2.1b illustrates a feedback system,

consisting of the unstable system that is to be controlled, a device that senses the current dynamical state of the system, a processor to generate an appropriate feedback signal, and an actuator that adjusts an accessible system parameter. Feedback control requires accurate sensing of the system and rapid real-time generation of the feedback signal. Such schemes are often more complicated to implement than open-loop methods, but can still be reasonably simple in certain implementations. Researchers have devised a variety of algorithms for generating the specific form of the feedback signal. One important feature common to all the feedback schemes I consider is that the feedback becomes very small (comparable to the noise level in the system) when the control is successful, indicating that an unstable state of the unperturbed system has been stabilized.

2.2.2 Feedback control in a simple system

Keeping the general ideas of control in mind, I will now consider the specific case of how one can stabilize an unstable steady state using feedback control (note that the basic concepts presented here can be generalized and applied to stabilizing unstable periodic orbits as well). The idea is simple: add feedback to a system in such a way that an unstable state becomes stable.

Before examining the pendulum example, we must briefly recall the basic mathematical description of linear stability. Consider a general system described by two coupled first-order differential equations,

$$\begin{aligned}\dot{x} &= f(x, y), \\ \dot{y} &= g(x, y).\end{aligned}\tag{2.1}$$

We first must locate the fixed points to determine their stability properties. The fixed points of the system, denoted by (x^*, y^*) , are determined by the conditions $f(x^*, y^*) = g(x^*, y^*) = 0$.

We are concerned with the local dynamics about a fixed point, and therefore we linearize the system by defining

$$\begin{aligned}x &= x^* + \delta x, \\y &= y^* + \delta y.\end{aligned}\tag{2.2}$$

Explicitly adding a control term, we now find that the dynamics of a small perturbation about the fixed point is given by

$$\begin{aligned}\begin{pmatrix} \delta \dot{x} \\ \delta \dot{y} \end{pmatrix} &= \begin{pmatrix} \frac{\partial f}{\partial x} & \frac{\partial f}{\partial y} \\ \frac{\partial g}{\partial x} & \frac{\partial g}{\partial y} \end{pmatrix}_{(x^*, y^*)} \cdot \begin{pmatrix} \delta x \\ \delta y \end{pmatrix} + \gamma \mathbf{M} \cdot \begin{pmatrix} \delta x \\ \delta y \end{pmatrix} \\ &= (\mathbf{J} + \gamma \mathbf{M}) \cdot \begin{pmatrix} \delta x \\ \delta y \end{pmatrix},\end{aligned}\tag{2.3}$$

where \mathbf{J} is the Jacobian matrix of the uncontrolled system evaluated at the fixed point (x^*, y^*) , and $\gamma \mathbf{M}$ introduces the control. Note that we have only retained terms that are linear in the small quantities δx and δy .

We can determine the stability of this system about the fixed point by analyzing Eq. 2.3 using standard linear algebra techniques [68]. The fixed point will be linearly stable if all the eigenvalues λ of $\mathbf{J} + \gamma \mathbf{M}$ have negative real parts; if not, it will be unstable. We determine the eigenvalues and eigenvectors by seeking solutions of Eq. 2.3 of the form $e^{\lambda t} \mathbf{v}$, corresponding to exponential growth or decay along the eigenvector \mathbf{v} . Substituting this form into Eq. 2.3 we get the usual eigenvalue equation

$$(\mathbf{J} + \gamma \mathbf{M}) \cdot \mathbf{v} = \lambda \mathbf{v},\tag{2.4}$$

and solve its characteristic equation $\det(\mathbf{J} + \gamma \mathbf{M} - \lambda \mathbf{1}) = 0$ to determine the values of λ .

2.2.3 Stabilizing the damped pendulum

We are now prepared to apply a similar analysis in a physical example. I use the damped pendulum as an example because it is a particularly simple system. It does

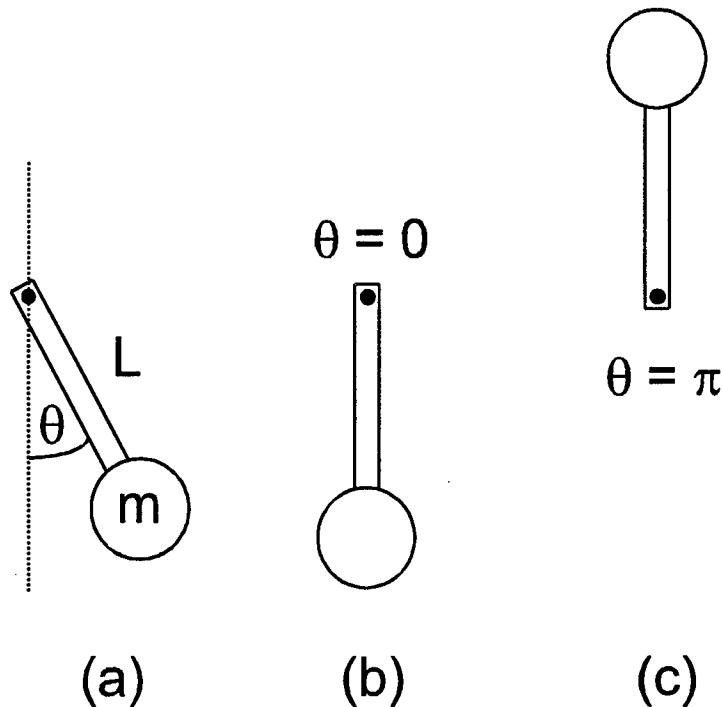


Figure 2.2: The damped pendulum (a) and its stable (b) and unstable (c) steady states.

not exhibit chaos, nor does it possess unstable periodic orbits. It merely has two steady states, one of which is unstable. Through illustration of control in such an uncomplicated case, we may better understand how similar concepts apply in more complex situations.

Consider the typical pendulum illustrated in Fig. 2.2a. It consists of a bob of mass m held a distance L from a pivot point by a rigid massless rod, subject to a uniform gravitational acceleration g . The angle θ of the pendulum is measured from the dashed vertical line, with $\theta = 0$ for the case with the bob directly below the pivot point. We also assume there is some frictional damping in the system.

This system has two steady states, shown in Figs. 2.2b and 2.2c. We intuitively expect that the pendulum will end up at rest in the downward position (2.2b) as

long as there is friction present in the system. This is an example of a *stable steady state*. It is a steady state because if we place the system at rest in that position, it will remain there. It is stable because the pendulum will return to that state even if we nudge the bob slightly away from $\theta = 0$. The inverted position (2.2c), however, is an *unstable steady state* (USS). It still meets the criterion to be a steady state: if we place the system at rest *exactly* at $\theta = \pi$, it will remain there. In contrast with the stable steady state, however, the pendulum will rapidly fall away from the USS in response to the slightest disturbance. This USS is the state we will stabilize using control.

To analyze the system mathematically, consider the usual equation for the damped pendulum,

$$\frac{d^2\theta}{dt^2} + B\frac{d\theta}{dt} + \frac{g}{L}\sin\theta = 0, \quad (2.5)$$

where B is a positive-valued damping coefficient and the other quantities are as defined above. To remove some of the constants, we can express the above equations in dimensionless form by defining the frequency $\Omega = \sqrt{g/L}$ and a dimensionless time $\tau = \Omega t$. If we express time derivatives as $\dot{\theta} = d\theta/d\tau$ and rescale $b = \Omega B$, we can rewrite the pendulum equation as

$$\ddot{\theta} + b\dot{\theta} + \sin\theta = 0, \quad (2.6)$$

which we can express as a set of two first-order differential equations,

$$\dot{\theta} = \omega, \quad (2.7)$$

$$\dot{\omega} = -b\omega - \sin\theta.$$

We can determine the location of the fixed points (θ^*, ω^*) by setting the time derivatives in Eq. 2.7 equal to zero. This leads to the requirements that these steady states have $\omega^* = 0$ and $\theta^* = k\pi$ where k is an integer. Since θ is on a circle, all the

θ^* with even values of k correspond to the stable state, and all the odd values of k correspond to the unstable inverted position.

How could we implement feedback control to stabilize the unstable steady state? One option is to use a simple proportional feedback algorithm, that is, the feedback signal could be defined as $F(\theta) = \gamma(\theta - \theta^*)$, proportional to the difference between the actual angle θ of pendulum and the angle θ^* corresponding to the steady state, multiplied by a gain factor γ (with appropriate units). To implement this feedback, we could detect the angle by attaching a potentiometer to the pivot point and measuring the resistance, and we could apply the feedback to the system as a torque to the pivot point. In simple terms, the feedback signal causes the application of a torque to the pivot if the pendulum's position deviates from the steady state, attempting to restore the position of the pendulum to the USS. The greater the deviation, the greater the restoring torque will be. When the system is on the USS, the feedback vanishes as required, because we do not wish to destabilize the pendulum with an unnecessary perturbation if it is on the USS.

We can now calculate the stability of the USS under feedback control. The equation for the pendulum including feedback is

$$\ddot{\theta} + b\dot{\theta} + \sin \theta = F(\theta), \quad (2.8)$$

leading to

$$\begin{aligned} \dot{\theta} &= \omega, \\ \dot{\omega} &= -b\omega - \sin \theta + \gamma(\theta - \theta^*). \end{aligned} \quad (2.9)$$

From this, the linearized system now can be written in the form of Eq. 2.3 as

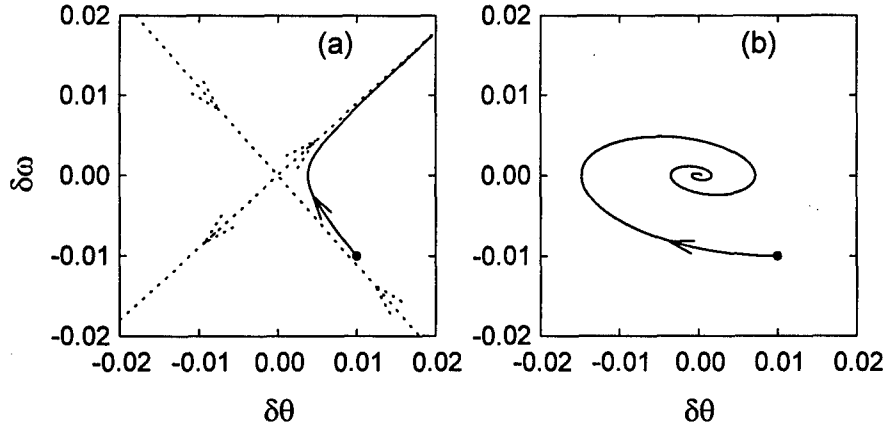


Figure 2.3: Linearized dynamics of the damped pendulum. The graphs show the trajectory without control (a) and when control is added (b), starting from the same initial conditions near the fixed point at $(0,0)$.

$$\begin{aligned} \begin{pmatrix} \delta\dot{\theta} \\ \delta\dot{\omega} \end{pmatrix} &= \begin{pmatrix} 0 & 1 \\ -\cos\theta^* & -b \end{pmatrix} \cdot \begin{pmatrix} \delta\theta \\ \delta\omega \end{pmatrix} + \gamma \begin{pmatrix} 0 & 0 \\ 1 & 0 \end{pmatrix} \cdot \begin{pmatrix} \delta\theta \\ \delta\omega \end{pmatrix} \quad (2.10) \\ &= \begin{pmatrix} 0 & 1 \\ -\cos\theta^* + \gamma & -b \end{pmatrix} \cdot \begin{pmatrix} \delta\theta \\ \delta\omega \end{pmatrix}. \end{aligned}$$

The characteristic equation at the unstable fixed point $(\pi, 0)$ is $\lambda^2 + b\lambda - (1 + \gamma) = 0$.

Solving this we find the values of the eigenvalues are

$$\lambda = \frac{-b \pm \sqrt{b^2 + 4(1 + \gamma)}}{2}. \quad (2.11)$$

We can see that one eigenvalue will always have a positive real part in the absence of control ($\gamma = 0$), confirming that this fixed point is indeed unstable. However, it is possible to force both eigenvalues to have negative real parts by a judicious selection of the feedback gain γ , thereby stabilizing the previously unstable fixed point. The specific condition is that $\gamma < -1$. If γ is sufficiently large and negative the eigenvalues will have an imaginary part, but this only indicates that the system will oscillate as it decays to the stabilized state.

Figure 2.3 illustrates the dynamics of the system in phase space when its initial conditions place it near the USS. The initial conditions are $\delta\theta = 0.01$ and $\delta\omega = -0.01$ (the point indicated by a dot in the diagram), and the damping parameter is $b = 0.2$ for both the uncontrolled (2.3a) and controlled (2.3b) cases. The dotted lines with arrows indicate the location and direction of the stable and unstable manifolds of the uncontrolled system. In the absence of control ($\gamma = 0$), the system approaches the fixed point along the stable direction, but then rapidly falls away along the unstable direction. In Fig. 2.3b, however, the introduction of feedback ($\gamma = -1.2$) stabilizes the fixed point, and the system spirals inward from the same initial conditions.

2.3 The Ott, Grebogi, and Yorke concept

The pendulum example shows that it is possible to stabilize an equilibrium point in a nonlinear system by means of a feedback controller. This concept is well known in control theory [69, 70, 71] and is hardly revolutionary. The idea of controlling *UPO's* in a *chaotic* system, however, is credited to Ott, Grebogi, and Yorke, as published in their 1990 paper [8]. They realized that an UPO could be stabilized since it too is an unstable solution of the system. They also pointed out that the system dynamics must eventually pass near a given UPO since the trajectory in a chaotic system is ergodic [72], thus allowing linearization techniques to be valid.

In their original conceptualization of the control scheme, OGY suggested the use of discrete proportional feedback because of its simplicity and the fact that the control parameters can be determined straightforwardly from experimental observations. In this particular form of feedback control, the state of the system is sensed and adjustments are made to the accessible system parameter as the system passes through a surface of section. The size of the adjustments is proportional to the difference between the current and desired states of the system. Following Ref. [22], consider

a system whose dynamics on a surface of section is governed by the m -dimensional map

$$\mathbf{z}_{i+1} = \mathbf{F}(\mathbf{z}_i, p_i), \quad (2.12)$$

where \mathbf{z}_i is its location on the i^{th} piercing of the surface and p_i is the value of an externally accessible control parameter that can be adjusted about a nominal value \bar{p} . Feedback control of the desired UPO (characterized by the location $\mathbf{z}_*(\bar{p})$ of its piercing through the section) is achieved by adjusting the accessible parameter by an amount

$$\delta p_i = p_i - \bar{p} = -\gamma \hat{\mathbf{n}} \cdot [\mathbf{z}_i - \mathbf{z}_*(\bar{p})] \quad (2.13)$$

on each piercing of the section when \mathbf{z}_i is in a small neighborhood of $\mathbf{z}_*(\bar{p})$ [72], where γ is the feedback gain and $\hat{\mathbf{n}}$ is a m -dimensional unit vector that is directed along the measurement direction [73]. The location of the unstable fixed-point $\mathbf{z}_*(\bar{p})$ must be known before control is initiated; it can be determined from experimental observations of \mathbf{z}_i in the absence of control. The feedback gain γ and the measurement direction $\hat{\mathbf{n}}$ necessary to obtain control is determined from the local linear dynamics of the system about $\mathbf{z}_*(\bar{p})$ using the standard ‘‘pole-placement’’ technique of modern control engineering [5, 22]. They are chosen so that the adjustments δp_i force the system onto the local stable manifold of the fixed point on the next piercing of the section. Successive iterates then collapse to $\mathbf{z}_*(\bar{p})$. As stated previously, δp_i vanishes when the system is stabilized; the control then only has to counteract the destabilizing effects of noise.

Ditto *et al.* [74] performed the first successful experiment using this technique by using it to control the dynamics of a chaotic magnetoelastic ribbon. They reconstructed the map using a time-delay embedding of a time series of a single variable and found that the discrete feedback control scheme is easy to implement, robust to noise, and rather insensitive to imprecise knowledge of $\mathbf{z}_*(\bar{p})$ and γ . Soon af-

ter this success, variants on the control algorithm were developed. Hunt [75] and Peng, Petrov, and Showalter [76] found that control can be obtained by occasionally delivering brief perturbations

$$\delta p_i = -\gamma[\zeta_i - \zeta_*(\bar{p})]\Theta(\tau_i) \quad (2.14)$$

to the system parameter, where $\zeta_i = \hat{\mathbf{n}} \cdot \mathbf{z}_i$, and $\Theta(\tau_i)$ is a square pulse function of duration τ_i . Carr and Schwartz [77, 78] have considered delays and τ_i as control parameters. Often, γ , $\hat{\mathbf{n}}$, ζ_* , and τ_i are determined empirically by adjusting their values to obtain controlled behavior. Note again that δp_i vanishes when the UPO is controlled successfully. In the ensuing years, several additional discrete feedback control schemes that refine the original OGY concept have been devised and applied to experimental systems with natural frequencies ranging from 10^{-2} to 10^5 Hz [10].

2.3.1 Control in fast systems

Scaling these schemes to significantly higher frequencies, such as those encountered in high-speed electronic or optical systems, for example, is challenging for several reasons. As mentioned in Chapter 1, one important issue in high-speed feedback control of chaotic systems is the latency through the control loop, that is, the time t_ℓ between the sensing of the state of the system and the application of the control signal. The latency of the control loop is affected by the propagation speed of the signals through the components of the loop and the processing time of the feedback signal. A second important issue is that it is difficult to accurately sample the state of the system at discrete times in order to compare it with the reference value and to rapidly adjust the control parameter on a time scale comparable to the response time of the system.

As noted in Sec. 2.2.1, open-loop control techniques are easily modified for high-frequency operation since the control signal generated is independent of the state of

the system, thus eliminating concerns about latency and accurate sensing of the system. Alternately, *continuous* closed-loop schemes also avoid or reduce these problems and hence may be useful for controlling high-speed chaos. For example, an obvious extension of the original OGY suggestion for controlling UPO's is to use continuous adjustment of the accessible system parameter by an amount

$$\delta p(t) = -\gamma \hat{\mathbf{n}} \cdot [\mathbf{x}(t) - \mathbf{x}_*(t)], \quad (2.15)$$

where $\mathbf{x}(t)$ is the system trajectory, $\mathbf{x}_*(t)$ is the trajectory of the UPO in m -dimensional phase space, and γ is a constant feedback gain [23, 79]. This scheme is not amenable for controlling the dynamics of high-speed systems, however, because it is difficult to accurately determine, store, and regenerate $\mathbf{x}_*(t)$.

Several researchers have suggested that unstable *steady states* can be stabilized in high-speed chaotic systems using a class of continuous feedback techniques that do not require rapid switching or sampling, nor do they require a reference signal corresponding to the desired orbit. The USS's of a laser [80], an electronic circuit [81], and a model chemical system [82] have been stabilized using continuous adjustment of the system parameter by an amount

$$\delta p(t) = -\gamma \hat{\mathbf{n}} \cdot [d\mathbf{x}(t)/dt], \quad (2.16)$$

often called derivative control. The feedback gain γ is determined from the local linear dynamics of the system about the USS using the standard techniques of modern control engineering, or it can be determined empirically in experiments. As required, $\delta p(t)$ vanishes when the system is stabilized to the USS. An advantage of this scheme is that no explicit knowledge of the USS is required to implement control, unlike the proportional feedback used in the pendulum example. One disadvantage, however, is that derivative control tends to overcorrect for high-frequency noise, possibly destabilizing the system.

There is an alternate method for stabilizing USS's that is not as susceptible to high-frequency noise. This technique prescribes the adjustment of the system parameter p by $\delta p(t)$ where $\delta p(t)$ evolves according to

$$\frac{d}{dt}\delta p(t) = -\gamma \frac{d\xi(t)}{dt} - \omega_o \delta p(t). \quad (2.17)$$

This equation is identical in form to that of a single-pole high-pass filter with a corner frequency ω_o . This feedback technique has been used to stabilize an USS of an electronic circuit [45], and is a limiting form of the ETDAS technique given by Eq. 1.2, described in greater detail later in this section. Further detail on this method is in Chapter 7, in which I apply it to the external cavity semiconductor laser.

Another class of feedback controls are time-delay methods, which take advantage of the information present in a chaotic signal. As first suggested by Pyragas [23], the UPO's of a dynamical system can be controlled using continuous feedback designed to synchronize the current state of the system and a time-delayed version of itself, with the time delay equal to one period of the desired orbit. Specifically, UPO's of period τ can be stabilized by continuous adjustment of the accessible parameter by an amount

$$\delta p(t) = -\gamma[\xi(t) - \xi(t - \tau)], \quad (2.18)$$

where γ is the feedback gain, $\xi(t) = \hat{\mathbf{n}} \cdot \mathbf{x}(t)$, and $\hat{\mathbf{n}}$ is the measurement direction. I refer to this method of control as 'time-delay autosynchronization' (TDAS). Note that as with the other feedback algorithms, $\delta p(t)$ vanishes when the system is on the UPO since $\xi(t) = \xi(t - \tau)$ for all t . I have experimentally demonstrated TDAS by controlling a circuit oscillating at 10 MHz [32]. Others have controlled a lower frequency electronic circuit [83, 84], a fiber laser [85], a glow discharge [86], a magneto-elastic ribbon [87], and a periodically driven yttrium iron garnet film [88]. In addition, TDAS has been demonstrated theoretically to be effective for stabilizing the dynamics

of a tunable semiconductor oscillator [89], neuronal networks [90], lasers [46, 47], and pattern forming systems [18]. The main drawback to TDAS is that it is not effective at controlling highly unstable orbits [83].

Recently we [20] introduced a generalization of TDAS that is capable of extending the domain of effective control significantly [91] and is easy to implement in high-speed systems. I will thoroughly investigate and characterize this new technique in Chapter 3, and test its effectiveness on a chaotic circuit in Chapter 4. The new technique is called “extended TDAS,” or ETDAS. As stated in Chapter 1, stabilization of UPO’s of period τ is achieved by feedback of an error signal that is proportional to the difference between the value of a state variable and an infinite series of values of that variable delayed in time by integral multiples of τ . Recalling Eq. 1.3, ETDAS prescribes the continuous adjustment of the accessible system parameter p by

$$\delta p(t) = -\gamma \left[\xi(t) - (1 - R) \sum_{k=1}^{\infty} R^{k-1} \xi(t - k\tau) \right], \quad (2.19)$$

where $0 \leq R < 1$ regulates the weight of information from the past [92]. This feedback protocol is superior to TDAS in that highly unstable orbits can be stabilized as $R \rightarrow 1$ (the case $R = 0$ corresponds to TDAS). I emphasize that, for any R , $\delta p(t)$ vanishes when the UPO is stabilized since $\xi(t - k\tau) = \xi(t)$ for all t and k , so there is no power dissipated in the feedback loop whenever ETDAS is successful. Note that no property of the UPO must be known in advance except its period. In periodically driven systems, where the period of the orbit is determined from the driving, no features of the UPO need ever be determined explicitly.

In this chapter I have motivated the study of control in fast nonlinear systems and reviewed the fundamental concepts of control. I have examined linear stability and control of the unstable steady state of a pendulum, and introduced a variety of techniques researchers have used to control both USS’s and UPO’s. I have emphasized

practical issues that arise for controlling systems that fluctuate on fast time scales, and introduced several techniques that are well-suited to address these issues. The feedback technique that is most important to this thesis is ETDAS, which will be studied in detail in the next chapter.

Chapter 3

Extended Time-Delay Autosynchronization

In this chapter I present a new continuous feedback scheme called “extended time-delay autosynchronization” (ETDAS) which is well-suited for controlling fast systems. It is designed to control unstable periodic orbits, but can also be adapted to stabilizing unstable steady states. It can be implemented all-optically, and therefore may hold promise for stabilizing the very high-speed dynamics of the semiconductor laser system. To develop an understanding of ETDAS, I first describe its time domain form and then review a general method for performing a linear stability analysis on systems under ETDAS control. A frequency domain analysis further elucidates the function of the control mechanism. I describe a general logical design for ETDAS, and then show how I have implemented it electronically for control of the diode resonator circuit. This study also provides an opportunity to explore some practical issues that may affect the effectiveness of ETDAS, such as designs that minimize latency while faithfully reproducing the ETDAS feedback form. Successful control results will be presented in the next chapter.

3.1 Understanding ETDAS

As introduced in Chapters 1 and 2, ETDAS is a feedback control protocol that is tailored to the demands of stabilizing unstable periodic orbits in fast dynamical systems. It is easily implemented in a completely analog fashion, thereby eliminating the need for accurate sampling of the fast system at discrete times. This relative simplicity also makes it possible to design ETDAS systems with small latencies, the

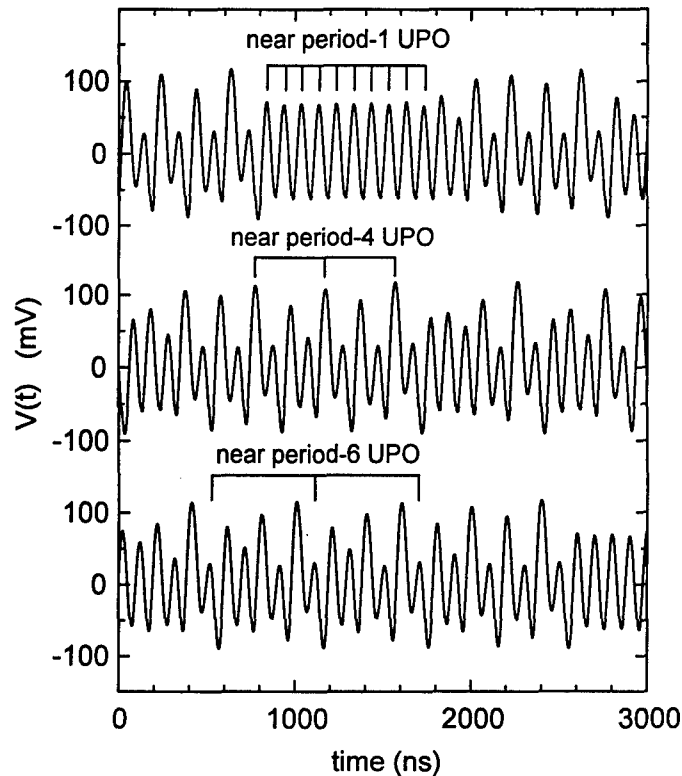


Figure 3.1: Evidence of unstable periodic orbits in the chaotic diode resonator. Three regions of approximately periodic behavior indicate the system is near an UPO.

time between sensing the state of the system and applying feedback based on that measurement. Furthermore, it does not require extensive *a priori* characterization of the state to be stabilized; all that must be known is the period of the UPO.

This new feedback protocol takes advantage of the dynamics of the system in a neighborhood of an UPO to effect stabilization. Recall that a chaotic system near a given UPO will remain in a neighborhood of that orbit for a short time before falling away to other behaviors, and if the system is placed *exactly* on an UPO it will reside there forever (assuming the a noise-free system). Figure 3.1 shows an example of chaotic oscillations in which the presence of UPO's is clearly evident with the appearance of nearly periodic oscillations for short intervals (this figure illustrates

the dynamical evolution of the diode resonator circuit described in the next chapter).

Fig. 3.2 is an abstract illustration that shows some of the quantities used in ETDAS. The system is initially very close to an UPO, and the measured variable $\xi(t)$ is nearly periodic. Later, the system begins to diverge from it (the location of the UPO is indicated by the dotted line). The ETDAS scheme generates feedback through a continuous comparison of the current state of a system variable $\xi(t)$ with its past values $\xi(t - k\tau)$ where τ is the period of the UPO to be controlled. The feedback is designed to vanish if the system is on an UPO, that is, if the past values $\xi(t - k\tau)$ are the same as the current value $\xi(t)$. However, ETDAS immediately detects changes and applies negative feedback to the system to compensate if the system begins to move away from the UPO due to noise or the natural instability of the orbit. This self-adjusting character may allow ETDAS to maintain control even if the underlying attractor gradually drifts, making it attractive for use with lasers in poorly regulated environments, for example [93].

3.1.1 The ETDAS feedback form

Stabilization of UPO's of period τ is achieved by feedback of an error signal that is proportional to the difference between the value of a state variable and an infinite series of values of that variable delayed in time by integral multiples of τ . As introduced in previous chapters, ETDAS prescribes the continuous adjustment of the system parameter p by

$$\delta p(t) = -\gamma \left[\xi(t) - (1 - R) \sum_{k=1}^{\infty} R^{k-1} \xi(t - k\tau) \right], \quad (3.1)$$

where γ is the feedback gain, and $\xi(t) = \hat{\mathbf{n}} \cdot \mathbf{x}(t)$ where $\mathbf{x}(t)$ is the state vector and $\hat{\mathbf{n}}$ is the measurement direction. The parameter R lies between 0 and 1, and regulates the "memory" of ETDAS, determining the relative weight given to information from

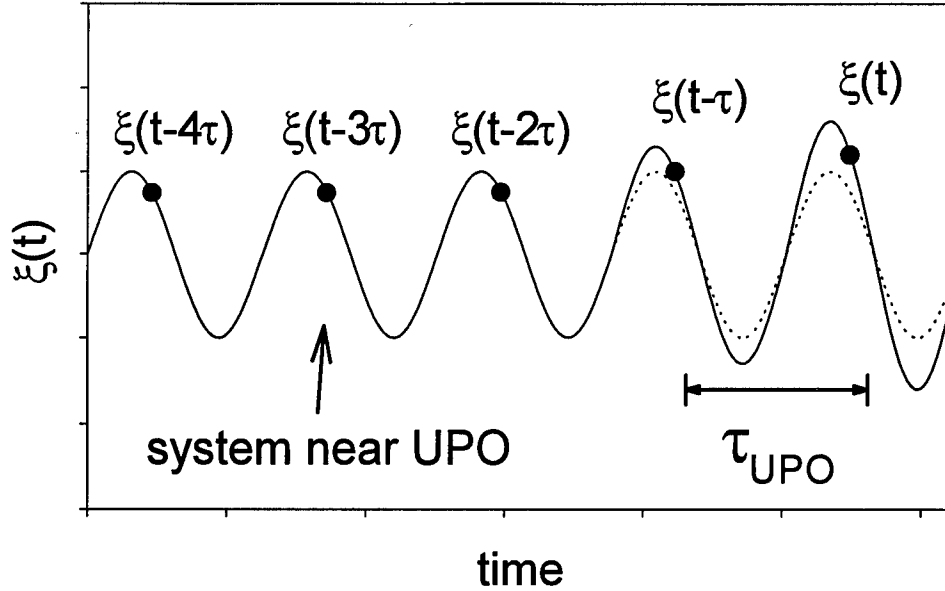


Figure 3.2: Illustration of ETDAS. The system is initially near an UPO, but then diverges from it. The dots indicate the values of $\xi(t)$ at various times, separated by the period τ of the UPO.

the past [92]. The case $R = 0$ reduces to the scheme introduced by Pyragas [23]. As $R \rightarrow 1$, however, highly unstable orbits can be stabilized, representing a significant improvement of the control scheme. The error signal $\delta p(t)$ vanishes when the UPO is stabilized since $\xi(t - k\tau) = \xi(t)$ for all t and k , regardless of the value of R chosen. No property of the UPO must be known in advance except its period. If the system is regularly driven, this task is simple since the period of the UPO must be an integral multiple of the drive period.

If the system to be controlled fluctuates on a very short time scale, it may be impossible to produce a feedback signal that faithfully reproduces the form of Eq. 3.1 due to the latency of the control loop. This problem is minimized with ETDAS but still may be of importance in very fast systems. Under conditions when the

latency is significant, the actual adjustment of the system parameter is given by $\delta p_{\text{actual}}(t) = \delta p(t - t_\ell)$.

3.1.2 Linear stability analysis

Successful use of ETDAS requires appropriate choices for the control parameters γ and R . Although it is often possible to determine suitable values empirically in an experiment, it is important to have some theoretical guidance. This can be accomplished by performing a linear stability analysis of the system in the presence of ETDAS feedback control for fixed \hat{n} and \bar{p} . Such an analysis can yield important information, such as identifying the orbits that may be controlled, and the range (if any) of feedback gain needed to achieve control for a particular R . The continuous time-delay nature of ETDAS makes this a difficult task. However, Bleich and Socolar [94] have formulated a general method to approach this analysis, which I briefly review in this section. Bleich [95] gives a thorough description of the details of the analysis and the numerical procedures needed, as well as results of its application to several theoretical systems, including the laser Swift-Hohenberg equations for a semiconductor laser with a single longitudinal mode [96, 97].

The analysis proceeds by considering a system described by

$$\begin{aligned}\dot{\mathbf{x}}(t) &= \mathbf{f}(\mathbf{x}(t), t; p), \\ p &= \bar{p} + \delta p(t),\end{aligned}\tag{3.2}$$

where the ETDAS feedback signal $\delta p(t)$ (given by Eq. 3.1) is included as a perturbation to the parameter \bar{p} . This analysis considers the case where the latency of the control loop can be ignored ($t_\ell = 0$).

Following Ref. [94], I consider small perturbations $\mathbf{y}(t) = \mathbf{x}(t) - \mathbf{x}_*(t)$ about a τ -periodic orbit $\mathbf{x}_*(t)$. The dynamics of the perturbations in a neighborhood of the

orbit are governed by

$$\dot{\mathbf{y}}(t) = \mathbf{J}(t) \cdot \mathbf{y}(t) - \gamma \mathbf{M}(t) \cdot \left[\mathbf{y}(t) - (1 - R) \sum_{k=1}^{\infty} R^{k-1} \mathbf{y}(t - k\tau) \right], \quad (3.3)$$

where $\mathbf{J}(\mathbf{x}_*(t)) \equiv \partial \mathbf{f} / \partial \mathbf{x} |_{\mathbf{x}_*(t), \bar{p}}$ is the Jacobian of the uncontrolled system and $\mathbf{M}(\mathbf{x}_*(t)) \equiv (\partial \mathbf{f} / \partial \mathbf{p} |_{\mathbf{x}_*(t), \bar{p}}) \otimes \hat{\mathbf{n}}$ is an $m \times m$ dyadic that contains all information about how the control is applied to the system and how small changes in p affect it. The general solution to Eq. 3.3 can be decomposed into a sum of periodic functions (modes) with exponential envelopes. The growth of an exponential envelope in a period τ is quantified by its Floquet multiplier μ which can be found from the modified eigenvalue equation

$$\left| \mu^{-1} \mathbf{T} \left[\exp \int_0^\tau \left(\mathbf{J}(t) - \gamma \frac{1 - \mu^{-1}}{1 - \mu^{-1} R} \mathbf{M}(t) \right) dt \right] - \mathbb{1} \right| = 0, \quad (3.4)$$

where the time-ordered product notation $\mathbf{T}[\dots]$ represents the operator which advances $\mathbf{y}(t)$ forward in time by an amount equal to τ , and $\mathbb{1}$ is the identity matrix. In general, the time-ordered product cannot be obtained analytically, although it can be found using numerical techniques. To simplify our discussion, we denote the left-hand-side of Eq. 3.4 by $g(\mu^{-1})$. Note that g has an infinite number of roots, corresponding to the infinite number of modes introduced by the time delay.

An UPO is linearly stable under ETDAS control for a given set of parameters if and only if all the Floquet multipliers lie inside the unit circle in the complex plane, that is, if $|\mu| < 1$ for all μ satisfying Eq. 3.4. Equivalently, the system is stable if and only if g has no roots on the unit disk since $g(\mu^{-1})$ has no poles on the unit disk. The number of roots of $g(\mu^{-1})$ on the unit disk can be determined by counting the number of times $g(\mathbf{z})$ winds around the origin as \mathbf{z} traverses the unit circle. A necessary and sufficient condition for linear stability of the UPO in the presence of ETDAS feedback control is that this winding number vanish. I note that an approximate stability analysis of Eq. 3.2 has been undertaken recently [98].

3.1.3 Frequency domain analysis

While the time-domain stability analysis outlined above gives a complete picture of ETDAS feedback in a neighborhood of the UPO, a frequency-domain analysis helps clarify the underlying reasons for its effectiveness in stabilizing highly unstable orbits as $R \rightarrow 1$. Specifically, it is instructive to consider the “transfer function” of ETDAS, which relates the output to the input as a function of frequency. Since the ETDAS feedback signal given by Eq. 3.1 linearly relates the input signal $\xi(t)$ with the output signal $\delta p(t)$, we can express $\delta p(f) = -\gamma T(f)\xi(f)$, where $\xi(f)$ and $\delta p(f)$ are the Fourier amplitudes of the input and output signals, respectively, and $T(f)$ is the transfer function. From this analysis, the expression for $T(f)$ is

$$T(f) = \frac{1 - \exp(i2\pi f\tau)}{1 - R \exp(i2\pi f\tau)}. \quad (3.5)$$

The transfer function “filters” the observed state of the dynamical system, characterized by $\xi(f)$, to produce the necessary negative feedback signal.

Figure 3.3 shows the frequency dependence of $|T(f)|$ for $R = 0$ (TDAS) and $R = 0.65$ (ETDAS). One important feature of this figure is the series of notches in $|T(f)|$ that drop to zero at multiples of the characteristic frequency of the orbit $f_* = \tau^{-1}$. These notches ensure that the feedback vanishes when the system is on the UPO, because the spectrum $\xi(f)$ of the system consists of a series of δ -functions at multiples of f_* when it is on the UPO, and therefore the filter must remove these frequencies so that $\delta p(f) = 0$. A second important feature of $|T(f)|$ is that the notches become narrower for larger R , which indicates that the ETDAS feedback is more effective in stabilizing UPO's partly because it is more sensitive to frequencies that could potentially destabilize the UPO. That is, the narrower notches imply that more feedback is generated for signals with frequency components that differ only slightly from the desired set. In addition, $|T(f)|$ is more uniform in magnitude

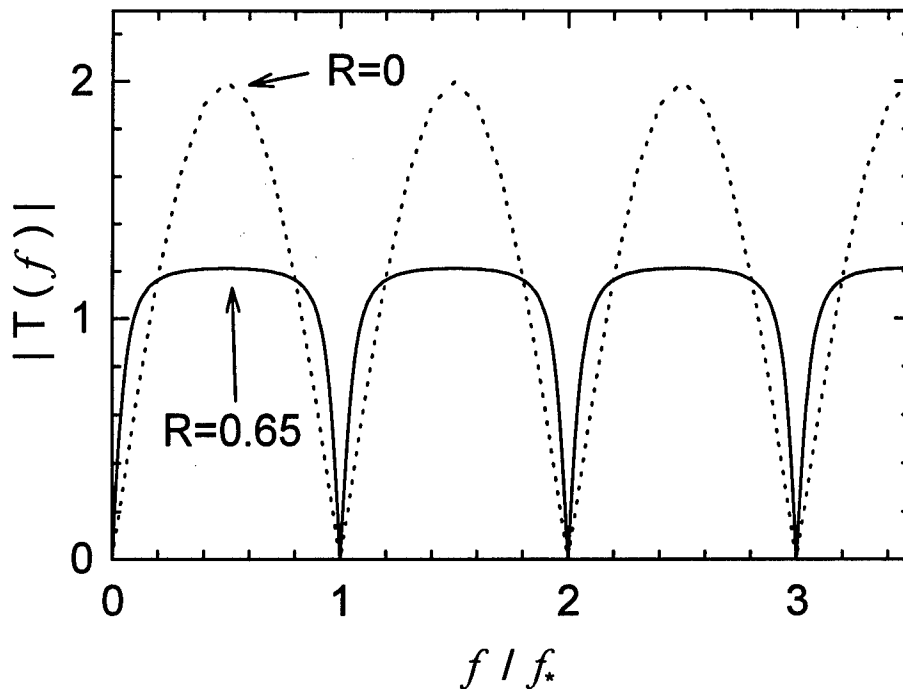


Figure 3.3: Transfer function of ETDAS. The “notches” at multiples of f_* indicate that no feedback is generated if the system is on the UPO.

between the notches for larger R , so the system is less likely to be destabilized by a unnecessarily large feedback response at intermediate frequencies.

Note that one could construct other transfer functions possessing notches at multiples of f_* that could also stabilize the dynamics of the UPO. For example, a continuous version of a map-based technique given by Flake *et. al.* [99] leads to a transfer function consisting of a truncated sum of Fourier components. In this case, $|T(f)|$ from $f = 0$ to f_* appears as a Fourier series approximation of a square wave. However, Eq. 3.5 is easy to implement experimentally.

3.2 Implementing ETDAS

3.2.1 General implementation

ETDAS feedback control of UPO's can be implemented straightforwardly using a variety of techniques, even on fast time-scales. One possible logical design of the feedback loop is shown schematically in Fig. 3.4. The bold letters are reference points used in the following description of the signal flow, as well as in the specific electronic implementation described in Sec. 3.3. I assume in this description that the components impart negligible propagation delays on the various signals (except, of course, for the intentional delay τ necessary to form the ETDAS feedback signal).

The dynamical variable $\xi(t)$ from the system is converted to a voltage $V(t)$ by a transducer. The power of this signal is split equally between two different paths (point **A**). Half of the signal is directed to one input port (point **B**) of a voltage subtraction device and is related to the first term on the right-hand-side of Eq. 3.1; the other half is directed to one input port (point **C**) of a voltage addition device forming part of the group of components (dashed box) generating the delay terms in Eq. 3.1. The signal in the latter path emerges from the addition device, propagates through a variable delay line with the delay time set equal to the period τ of the desired UPO (point **D**), is attenuated by an amount R , and is injected into the second port (point **E**) of the addition device where it is combined with the original signal. A high-impedance buffer senses the voltage signal at the output of the delay line (point **D**). The signal emerging from the buffer is attenuated by $(1 - R)$ and injected into the second port (point **F**) of the voltage subtraction device, representing the second term on the right-hand-side of Eq. 3.1. The signal emerging from the subtraction device (point **G**) is proportional to the ETDAS error signal; it is amplified and injected into a transducer that adjusts the accessible control parameter by $\delta p(t)$.

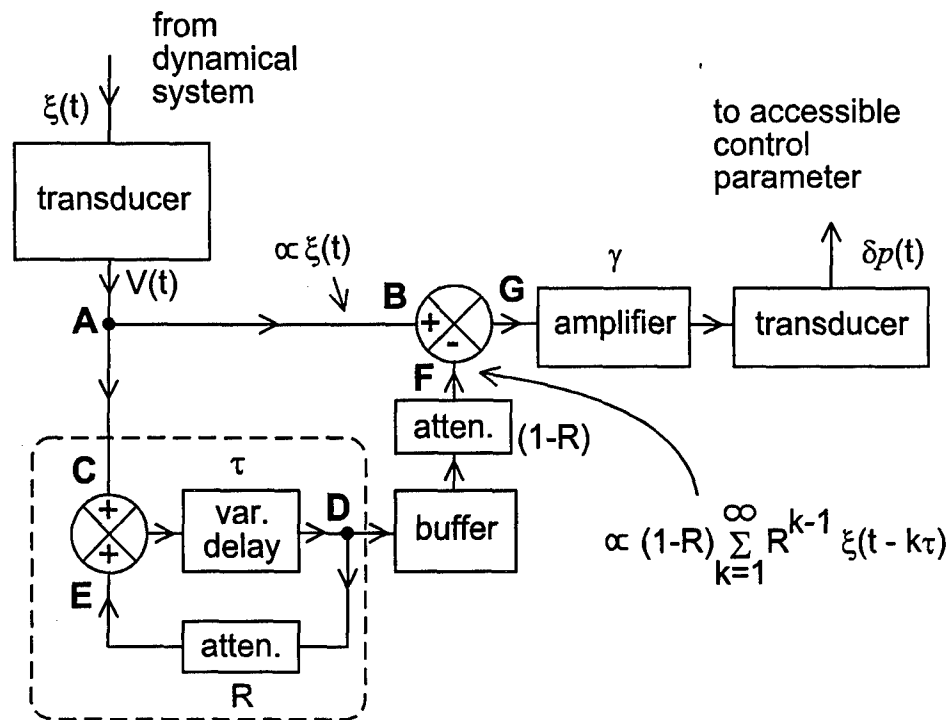


Figure 3.4: Logical design for an ETDAS system. The signal $\xi(t)$ from the dynamical system is processed to generate $\delta p(t)$. The components in the dashed box generate the infinite series of time-delay terms using a single delay line.

The ability of ETDAS to be implemented using only analog components makes this design amenable to high-speed operation, although the unavoidable propagation delays through components must be thoroughly characterized in any real implementation for fast systems. As described in Sec. 3.3, small additional time delays must be added to the feedback system and adjustments must be made to compensate for the time delays inherent in the components. However, ETDAS need not be implemented in an analog fashion, if the dynamics to be controlled are sufficiently slow. In this case, all of the operations performed by the components between the input and output transducers could be accomplished by a digital computer equipped with analog-to-digital and digital-to-analog converters.

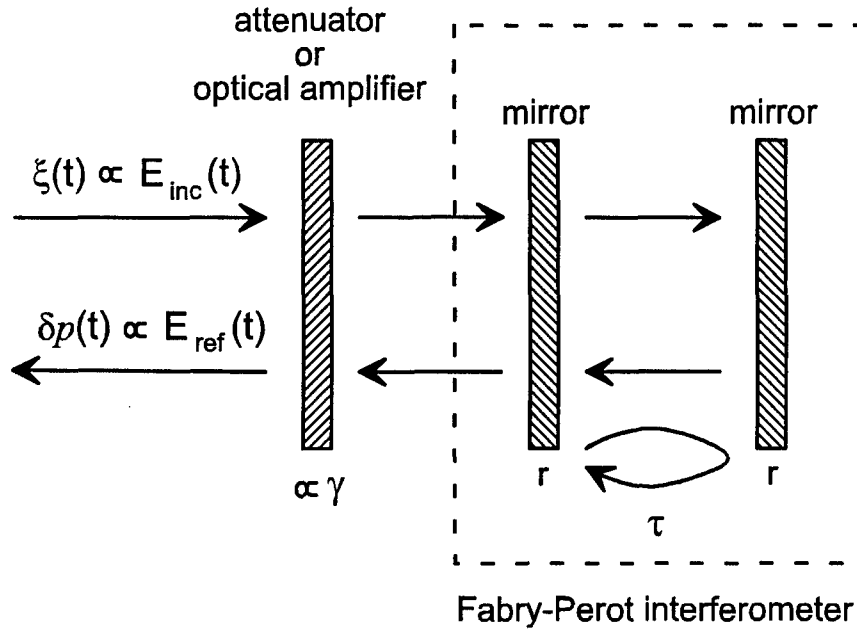


Figure 3.5: All-optical implementation of ETDAS. The interferometer in the dashed box creates the time-delay series, with τ equal to the roundtrip time of light in the cavity.

3.2.2 All-optical implementation

One useful feature of ETDAS feedback is the ability to generate the error signal using an all-optical technique [17, 20, 46, 47]. Specifically, the form of the ETDAS error signal given by Eq. 3.1 is identical to an equation that describes the reflection of light from a Fabry-Pérot interferometer [100], where $R = r^2$ corresponds to the weighted average of the amplitude-reflection-coefficients r of the mirrors, and τ corresponds to the round-trip transit-time of light in the cavity. In one possible scenario, the input transducer shown in Fig. 3.4 generates a laser beam of field strength $E_{inc}(t)$ that is directed toward an optical attenuator or amplifier (controlling γ) and a Fabry-Pérot interferometer as shown in Fig. 3.5. The field $E_{ref}(t)$ reflected by the interferometer passes through the attenuator/amplifier and is converted to the ETDAS error signal

$\delta p(t)$ by the output transducer. It may be possible to control fast dynamics of optical systems that generate directly a laser beam, such as semiconductor diode lasers, using the field generated by the laser as the measured system parameter $\xi(t)$ and as the accessible system parameter $\delta p(t)$; no transducers are required [17, 20, 46, 47].

3.3 Implementation for the diode resonator

3.3.1 Electronic circuit layout

I use an analog-electronic implementation of ETDAS to control the dynamics of a fast chaotic electronic circuit known as a diode resonator, described in the next chapter. The circuitry is shown schematically in Fig. 3.6 (component values are given in Table 3.1). This implementation attempts to mimic as closely as possible the generic design illustrated in Fig. 3.4. It addresses practical considerations such as the finite propagation time of the signals through the components, distortion of the signals, and noise, balanced against the simplicity of the layout, ease of construction, and price.

The electrical signals propagate through the circuit in a fashion similar to that described in Sec. 3.2.1 for the generic implementation of ETDAS; points (A-F) in Fig. 3.6 for the specific implementation correspond to the same points in Fig. 3.4 for the generic implementation. One crucial goal of the circuit layout shown in Fig. 3.6 is to ensure both that the difference in propagation time of signals from points A→G' and A→D'→D→F→G' is equal to τ and the time in the delay loop D→E→D'→D is also equal to τ , in order to faithfully produce the ETDAS error signal. This task is complicated by the nonzero propagation delays through the electronic components.

In my layout, the measured system parameter $V(t)$ is sensed by a high-impedance buffer (B1) and the power associated with this signal is split equally between two different paths (point A). Half of the signal is directed to the input (point B) of

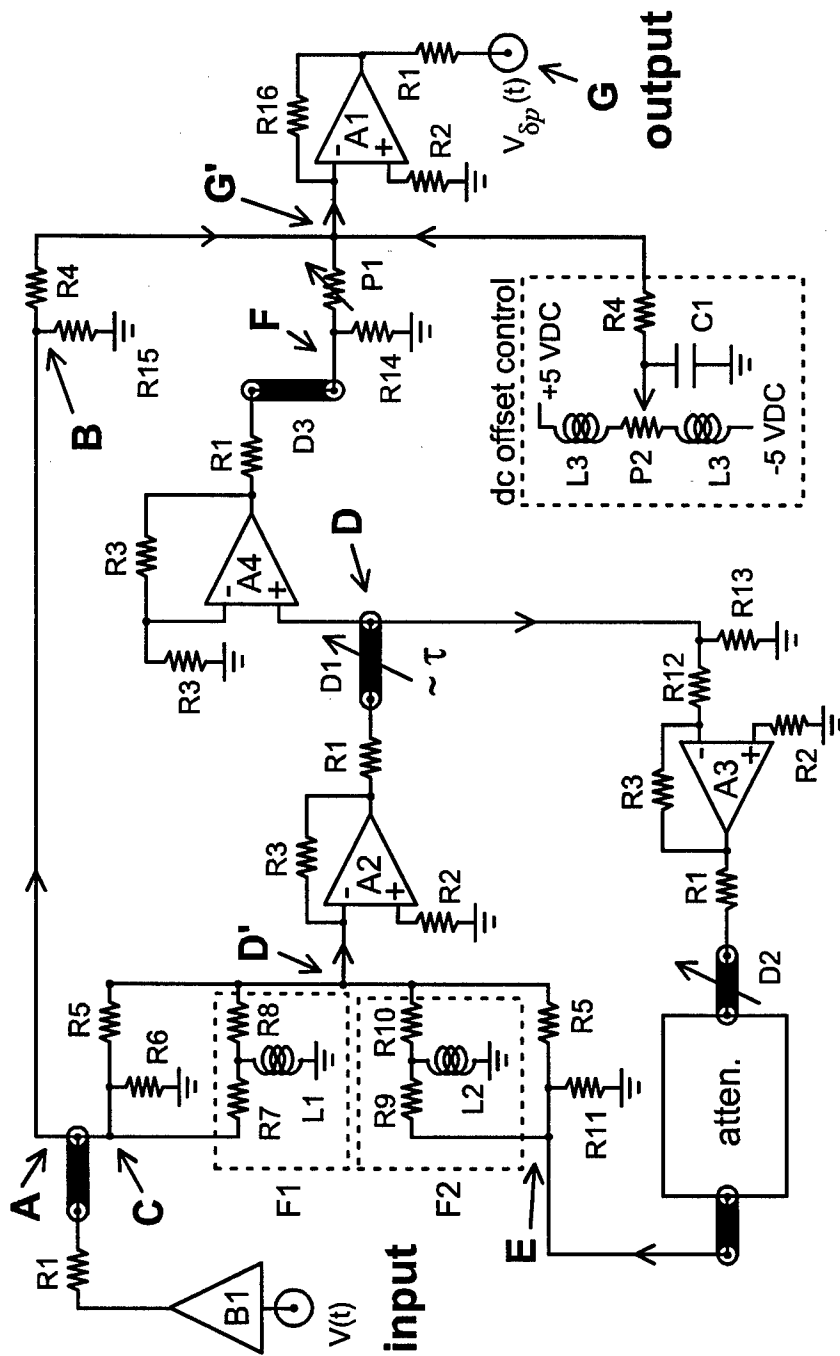


Figure 3.6: Electronic implementation of ET DAS for control of the fast diode resonator. See text of Sec. 6.3.2 for a description.

Component	Value
R1	50 Ω
R2	100 Ω
R3	715 Ω
R4	499 Ω
R5	357 Ω
R6	255 Ω
R7	150 Ω
R8	402 Ω (590 Ω for p-4)
R9	100 Ω
R10	825 Ω (1540 Ω for p-4)
R11	140 Ω
R12	324 Ω
R13	59 Ω
R14	53.6 Ω
R15	215 Ω
R16	1000 Ω
L1	0.33 μH (1.0 μH for p-4)
L2	0.33 μH (1.0 μH for p-4)
L3	3.3 μH
C1	0.1 μF
P1	5 $k\Omega$
P2	1 $k\Omega$

Table 3.1: Component values for electronic implementation of ETDAS.

an inverting, summing operational amplifier ($A1$) and the other half is directed to the input (point **C**) of a second inverting, summing amplifier ($A2$) where it is filtered with predistortion circuitry ($F1$). The signal emerging from $A2$ propagates through a long, variable delay line ($D1$) with a delay time set close to, but less than, the period τ of the desired UPO. It is then inverted and amplified ($A3$) by a fixed amount to compensate for the average loss of the delay line, passed through a short variable delay line ($D2$), attenuated to set the control parameter R , and directed to the input (point **E**) of $A1$ where it is filtered with predistortion circuitry ($F2$). The signal emerging from the long delay line (point **D**) is sensed with a noninverting amplifier ($A4$), passes through a short variable delay line ($D3$, point **F**), and is directed to the input of the summing amplifier $A1$ where it is attenuated by a factor equal to $(1 - R)$ by adjusting $P1$. The signal emerging from $A1$ (point **G**) is proportional to the ETDAS error signal; it is directed to additional amplifiers to set the feedback gain γ and injected into the diode resonator.

3.3.2 Selection of components

I have emphasized that a primary issue in designing the ETDAS circuitry is minimizing the control-loop latency t_ℓ . The latency must be much less than ~ 100 ns to control the diode resonator, as will be shown experimentally in the next chapter. In this proof-of-principle investigation of ETDAS, I select commercially available, inexpensive operational amplifiers and buffers which add very little to t_ℓ yet are easy to obtain and incorporate into the design. For our choice of components, $t_\ell \sim 10$ ns. Smaller latencies may be possible using custom-built microwave circuitry; I do not explore this option, mainly due to the greatly increased cost of such an implementation.

The control-loop latency is governed by the time it takes for the signal to prop-

agate from the input to the output of the ETDAS circuitry following the path $A \rightarrow B \rightarrow G$, since the portion of the signal at G ideally should be proportional to the input signal (with no time lag). Propagation delays of the signal along other paths are not as important because they can be compensated for by using a slightly shorter coaxial cable ($D1$). I use the AD9620 unity-gain buffer (Analog Devices [101], propagation delay $\lesssim 1$ ns, bandwidth 600 MHz) for $B1$ and the AD9618 amplifier (Analog Devices, propagation delay $\simeq 3$ ns, bandwidth 160 MHz) for $A1$ because they have short propagation delays, are relatively easy to use, and are low cost. In the parts of the circuit where propagation delays are not as important ($A2$ - $A4$), I select the AD811 amplifier (Analog Devices, propagation delay $\simeq 6$ ns, bandwidth 140 MHz) because its stability is less sensitive to the precise layout of the components. Note that the bandwidth of all components is significantly larger than the characteristic frequency of the chaotic system (10.1 MHz), thereby minimizing the distortion of the ETDAS feedback signal. Operational amplifiers and buffers with similar or better specifications should produce similar results.

Due to the high bandwidth of these devices, I use standard high-frequency analog electronic techniques. The components are laid out on a home-made, double-sided printed circuit board in which the signal traces form a transmission line (nominal impedance 50Ω) and are kept under 2 cm. Also, proper ground planes are maintained under all components, and PC board mounted SMA jacks are used to transfer the signals from the board to coaxial cables. The printed circuit boards are fabricated in the following multi-step process: I create a graphical layout of the traces using a simple drawing program on a personal computer; the drawing is printed on a 'transfer film' with a laser printer [102]; the traces are transferred to the clean, bare copper surface of the board; the plastic backing of the transfer film is removed; the board is etched using a hot ammonium persulfate solution; holes are drilled for the leads of the

components; and the components are soldered to the board. The power supply leads to all operational amplifiers are bypassed with ceramic and tantalum capacitors as close as possible to the power supply pins, and ferrite beads isolate the power supply lines between components. The DC offset voltage of the amplifiers is compensated at the last stage of the circuitry (point G') by adding a DC voltage to the signal from a filtered, adjustable power supply, as shown in Fig. 6. All signals routed between the ETDAS and other circuit boards propagate through short 50Ω coaxial cables (type RG-58/U).

Another critical issue in the implementation of ETDAS feedback is minimizing the distortion of signals propagating through the coaxial delay line $D1$, due to frequency-dependent attenuation and phase shift. Distortion is difficult to avoid for the high-period UPO's because the delay line is long, and for the case when the feedback parameter $R \rightarrow 1$ since the signals circulates many times through the delay line. To minimize the distortion, I use low-loss, semi-rigid 50Ω coaxial cable (1/4" HELIAX type FSJ1-50A [103]). I find that this delay line gives superior performance in comparison to standard coaxial cable (type RG-58/U). The attenuation characteristics of the HELIAX cable is 0.175 dB/100 ft. at 1 MHz and 1.27 dB/100 ft. at 50 MHz which should be compared to 0.33 dB/100 ft. at 1 MHz and 3.15 dB/100 ft. at 50 MHz for the RG-58/U cable. Previous implementations of TDAS have used for the delay line a variable length transmission line [20], electro-optic delay line [85], or digital first-in-first-out delay device [86].

3.3.3 Adjustment of circuit parameters

The final preparation step for controlling the dynamics of the chaotic system using ETDAS feedback is to adjust the time delay τ and the feedback parameter R . I note that setting τ requires adjusting the propagation time of signals following *two*

different paths. Referring again to Fig. 3.6, the difference in time it takes for signals to propagate from $A \rightarrow B \rightarrow G'$ and from $A \rightarrow D \rightarrow F \rightarrow G'$ must be equal to τ . *In addition*, the propagation time around the delay loop ($D \rightarrow E \rightarrow D' \rightarrow D$) must also equal τ . Note that these times include the propagation time through all components: the coaxial cable, the amplifiers and attenuators, and the signal traces and connectors. The timing can be achieved straightforwardly using three coaxial delay lines $D1$ - $D3$. The long delay line $D1$ consists of the combination of a HELIAX cable whose propagation time is close to but less than τ , connected to a short coaxial cable (type RG-58/U) and a constant-impedance adjustable delay line (Hewlett-Packard model 874-LK10L [104]) for fine and ultra-fine adjustment of $D1$, respectively. The short variable delay line $D2$ consists of another adjustable delay line and coaxial cable (type RG-58/U) whose length is just long enough to connect the variable delay to the printed circuit board. Finally $D3$ is simply a short, fixed coaxial cable (type RG-58/U).

Initial adjustment of the timing is achieved by injecting a weak sinusoidal voltage whose period is equal to τ at point A . The first step is to adjust the circuitry for TDAS feedback ($R = 0$), that is, to set the path difference between $A \rightarrow B \rightarrow G'$ and $A \rightarrow D \rightarrow F \rightarrow G'$ exactly to τ . To accomplish this, the circulating loop is temporarily disabled by disconnecting the attenuator (Kay Elemetrics model 1/839 manual step attenuator[105]). The length $D1$ is then set so that the sinusoidal signal at point F is delayed by one period from the signal at point B . The amplitude of the delayed signal is adjusted using the variable resistor $P1$ so that the signal at the output of the ETDAS circuitry (point G) is minimized; iterating this procedure while monitoring the signal at G results in precise adjustment of $D1$. Next, the circulating loop is reconnected with the attenuator set so that R is small, and the delay $D2$ and the variable resistor $P1$ are adjusted to minimize the signal at G . Sensitive adjustment of $D2$ is achieved by decreasing the attenuation (increasing R) and iterating the

setting of $D2$ and $P1$. Adjusting the feedback parameter R to any desired value is straightforward once the timing of the circuit is achieved. A new value of R is selected by setting the attenuator and also adjusting the variable resistor $P1$ which sets the value of $(1 - R)$ in Eq. 3.1. Typically, the 10.1 MHz sinusoidal input signal is suppressed at point G by ~ 50 dB at 10.1 MHz.

This procedure results in a ETDAS feedback signal $V_{\delta p}(t) = V_{\delta p}^{ideal}(t - t_\ell)$, where $V_{\delta p}^{ideal}(t)$ is the ideal feedback signal in the absence of control-loop latency. The latency t_ℓ includes contributions from the *total* time lag of the signal as it propagates from the diode resonator, through the ETDAS circuitry and additional amplifiers setting the feedback gain γ , and the summing amplifier that injects the feedback signal into the diode resonator.

3.3.4 Compensating for nonideal circuit behavior

I characterize the quality of the ETDAS circuitry by measuring its frequency-domain transfer function $|T(f)|$ (recall the ideal shape of $|T(f)|$ shown in Fig. 3.3). I measure $|T(f)|$ by applying a weak sinusoidal signal (300 mV_{pp}) of frequency f at the input and measuring the output signal on a 100 MHz oscilloscope. Figure 3.7 shows $|T(f)|$ for $\tau = 400$ ns (corresponding to a fundamental frequency $f_* = 2.5$ MHz) for two cases, $R = 0$ (dashed line) and $R = 0.65$ (solid line). This configuration is used to stabilize the period-4 UPO of the diode resonator. I adjust the circuit parameters so that the notch at 10.1 MHz is as close to zero as possible, rather than optimizing at 2.5 MHz because the spectrum of the period-4 orbit has a large peak at 10.1 MHz. All other notches have a transmission less than 0.047 for $R = 0.65$ and less than 0.017 for $R = 0$. The agreement between the observed and predicted behavior is very good, especially when one considers that the sensitivity of the shape of the notches on the distortion of the delay line increases as $R \rightarrow 1$.

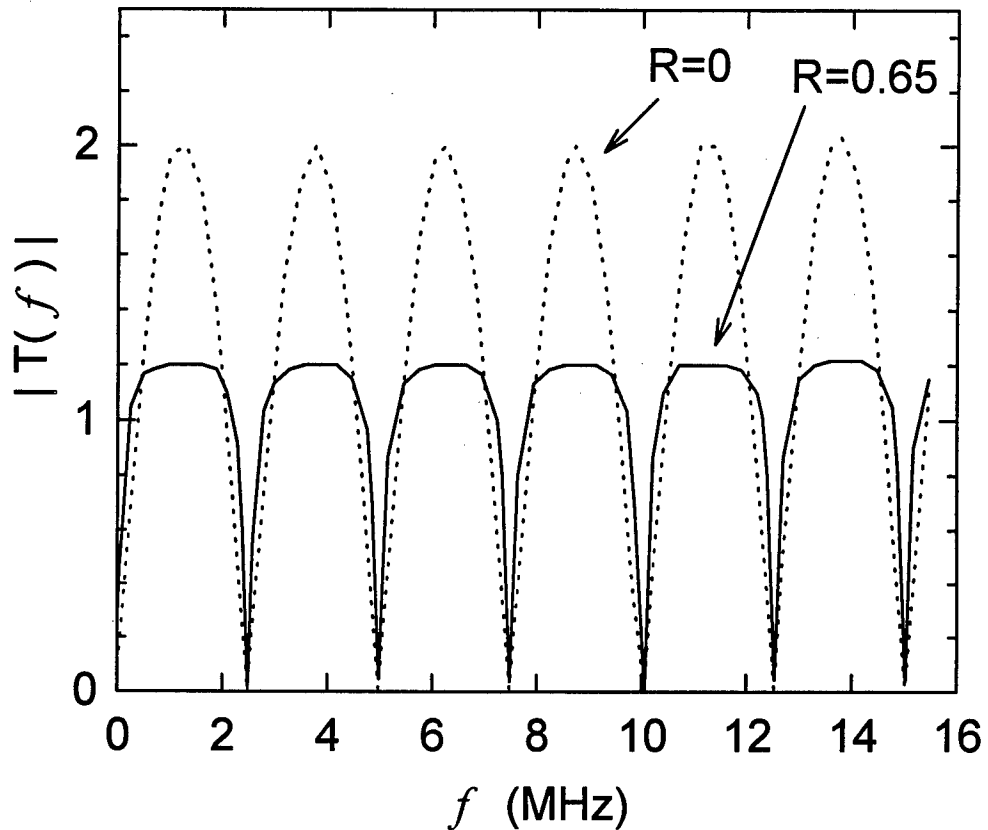


Figure 3.7: Experimental ETDAS transfer functions. They are very similar in shape to the ideal transfer functions in Fig. 6.3, indicating that the circuitry faithfully reproduces the form of the ETDAS feedback signal.

These high-quality results are only possible when the signals are filtered with predistortion circuitry ($F1$ and $F2$ in Figure 3.6) that attempt to cancel the small distortion caused by the HELIAX cable. The filters, consisting of two resistors and an inductor, do not significantly effect the signals at low frequencies but boost their amplitudes at high frequencies in a fashion opposite to the small frequency dependent attenuation of the coaxial cable. For comparison, Fig. 3.8 shows $|T(f)|$ with the predistortion filters ($F1$ and $F2$) removed, after I make minor adjustments of the circuit parameters to optimize the notch at 10.1 MHz. It is seen that the performance

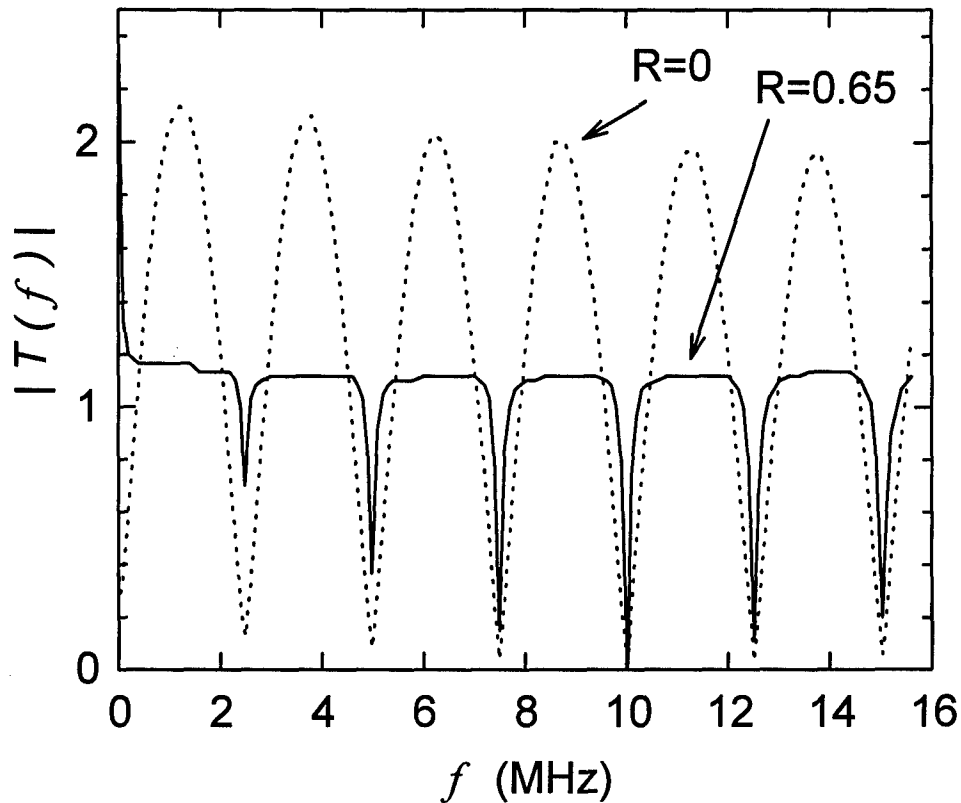


Figure 3.8: Experimental ETDAS transfer functions without predistortion filters. Performance of the circuit is severely degraded, as the notches no longer go to zero and the peak heights are not uniform.

of the device is severely degraded, especially for $R = 0.65$. I note that acceptable behavior of the ETDAS feedback circuitry with $\tau = 400$ ns and $R = 0.65$ cannot be obtained using standard coaxial cable (type RG-58/U) even with the predistortion filters.

In this chapter, I have described the ETDAS feedback scheme in detail, considering both its time- and frequency-domain properties. I have illustrated the basic elements required to implement ETDAS, and have presented a detailed high-speed electronic version that takes into account practical experimental considerations. We

are now prepared to apply this electronic implementation to the chaotic diode resonator system; results of this study will be presented in the next chapter.

Chapter 4

ETDAS Control of the Fast Chaotic Diode Resonator

This chapter describes the experimental and theoretical results I obtain when using ETDAS feedback to control the dynamics of the fast diode resonator circuit. I first describe the diode resonator, detailing its construction and outlining its theoretical description. I characterize its dynamics without feedback and demonstrate successful control, after which I determine regimes for which control is successful, varying feedback and system parameters. I use the theoretical model of the system to investigate the effects of latency on the domain of control. Transient behavior and times to attain control are explored, and I also investigate the mechanisms by which control is lost.

The results of this chapter demonstrate several important features of ETDAS control. Most importantly, I find that larger values for the feedback parameter R improve performance in several important respects. It greatly enlarges the domain of control for highly unstable orbits, such that stabilization is achieved for a wide range of gains γ , even for values of the bifurcation parameter for which no control is possible if $R = 0$. I find that increasing R extends the domain of control in the presence of significant latencies as well, and that it results in a wide range of gains for which the system rapidly converges to the UPO following the initiation of control. Theoretical results and numerical simulations show good agreement with experimental data.

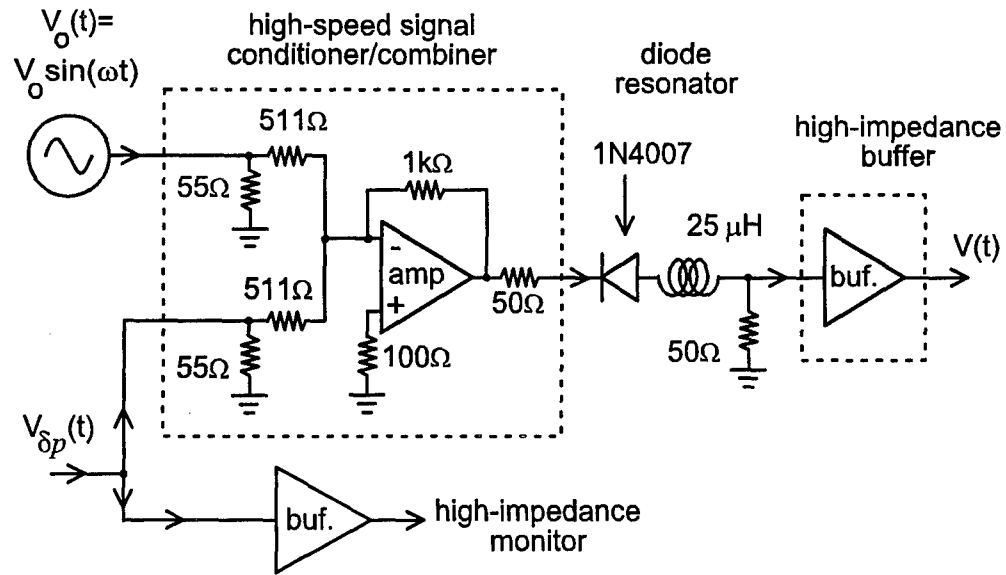


Figure 4.1: The high-speed diode resonator. The signal conditioner isolates the drive from the circuit and adds to it the ETDAS feedback. The behavior of the system is sensed with a high-impedance buffer.

4.1 Experimental system: the fast diode resonator

In my experimental studies of controlling chaos using ETDAS, I use a “diode resonator” because it displays a wide variety of nonlinear behaviors including period doubling bifurcations, hysteresis, intermittency, and crisis. In addition, it is easy to build and customize, and it is well characterized on slow time-scales [24]-[31]. The low-speed diode resonator typically consists of an inductor and a diode connected in series, driven by a sinusoidal voltage.

The high-speed version of the diode resonator, shown schematically in Fig. 4.1, has additional components needed to implement high-speed control. It consists of a rectifier diode (type 1N4007, hand-selected for low junction capacitance) in series with a $25 \mu\text{H}$ inductor (series DC resistance of 2.3Ω) and a resistor $R_s = 50 \Omega$. These components are driven by a leveled sinusoidal voltage $V_o(t) = V_o \sin(\omega t)$ ($\omega/2\pi \cong 10.1$

MHz) that passes through a high-speed signal conditioner (50Ω output impedance). The resistor R_s converts the current flowing through the diode resonator (the measured dynamical variable) into a voltage $V(t)$ which is sensed by a high-impedance buffer (Analog Devices AD9620, propagation delay $\lesssim 1$ ns). The signal conditioner consists of a high-speed inverting amplifier (Analog Devices AD9618, propagation delay $\simeq 3$ ns) and serves two purposes: it isolates the sine-wave generator (Tektronix model 3325A [106]) from the diode resonator and it combines the sinusoidal drive signal $V_o(t)$ with the ETDAS feedback signal $V_{\delta p}(t)$.

I construct the system using the same PC board etching techniques that were used for the construction of the ETDAS circuitry (Sec. 3.3.2). An additional high-impedance buffer (Analog Devices AD9620) is also included to monitor the ETDAS feedback signal, to verify that $V_{\delta p}(t)$ becomes sufficiently small when an UPO is stabilized. As a design note, I find that it is important to incorporate elements of the feedback loop into the architecture of the chaotic system, such as the signal combiner and the 50Ω current-to-voltage conversion resistor. This helps to minimize the latency of the feedback loop.

4.1.1 Model of system

It is a complex task to predict theoretically the stability of the high-speed diode resonator in the presence of ETDAS feedback based solely on experimental measurements. Therefore, I use a simple model of the resonator that captures the essence of its behavior. I will briefly outline this model here to make the numerical results meaningful; a more complete description of the model, as well as parameter values and methods for their determination, are given in Appendix A.

The system is described by two differential equations that can easily be derived from basic circuit analysis. They describe the evolution of the voltage drop V_d across

the diode and the current I flowing through the resonator as

$$\begin{aligned}\frac{dV_d}{dt} &= \frac{(I - I_d)}{(C_d - C_J)}, \\ \frac{dI}{dt} &= \frac{[-V_d - IR_s + V_0(t)]}{L}.\end{aligned}\tag{4.1}$$

Several parameter in this model arise from treating the real components of the resonator as collections of ideal components in a fashion similar to that used in commercially available electronic simulation software packages. Specifically, the behavior of the 1N4007 diode is treated as an ideal diode (described by the Shockley formula, which includes the parameter I_d) in parallel with two voltage-dependent capacitances C_d and C_J . The quantities L and R_s are the total inductance and resistance in the circuit, respectively. All parameters of the model are determined by independent measurements of the components. As we will see in Sec. 4.6, this model is adequate to predict with good accuracy the stability of the controlled resonator.

4.1.2 Characterization of uncontrolled system

It is valuable to characterize the dynamics of the uncontrolled system, in order to locate regimes of different behavior and provide a basis for comparison once control is introduced. I characterize the diode resonator's dynamics by construction of bifurcation diagrams and first-return maps, using the sinusoidal drive amplitude V_o as the bifurcation parameter. In the experiments, I capture multiple (typically three) 40- μ s-long time-series data of $V(t)$ using a 100 MHz, 8-bit digitizing oscilloscope (Tektronix model 2221A) and determine the maxima of $V(t)$, denoted by V_n , using a second-order numerical interpolation routine. The bifurcation diagram (Fig. 4.2a) is generated by plotting approximately 300 values of V_n for each value of V_o as it is varied from small to larger values (hysteresis in the system is evident when V_o is varied from large to smaller values of V_o , but it is not shown in this diagram for

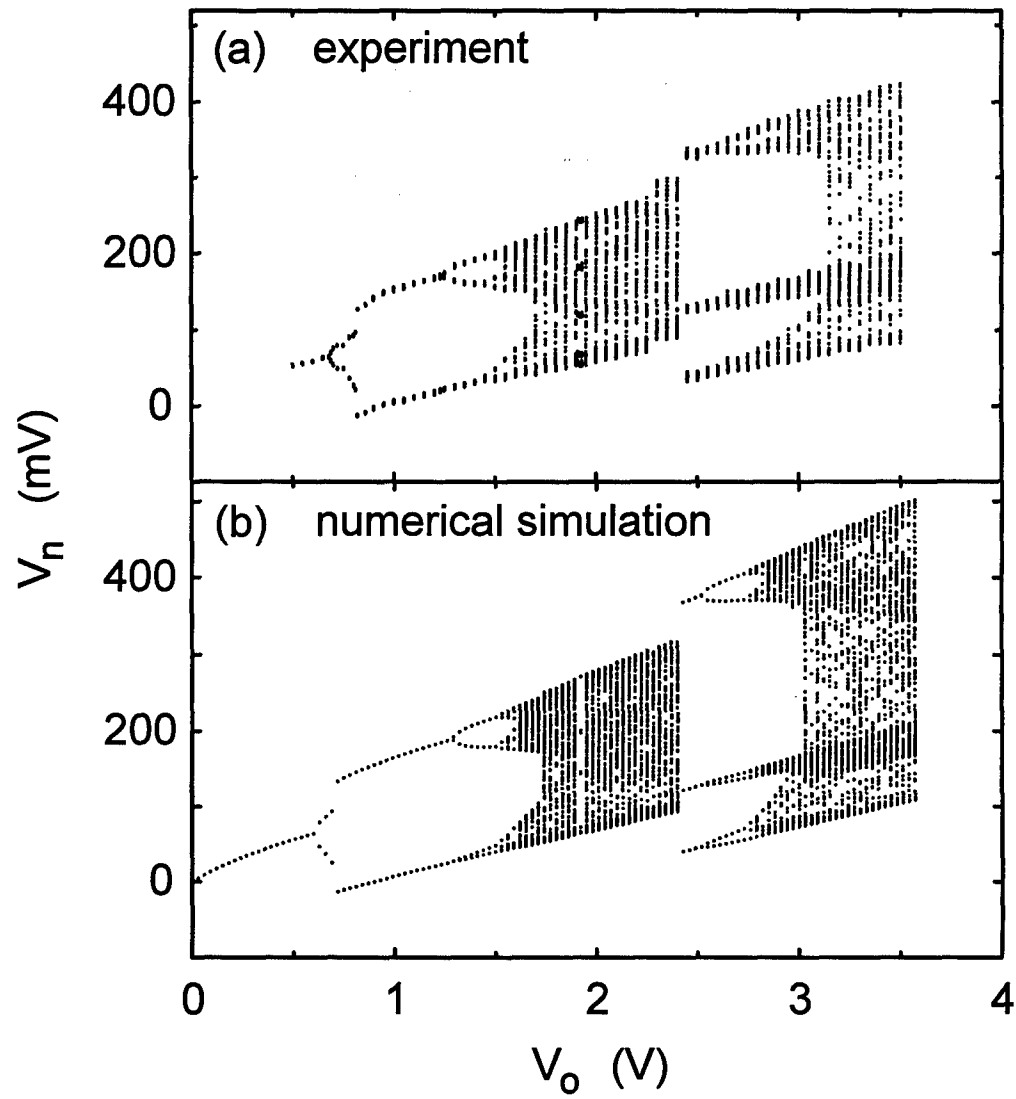


Figure 4.2: Experimental and numerically generated bifurcation diagrams of the uncontrolled diode resonator. All major features are reproduced by the model.

clarity). It displays a typical period-doubling cascade to chaos where the transition to chaos occurs at $V_o \simeq 1.5$ V. Also evident are a narrow period-5 periodic window at $V_o \simeq 1.8$ V and a large period-3 window starting at $V_o \simeq 2.4$ V.

I generate the simulated bifurcation diagram by numerically integrating a dimensionless form of Eqs. 4.1 (see Appendix A) using a fourth-order Adams-Bashforth-Moulton predictor-corrector routine, taking 1000 integration steps per drive cycle. I integrate for fifty cycles to allow the system to evolve through any transients and then record 300 current maxima, converting to voltages V_n for comparison with experiment. I find very good agreement between the experimentally observed and numerically generated bifurcation diagrams (Fig. 4.2b). The model predicts all features observed in the experiment, although there is a slight discrepancy in the size of V_n . We will see in Sec. 4.6 that the model also predicts the stability of the controlled resonator with good accuracy.

The first-return maps are generated by plotting V_n vs. V_{n+1} for fixed values of V_o . The experimentally observed chaotic maps of the system below ($V_o = 2.2$ V) and above ($V_o = 3.6$ V) the period-3 window are shown in Fig. 4.3a and 4.3b, respectively. The general structure of these maps is similar to that observed in low-frequency diode resonators [30]. The numerically generated first return maps for the same drive values (Fig. 4.3c and 4.3d) show good agreement.

4.2 Experimental observation of control

With the chaotic diode resonator well characterized and modeled, I now apply ETDAS control to the circuit. The main tasks for the experiment when feedback is introduced are to determine the criteria for successful control and to locate regimes of τ and R that meet those criteria. To prepare the ETDAS electronics, I set the delay-time τ , the feedback parameter R , and optimize the circuitry off-line as de-

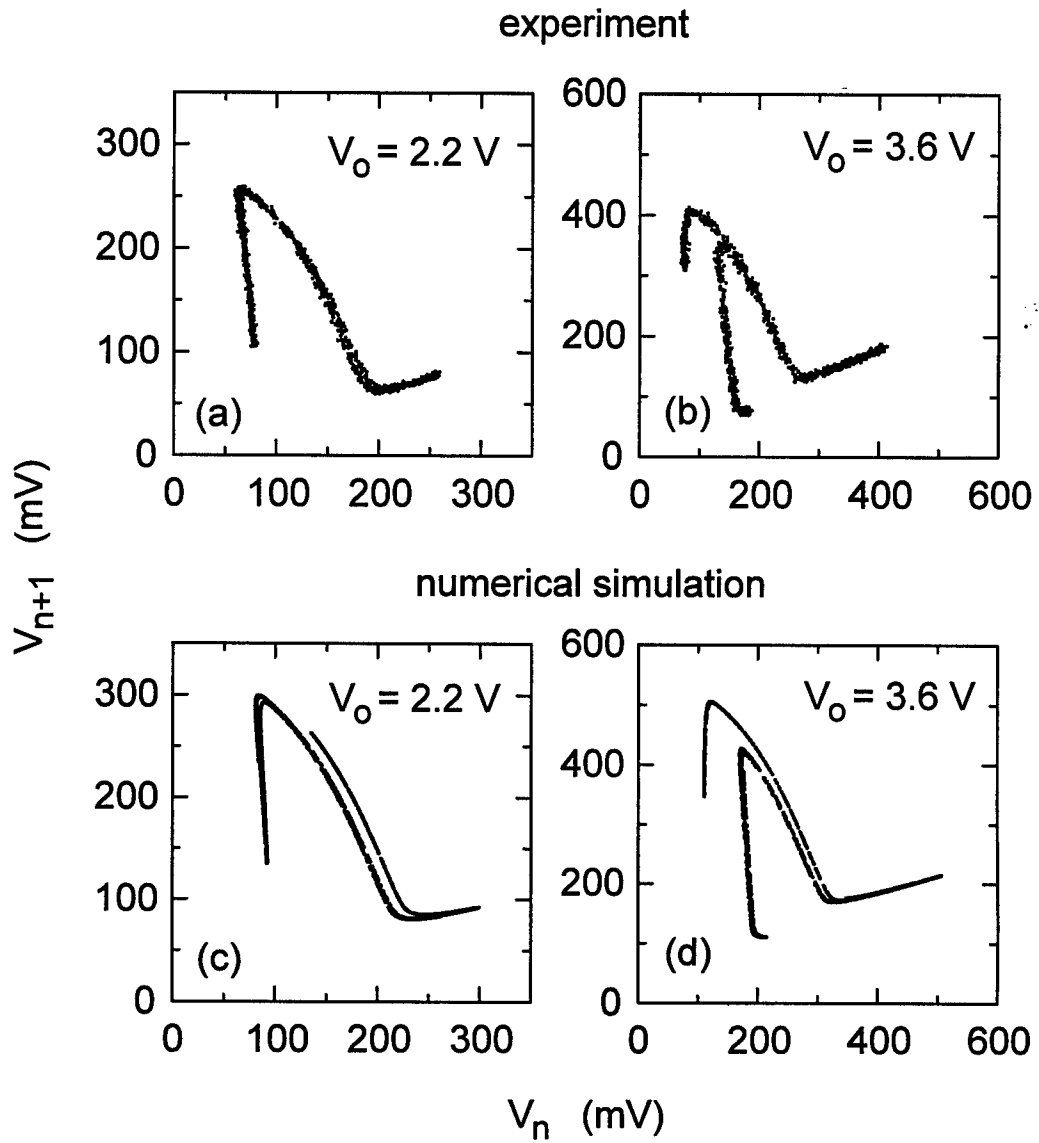


Figure 4.3: Experimental and numerically generated first-return maps of the uncontrolled diode resonator.

scribed in Sec. 3.3.3. I then connect the ETDAS circuitry to the diode resonator using short coaxial cables and search for control while adjusting the feedback gain γ .

The conditions for successful experimental control are that $V(t)$ is periodic with the desired period τ and the magnitude of the feedback signal $V_{\delta p}(t)$ drops below a predetermined level. In principle, $V_{\delta p}(t)$ should vanish for a perfect reproduction of ETDAS in a noise-free system, but noise and nonideal behavior of the ETDAS circuitry lead to a nonzero value of $V_{\delta p}(t)$ in practice. I characterize the nonideal characteristics of the ETDAS circuitry using the transfer function $|T(f)|$, as measured in Sec. 3.3.4. Specifically, the transmission at the worst “notch” (see Fig. 3.7) determines how much feedback is generated even when the system’s behavior is perfectly periodic. Based on observations of this value and the noise level in the system, I set the upper limit on the magnitude of the feedback to be that $|V_{\delta p}(t)| < 5 \times 10^{-3}V_o$.

I test the validity of the above experimental criteria by verifying that the controlled orbits are indeed UPO’s of the chaotic system by comparing the return maps of the controlled and uncontrolled systems. The first-return map of a stabilized orbit must fall on that of the unperturbed chaotic system if it is an UPO of that system. I note that periodic states that are *not* UPO’s of the system can be obtained under different experimental conditions; however, in this case the feedback signal is large (of the order of V_o). An example of this behavior will be shown in Sec. 4.8.

Figures 4.4a and 4.4b show the temporal evolution of $V(t)$ when the ETDAS feedback circuitry is adjusted to stabilize the period-1 and period-4 UPO’s, respectively, together with the associated feedback signal. The solid lines represent $V(t)$, and the dotted lines correspond to the associated ETDAS feedback. The sinusoidal drive amplitude is 2.4 V (a chaotic regime in the absence of control) and the feedback parameters are $\gamma = 6.2$, $R = 0.28$ for the stabilized period-1 orbit and $\gamma = 4.2$, $R = 0.26$ for the period-4 orbit. It is seen that the feedback signal is a small fraction

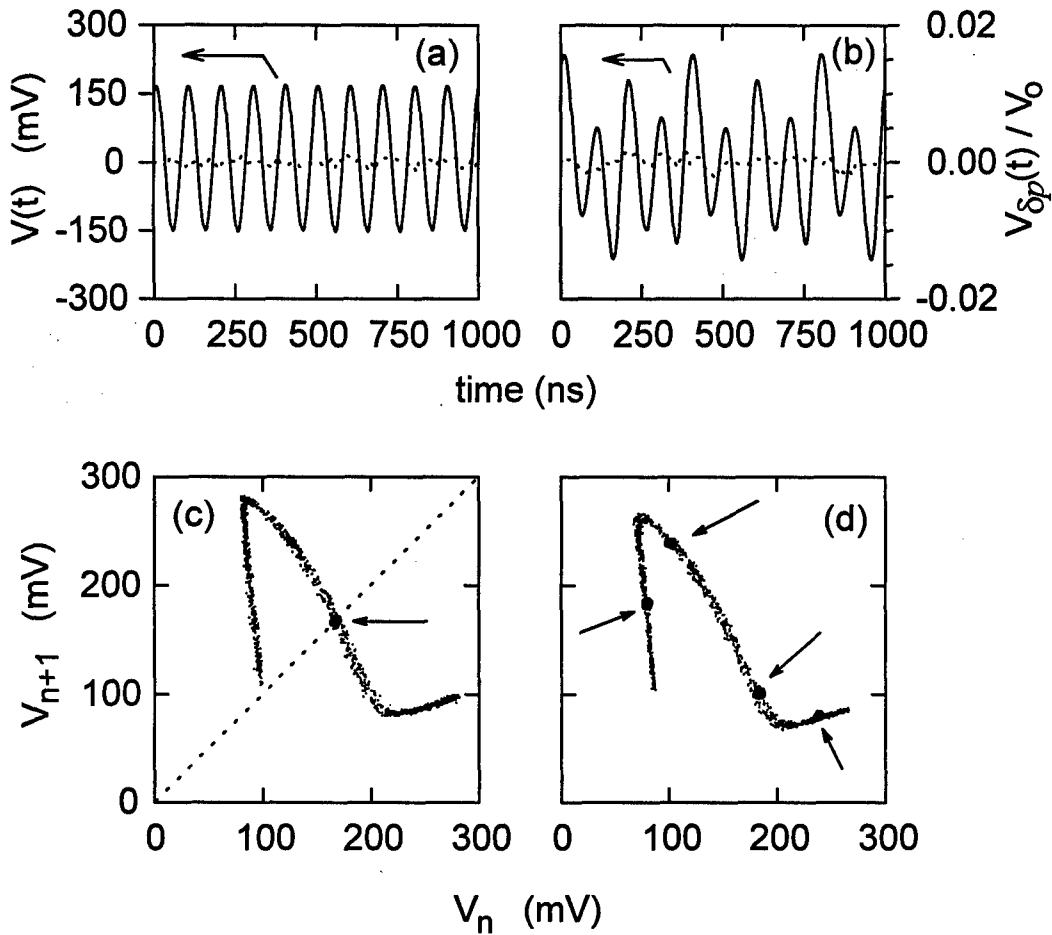


Figure 4.4: Time series data and first return maps illustrating successful ETDAS control. Temporal evolution (solid line, scale on left) is shown for the stabilized period-1 (a) and period-4 (b) UPOs, along with their associated ETDAS error signals (dashed line, scale on right). Similar data are shown as first-return maps for the controlled period-1 (c) and period-4 (d) trajectories. The controlled maps are highlighted by dark dots indicated by arrows, superimposed on lighter dots representing the uncontrolled system. Parameter values are given in the text.

of the drive amplitude ($< 2 \times 10^{-3}$ for both cases). The slight increase in $V_{\delta p}(t)$ for the period-4 orbit is mainly due to imperfect reproduction of the form of the ETDAS feedback signal by our circuitry. This effect is more prevalent for the period-4 setup because the delay line is longer and hence causes more distortion of the signals due to the dispersion and frequency-dependent loss of the coaxial cable.

Figures 4.4c and 4.4d present further evidence that the ETDAS feedback indeed stabilizes the UPO's embedded within the strange attractor of the diode resonator. I show return maps for the uncontrolled system (light dots) and the controlled system (dark dots indicated by arrows) for the stabilized period-1 orbit (Fig. 4.4c, $R = 0$, and $\gamma = 4.4$) and the period-4 orbit (Fig. 4.4d, $R = 0.26$, and $\gamma = 3.1$) for $V_o = 2.4$ V. It is clear that the stabilized orbits lie on the unperturbed map, indicating that they are periodic orbits internal to the dynamics of the uncontrolled system.

I find that the period-1 and period-4 UPO's shown in Fig. 4.4 can be stabilized by initiating control at an arbitrary time; it is unnecessary to wait for the system to naturally approach the neighborhood of the UPO nor target the system to the UPO before control is initiated. This is possible for several reasons: the system is particularly simple in that there is only one period-1 and one period-4 UPO; the basin of attraction of these UPO's in the presence of ETDAS feedback is large; and I apply large perturbations ($V_{\delta p}(t)$ is comparable to $V_d(t)$) to the system during the transient phase.

4.3 Domain of control

The wide range of feedback parameters that stabilize these UPO's can be visualized quickly from a plot of the "domain of control." The domain of control for a given UPO is mapped out by determining the range of values of the feedback gain γ at a set value of the feedback parameter R that successfully stabilizes the orbit as a

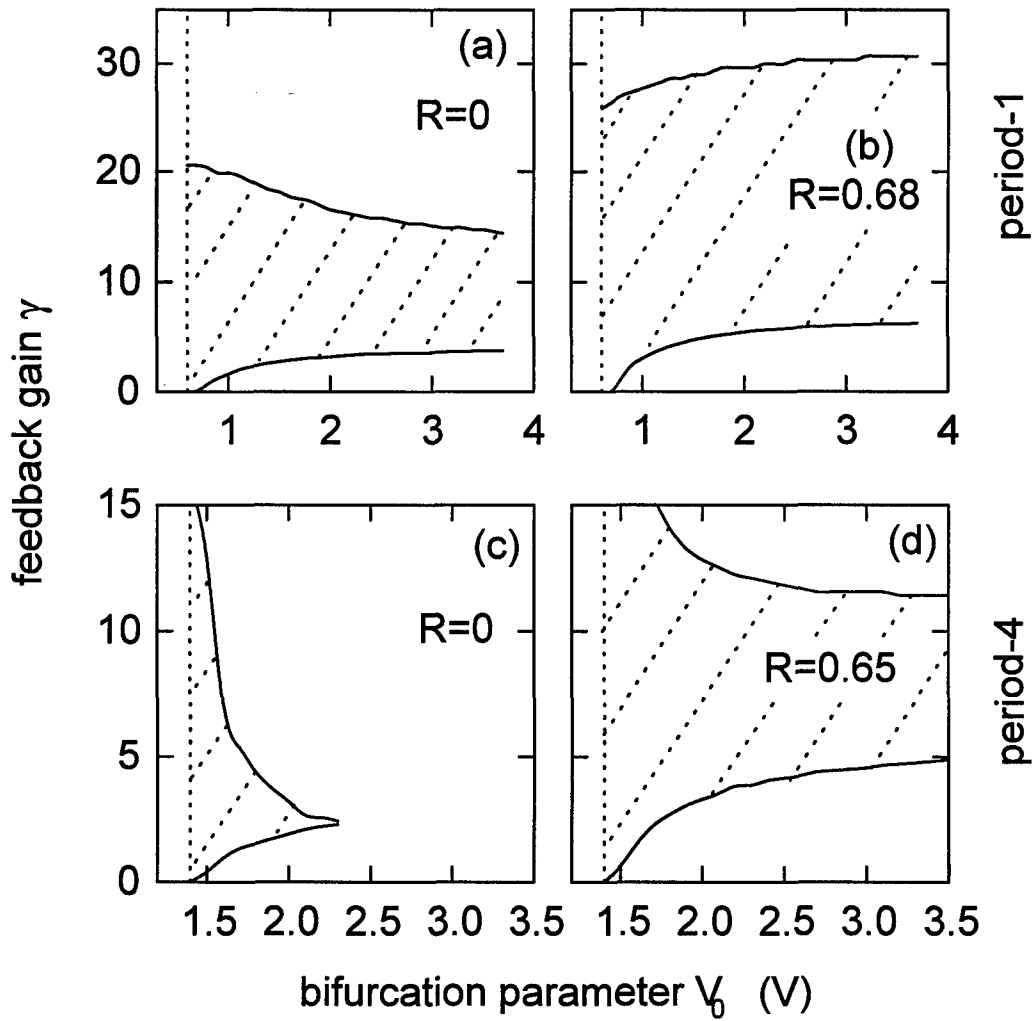


Figure 4.5: Experimental domains of control as a function of drive amplitude for period-1 and period-4 UPOs for two different values of R . The shaded regions indicate period-1 domains for $R = 0$ (a) and $R = 0.68$ (b), and period-4 domains for $R = 0$ (c) and $R = 0.65$ (d). The dashed lines mark the points at which the orbit becomes unstable in the absence of feedback.

function of the bifurcation parameter V_o . In general, increasing the feedback parameter R tends to enlarge the domain of control and shift it to slightly larger values of γ . The period-1 orbit can be stabilized using ET DAS feedback for all available V_o when $R = 0$ and $R = 0.68$ as seen in Fig. 4.5a and 4.5b, respectively. It is clear that the range of γ that successfully stabilizes the orbit for a given value of V_o increases significantly for $R = 0.68$ in comparison to $R = 0$, especially for larger values of V_o .

The largeness and shape of the domain of control is important for several practical reasons. Since the domain is large, the system is rather insensitive to drift in the feedback parameters or the state of the chaotic system, and control can be obtained even with imprecise *a priori* knowledge of the proper feedback parameters. Also, the ET DAS feedback can automatically track changes in V_o over its entire range without adjusting γ because the shape of the domain is a wide, horizontal band.

Increasing the size of the feedback parameter R gives rise to more dramatic effects on the domain of control when stabilizing the period-4 orbit, as shown in Figs. 4.5c and 4.5d. It is apparent that TDAS feedback ($R = 0$) fails at even moderate values of the bifurcation parameter. However, the domain of control can be extended to include the entire range of V_o using $R = 0.65$, illustrating the superiority of ET DAS for controlling highly unstable orbits. Also, the size and shape of the domain of control for this case has all of the advantages mentioned previously for the period-1 domain of control.

4.4 Transient behavior

I stated in Sec. 4.2 that control could be successfully initiated at any time in certain cases, regardless of the state of the system. This does require fairly large feedback levels, however, and the dynamics during the initial transient can be quite rich. The nature of the convergence of the system to the UPO is a function of the

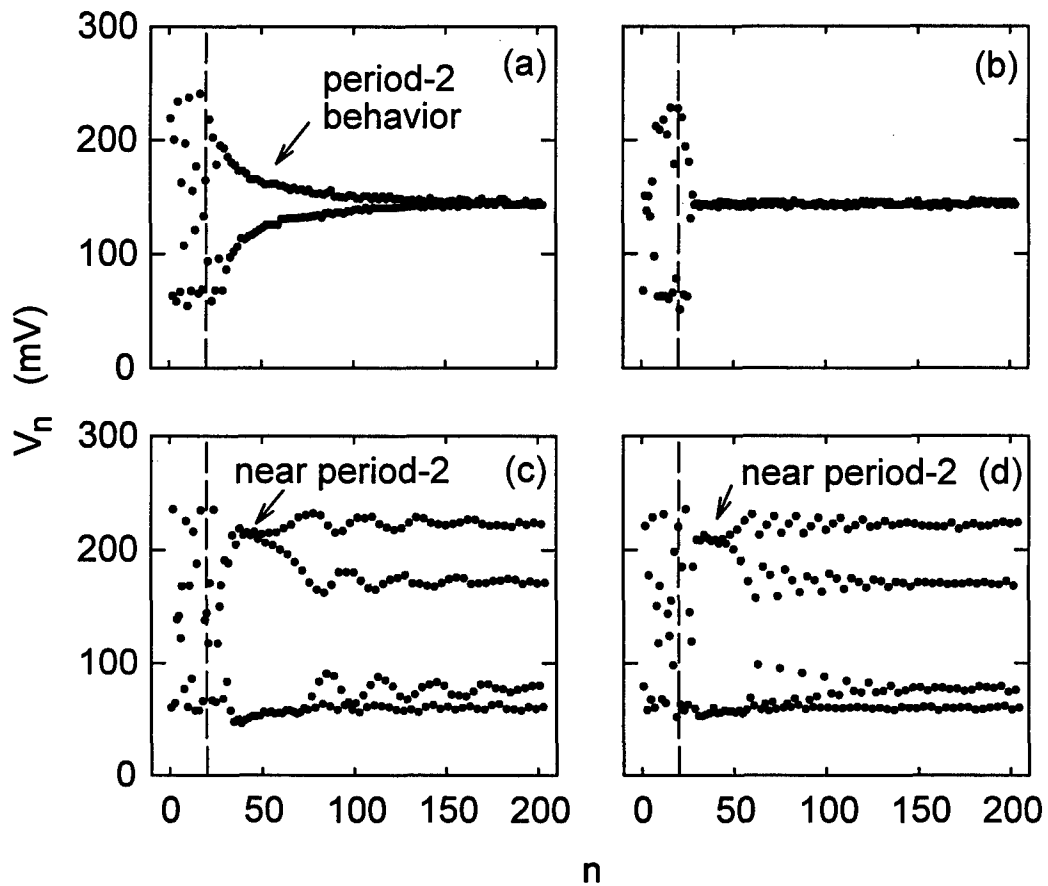


Figure 4.6: Transient dynamics of the diode resonator following initiation of ETDAS control. The dots represent the peak values V_n of $V(t)$, and the dashed vertical lines mark the points at which control is initiated. Graphs (a) and (b) show convergence to the period-1 UPO, and (c) and (d) show approaches to the period-4 UPO. Note that the transients have brief sections of decaying period behavior. Parameter values are given in the text.

precise state of the system when control is initiated and the value of the control parameters. When the control parameters are adjusted such that the system is near but within the boundary of the domain of control, the system often displays brief intervals of periodic behavior other than the desired behavior during the transient phase. Figures 4.6a and 4.6b are two examples of the approach to the period-1 UPO for $V_o = 1.9$ V, $R = 0.68$, and $\gamma = 5.2$ (a) or $\gamma = 7.0$ (b), where I plot the peak value V_n of $V(t)$ as a function of the peak number n . Control is initiated near $n = 20$, marked by the dashed vertical line. In one case (Fig. 4.6a), an initial chaotic transient gives way to a period-2 behavior that decays exponentially to the desired UPO. In the second (Fig. 4.6b), an initial chaotic transient abruptly switches to controlled behavior.

Richer transient dynamics are observed when stabilizing the period-4 UPO, as shown in Fig. 4.6c and 4.6d for $V_o = 1.9$ V, $R = 0.26$, and $\gamma = 6.1$ (c) or $\gamma = 2.6$ (d). In one case (Fig. 4.6c), I observe a brief interval of period-2 behavior that eventually destabilizes and decays in an oscillatory fashion to the desired UPO. In the other case (Fig. 4.6d), the system passes through intervals of period-2 and period-16 behavior before converging to the period-4 UPO. It is not surprising that the system resides near a period orbit with a period longer than the desired UPO since the ETDAS feedback cannot distinguish between the two different behaviors. However, the low-period behavior is not stable for long times since the ETDAS feedback is not sensitive to and does not correct for noise and fluctuations that destabilize this undesired low-period orbit.

4.5 Average time to attain control

While the transient dynamics are quite rich near the boundary of the domain of control, ETDAS feedback stabilizes rapidly the desired UPO over most of the domain.

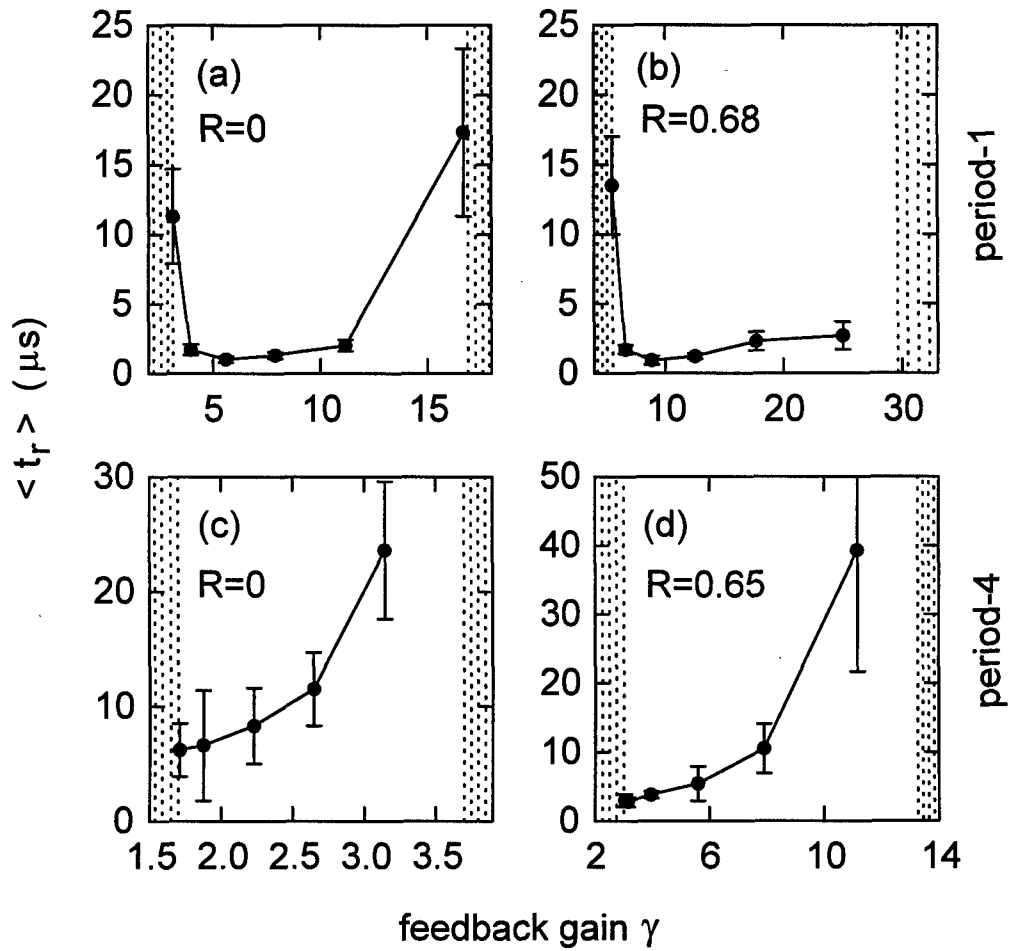


Figure 4.7: Average transient times $\langle t_r \rangle$ as functions of feedback gain γ for the period-1 UPO for $R = 0$ (a) and $R = 0.68$ (b), and the period-4 UPO for $R = 0$ (c) and $R = 0.65$ (d). The error bars indicate the standard deviation of $\langle t_r \rangle$, and the hashed regions indicate the range of γ for which control is not achieved.

Figure 4.7 shows the average time $\langle t_r \rangle$ to obtain control of the period-1 UPO from an arbitrary starting time as a function of the feedback gain γ for $V_o = 1.9$ V and $R = 0$ (Fig. 4.7a) and $R = 0.68$ (Fig. 4.7b). The hashed regions indicate values of γ for which stable period-1 behavior is not observed. The data points represent the average of 20 trials and the error bars indicate the standard deviation of the times to obtain control. It is seen that $\langle t_r \rangle$ is less than $3 \mu\text{s}$ and typically less than $1 \mu\text{s}$ (10 orbital periods), except near the edge of the domain of control where $\langle t_r \rangle$ grows rapidly. In addition, it is seen that the range over which rapid control is obtained increases significantly by increasing R to 0.68, highlighting one of the advantages of ETDAS feedback control over TDAS feedback. Figures 4.7c and 4.7d show similar data for the period-4 UPO. I note that $\langle t_r \rangle$ should increase rapidly near the edges of the domain of control for this UPO (as it does in the period-1 case). In the experiment, however, limited precision in γ makes it impossible to get sufficiently close to the low-gain boundary to detect the rapid increase.

4.6 Theoretical analysis

The experimentally measured domains of control can be predicted theoretically with good accuracy using the techniques described in Sec. 3.1.2. Briefly, the procedure to determine the domain is to [94]:

- determine the trajectory of the desired UPO for one value of the bifurcation parameter V_o by analyzing the coupled nonlinear differential equations describing the dynamics of the diode resonator (see Eq. 4.1);
- choose the feedback parameters \hat{n} and R (note that \hat{n} is set throughout the experiment by our choice of measured system variable and control parameter);

- find the boundaries of the domain of control (the points at which the winding number jumps from zero to a positive integer, see Eq. 3.4) for one value of the bifurcation parameter V_o using standard numerical root-finding algorithms;
- follow the boundary by repeating this procedure for the other values of V_o .

I carry out this series of procedures using code written by M. E. Bleich, specifically with the programs `hunter` (first step) and `crawl` (last two steps). A more detailed description of these programs can be found in Ref. [95]. Note that one important simplification in this analysis is that it does not include the effects of control-loop latency.

Figure 4.8 compares experimentally measured and theoretically predicted domains of control. These are shown for the period-1 UPO with $R = 0.68$ in Figs. 4.8a and Fig. 4.8b, respectively. The theoretical analysis correctly predicts the general horizontal banded shape of the domain, and the low-gain boundary is in good quantitative agreement with the experimental observations. However, in contrast with the observations, the theoretical analysis predicts that very large values of the feedback parameter ($\gamma > 1000$) will give rise to successful control. Somewhat closer agreement between the observed and predicted domain of control is obtained for the period-4 orbit ($R = 0.65$) as shown in Fig. 4.8c and 4.8d, respectively. I obtain similar results for other values of the control parameter R .

The discrepancy between the theoretically predicted and experimentally observed domains of control is due primarily to the effects of control-loop latency ($t_\ell = 10$ ns for our implementation of ETDAS). To investigate the effects of t_ℓ , I turn to direct numerical integration of the time-delay differential equations describing the diode resonator with feedback, made dimensionless for ease of computation. The equations are integrated using a fourth-order Adams-Bashforth-Moulton predictor-

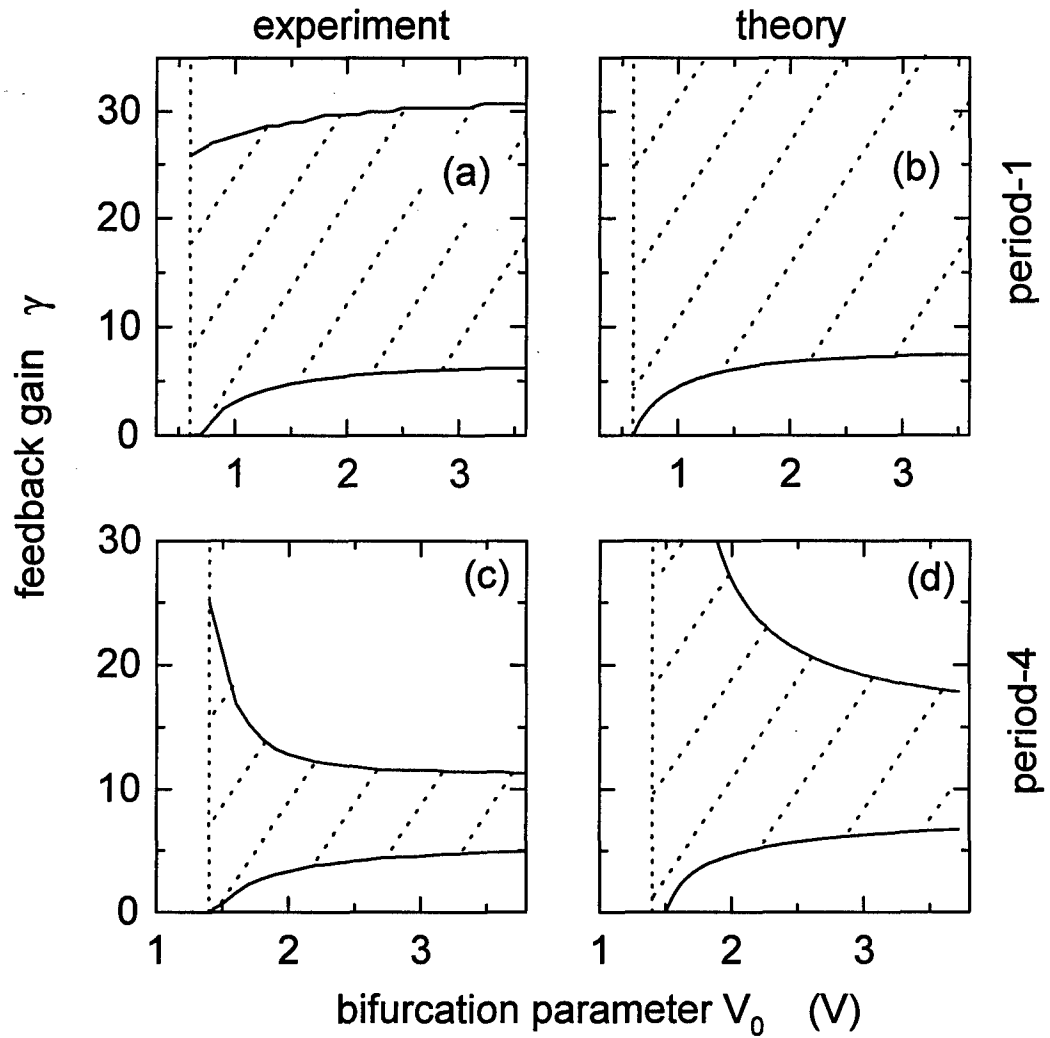


Figure 4.8: Comparison of experimental and theoretical domains of control. Period-1 domains (a) and (b) have $R = 0.68$, and period-4 domains (c) and (d) have $R = 0.65$. The vertical lines indicate the points at which the orbits become unstable in the absence of feedback. The theoretically predicted domains assume $t_\ell = 0$.

corrector scheme with a step size of 0.1 ns. Successful control is indicated when the ETDAS error signal falls to the machine precision in a time equal to 20,000 orbital periods. I note that this procedure may underestimate the size of the domain of control when the convergence is slow. To set the initial conditions for the time-delay differential equations, I integrate the equations without the time-delay terms (equivalent to the diode resonator in the absence of control), initially using a fourth-order Runge-Kutta algorithm. I store variable values, derivatives, and calculated time-delay in arrays as I integrate; these values are needed for the predictor-corrector routine and to determine $V_{\delta p}(t)$. I switch to the predictor-corrector integrator after ten cycles of Runge-Kutta and add the control terms. I note that despite the infinite series in Eq. 3.1, it is not required to retain all past variable values to calculate $V_{\delta p}(t)$; ETDAS can be expressed recursively, requiring only storage of the information from one past orbital cycle [20].

As a note on numerical methods, I choose not to use the more common fourth-order Runge-Kutta algorithm when time-delay terms are included because it is not simple to properly account for the delay terms at the trial midpoints this algorithm uses in calculating each integration step. In contrast, the predictor-corrector routine uses computations only at the full integration steps, thereby avoiding the difficulty. See Ref. [107] for more details on these methods.

Figure 4.9 shows the experimental (period-1, Fig. 4.9a; period-4, Fig. 4.9c) and numerically predicted (period-1, Fig. 4.9b; period-4, Fig. 4.9d) domains of control for the UPO's with $t_\ell = 10$ ns and $R = 0.68$ (period-1) and $R = 0.65$ (period-4). The agreement is much improved, highlighting the extent to which even small control-loop latencies (only 10% of the orbital period for the period-1 UPO) can shift the domain of control.

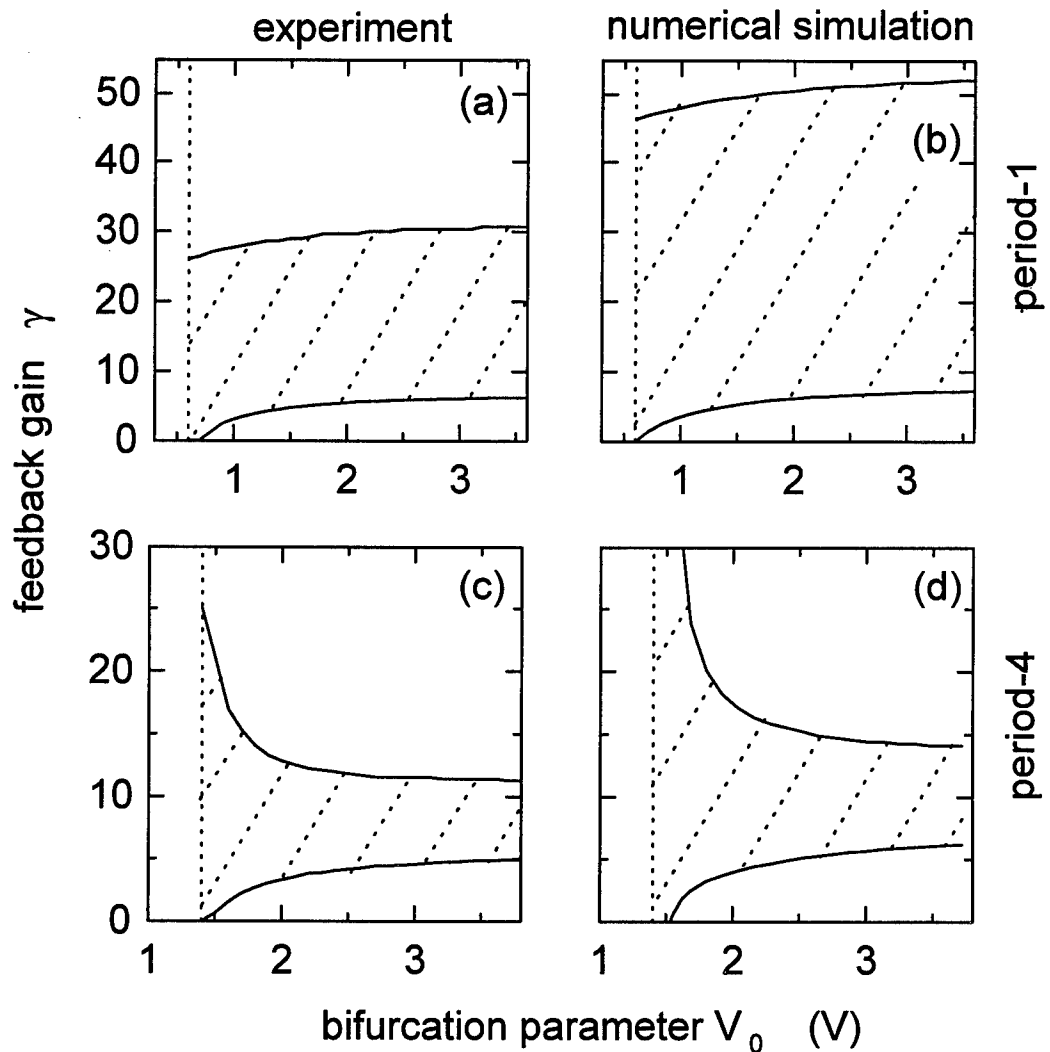


Figure 4.9: Comparison of experimental and numerically simulated domains of control. The numerical simulations include control-loop latency equal to that of the experiment, $t_\ell = 10$ ns. Other parameter values are the same as Fig. 7.8. Note that inclusion of nonzero t_ℓ improves the quantitative agreement of the domains.

4.7 Effects of control-loop latency

To further probe the deleterious effects of large control-loop latency, I add additional delays to the feedback signal by inserting various lengths of coaxial cable (type RG-58/U) between the output of the ETDAS error generating circuitry and the signal conditioning device at the input to the diode resonator. In this case, the total latency t_ℓ is the sum of the time lags of the ETDAS circuitry (10 ns) and that incurred by the additional coaxial cable. This mimics the situation in which slower electronic components are used in the ETDAS circuitry.

Figure 4.10 shows the ranges of γ that give rise to successful control of the period-1 UPO as a function of t_ℓ for $V_o = 1.9$ V, $R = 0$ (Fig. 4.10a) and $R = 0.68$ (Fig. 4.10b). The vertical dashed line is at $t_\ell = 10$ ns, marking the minimum possible for this experimental configuration. For both cases, it is seen that increasing t_ℓ causes the range of γ to decrease until control is unattainable when the time-lag is approximately one-half of τ (100 ns). Stabilization of the orbit is possible for larger values of t_ℓ as a new region of control appears, although with the opposite sign of the feedback parameter γ . It is also seen that the range of γ that gives rise to control when $R = 0$ is much less than that when $R = 0.68$, indicating that ETDAS is more effective than TDAS in the presence of a time lag. Control is not possible for $t_\ell > 120$ ns.

I obtain similar results when stabilizing the period-4 orbit at $V_o = 1.9$ V, although control fails for much smaller t_ℓ , as shown in Fig. 4.11. Control is possible only to $t_\ell \simeq 26$ ns for $R = 0$ (4.11a) and $t_\ell \simeq 70$ ns for $R = 0.65$ (4.11b). Also, the range of γ that gives rise to successful control is much larger for $R = 0.65$. The fact that ETDAS feedback significantly extends the range t_ℓ in comparison to that achievable by TDAS suggests that ETDAS may be effective in controlling the dynamics of systems that fluctuate on the nanosecond or even sub-nanosecond scale for which relatively small

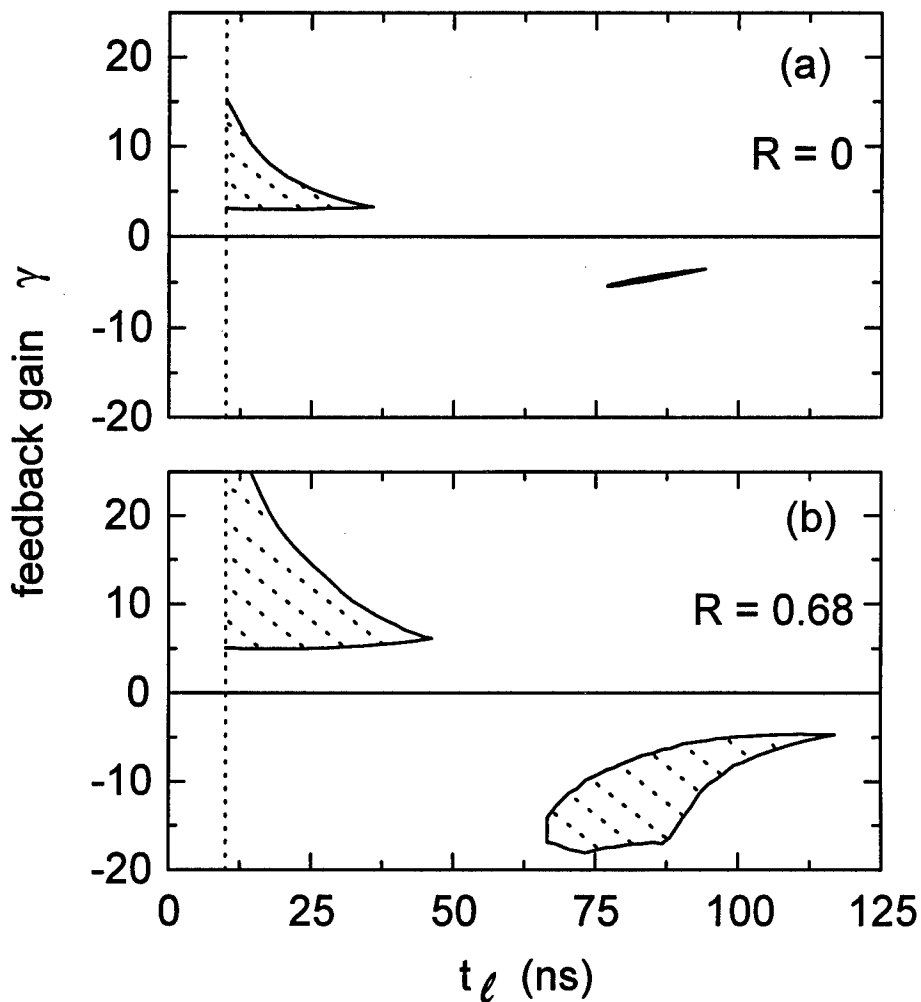


Figure 4.10: Effects of control-loop latency on the domain of control for the period-1 UPO. The dashed vertical line at $t_\ell = 10$ ns indicates the minimum latency of the ETDAS circuitry. Note that the larger R value has a much larger domain of control at large t_ℓ .

t_ℓ may be difficult to achieve.

In contrast to the behavior observed for the period-1 orbit, I find no islands of stability for $\gamma < 0$ at the longer time-lags. I do find, however, a small region around $t_\ell \simeq 107 - 117$ ns where the orbit is stabilized intermittently when $R = 0.65$. The system alternates irregularly between intervals of “noisy” period-4 behavior and intervals of chaotic behavior. The indicated region of Fig. 4.11b is the where the system resides near the period-4 orbit for at least 10% of the time on average. Under some conditions, the systems remains near the UPO for ≈ 16 ms, corresponding to 40,000 orbital periods. Figure 4.12 shows examples of the dynamical evolution of the peaks V_n of $V(t)$ during this intermittent behavior. It is seen that the orbit can regain stability abruptly (Fig. 4.12a), but may destabilize via a gradual transition through other periodic behaviors (Fig. 4.12b). Note that these transitions do not result from a change in the feedback level, but occur spontaneously in the system.

4.8 Dynamics of the system outside the domain of control

It is instructive to investigate the dynamics of the diode resonator in the presence of ETDAS feedback *outside* the domain of control. This study helps to identify mechanisms by which control is lost, which may serve as a guide when attempting to control the dynamics of new systems. I explore the range of different behaviors by adjusting the feedback gain γ while fixing the other control parameters at $V_d = 1.9$ V, $\tau = 100$ ns (period-1 UPO control), $R = 0$, and $t_\ell = 10$ ns. For these parameters, the range of successful control of the period-1 orbit is approximately $3.14 < \gamma < 16.9$. Similar behaviors can be obtained by fixing γ and adjusting a different parameter or when attempting to control longer-period orbits.

As γ increases from zero to the lower boundary of the domain of control ($\gamma \sim$

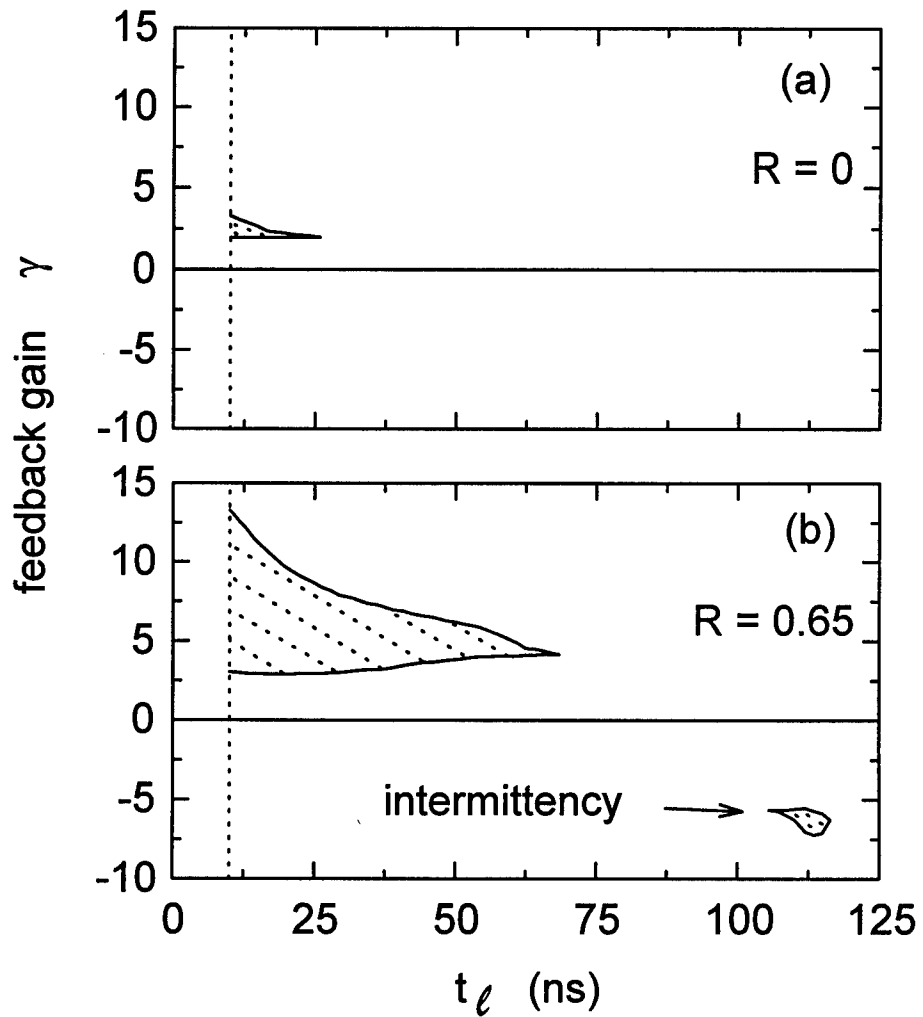


Figure 4.11: Effects of control-loop latency on the domain of control for the period-4 UPO. The vertical dashed line again indicates the minimum t_ℓ for the ETDAS circuitry. Note the region of intermittency for $\gamma < 0$ at large t_ℓ in (b).

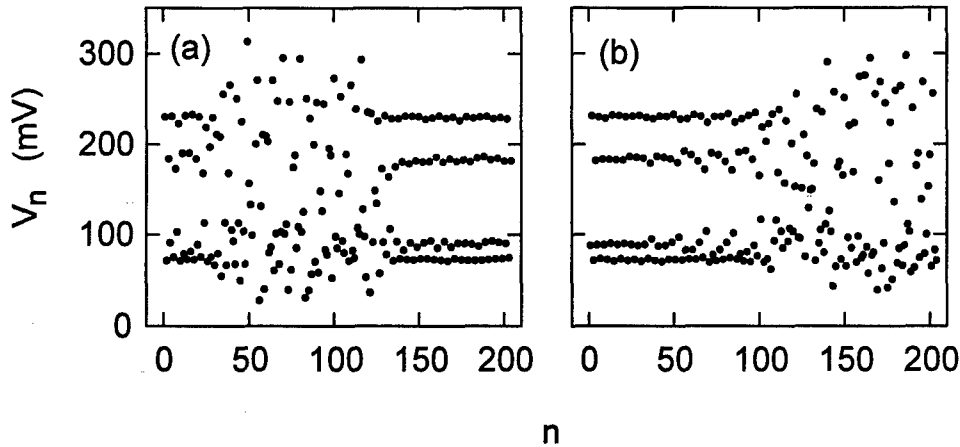


Figure 4.12: Intermittent chaotic bursts away from period-4 UPO. The dots represent peaks V_n of $V(t)$. Note that control is regained abruptly (a), but the system destabilizes gradually through higher-periodic behavior (b).

3.14), the system goes from the chaotic state to the desired period-1 UPO through an inverse period-doubling cascade. Figure 4.13a compares the return map of the system without ETDAS feedback (light collection of points) and with feedback (dark collection of points indicated by arrows) for $\gamma = 2.5$. It is seen that the system with feedback displays period-2 behavior that is not part of the original chaotic attractor since the points do not fall on the chaotic return map. The error signal $V_{\delta p}(t)$ is large in this case.

I find that the system displays quasi-periodic behavior when the feedback gain is larger than the higher boundary of the domain of control ($\gamma \sim 16.9$). Figure 4.13b shows the return maps of the system with and without feedback for $\gamma = 17.5$ where it is seen that the points fall on an oval centered on the location of the period-1 fixed point. The temporal evolution of $V(t)$ displays oscillations around 10.1 MHz whose amplitude is modulated by low-frequency (~ 2 MHz) oscillations. For large values

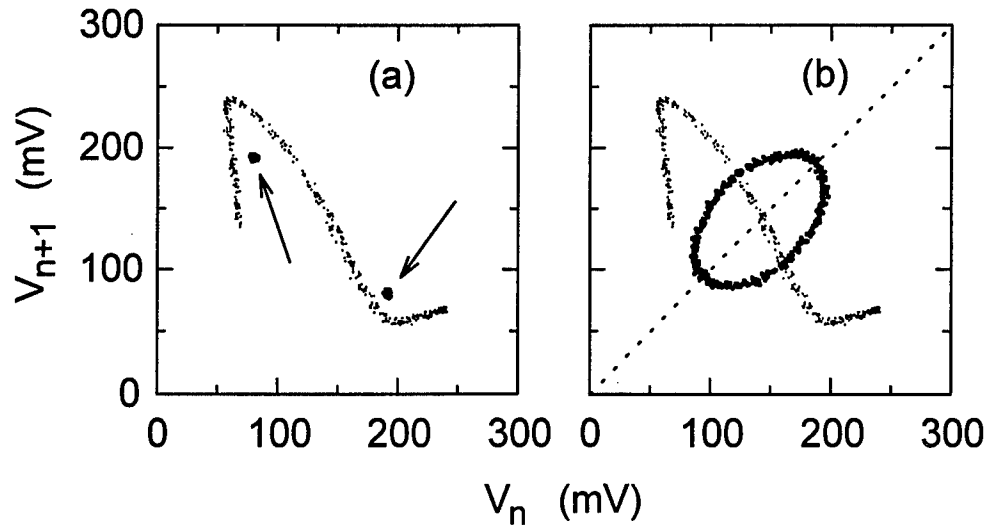


Figure 4.13: First return maps illustrating the dynamics of the system outside the period-1 domain of control. In (a), the system displays period-2 behavior (two dark dots indicated by arrows) when the feedback gain γ is too weak. These dots do not fall on the return map of the unperturbed system (lighter dots), indicating this period-2 orbit is not a true UPO of the original system. In (b), the system undergoes quasi-periodic dynamics (the dark oval centered on the period-1 fixed point) when the feedback gain is too large.

of γ , the low frequency oscillations become more pronounced and the oval-shaped return map increases in size.

Note that these mechanisms by which control may fail bear a relation to the transient dynamics described in Sec. 4.4. If the control is weak, the system tends toward higher periodicities; if the control is strong, low-frequency oscillations become prevalent in the dynamics.

A more sensitive technique for investigating the dynamics close to the boundary of the domain of control is to perform a spectral analysis of $V(t)$. Figure 4.14a shows the spectrum of the signal $V(f)$ for $\gamma = 3.1$, just outside the lower boundary of the domain of control. Clearly evident are spectral features at multiples of 5 MHz (the

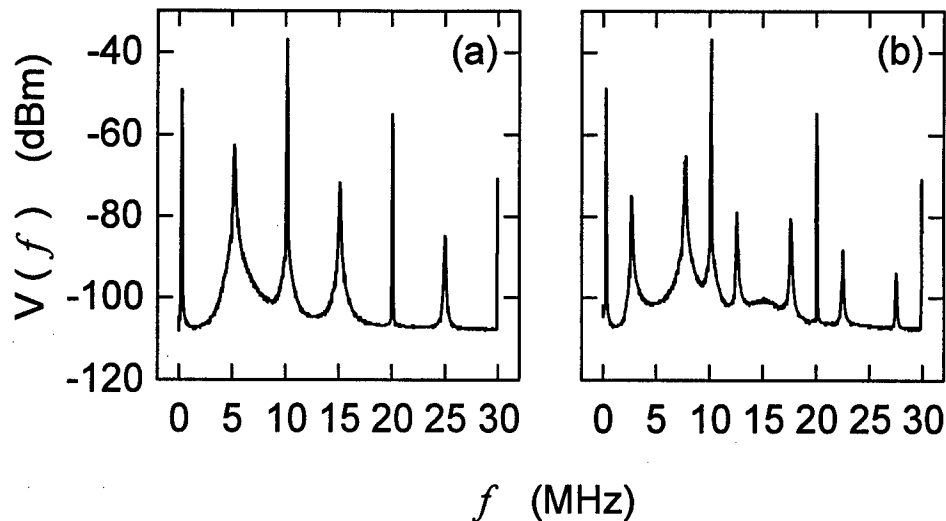


Figure 4.14: Power spectra of $V(t)$ outside the domain of control for the period-1 UPO. The cases shown are similar to those in Fig. 7.13. In (a) the spectrum has features at multiples of 5 MHz, indicating period-2 behavior when the feedback gain is too weak. In (b) the spectrum displays sidebands displaced by ~ 2 MHz, indicating low-frequency modulation of the fundamental frequency when the feedback gain is too strong.

subharmonic of the fundamental frequency) indicating period-2 behavior. Note that subharmonic peaks are >30 dB below the peaks of the fundamental frequency. Figure 4.14b shows the spectrum for $\gamma = 17.2$, just above the upper boundary of the domain of control. Sidebands about the fundamental spectral features displaced by ~ 2 MHz appear in the spectrum, indicating the low-frequency modulation of the fundamental frequency. Note that these frequencies appear where the ETDAS feedback is less sensitive (recall the form of the transmission function of the ETDAS circuitry shown in Figure 3.3). Hence, increasing R tends to suppress the growth of these frequencies and enlarge the domain of control.

This chapter has presented the experimental results of ETDAS control of the diode resonator. I have demonstrated successful control, meeting appropriate experimental

criteria. I have measured domains of control, and demonstrated that nonzero values of R enlarge the domains considerably, particularly for highly unstable orbits and in the presence of significant latencies (although no control is possible when the latency becomes too large). These results have been supported by good agreement with numerical predictions. Finally, I have explored the transient dynamics of the system and the behavior of the system outside the domain of control. This completes my study of ETDAS control of the diode resonator. In the chapter which follows I will introduce another experimental system, the external cavity semiconductor laser.

Chapter 5

Power Dropout Events in an External-Cavity Semiconductor Laser

This chapter is the first of three in which I study the external cavity semiconductor laser, my second experimental system. Its purpose is to characterize and understand the instability known as “low-frequency fluctuations” (LFF), or “power dropout events.” This chapter is devoted strictly to the dynamics of this system in the *absence* of control, which is necessary because the LFF regime is not well understood. For example, the LFF dynamics have been modeled as a stochastically-driven particle in a potential well [108], as a “time-inverted type II intermittency,” [109], and as deterministic antimode dynamics [39, 110]. Furthermore, it has been shown that spontaneous emission noise can strongly affect the characteristics of the power dropout events [38]. I therefore perform new measurements that provide additional knowledge about the long-time behavior of the system, in the hope that better understanding of the laser dynamics will naturally lead to more effective control.

I begin by introducing the relevant general features of semiconductor lasers subjected to optical feedback, and discuss the Lang-Kobayashi delay-differential rate equation model of the system. Subsequently, I describe the experimental apparatus, after which I characterize LFF both experimentally and theoretically. Finally, I consider the power dropout behavior from the point of view of a first-passage time problem. Specifically, I model the system as a noise-driven particle in a potential well with a barrier, where a power dropout occurs when the particle escapes over the barrier. This analysis produces reasonable agreement with experimental data measured at low laser powers, but misses some interesting and unexplained results

appearing at higher powers.

5.1 Introduction to semiconductor lasers in external cavities

The semiconductor laser, introduced in 1962 [111]-[114], has made an enormous technological impact, particularly in applications of telecommunications and data storage. They are cheap, reliable, and efficient, making them ideal for commercial production and use; they are also very small, allowing their incorporation in technologies where miniaturization is desirable. Recent decades have witnessed the proliferation of efficient fiber-optic communication systems, possessing information-carrying capacities that are orders of magnitude greater than the copper wires that preceded them. Similarly, digital optical discs read by diode lasers are rapidly replacing magnetic storage media in audio, video, and computing applications. This extraordinary usefulness has led to a very large research effort devoted to the understanding and use of these devices.

Much of the research has been at a fundamental level, due to the important differences between the semiconductor laser and other types of lasers; I will discuss some of these characteristics in the next section. Nonlinear dynamicists have had a long-standing interest in lasers, largely originating in Haken's discovery of the isomorphism between laser dynamics and turbulent convective flow [115]. One particularly important development in the study of nonlinear dynamics of semiconductor lasers is Lang and Kobayashi's paper on the effects of time-delay optical feedback [36]; the degrees of freedom in the system become infinite when such feedback is introduced, allowing a variety of complex behaviors to occur. This branch of study connects directly with the major technological applications, since optical feedback is often hard to avoid in fiber-optic and optical disc applications.

5.1.1 The semiconductor laser

Any laser has two required components: (1) a medium that provides optical gain by stimulated emission, and (2) a cavity that provides a feedback mechanism and frequency selection. As the name implies, semiconductor lasers employ semiconductor materials as a gain medium, which can be pumped using electrical or optical methods. They have high gains, such that lasing action can be sustained even if the cavity is formed by the cleaved facets of the semiconductor material, with reflectivities of about 30%. This reflectivity arises because the index of refraction of the gain medium is so high (~ 3.5) relative to air. However, coatings are frequently used in commercial lasers, both to increase or decrease the reflectivity of the facets depending on the application.

Historically, the first semiconductor lasers used a forward-biased p - n junction as the gain medium, known as homostructure lasers. Later, the heterostructure laser was developed, employing an “active layer” of one semiconductor material sandwiched between two cladding layers of a different semiconductor. This configuration has important advantages. First, the active layer is designed to have a smaller band gap than the cladding layers, which helps to confine the electrons and holes to the active region, thereby reducing the threshold current. In addition, it has a higher refractive index which helps confine the optical mode to the active layer, creating a laser with a high transverse and longitudinal coherence. This feature is important to my research, since the Lang-Kobayashi model I use for theoretical investigations assumes the laser operates in a single longitudinal mode.

To place semiconductor lasers in a familiar framework, they are considered to be Class B lasers along with Nd:YAG, CO₂, and Ti:sapphire lasers, in the classification scheme described by Arecchi [116]. The criterion for such categorization is that

the characteristic decay rate for the polarization density of the gain medium is at least an order of magnitude greater than the decay rates for the field and inversion (this classification scheme is based on semiclassical laser theory, in which lasers are described with three rate equations, one each for electric field strength, macroscopic polarization, and inversion density). In the case of semiconductor lasers, the decay times for the inversion, electric field, and polarization are on the order of 1 ns, 1 ps, and 0.1 ps, respectively [117]. The polarization density can be eliminated adiabatically from the equations, and thus a semiconductor laser is well described by the two remaining equations. Class B lasers by themselves cannot exhibit chaotic behavior, unlike the Class C lasers that require all three equations (as was illustrated in Sec. 1.1). However, they readily display instabilities and chaos if additional degrees of freedom are introduced, by such means as optical feedback, for example. I will discuss the case of optical feedback from a distant reflector in the next section.

Although they are categorized as Class B lasers, semiconductor lasers have several characteristics that distinguish them from conventional types. They are very small, with typical dimensions of the active region of $300 \times 1.5 \times 0.2 \mu\text{m}$. They are also very “open,” meaning that relatively low reflectivity surfaces form the cavity, whereas conventional lasers generally use much higher reflectivities. This openness is possible due to the high gain of the device. One consequence of this property is that semiconductor lasers are very susceptible to external optical signals. This can be beneficial, allowing both tuning and linewidth reduction by means of grating feedback, for example, but unplanned optical perturbations more often lead to diminished performance. Finally, a phenomenon called *phase-amplitude coupling* is very important in semiconductor laser physics, whereby fluctuations in the phase of the optical field affect the amplitude, and vice versa. This interaction arises through the coupling of the gain and frequency of the optical field through the complex refractive index of

the semiconductor medium. The strength of this coupling is usually quantified by the *linewidth-enhancement parameter* α [118], which is proportional to the relative changes in the index and gain with carrier density. Semiconductor lasers have large values of α (typically 3 - 7), whereas it is approximately zero for most other lasers.

5.1.2 External cavity effects

As stated previously, semiconductor lasers are very susceptible to optical perturbations due to their openness and the high optical gain of the active medium. I study the case where optical feedback arises from an *external cavity*. This system is really a compound-cavity configuration with *two* distinct laser cavities, as illustrated in Fig. 5.1. One is formed by the cleaved facets of the semiconductor material r_1 and r_2 , creating the *solitary laser*. The other is the external cavity, formed by a distant reflector R and the rear facet of the laser chip. This system would be equivalent to a single-cavity laser with the gain medium located in one end of the long cavity if the right facet of the chip were completely antireflection-coated ($r_2 = 0$), whereby this could accurately be called an external-cavity laser. Unfortunately, the standard nomenclature is unclear, and the compound-cavity system that I study is usually referred to as an external-cavity laser system, which is the name I use throughout this thesis.

The optical feedback can have varied and profound effects on the laser dynamics; the specific behavior depends primarily on the roundtrip time in the external cavity and the power reflected from the distant surface (as well as on the physical parameters of the semiconductor laser itself). In theoretical terms, the distant reflector introduces a time-delay term representing the reinjected field after one roundtrip time in the external cavity, causing the laser equations to become infinite-dimensional. The instantaneous state of the solitary laser as well as the state of the propagating field

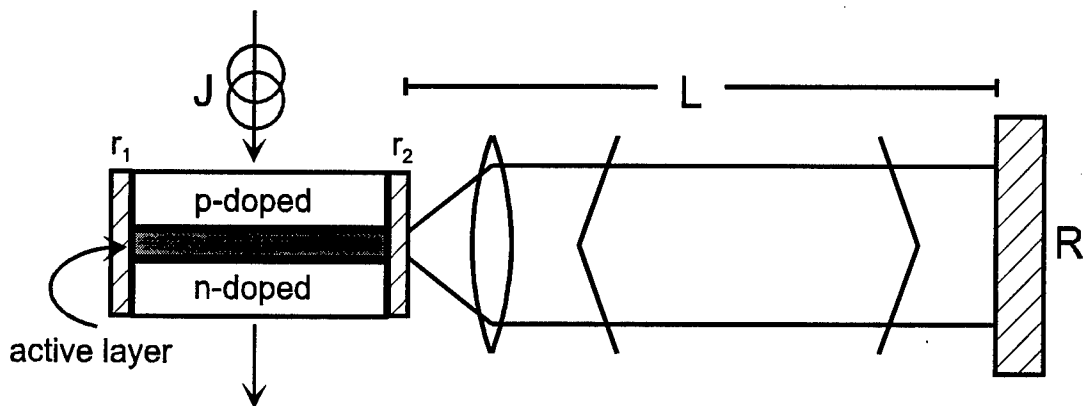


Figure 5.1: External-cavity semiconductor laser. The active region of the solitary laser is sandwiched between p-type and n-type cladding layers that provide electron-hole pairs generated by the current J . The solitary laser cavity is formed by the mirrors r_1 and r_2 , whereas the external cavity is formed by r_1 and the reflector R located a distance L from the right facet of the laser.

everywhere in the external cavity must be specified to completely describe the state of the dynamics. From a different point of view, the distant reflector creates new external cavity modes that differ from those of the solitary laser.

Researchers have found several classes of dynamics resulting from the introduction of the external cavity. One useful effect is that the linewidth of the laser can be significantly narrowed [119]-[121], but there are several other types that are more interesting from the nonlinear dynamics point of view. For example, the laser may exhibit intermittency [109, 122] or multistability [123]-[125], and spontaneous emission noise may cause the laser to hop from one external cavity mode to another [126]. Dramatic spectral broadening of the laser linewidth, the phenomenon known as “coherence collapse,” has been identified as a form of chaos [127, 128].

The dynamics of these behaviors are generally believed to be well understood [33]. One notable exception, however, is known as “low-frequency fluctuations (LFF)” [37], sometimes called “power dropout events.” This is the instability I study in this

chapter and try to control in the subsequent two chapters. It occurs when the external cavity is long (tens of cm) and the optical feedback strength is weak to moderate. Its dominant feature is spontaneous, rapid decreases of the average laser intensity that occur at irregular intervals. In addition, researchers have recently found that a semiconductor laser exhibiting LFF dynamics generates a train of ultrashort pulses [40] that are irregular in width, spacing, and amplitude. I characterize the LFF dynamics in detail in Sec. 5.4.

5.2 Model of the system

The model for semiconductor lasers with external cavities put forth by Lang and Kobayashi (LK) in their 1980 paper [36] is a reasonably simple theoretical description yet captures the essential physics of the system. It has been widely studied and found to be in good agreement with experimental observations. I use the LK equations in my theoretical work studying the LFF dynamics. In this section I discuss the origins of these equations, their relationship to standard semiclassical laser theory, and their most important features and limitations. I consider their steady-state solutions, which are important for understanding the mechanisms of LFF and introduce a dimensionless form that I use for computations. Derivations for the LK equations and their dimensionless form are provided in Appendix B.

5.2.1 The Lang-Kobayashi equations

The LK equations are *not* derived entirely from first principles, unlike those of standard semiclassical laser theory. Rather, they are a reasonable compromise between first principles and phenomenological considerations. For the sake of comparison, consider the outline of the usual semiclassical approach [3]. The electromagnetic field is described classically by Maxwell's equations [129], whereas the gain medium

is treated quantum mechanically, typically as an ensemble of quantum oscillators with two well-defined energy eigenstates. The classical field \mathcal{E} induces microscopic electric dipole moments in these two-level systems, which are then statistically summed using a density-matrix approach to obtain a macroscopic polarization \mathcal{P} . This polarization becomes the source term in the electromagnetic wave equation, which is then reduced to a set of rate equations (first-order differential equations) using the slowly-varying envelope approximation. These equations describe the evolution of \mathcal{E} , \mathcal{P} , and the population inversion \mathcal{N} .

In deriving the semiconductor laser rate equations, I follow a similar procedure in that the field \mathcal{E} is treated classically. In contrast, however, the semiconductor material cannot be treated simply as a set of independent two-level atoms. The semiconductor medium behaves only *approximately* as a collection of two-level atoms; population inversion occurs between continuous energy *bands* separated by a band gap. Light is emitted when electrons that have been excited to the conduction band (usually by applying an electrical current) recombine with holes in the valence band, with the photon energy $\hbar\omega$ approximately equal to the band gap energy. To treat this system in a fully quantum mechanical fashion would require detailed knowledge of the band structures, correlations between electrons and holes (many-body effects), and decay mechanisms. Therefore, the semiconductor medium is treated in a more phenomenological fashion.

For the purposes of this chapter, it will suffice to merely sketch the derivation of the LK model that describes an external cavity semiconductor laser, leaving the full derivation to Appendix B. The classical treatment of the electric field \mathcal{E} begins with Maxwell's equations in a nonmagnetic medium, leading to the wave equation

$$\nabla^2 \mathcal{E} - \frac{\sigma}{\epsilon_0 c^2} \frac{\partial \mathcal{E}}{\partial t} - \frac{1}{c^2} \frac{\partial^2 \mathcal{E}}{\partial t^2} = \frac{1}{\epsilon_0 c^2} \frac{\partial^2 \mathcal{P}}{\partial t^2}, \quad (5.1)$$

where \mathcal{P} is the polarization, c is the speed of light, σ is the conductivity of the medium, and ϵ_0 is the permittivity of free space. Next, I Fourier transform Eq. 5.1, assume that the field is linearly polarized and propagates in the z -direction, and eliminate the transverse structure to obtain a simplified equation for the z -dependent part of the field $E_\omega(z)$ at frequency ω , given as

$$\left[\frac{\partial^2}{\partial z^2} + k^2(z) \right] E_\omega(z) = 0, \quad (5.2)$$

where the wavevector $k(z)$ contains the physics of the interaction of the field with the semiconductor medium. At this point, I introduce the phenomenological form for $k(z)$, given by [130]

$$k(\omega, N) = \frac{\omega}{c} n(\omega, N) + i \frac{1}{2} [g(\omega, N) - a_i], \quad (5.3)$$

where ω is the angular optical frequency of the lasing mode, N is the average carrier density of the active region, n is the real refractive index, a_i is the internal loss per unit length, and g is the modal gain representing the difference of the stimulated emission and stimulated absorption per unit length. It is assumed that n and g vary linearly with N about some stationary operating point.

Equation 5.3 is then incorporated in a travelling-wave model of the external cavity semiconductor laser [130]. The threshold condition in this model determines which optical frequencies are supported by the solitary laser cavity. In addition, I derive a rate equation for the slowly-varying complex envelope function of the electric field using a Taylor expansion of k about the stationary point, then transforming back to the time domain. To complete the set of equations, I also assume the rate equation for N is of the usual form [131], choosing a simple expression for the rate of spontaneous recombination of carriers. These two rate equations together are called the Lang-Kobayashi equations,

$$\frac{dE}{dt} = \frac{1}{2} (1 + i\alpha) G_N (N - N_{th}) E + \frac{\kappa}{\tau_{in}} e^{-i\omega_0 \tau} E(t - \tau), \quad (5.4)$$

$$\frac{dN}{dt} = J - \frac{N}{\tau_s} - \left[\frac{1}{\tau_p} + G_N (N - N_{th}) \right] |E|^2, \quad (5.5)$$

where $E(t)$ is the slowly-varying complex envelope function of the electric field, $N(t)$ is the carrier density, α is the linewidth-enhancement parameter, $G_N = (\partial G / \partial N)_{th}$ where $G(N)$ is the gain rate, N_{th} is the carrier density at the threshold of the solitary laser, κ is the optical feedback parameter, ω_o is the angular optical frequency of the solitary laser, J is the carrier density pump rate, τ_s is the carrier lifetime, τ_p is the photon lifetime, τ_{in} is the roundtrip time inside the solitary laser cavity, and τ is the roundtrip time in the external cavity. Note that $E(t)$ is normalized in these equations such that $|E(t)|^2$ is the *photon number density*. That is, the number of photons in the lasing mode is $I(t) = V_c |E(t)|^2$, where V_c is the volume of the active region. Note also that the expression in brackets in Eq. 5.5 is just an alternate expression for $G(N)$, which can be seen by noting that $G(N_{th}) = (1/\tau_p)$ and considering that

$$G(N) = G_N (N - N_o) = G(N_{th}) + G_N (N - N_{th}) = \frac{1}{\tau_p} + G_N (N - N_{th}), \quad (5.6)$$

where N_o is a constant, usually the carrier density at transparency.

The LK equations as given by Eqs. (5.4,5.5) are frequently studied because they contain much of the essential physics of the system without being excessively complicated in form. In using such equations it is important to be aware of the simplifications that are made, as well as additional fine-tuning that may improve agreement between theoretical predictions and experimental results. One important simplification is that the theory assumes single-mode behavior, which may be questionable if the laser is near threshold. Also, spatial effects such as carrier diffusion are ignored, assuming instead a uniform average carrier density in the semiconductor.

Various improvements to these equations have been considered. For example, some researchers model the experimentally observed effect of gain saturation [132] by expressing the gain as $G(N) = G_o(N) / (1 + \varepsilon |E|^2)$ where $\varepsilon |E|^2 \ll 1$. Other models

include multiple longitudinal lasing modes, which may interact through the carrier reservoir [124, 130, 133]. In such a theory, the frequency dependence of the gain must be taken into account. These additional complications will not be considered in this thesis.

Finally, in many studies it is desirable to include one or more stochastic terms to the rate equations to take into account random processes such as spontaneous emission. It is usually assumed that spontaneous emission into the lasing mode is the dominant random force, and thus a Langevin force term $F_E(t)$ is added to the right hand side of Eq. 5.4. It is a Gaussian white-noise function described by

$$\langle F_E(t) \rangle = \langle F_E(t)^* \rangle = 0, \quad (5.7)$$

$$\langle F_E(t) F_E(t')^* \rangle = 2D_{EE^*} \delta(t - t'). \quad (5.8)$$

In these expressions, the diffusion coefficient $2D_{EE^*} = R/V_c$ [134], where R is the rate of spontaneous emission into the lasing mode, given by $R = n_{sp}G(N_{th})$ [124]. The spontaneous coefficient n_{sp} is a constant given by [134]

$$n_{sp} = \frac{1}{1 - \exp[(\hbar\omega - eV) / (k_B T)]}, \quad (5.9)$$

where $\hbar\omega$ is the photon energy, eV is the band gap energy of the semiconductor, k_B is Boltzmann's constant, and T is the absolute temperature. Spontaneous emission is included in my investigations of LFF, and it will be shown to play an important role.

The LK equations (including the Langevin force) can be expressed in terms of dimensionless quantities [135]; it is this form that I use for all numerical simulations of the laser in this thesis. The equations for the dimensionless field Y and the dimensionless carrier number above threshold Z ($\propto N - N_{th}$) are given by

$$\frac{dY}{ds} = (1 + i\alpha)ZY + \eta e^{-i\Omega\theta}Y(s - \theta) + \tilde{F}_Y(s), \quad (5.10)$$

$$T \frac{dZ}{ds} = P - Z - (1 + 2Z) |Y|^2, \quad (5.11)$$

where $s = t/\tau_p$ is the dimensionless time, the pump parameter P is related to the driving current J , $\tilde{F}_Y(s)$ is the dimensionless Langevin force, and η , Ω , θ and T are normalized to the photon lifetime τ_p . A complete description of this transformation is given in Appendix B, along with the parameter values I use in all numerical simulations.

5.2.2 Steady states of the laser with optical feedback

The Lang-Kobayashi equations in the LFF regime possess a large number of stationary solutions that play a important role in the dynamics of LFF. I find their steady states by following a procedure similar to that of Ref. [136]. The solutions are assumed to have the form

$$E(t) = E_s \exp(i\Delta\omega_s t), \quad (5.12)$$

$$N(t) = N_s, \quad (5.13)$$

where E_s , N_s , and $\Delta\omega_s = \omega_s - \omega_o$ are real constants. I insert Eq. 5.12 into Eq. 5.5 to immediately obtain the condition

$$E_s^2 = \frac{1}{G(N_s)} \left(J - \frac{N_s}{\tau_s} \right). \quad (5.14)$$

Next, I substitute Eqs. 5.12,5.13 into Eq. 5.4 and split the resulting equation into real and imaginary components. These equations yield the conditions

$$N_s - N_{th} = -\frac{2\kappa}{G_N \tau_{in}} \cos(\omega_o \tau + \Delta\omega_s \tau), \quad (5.15)$$

$$\Delta\omega_s \tau = -C \sin[\Delta\omega_s \tau + \omega_o \tau + \arctan(\alpha)], \quad (5.16)$$

where $C \equiv \kappa \tau \sqrt{1 + \alpha^2} / \tau_{in}$ is the effective feedback strength. The solutions to Eqs. 5.14 - 5.16 define one or more fixed points $(E_s^2, \Delta\omega_s, N_s)$; this coordinate system

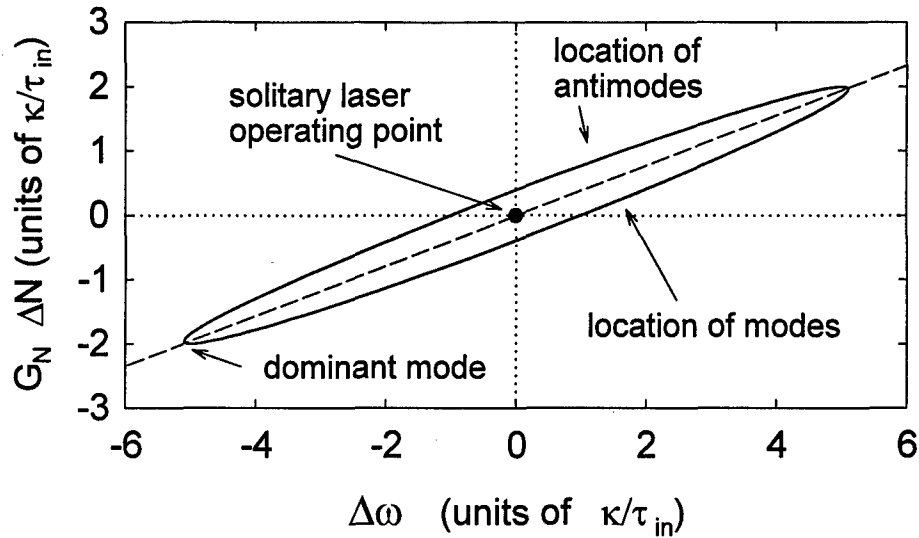


Figure 5.2: Phase space ellipse indicating possible locations of fixed points. Unstable antimodes occur on the branch of the ellipse above the dashed line, and modes occur below. The dominant mode is the fixed point at which the output power is maximized. The operating point of the solitary laser is at the origin. The linewidth enhancement parameter is taken to be $\alpha = 5$.

describes a phase space that is very useful for understanding the dynamics of external cavity semiconductor lasers [108].

Equation 5.16 is transcendental and must be solved numerically or graphically. Multiple solutions for $\Delta\omega_s\tau$ will exist if $C > 1$ [123, 137]; this condition is easily met for the case of LFF dynamics when κ is not too small, since $\tau \gg \tau_{in}$ (there is only a single solution for $\Delta\omega_s$ at zero feedback). The quantity $\Delta\omega\tau$ is an important dynamical variable for the system because it represents the difference of the phase of the slowly-varying complex electric field variable $\phi(t) \equiv \Delta\omega t$ and its value one cavity-roundtrip time earlier $\phi(t - \tau)$.

Henry and Kazarinov recognized that a relationship exists between N_s and $\Delta\omega_s$, such that the fixed points must fall on an ellipse in the $(N, \Delta\omega)$ plane [108]. Specifi-

cally, the fixed points must lie on the curve defined by

$$\left(\Delta\omega - \frac{\alpha}{2}G_N\Delta N\right)^2 + \left(\frac{G_N}{2}\Delta N\right)^2 = \left(\frac{\kappa}{\tau_{in}}\right)^2, \quad (5.17)$$

where $\Delta N = N - N_{th}$. This ellipse is shown in Fig. 5.2. The fixed point with the lowest carrier density is called the *dominant external cavity mode* [128]. For systems exhibiting LFF, the cavity length and feedback parameter are sufficiently large that many fixed points exist, in which case the fixed points are assumed to be quasi-continuous on the ellipse. The dominant mode then can be taken to satisfy $\omega_s\tau \pmod{2\pi} = 0$. This point is indicated by the arrow in Fig. 5.2, and corresponds to the minimum carrier density (maximum output power) possible on the ellipse. Note that the point corresponding to the solitary laser threshold condition is located in the center of the ellipse at $(N, \Delta\omega) = (0, 0)$.

The fixed points are typically classified into two types, based on an approximate linear stability analysis [136]. One type is *always* unstable, and is called an antimode; the other may be either stable or unstable depending on the system parameters, and is referred to as an external cavity mode (or simply a “mode”) [138]. They are created in pairs via a saddle-node bifurcation as the effective feedback level increases [137]. Referring again to Fig. 5.2, all antimodes are located on the half of the ellipse above the dashed line, and all modes are located below.

Physically, antimodes correspond to destructive interference between the field returning from the external cavity after one roundtrip and the field in the solitary laser at the output facet. Mathematically, a necessary and sufficient condition for a fixed point to be an antimode is given by [138]

$$1 + C \cos[\Delta\omega_s\tau + \omega_o\tau + \arctan(\alpha)] < 0. \quad (5.18)$$

All such fixed points exhibit a saddle-node instability, where the three dominant eigenvalues consist of a complex-conjugate pair with a negative real part and a posi-

tive real root [39]. In contrast, the external cavity modes indicate constructive interference between the fields. These fixed points may be stable, or they may undergo Hopf bifurcations, indicating that relaxation oscillations for that point have become undamped [136, 139]. Destabilized external cavity modes are sometimes called quasiattractors or attractor ruins [110] when they collide with other such modes, giving rise to transient chaos and chaotic itinerancy. This mode-antimode structure is considered to be a primary mechanism of LFF, with power dropouts occurring due to a destabilized external cavity mode coming into crisis with an antimode. These dynamics will be explored in Sec. 5.4.2, where I characterize the LFF dynamics in detail.

5.3 Experimental apparatus

With an understanding of the basic theory of the external cavity semiconductor laser well in hand, I now describe the experimental system with which I investigate the characterization and control of LFF. The system is relatively simple, consisting of the external cavity system itself, designed to provide a tunable level of optical feedback, and the actual semiconductor laser with its associated electronics for temperature stabilization and current injection. I describe each of these elements in this section.

5.3.1 External cavity configuration

The layout of the external cavity semiconductor laser system is illustrated in Fig. 5.1. The solitary laser diode is a Spectra Diode Labs SDL-5401-G1 laser [140], which is a GaAs/AlGaAs heterostructure index-guided laser with a nominal wavelength of $\lambda = 789$ nm and threshold injection current of 17 mA. It is placed in a mount specially designed for temperature stabilization, described in detail in Sec. 5.3.2. The laser is pumped electrically using an injection current that enters through the DC port

of a bias-tee (Mini-Circuits ZFBT-6GW) and is connected to the laser with RG-174 coaxial cable. The beam generated by the laser is collimated with a high numerical aperture lens (Melles Griot type 06GLC002, numerical aperture = 0.5) and directed into an external cavity formed by a series of mirrors. The most distant mirror reflects the beam back to the laser from a distance of ~ 71 cm. I place a polarizing cube and a quarter-wave plate in the beam path to control the optical feedback strength. The $\lambda/4$ plate is mounted on a rotatable stage, providing a mechanism for smooth adjustment of the optical feedback. I also place a beamsplitter in the beam path which directs $\sim 30\%$ of the laser's output out of the box through a glass plate to the photoreceiver. This beamsplitter is placed near the laser so that the beam is sampled immediately after it emerges from collimating lens, a configuration intended to minimize latency in a feedback control situation.

The entire external cavity laser system is placed in a cast aluminum box, to shield the laser from electromagnetic noise and from air currents that may disrupt its temperature stability. To further isolate the system from noise, the components are fixed onto a large aluminum plate that is mounted on compressed pads of a visco-elastic acoustical-damping material inside the aluminum box.

5.3.2 Stabilized semiconductor laser

It is necessary to stabilize the temperature of the semiconductor laser to perform consistent studies of its dynamics. It is well known that a semiconductor laser's wavelength changes with temperature since the parameters that generally determine the wavelength are temperature-dependent. Specifically, both the optical path length of the cavity and the band gap of the semiconductor are sensitive to changes in temperature. This tunability is an advantage in atomic physics applications, for example, where it is desirable to operate lasers at particular atomic resonance frequencies [141].

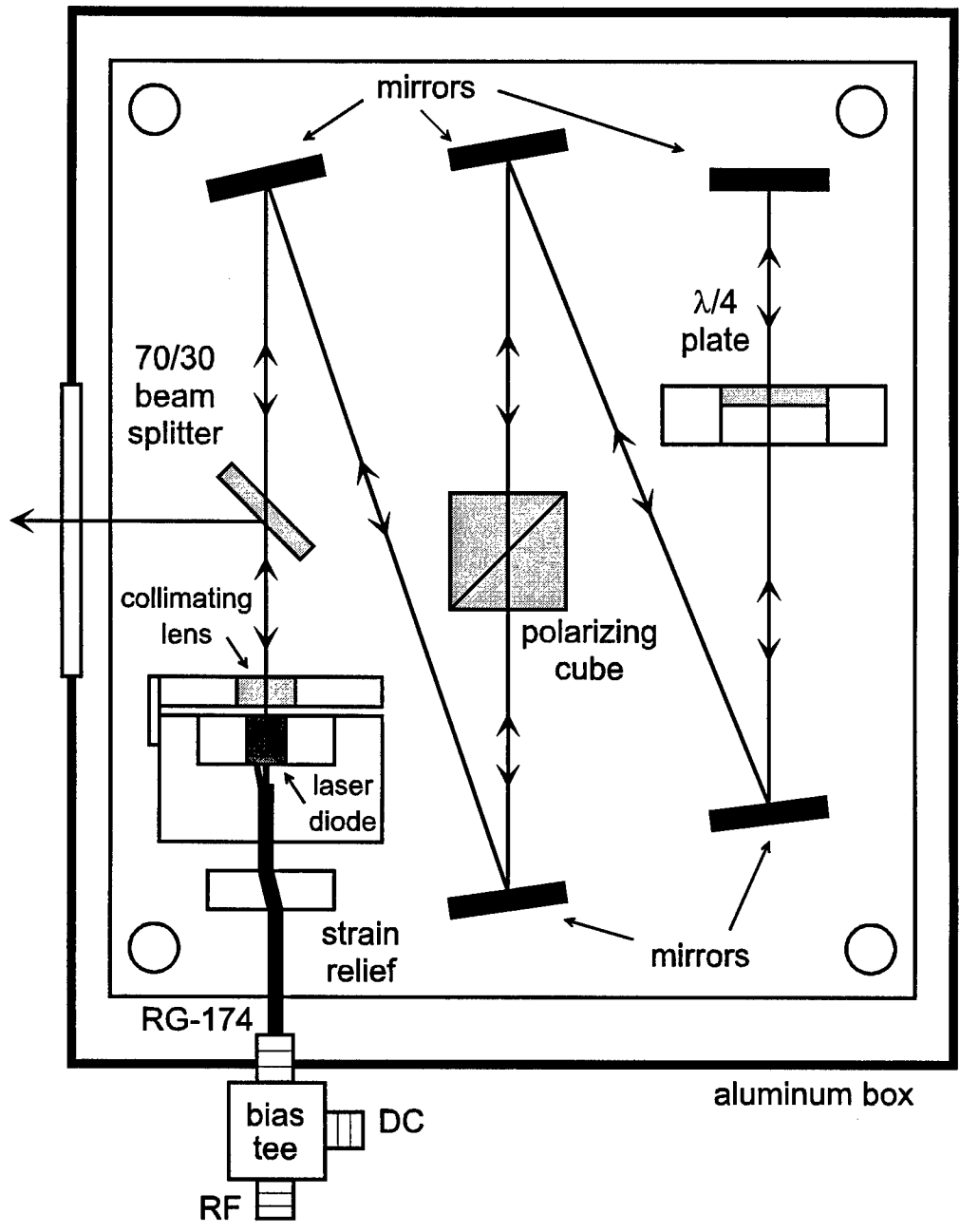


Figure 5.3: Experimental layout of the external cavity semiconductor laser.

In this nonlinear dynamics study, however, it is not the particular value of the wavelength but rather its stability that is important.

I design and construct a temperature control system to keep the laser at a constant temperature. The system is very effective, stabilizing the temperature to better than 1 mK, and is illustrated schematically in Fig. 5.4. The key elements of this system are a thermistor to measure the temperature of the laser mount, a thermoelectric cooler to change the temperature, and feedback electronics that determine the level of current driving the cooler. The electronics are designed to force the thermistor's resistance to match a predetermined adjustable resistance, thereby locking the temperature to the value corresponding to that resistance.

The operation of the system is straightforward. The LM399 in the upper left of Fig. 5.4 is a stabilized zener diode, which provides a stable reference voltage of nominally 6.9 V that is applied to a resistor bridge. One arm of the bridge includes the thermistor, and the other contains the series combination of a rotary switch resistance (S1) and a 5 k Ω potentiometer (P1) to which the thermistor resistance is to be matched (this combination provides much finer control of the desired matching resistance than would a single large potentiometer). The thermistor (Fenwal Electronics #121-503JAJ-Q01) has a nominal resistance of 44 k Ω at 25 °C and varies approximately as 1.47 k Ω /°C. The remaining 50 k Ω resistors in the bridge are 1% precision metal film types.

I use a precision instrumentation amplifier (Analog Devices AD620) to measure and amplify the voltage difference that results when the resistance of the thermistor is not equal to the sum of S1 and P1. This signal is then sent to an integrator with an RC constant of approximately 4 seconds. The output of the integrator drives the base of a Darlington transistor (TIP 122, $h_{FE} \approx 1000$) that is powered by an independent 12 V / 1.25A supply, and drives a 1 cm² thermoelectric cooler (Melcor

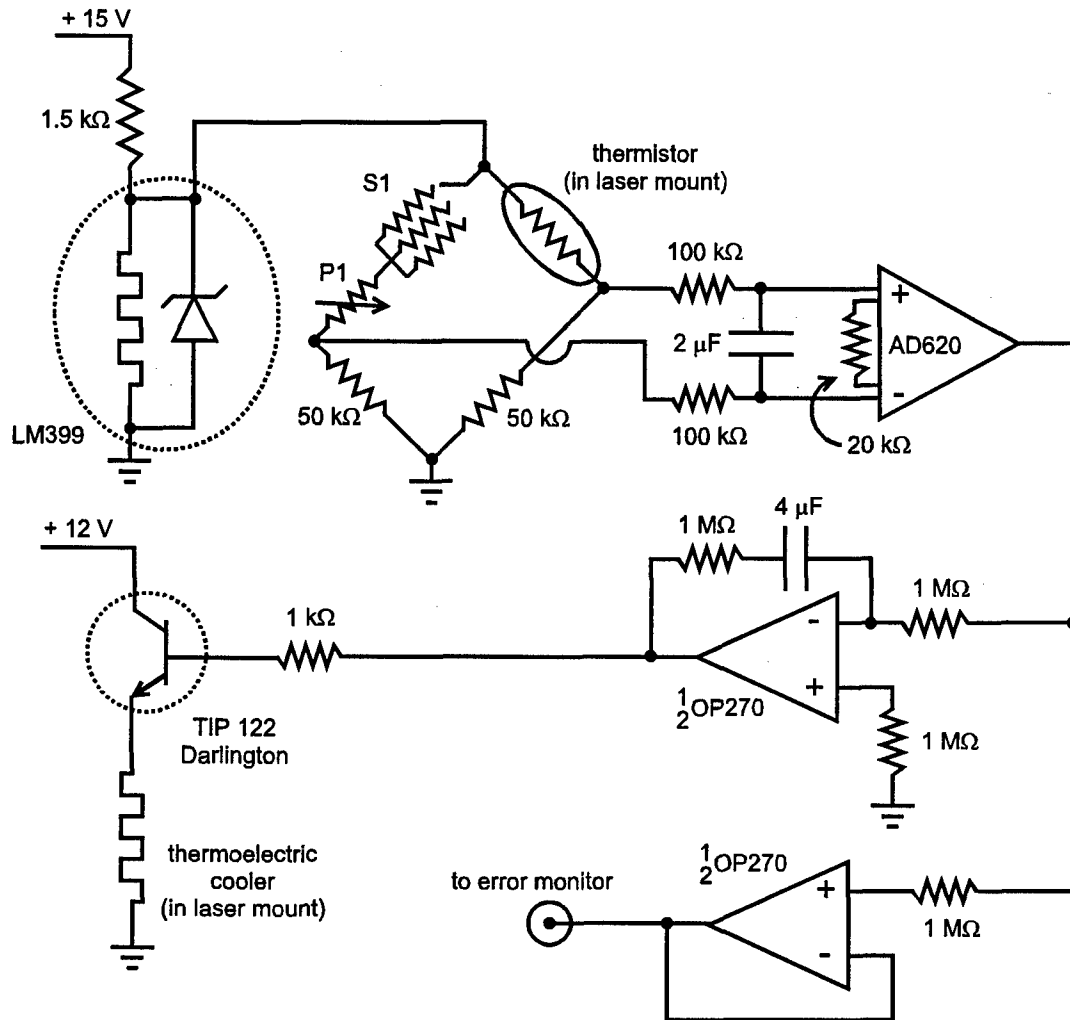


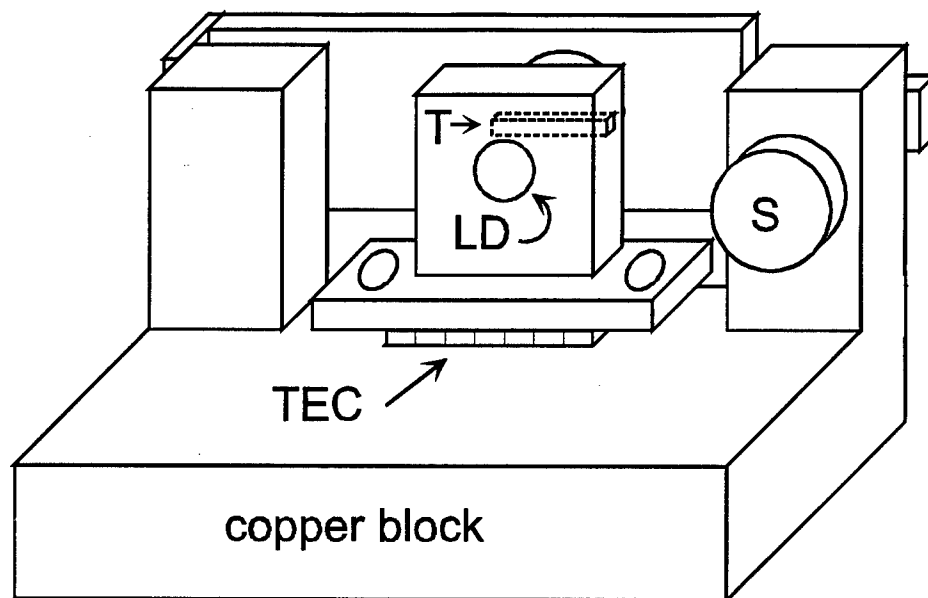
Figure 5.4: Temperature control system for semiconductor laser. The system is designed to force the resistance of the thermistor in the laser mount to match the sum of the resistances S1 and P1. The difference of these resistances is measured by an instrumentation amplifier and fed to an integrator. The integrator drives the base of a Darlington transistor, which generates the current that drives the thermoelectric cooler in the laser mount.

CP1.0-17-05L) located in the base of the diode laser mount.

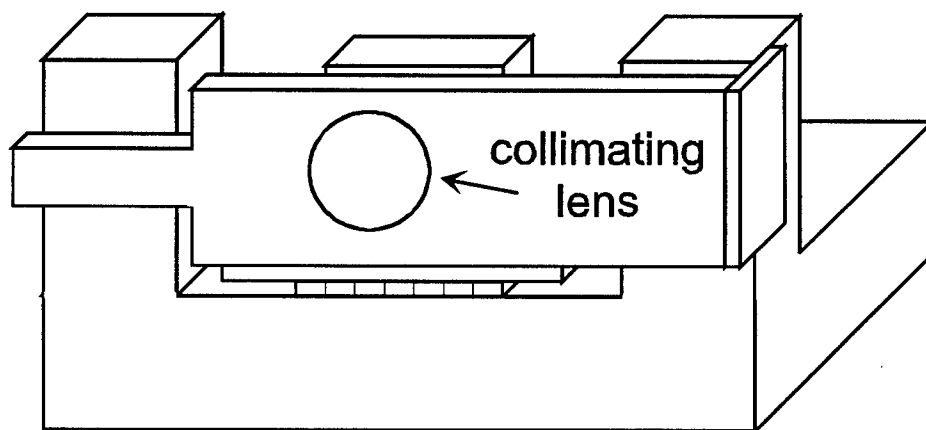
I include an error monitor in the circuitry to verify that the temperature of the mount is stable. This is simply a buffer that reads the voltage from the instrumentation amplifier, which is proportional to the difference of the thermistor resistance and the preset matching resistances S1 and P1. When the temperature is successfully stabilized, the error monitor gives a very small voltage (nominally 0.3 mV). Small fluctuations about the operating point indicate variations in temperature with a scaling factor of 0.18 mV per mK. Typically, the error signal varies ± 0.15 mV, indicating temperature stability of approximately ± 1 mK.

The thermistor and thermoelectric cooler are located in the laser mount (the remaining circuitry is contained in an external unit). This mount is designed to allow both for effective stabilization as well as ease of collimation for the laser beam. Figure 5.5 illustrates the basic construction of the mount. There are three major pieces of the assembly: the laser holder itself, the base, and the holder for the collimating lens. The laser holder is a small copper piece into which the laser diode (LD) and the thermistor (T) are inserted. It rests on the thermoelectric cooler (TEC), making good thermal contact using a thermally conductive compound. This block is held to the base by nylon screws to minimize direct heat transfer. The TEC cools the laser holder, stabilizing the laser's temperature, and dumps heat into the larger copper base. The base also supports the lens holder; they are joined by a piece of spring steel that is pre-bent such that the lens holder is pressed against the base. The distance from the collimating lens to the laser diode is controlled by means of a fine-pitch adjustable screw (S) that pushes against the lens holder.

The laser mount (Fig. 5.5) and the electronics (Fig. 5.4) comprise the temperature control system. The other important piece of equipment needed to operate the semiconductor laser is a stable, low-noise current supply. I use a design that provides



(a) rear view



(b) front view

Figure 5.5: Rear (a) and front (b) views of laser mount assembly. The thermoelectric cooler (TEC) cools the small piece that contains the laser diode LD, and the temperature is sensed with a thermistor T. The copper block at the base acts as a heat sink. The screw S dictates the distance from the collimating lens and the laser diode.

accurate tuning of the drive current, as well as stable, quiet operation. The current is provided by a FET that is controlled by a feedback loop, where the dc current level is regulated by a voltage divider referenced to a stabilized zener diode breakdown voltage. This design also includes protection against large current or voltage spikes, which can quickly destroy a laser. As additional protection, 1N914 diodes are placed in close proximity to the laser itself, preventing both forward and reverse voltage spikes. Details of these electronics, including diagrams of the current supply and the protection diodes, can be found in Ref. [142].

5.4 Characterization of low-frequency fluctuations

Previous sections of this chapter have introduced the basic theory of the external cavity semiconductor laser, and the experimental apparatus I use to investigate this system. I now characterize the LFF instability from both experimental and theoretical viewpoints. The LFF dynamics are very complicated, and it is necessary to be familiar with the instability to understand how it is affected by control perturbations. To this end, I present experimental time series data and power spectra, as well as computer simulations based on the Lang-Kobayashi equations. The power spectra indicate the presence of ultrafast dynamics hidden beneath the slower power dropout events. Numerical simulations predict the ultrafast dynamics, and are also used to reconstruct the dynamics in phase space as presented in Sec. 5.2.2.

All experimental data representing the laser's dynamics is based on measurement of its output intensity. As was illustrated in Fig. 5.3, a beamsplitter near the laser directs a portion of the beam out of the aluminum box through a glass plate; this beam is focused onto the photoreceiver, whose output is then directed to an oscilloscope or spectrum analyzer. The photoreceiver is a New Focus model 1537-LF, consisting of the combination of a InGaAs Schottky photodiode housed with a low-

noise transimpedance amplifier. This detector is specified to have a flat frequency response to 6 GHz and has a low-frequency cutoff of 10 kHz, an ample range to study LFF dynamics. One important experimental consideration in using this device is the small size of the active region of the photodetector, at a diameter of 25 μm . The laser must be focused carefully onto this spot; the frequency response of the photoreceiver is severely degraded if the beam waist is too large, or if the detector is not in the focal plane. Therefore, the detector is mounted on an XYZ-translation stage for micropositioning, and the sampled laser beam is focused using a lens with a focal length of 32mm. I note that anamorphic prisms may be used to shape the beam and allow it to be more tightly focused. However, I do not use them because they add path length and latency in feedback control experiments, and they are unnecessary since the lens brings the beam to a sufficiently tight focus. I limit the incident power on the detector using neutral density filters, since its damage threshold is approximately 3 mW.

I use a digitizing oscilloscope and a spectrum analyzer to record and analyze the photodetector output. The oscilloscope is a Tektronix model TDS680B, with an analog bandwidth of 1 GHz (rise time of 350 ps) and a maximum sampling rate of 5 Gs/s. It has the capacity to store 15,000 data points. This oscilloscope is state-of-the-art equipment, allowing both for excellent resolution in time and the ability to record long time traces. I note that faster devices are available, in the form of transient digitizers and streak cameras, but neither of these have the capability to record the long time series needed to fully analyze the LFF system. The spectrum analyzer is a Tektronix model 2711, with a bandwidth of 9 kHz to 1.8 GHz.

5.4.1 Power dropout events

The most prominent feature of LFF is a spontaneous, rapid decrease in the laser's

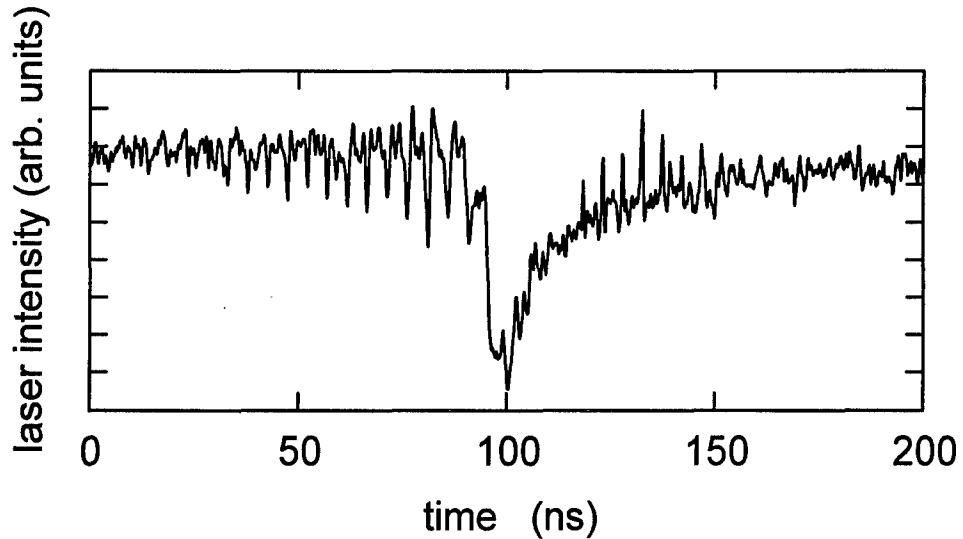


Figure 5.6: Experimental time series showing a typical power dropout. Note the small scale structure, evidence of faster dynamics hidden by bandwidth limitations of the digitizing oscilloscope.

intensity followed by a slower turn-on phase during which the average power builds up to an approximately constant level. An example of a typical dropout event is shown in Fig. 5.6. Initially, the laser intensity is nearly constant, but then drops to a fraction of its former level within about one nanosecond (the bottom of the graph is *not* zero intensity, however). Following the catastrophic drop, the intensity builds up to its initial level in a comparatively long time, equal to ~ 10 external cavity roundtrip times ($L \simeq 71$ cm, giving a roundtrip time of about 4.7 ns).

Fig. 5.6 also illustrates some interesting details, in addition to the main features. Most notably, there appears to be some small-scale structure, both in the steady-state level operation and the stepwise quality of the turn-on phase. This is indicative of the ultrafast dynamics present in the system, which are not clearly resolved due to the bandwidth limitations of our experimental equipment. The small-scale structure appears because the laser is actually emitting a train of pulses of width 50-200 ps, dynamics which have been predicted [39] and experimentally confirmed recently by

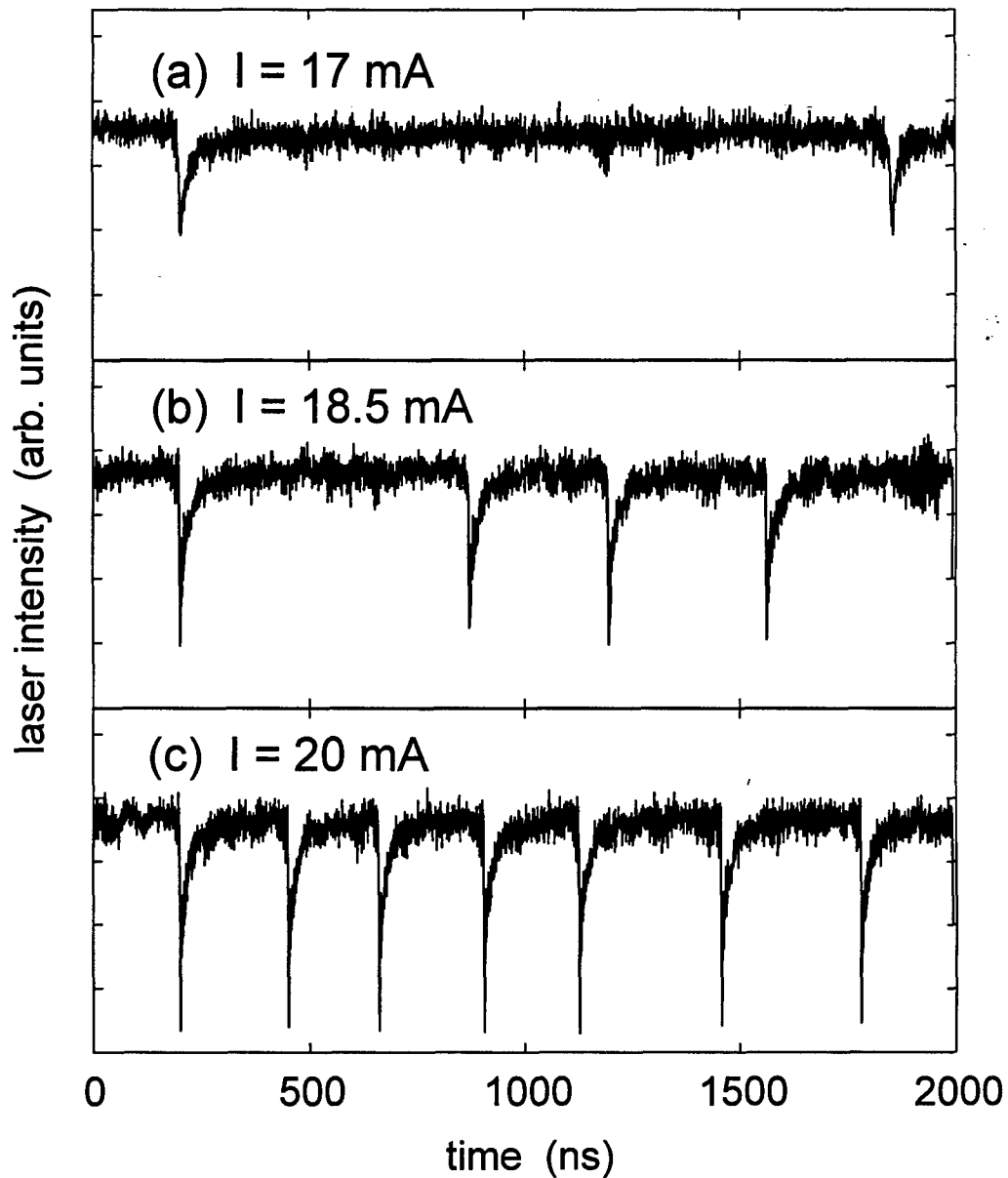


Figure 5.7: Experimental time series data illustrating the dependence of power dropout behavior on drive current level. Increasing the current increases the average rate at which the dropouts appear, and also changes their shape.

Fischer *et al.* [40]. This pulsing behavior will be discussed later in this section.

One intriguing quality of the power dropouts is that they occur at irregular time intervals (“interspike intervals”) about some average time. This time depends on the system parameters, such that the average interspike interval becomes smaller as the electrical pumping increases or as the optical feedback decreases [38, 108]. I illustrate this phenomenon in Fig. 5.7, which shows a sequence of three time series for increasing pump currents with the optical feedback held constant. It is apparent that the power dropouts become more frequent as the current increases; they also change shape, appearing deeper for higher currents (the relative scales for each graph are the same). Considerable effort has been devoted to understanding and predicting the average interspike interval time [38, 108]. I investigate and measure the probability distribution of interspike intervals in Sec. 5.5.

The role of spontaneous emission noise is an important question in the investigation of low-frequency fluctuations. Some theories approach LFF from the point of view that noise drives the system in a potential landscape, causing power dropouts when the system escapes over a barrier [108] or as the result of a dynamical bistability [124]. However, Sano [110] showed that power dropouts occur spontaneously in simulations of the Lang-Kobayashi equations in the *absence* of noise. This led him to suggest that LFF dynamics may occur through motion on a chaotic attractor, an idea that has been subsequently investigated by other researchers [39, 109, 122]. More recently, a comparison of Lang-Kobayashi simulations with and without noise has shown that spontaneous emission can significantly alter the statistical distribution and shape of the dropouts [38]. Thus, we are faced with a system that requires consideration of stochastic effects coupled with deterministic chaotic dynamics to understand its behavior.

To illustrate the effects of noise, Fig. 5.8 shows two times series obtained by inte-

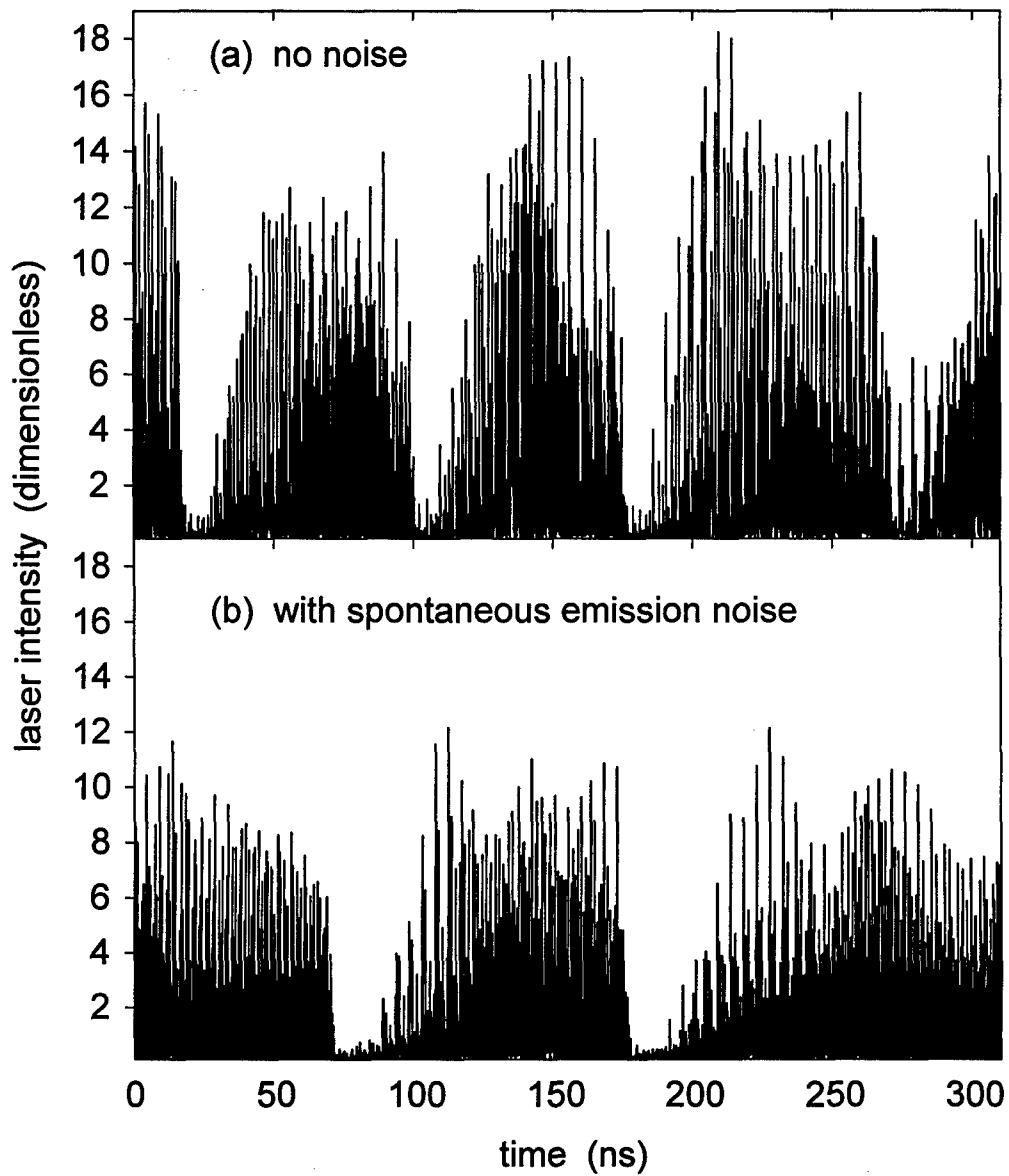


Figure 5.8: Simulated time series of LFF dynamics illustrating the influence of noise. Compared with the purely deterministic time series (a), the inclusion of noise (b) decreases the maximum intensity peaks, alters the shape of the dropouts, and changes the distribution of interspike intervals.

grating the Lang-Kobayashi equations. Graph (a) illustrates the purely deterministic case, whereas for graph (b) spontaneous emission is included. I use the dimensionless form of Eqs. 5.10, 5.11 for these simulations, where the intensity is expressed as $|Y|^2$. I integrate the equations using the same fourth-order predictor-corrector algorithm that was used for the diode resonator studies (see Sec. 4.1.2), with a constant step-size of 0.5 ps. The time series data is recorded after an initial transient period of 50 external cavity roundtrip times. In both graphs the pump current and feedback strength are $J/J_{th} = 1.01$ and $\kappa = 0.3$, respectively, and the physical parameters are listed in Appendix B. It is evident through a comparison of Figs. 5.8a and 5.8b that the addition of spontaneous noise qualitatively changes the power dropout events. With noise, the dropouts become somewhat wider, although their falling edges appear sharper. The average interspike interval appears to change (although much longer time series would be required to make this claim with any certainty), and the maximum value of the intensity is lowered significantly.

A notable difference between the simulated time series of Fig. 5.8 and the experimental data of Fig. 5.7 is that the intensity often approaches zero in the simulation. This is due to the fast pulsing dynamics which are not faithfully captured in the experimental data. To make the pulses more clearly apparent, I examine in Fig. 5.9 a short section of the time series of Fig. 5.8b at the point where a dropout occurs. The pulses are irregular in amplitude, spacing, and width, although they do follow a somewhat repetitive sequence with a period of 4.7 ns, corresponding to the pulse traversing the external cavity and causing stimulated emission as it is reinjected into the gain medium.

The fast pulses shown in Fig. 5.9 are not clearly reproduced in the experimental time series data, due to the bandwidth limitation of the oscilloscope. I note, however, that the pulses remain quite apparent in simulations when the numerically

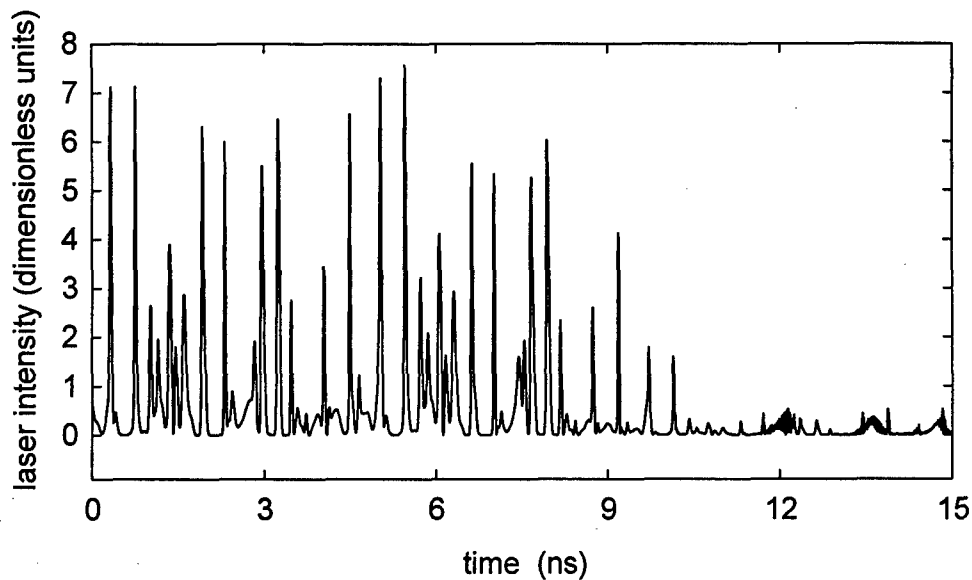


Figure 5.9: Simulated fast pulsing dynamics of LFF near the beginning of a dropout event. The pulses are short (50-200 ps wide) and have irregular spacing and height.

generated time series is convolved with a response function of a 1 GHz bandwidth filter, suggesting that the details of the simulated pulse shape and spacing may not be in good agreement with the experiment. The existence of the pulses is not in question; they have been experimentally observed [40] using a streak camera. Such equipment is not currently available to our laboratory, and although it would be very useful for experimental visualization of the ultrafast dynamics, it is not as well suited for studies of the power dropouts or their statistical properties. This is due to the disparate timescales of LFF dynamics. For example, the streak camera used in Ref. [40] could capture a single-shot trace of 6.6 ns, but this length of time is significantly shorter than the width of the dropout itself, and is at least an order of magnitude too small to register multiple dropout events.

Measuring the RF power spectrum is another technique that provides information about the fast dynamics. A typical experimental power spectrum is shown in

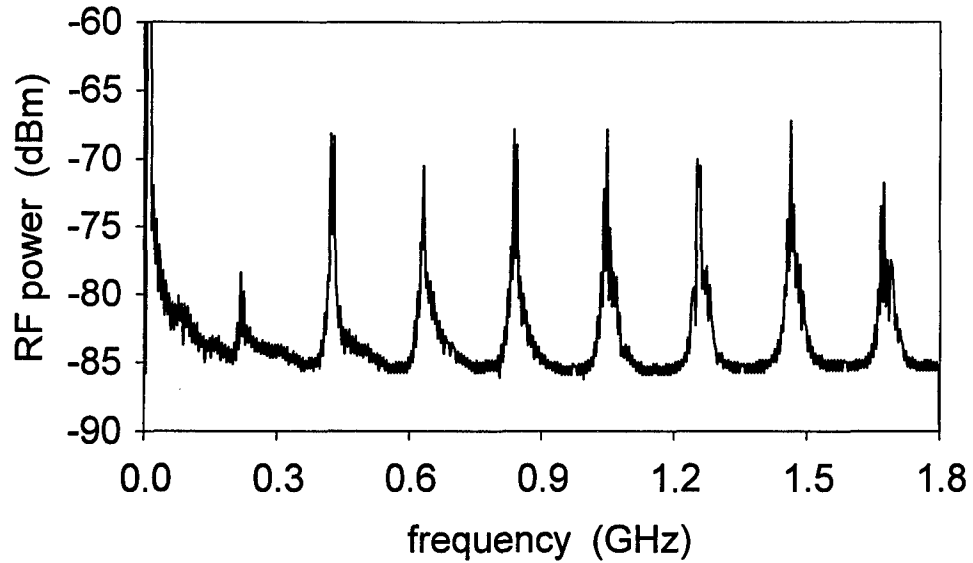


Figure 5.10: Typical experimental power spectrum of a system undergoing LFF. The low-frequency noise results from the irregular power dropouts. The regularly-spaced peaks are at harmonics of the external cavity, and are related to the fast pulsing dynamics of the laser.

Fig. 5.10. The regularly-spaced peaks correspond to the fundamental frequency of the external cavity (~ 212 MHz, corresponding to a cavity of ~ 71 cm length) and its harmonics. The logarithmic dBm power scale refers to RF power from a sinusoidal wave dissipated in a 50Ω load, such that 0 dBm = 1 mW of RF power. To convert from optical power to the RF dBm scale in this experimental system, a 1 mW sinusoidal fluctuation in optical power reflected from the 30% beamsplitter is equivalent to -32 dBm, accounting for the neutral density filter and conversion gain of the photoreceiver. The nearly constant level of the peaks suggests that additional peaks occur beyond the range of the instrument, which would indicate the existence of short pulses in the laser beam. The low-frequency noise that extends from dc to about 100 MHz is a result of the irregular power dropouts themselves (this is the origin of the term “low-frequency fluctuations”). This power spectrum was captured on

the spectrum analyzer using a 5 MHz resolution bandwidth and 1 kHz video filtering.

5.4.2 Dynamics on the attractor

Time series and spectral data provide valuable information regarding the mechanisms of LFF. Further insights can be gained by studying the behavior of the system in the phase space that was introduced in Sec. 5.2.2. Recall that the steady-state solutions of the Lang-Kobayashi equations (5.4,5.5) defined a set of points $(E_s^2, \Delta\omega_s\tau, N_s)$, where E_s^2 , $\Delta\omega_s\tau$, and N_s are the steady state values for photon density, roundtrip phase difference, and carrier number density, respectively. These fixed points, either modes or antimodes, reside on an ellipse in the phase space (Eq. 5.17).

It is possible to represent the simulated time series of Fig. 5.8b in terms of equivalent dimensionless quantities, thereby generating the phase space trajectory shown in Fig. 5.11a. The vertical axis represents the (dimensionless) carrier density Z and the horizontal axis is the roundtrip phase difference $\varphi(s) - \varphi(s - \theta)$, where s is the dimensionless time, θ is the external cavity roundtrip time, and φ is the phase of the complex field Y where $Y(s) = |Y(s)| \exp(i\varphi(s))$. The trajectory shown in graph (a) represents one complete dropout cycle, demonstrating that the dynamics take place almost entirely within the lower left-hand quadrant of the phase plane (note the location of the origin).

The dropout can be understood as follows. In the vicinity of point A , the system wanders along the external cavity modes as it nears the tip of the ellipse of fixed points, attempting to reach the maximum gain state. In this region, the antimodes begin to draw close to the external cavity modes and come into crisis with them. When the dynamics remain for too long near a mode that is near collision with an antimode, the system eventually will pass too near the antimode. The unstable antimode then rapidly drives the system away from the external cavity modes, as

indicated by the arrow. The carrier density increases to the level associated with the solitary laser threshold as the optical intensity goes to zero. The system subsequently returns near the solitary operating point (the origin) and is reinjected onto the ellipse of fixed points, indicated by arrow *B*. The laser again feels the effects of the external cavity, and increases its average power as it moves along the cavity modes (arrow *C*). This build-up of intensity is fairly rapid at first, but as the system approaches point *A* once again, the dynamics begin to dwell for longer and longer times near a given external cavity mode. It may “hop” back and forth between attractor ruins (called “inverse switching”), although the overall trend is toward the maximum gain mode. When the system reaches an external cavity mode that is near crisis with an antimode, the cycle is ready to repeat.

Figure 5.11b is a close-up view of the trajectory at the point where the dropout is initiated. The attractor ruins are clearly visible. The trajectory enters from the lower right hand side of the graph, moves along the series of external cavity modes, undergoes inverse switching between the last two modes, and eventually experiences the power dropout.

5.5 Distribution of interspike intervals

From the analysis of the dynamical mechanisms of power dropout events, it is clear that an external cavity semiconductor laser undergoing LFF is an extraordinarily complex system. There are antimodes and destabilized external cavity modes numbering in the hundreds, and the system has an infinite number of degrees of freedom due to the time delay. The dynamics occur on timescales covering several orders of magnitude, from pulses 100 ps wide to interspike intervals that can be on the millisecond scale. Furthermore, modeling its behavior from a wholly deterministic point of view may not be adequate since spontaneous emission noise plays an important

role, as illustrated in Fig. 5.8. To what extent is it possible to describe the behavior of the system in a simple analytical way? I address this question in this section by studying the probability distributions of the interspike intervals. I formulate a first-passage time theory based on the work of Henry and Kazarinov [108] to describe the distributions, and compare these predictions with experimental results.

5.5.1 Theoretical analysis

The probability distribution of interspike intervals is a readily measurable quantity of the LFF dynamics that provides sensitive information about the long-term dynamics of the system, and may be used to constrain analytical models. The intervals are easily extracted from experimental time series data, since the dropout features are quite wide and therefore can be measured without especially fast and expensive equipment (in contrast with time-domain visualization of the ultrafast pulses). Unfortunately, computer simulations are of limited usefulness for this investigation, because the fast pulsing dynamics make the LK equations quite stiff and therefore very time-consuming to integrate for sufficient length to gather good statistics on dropout behavior.

An alternate analytical approach was developed in 1986 by Henry and Kazarinov [108], which I use as a basis for my analysis. They perform a nonlinear stability analysis of the LK equations including spontaneous emission about the maximum gain mode (the dominant mode indicated in Fig. 5.2), describing the dynamics in terms of fluctuations n in the carrier density about the maximum gain mode value N_s . They show that n evolves according to an equation analogous to that of a stochastically-driven, overdamped particle moving in a one-dimensional potential well with a finite barrier, where the coordinate of the potential function is n . A dropout occurs when large stochastic fluctuations drive the system over the barrier. The question of when

this noise-induced dropout occurs is a *first-passage time* problem, and the distribution of times may be obtained by solving the associated forward Fokker-Planck or Kolmogorov equation [143]. Henry and Kazarinov determine an approximate solution for the average escape time rather than solving the full Fokker-Planck equation, and find that experimental measurements [144] are in qualitative agreement with the parameter dependences expressed in their solution. This description of LFF differs greatly from that given in Sec. 5.4.2, in that it does not consider the dropouts to be caused by chaotic dynamics. Instead, it assumes that fluctuations in spontaneous emission dislodge the laser from a locally stable state, causing the dropout. The mathematics of the approximate solution for the first-passage time problem are more complicated and perhaps a bit foreign, so I relegate those details to Appendix C, simply stating the results where needed in this chapter.

Henry and Kazarinov consider the LFF dynamics as a particle in a potential well. I review their 1986 analysis here, noting that there seem to be some inconsistencies in their theory. Starting from Eqs. 5.4 and 5.5 with the Langevin force $F_E(t)$ included, they consider small fluctuations about the maximum gain mode $(I_s, \Delta\omega_s, N_s)$ described by

$$E(t) = [I_s + p(t)]^{\frac{1}{2}} \exp[i\Delta\omega_s t + i\phi(t)], \quad (5.19)$$

$$N(t) = N_s + n(t), \quad (5.20)$$

where p , ϕ , and n are small fluctuations in photon number density, phase, and carrier density, respectively. They insert these forms into the LK equations and split the complex field into two real equations. They also assume that fluctuations occur in a time less than the roundtrip time in the cavity, so the reflected field takes on the steady-state value $\sqrt{I_s} \exp[i\Delta\omega_s(t - \tau)]$. This leads to

$$\dot{p} = G_{NN}I_s - \frac{2\kappa I_s}{\tau_{in}} [\cos \Phi - \cos(\Phi + \phi)] - \frac{\kappa p}{\tau_{in}} \cos \Phi + F_I(t), \quad (5.21)$$

$$\dot{\phi} = \frac{1}{2}\alpha G_N n - \frac{\kappa}{\tau_{in}} [\sin(\Phi + \phi) - \sin \Phi] + F_\phi(t), \quad (5.22)$$

where $\Phi \equiv (\omega_o + \Delta\omega_s)\tau$, and the Langevin force $F_E(t)$ has been split into phase and intensity components, $F_\phi(t)$ and $F_I(t)$, respectively. Equations 5.21 and 5.22 retain only linear terms in p and n as expected, but also neglect $\kappa p \sin(\Phi + \phi) / (2\tau_{in}I_s)$ and assume that $\kappa p \cos(\Phi + \phi) / \tau_{in} \approx \kappa p \cos(\Phi) / \tau_{in}$, which are valid if $p\phi$ is small. Henry and Kazarinov then expand the trigonometric terms $\cos(\Phi + \phi)$ and $\sin(\Phi + \phi)$ to *quadratic* order in ϕ to find

$$\dot{n} = -\frac{1}{T}n - G(N_s)p, \quad (5.23)$$

$$\dot{\phi} = \frac{1}{2}\alpha G_N n - \frac{\kappa}{\tau_{in}}\phi \cos \Phi, \quad (5.24)$$

$$\dot{p} = G_N n I_s - \frac{\kappa I_s}{\tau_{in}}(2\phi \sin \Phi + \phi^2 \cos \Phi) - \frac{\kappa p}{\tau_{in}} \cos \Phi + F_I(t), \quad (5.25)$$

where $T = 1/\tau_s + G_N I_s$. Intensity fluctuations $F_I(t)$ are the dominant random force [118], and therefore $F_\phi(t)$ is ignored as well as sources of carrier density fluctuations. The next step in the analysis requires two additional approximations. First, Henry and Kazarinov assume that the dominant operating point is at $\Phi = 0$ (corresponding to the maximum gain mode of Sec. 5.2.2). Second, they assume that the phase adiabatically follows the carrier density, meaning that the decay rate of ϕ is much greater than the rate at which n changes. This approximation leads to $\phi = \alpha G_N \tau_{in} n / 2\kappa$ by setting $\dot{\phi} = 0$ in Eq. 5.24. They then manipulate Eqs. 5.23 and 5.25 to obtain a single second-order differential equation in n . At this point in the derivation they retain n^2 terms, despite keeping only linear terms in p and n previously. This leads to

$$\ddot{n} = -\left(\frac{1}{T} + \frac{\kappa}{\tau_{in}}\right)\dot{n} - \left(\Omega^2 + \frac{\kappa}{T\tau_{in}}\right)n + \frac{\alpha^2 \Omega^2 G_N \tau_{in}}{4\kappa} n^2 - G(N_s) F_I(t), \quad (5.26)$$

where $\Omega = \sqrt{G(N_s)G_N I_s}$ is the relaxation oscillation frequency of the solitary laser. Equation 5.26 may be interpreted as a stochastically-driven particle undergoing

damped motion in an anharmonic well $U(n)$. Henry and Kazarinov then assume that the \ddot{n} term is negligible, which requires that the damping is strong. The resulting equation can be written as the Langevin force equation

$$\dot{n} = -\frac{\partial U}{\partial n} + F(t), \quad (5.27)$$

where the potential $U(n)$ has the form

$$U(n) = \gamma \left(\frac{n^2}{2} - \frac{n^3}{3n_o} \right). \quad (5.28)$$

The barrier of height $U(n_o) = \gamma n_o^2/6$ is located at n_o , and γ is interpreted as the characteristic sliding rate in the well. The random force $F(t)$ is simply a rescaled version of $F_I(t)$, with several constants combined in the diffusion coefficient D . It obeys

$$\langle F(t) F(t') \rangle = 2D\delta(t-t'), \quad (5.29)$$

$$D = \frac{G(N_s)^2 \tau_{in}^2}{\kappa^2} D_{II} = \frac{G(N_s)^2 \tau_{in}^2}{\kappa^2} R_{sp} I_s, \quad (5.30)$$

where R_{sp} is the spontaneous emission rate [134].

My goal is to obtain a first-passage time probability density $\zeta(n', t)$ from Eq. 5.27, that is, the probability that the particle will be driven over the barrier between the times t and $t + dt$ given that it was initially at the location n' . The most convenient approach to this problem is to consider the moments of the *integral* first-passage time distribution, that is, the probability $\psi(n', t)$ that the first passage time is less than t given that the initial position was n' [145, 146]. The derivative of $\psi(n', t)$ with respect to t returns the usual first-passage time probability density $\zeta(n', t)$. The equation describing the time evolution of $\psi(n', t)$ is the Kolmogorov equation

$$\frac{\partial \psi(n', t)}{\partial t} = a_1(n') \frac{\partial \psi(n', t)}{\partial n'} + \frac{a_2(n')}{2} \frac{\partial^2 \psi(n', t)}{\partial n'^2}, \quad (5.31)$$

where a_1 and a_2 are infinitesimal transition moments. Eq. 5.31 is described in more detail in Appendix C. Using it, I find an approximate expression for the first passage time distribution,

$$\zeta(n', t) \simeq \frac{1}{\tau_{FP}} \exp\left(-\frac{t}{\tau_{FP}}\right), \quad (5.32)$$

where the mean first-passage time τ_{FP} is approximately

$$\tau_{FP} \simeq \frac{\pi}{\gamma} \exp\left(\frac{1}{3\mathcal{D}}\right), \quad (5.33)$$

and $\mathcal{D} = D/2U(n_o) = 2D/\gamma n_o^2$ is a dimensionless diffusion coefficient (D is defined in Eq. 5.30).

It may seem surprising that $\zeta(n', t)$ is independent of n' ; this points to the approximations made in its derivation. Eq. 5.32 is valid only when the following two criteria are met: the initial location of the particle must not be close to the barrier, such that $n(t=0) \ll n_o(1 - \sqrt{\mathcal{D}})$; and the dimensionless diffusion coefficient must be small $\mathcal{D} \ll 1$. The reasons for these stipulations are explained in Appendix C.

It is important to establish the connection between the theoretical results and the measured experimental quantities. Henry and Kazarinov addressed this need, showing that the mean first passage time can be expressed as

$$\tau_{FP} = \frac{\pi}{a(1 + 4P/P_1)} \exp\left[\frac{1}{b} \left(1 + \frac{P_1}{4P}\right)^3 \left(\frac{\Delta C}{C}\right)^3\right], \quad (5.34)$$

where P is the laser power, P_1 is the laser power with feedback at the solitary threshold current J_{th} , and $\Delta C/C = (J_{ext} - J_{th})/J_{th}$ is the relative reduction of threshold current due to the optical feedback. All these values may be experimentally determined. The parameters a and b represent poorly-known laser-specific parameters, which I find via fits to experimental data.

This concludes the theoretical formulation of power dropout events as a first-passage time problem. It is appropriate at this time to consider exactly how these

results reflect the interspike intervals that occur in the experimental system. The potential barrier described by Eq. 5.28 is designed to be valid near the maximum gain mode, and the first-passage time distribution expresses the likely time at which the system will escape over the barrier. However, recalling Fig. 5.11, we know that the dynamics leave the phase space vicinity of the maximum gain mode following a dropout, whereupon they return near the solitary laser state before reentering the external cavity mode structure. These effects are not explicitly taken into account by the Henry and Kazarinov model, but experiments indicate that we must consider the characteristics of the reinjection process. Therefore, I make an explicit distinction in notation between the theoretically calculated first-passage time $\zeta(n, t)$, and the experimentally measured interspike interval probability distribution $\eta(t)$. I compare experimental results with the theoretical predictions to investigate these issues in the following section.

5.5.2 Comparison with experimental results

The theoretical analysis I have described provides expressions related to several measurable quantities of the interspike intervals. The mean first-passage time is expected to scale with experimental parameters according to Eq. 5.34, and an approximate solution for the first-passage time probability (Eq. 5.32) predicts an exponentially decreasing distribution, scaled by the mean time. I now compare these theoretical expectations with experimental data.

I measure average times and probability distributions for interspike intervals, holding the optical feedback fixed for several levels of the drive current. The process involves selecting an optical feedback level at which the laser operates in the LFF regime. I set the drive current at an initial level and observe time series from the photoreceiver on the digitizing oscilloscope, setting the sampling rate such that several

dropouts are recorded within a single 5000-point trace. I then use a program written in LabVIEW to automate the data acquisition process. This program downloads a single time series trace from the oscilloscope to a computer via GPIB, and extracts the interspike intervals in sequence using a peak-finding algorithm. The program saves these intervals, and then reads another time series from the scope, repeating the process for a predetermined number of runs (typically ~ 500). The program also records a cumulative histogram of the interspike intervals that are collected. At the conclusion of the run, I increment the drive current level and repeat the process.

I find that it is important to test the peak-finding algorithm prior to commencing an acquisition run. The peak finder requires two parameters from the user: peak threshold and duration. A peak (inverted dropout) is determined to have occurred if the measured data exceeds the threshold value *and* remains above that value for the time specified by the duration parameter. A new peak may not occur until the data has dropped back below the threshold level. This algorithm provides needed flexibility, since the sampling rate must be changed over the range of operating conditions, balancing good time resolution with the need to capture several dropouts per time series. Another feature of the oscilloscope that improves the consistency of the peak-finder is the option to reduce the front-end analog bandwidth from 1 GHz to 250 MHz. This still allows for good time resolution, especially when the time between dropouts is fairly long, but eliminates most of the short-timescale fluctuations caused by the fast pulsing dynamics.

Following this procedure, I measure the mean times τ_{II} of the interspike intervals (to distinguish from τ_{FP} , the mean first passage time) and their probability distributions $\eta(t)$. Fig. 5.12 shows τ_{II} plotted as a function of drive current. More than 5000 interspike intervals are recorded for each point, leading to the rather small statistical error bars. The dashed line is generated from fitting the form of Eq. 5.34 to the

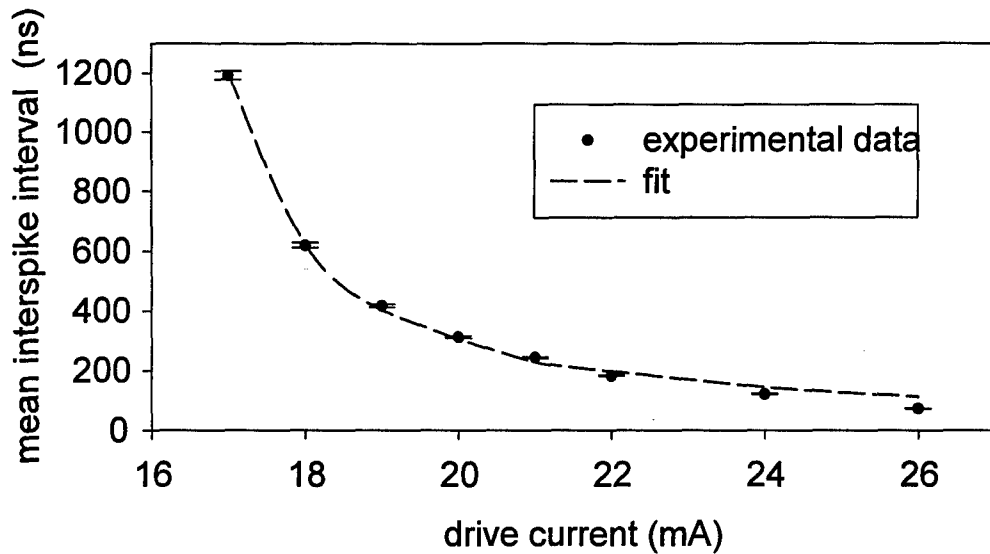


Figure 5.12: Average times between power dropout events as a function of drive current. The error bars represent only statistical errors. The dashed line is a fit to the experimental data using the functional form of Henry and Kazarinov (Eq. 5.32).

experimental data, which gives values for the free parameters $a = 19.4 \text{ ps}^{-1}$, and $b = 5.73 \times 10^{-4}$. For this data set, I adjust the quarter-wave plate in the external cavity (see Fig. 5.3) such that the effective threshold is lowered to $J_{ext} = 14.5 \text{ mA}$ from a solitary level of $J_{th} = 17.0 \text{ mA}$, corresponding to a relative threshold reduction $\Delta C/C = 0.147$. I note that the dimensionless diffusion coefficient can be determined from these parameters; its value is $\mathcal{D} = 0.092$ for $P/P_1 = 1$, meeting the condition that $\mathcal{D} \ll 1$ for Eq. 5.32 to be valid.

Additional interesting information can be gained from the same data runs by plotting the probability distributions of the interspike intervals $\eta(t)$. I plot in Fig. 5.13 an example of an experimentally measured distribution, the $J = 17 \text{ mA}$ case with the same system parameters as were used in collecting the mean times. This data is shown by the solid line (the dashed and dot-dashed lines are theoretically calculated distributions, discussed later). The data is normalized by the total number of counts

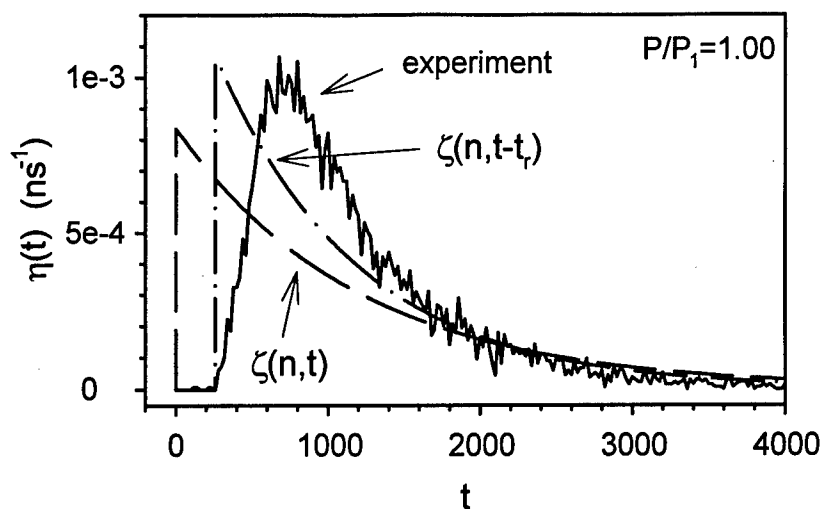


Figure 5.13: Comparison of experimental interspike interval probability distribution and theoretical first-passage time distributions.

and the width of the histogram bins to reproduce $\eta(t)$. The general features of these distributions consist of a region near $t = 0$ where the probability of a dropout is essentially zero, followed by a rapid rise to a peak value, which then exponentially decays as t increases. I also find additional structure for the cases when the drive current is well above solitary threshold. It is clear that the experimentally measured histograms have a more complicated structure than is expected from Eq. 5.32.

One probable reason for the disagreement lies in the interpretation of how the Henry and Kazarinov theory is related to the experimentally measured interspike intervals, as was mentioned briefly at the end of the previous section. The distribution $\zeta(n, t)$ of Eq. 5.32 describes the likelihood of the system crossing the potential barrier (causing a dropout) at a given time, assuming that it is initially located at $n = 0$. Recalling Fig. 5.11, the dynamics then are rapidly driven from the region of phase space in which the external cavity modes are located before being reinjected near the middle of the ellipse, a process which occurs in about one roundtrip time. One

plausible interpretation of this process is to consider the system to be reinjected into the well as soon as it reaches the ellipse, in which case the interspike interval distribution should be very nearly equivalent to that of the first passage time, that is, $\eta(t) \simeq \zeta(n, t)$.

In contrast, an alternate interpretation is to say that the system enters the well only when the dynamics are in the vicinity of the maximum gain mode, after traversing much of the ellipse. In this situation, we must carefully distinguish between $\zeta(n, t)$ and $\eta(t)$. Specifically, the interspike interval distribution will include a reinjection time t_r which may be a function of the laser parameters. The proper expression for η then becomes $\eta(t) = \zeta(n, t - t_r)$, with the understanding that ζ may have nonzero values only if its time argument is positive. In this case, the average times are related by $\tau_{FP} = \tau_{II} - t_r$.

The distributions obtained from these two interpretations are plotted in Fig. 5.13. The dashed line indicates the approximate analytical solution assuming a negligible reinjection time t_r , using the measured value for the mean time of 1,192 ns. The maximum height and the long-term decay predicted by the theory are in questionable agreement with the experimental distribution. The dot-dash line represents the distribution obtained by assuming that a significant reinjection time exists prior to the system entering the well. This plot gives a better qualitative reproduction of the major elements of the distribution shape, and the maximum height and exponentially decaying tail are in better quantitative agreement. This change of shape reflects the adjustment of the mean time $\tau_{FP} = \tau_{II} - t_r$, which alters $\zeta(n, t)$ according to Eq. 5.32. The value of t_r is determined empirically, and is taken to be the point at which the experimental distribution first reaches one percent of the maximum height. For the data shown, this time is 260 ns.

From Fig. 5.13, it is apparent that $\eta(t) = \zeta(n, t - t_r)$ gives the best fit to ex-

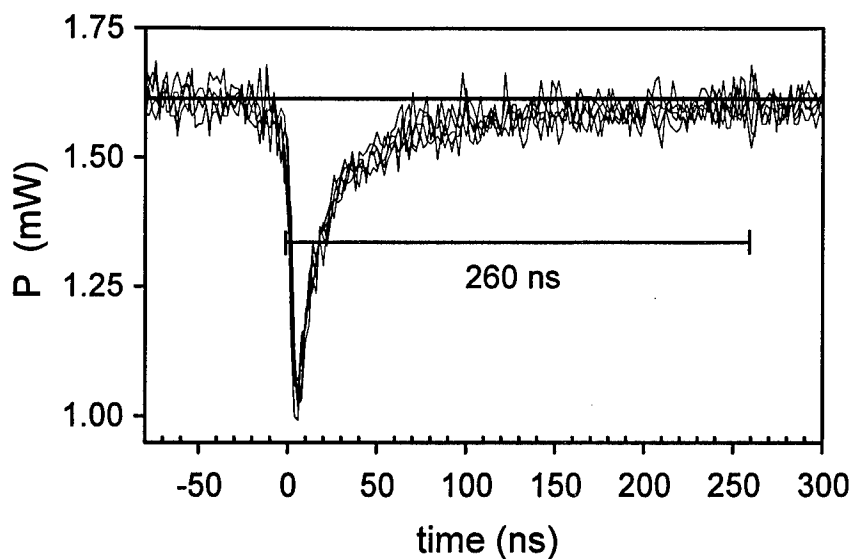


Figure 5.14: Overlay of multiple power dropouts, illustrating the relevance of the reinjection time t_r . The average laser intensity has essentially recovered to its level prior to the dropout after $t_r = 260$ ns.

perimental results. However, the agreement still leaves much room for improvement, particularly in that the theoretical distribution rises to its maximum much more rapidly than the experimental data. It is useful to check whether the theoretical discrepancies described above are inherent to the Henry and Kazarinov formulation or whether they result from the approximations underlying the derivation of Eq. 5.32. As a test of this idea, I numerically integrate the Kolmogorov equation for the integral first passage time $\psi(n, t)$ using the calculated value of \mathcal{D} and differentiate the result to find $\zeta(n, t)$. The numerically calculated distribution accurately reproduces the shape of the analytical solution, so the source of the discrepancies is indeed elsewhere.

The meaning of the reinjection time t_r can be explored by close examination of experimental time series data of power dropouts. In Fig. 5.14, I plot several dropout events on the same graph for the case where $P/P_1 = 1$, illustrating that

the slow recovery process is essentially the same for all events for a given set of laser parameters. Note that $t_r = 260$ ns, corresponding to the region of low dropout probability in Fig. 5.13, agrees well with the time required for the average power to return to the level it had just before the dropout occurred. This supports the interpretation that the system only reenters the well after the dynamics have traversed the ellipse and reached the vicinity of the maximum gain mode, and that a complete model for $\eta(t)$ will require an understanding of the reinjection dynamics.

I have demonstrated that the Henry and Kazarinov theory with a simple adjustment for the reinjection dynamics yields a reasonably accurate prediction of the distribution $\eta(t)$ for the case when the $P/P_1 = 1$ and the relative threshold reduction is $(J_{ext} - J_{th})/J_{th} = 0.147$. However, I find that $\eta(t)$ changes qualitatively as the drive current for the laser increases. Fig. 5.15 shows such distributions for six different values of P/P_1 , plotted with $\zeta(n, t - t_r)$ represented by the dashed lines. The histograms corresponding to values of the pump current near solitary threshold are represented by graphs (a) and (b). These two have a similar shape, beginning with an interval of essentially no counts, followed by a rapid rise to a peak value and an exponential decay. The agreement between the experimental $\eta(t)$ and $\zeta(n, t - t_r)$ worsens as the drive current increases, shown in graphs (c) and (d), as the shape of the exponential tail begins to show large errors. At still higher drive currents, increased structure in the experimental histograms becomes apparent, and the simple theory no longer captures the main features of $\eta(t)$, as shown in graphs (e) and (f).

The probability distributions shown in Fig. 5.15 demonstrate that the dynamics governing the power dropout events are more complex than the theory predicts. One error common to all six cases is that the theory predicts a much sharper rising edge for the distributions than is found experimentally. This could possibly be explained by recalling the small-scale structure of the phase space. The laser dy-

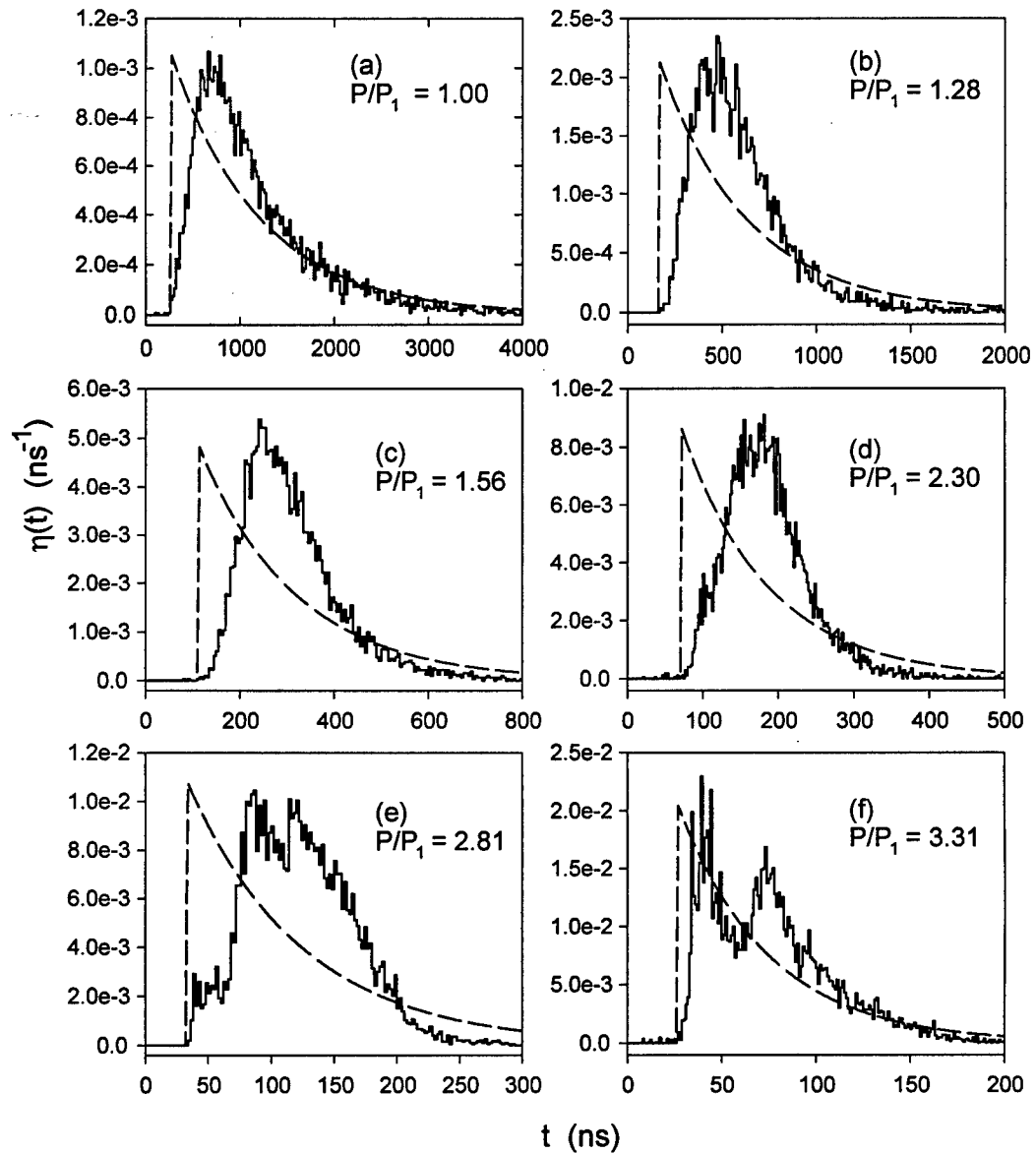


Figure 5.15: Experimental and theoretical interspike interval probability distributions, for increasing power levels with the optical feedback level held constant. The dashed lines represent $\zeta(n, t - t_r)$. The agreement is clearly best at lower powers.

namics must hop from one external cavity mode to another as it moves from the middle of the ellipse toward the maximum gain mode following a dropout event. Mode-hopping in external-cavity lasers has been considered by Lenstra and Mork *et al.* as a stochastically-driven particle moving in a single potential well with multiple minima, where each local minimum corresponds to a quasistationary laser mode [126, 147]. The stochastic nature of this process could have the effect of spreading out the reinjection times. Another possibility may be to allow the shape of the potential well to vary, perhaps depending on the location of the dynamics in phase space or on the time the particle has been in the well. An additional unexplained result is the appearance of considerable structure in $\eta(t)$ as the power level is increased. The peculiar bimodal structure of graph 5.15f, for example, may indicate that there are two different phase space locations at which the dropout may occur.

In this chapter I have provided a general introduction to external cavity semiconductor lasers, explaining the important features of the Lang-Kobayashi equations that describe them and the basic elements that govern their dynamics. I have described the experimental apparatus that I use to investigate low-frequency fluctuations, and shown experimental and theoretical results to elucidate the mechanisms of power-dropout events. Finally, I have studied the statistics of the interspike intervals, finding that they can be reasonably described in some regimes by a modified first-passage time theory based on the work of Henry and Kazarinov. In the next chapters, I move on to the question of how this highly complex instability responds to control perturbations.

Chapter 6

Open-Loop Regulation and Entrainment of Power Dropout Events

In the last chapter, I introduced the external cavity semiconductor laser and described in detail the LFF instability occurring in this system. The focus of this chapter is to determine how LFF responds to control perturbations. Specifically, I apply open-loop control in the form of a sinusoidal perturbation to the drive current while the laser system is in the LFF regime. This study represents the extension of open-loop control research to a very fast and complex system; previous experiments have focused on low-dimensional systems, such those by Ciofini *et al.* [65, 148] on a CO₂ laser with modulated losses. Liu *et al.* [149] have studied theoretically the technologically important high-frequency injection technique for reduction of relative intensity noise in external cavity diode lasers, stimulating further interest in semiconductor laser experiments.

Open-loop perturbation of LFF dynamics is also interesting from the viewpoint of stochastic resonance. Stochastic resonance is a phenomenon in which noise in a nonlinear system may enhance a weak periodic input [150, 151]. There is a wide range of natural frequencies present in the LFF system, from GHz scale pulsing to kHz scales associated with interspike intervals. Furthermore, spontaneous emission noise is present and known to be an important factor in the dynamics. Thus, stochastic resonance effects may become important in my results.

Regarding control, there are many possible goals, the usefulness of which may depend on the application being considered. In some cases, full stabilization of an unstable steady state may be desired, suppressing both power dropouts and picosec-

ond pulses. In others cases, the frequency components attributed to the short pulses (at the harmonics of the external cavity resonance) may be well above the characteristic rates in the application, so the elimination of the power dropouts may be all that is required. Finally, it may suffice to simply regulate the occurrence of the power dropouts rather than suppress them, eliminating the broad low-frequency noise in the system.

In this chapter I begin with a short discussion reviewing open-loop control in lasers and its implementation for my system, after which I present experimental results obtained by applying the modulation. One important result is that the dropouts can be entrained with a low-frequency perturbation (~ 20 MHz) such that one power dropout occurs per drive cycle. I also find that higher-frequency modulation has the effect of generating a comb in the interspike interval distribution, indicating that the dropouts occur preferentially at times corresponding to the period of the driving signal. This preference disappears, however, when the driving frequency is set equal to that of the cavity resonance.

There is a complicated dependence of the mean interspike time τ_{II} on the perturbation's frequency and amplitude. The most common result is that the average rate of dropouts increases. However, a sufficiently strong, high-frequency modulation can drive the system out of the LFF regime into a behavior similar to "coherence collapse," such that fully-developed dropouts are no longer recognizable. Another unusual result arises when the modulation is at the resonant frequency of the external cavity; in this case, τ_{II} is unchanged. I note that I find no modulation frequencies that have the effect of fully eliminating or suppressing the instability in this study, nor do they increase τ_{II} , a result that would indicate the dropouts are being suppressed.

6.1 Open-loop control

Open-loop control is a technique that is relatively easy to implement in experimental systems, is easily adapted for high-speed operation, and has been successful in altering the dynamics of unstable laser systems. Recalling the discussion of section 2.2.1, an accessible control parameter is adjusted about its nominal value by a periodic signal in open-loop control. The control signal is usually in the form of a sinusoidal perturbation, and is generated without regard for the current state of the system. This independence of the control signal from measurement of the system dynamics is partly responsible for the high-speed capabilities of this approach. That is, generation of the control signal does not depend on real-time measurement and processing, and latency is not a consideration.

I pursue this method of control both for its high-speed applicability and because it has been proven successful in several previous laser studies. For example, researchers have found that a chaotic CO₂ laser with modulated losses can be entrained to a periodic orbit using small sinusoidal perturbations [41, 65, 148]. Also, I have studied the effects of subharmonic perturbations on a modulated Nd-doped fiber laser [44, 152] in research not included in this thesis. Many researchers have studied modulation effects in semiconductor laser systems as well. For example, it is well known that high-frequency modulation reduces the relative intensity noise in external cavity diode lasers where the cavity is short (~ 10 cm) [153]-[155]; these studies have more recently been considered from the chaos control viewpoint [42].

The apparatus required to implement open-loop control in my experimental system is very simple. All that is required is a function generator (Tektronix SG503) and a bias-tee (Mini-circuits ZFBT-6GW) with which to add the modulation to the dc component of the drive current. The injection current produced by the function

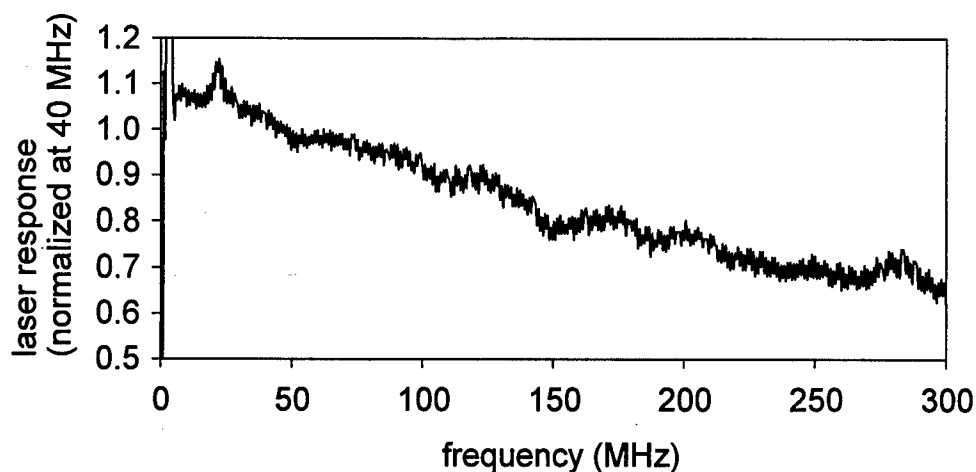


Figure 6.1: Frequency response of solitary laser to external modulation applied through the bias-tee. The laser response is normalized to one at 40 MHz.

generator is frequency-dependent, and therefore it is necessary to calibrate the response of the solitary laser to the applied voltage at the bias-tee. There are two issues to consider: the conversion from applied voltage to drive current, and the frequency dependence of that relationship. To address the first issue, I begin by measuring the output power of the solitary laser as a function of injection current. I then measure the change in optical power induced by a low-frequency modulation of known amplitude, thus providing a reference level for the voltage-to-current conversion. For reference, a 40 MHz sinusoidal voltage applied to the bias-tee results in a change of laser current at a rate of about 0.032 mA per mV. I then use the tracking generator of the spectrum analyzer to measure the frequency dependence of the laser's response (the response of the photoreceiver is specified to be flat to several GHz). This frequency response is shown in Fig. 6.1, where the laser response is normalized to unity at 40 MHz, the reference given above.

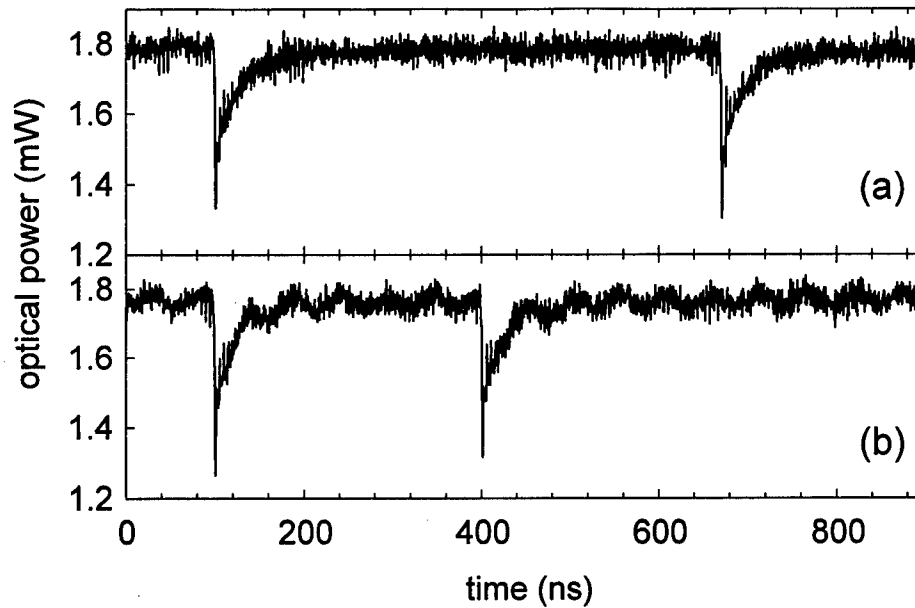


Figure 6.2: The effect of weak 19 MHz modulation on power dropouts. The dropouts still occur and have the same general shape for both the (a) unperturbed and (b) modulated behavior.

6.2 Low-frequency modulation

I begin investigating modulation effects in the low-frequency regime. The perturbation frequency is 19 MHz, although most of the effects described in this section occur to varying degrees in a region about that frequency, nominally from 10 - 25 MHz. The frequency is chosen on empirical grounds to be 19 MHz because the threshold for entrainment occur at the lowest drive amplitude for this frequency. I first show the effects of weak perturbations, demonstrating that the probability distribution of the interspike intervals is a sensitive measure of the presence of the modulation. Subsequently, I show that stronger perturbations can entrain effectively the power dropouts such that one dropout occurs every (or every other) drive cycle.

6.2.1 Sensitivity to weak driving

The effect of weak pump current modulation on the power dropouts is not remarkable from examination of a time series of the laser's intensity, as illustrated in Fig. 6.2. Graph (a) displays the behavior of the system in the absence of perturbations. The mean interspike interval time τ_{II} in this case is about 600 ns. Graph (b) shows the same system when a 10 mV_{pp} modulation at 19 MHz is added to the pump current, producing a modulation amplitude of about 0.7% of the dc pump current. A small oscillation can be seen in the average power level between dropouts, but it appears quite small compared to the depth of a dropout. The shape of the dropout is the same as in the unperturbed case. The system parameters are: drive current 22 mA, relative threshold reduction $\Delta C/C = 0.176$ (see Eq. 5.32), and $P/P_1 = 2.07$.

In contrast, the presence of such a modulation has a dramatic effect on the probability distribution of interspike intervals $\eta(t)$, as illustrated in Fig. 6.3. It is important to be aware of exactly what these graphs represent; they show the relative frequency of occurrence of times *between* individual power dropout events. To measure these individual intervals from a given time series, the data analysis program triggers on the downstroke of the first dropout and calculates the time that elapses until the next downstroke occurs. It then uses the second event as the initial time and repeats this process until the end of the time series is reached. Graph (a) shows $\eta(t)$ for the system parameters given above with no modulation. Graph (b) shows the probability distribution corresponding to a much longer time series with the same system parameters as Fig. 6.2b, with a modulation of 10 mV_{pp} at 19 MHz. The change in the appearance of $\eta(t)$ is striking; the smooth distribution has become a comb, with peaks separated in time by multiples of the modulation period ($\sim 53 \text{ ns}$). Interestingly, the overall envelope of the distribution is not drastically changed; the mean time τ_{II} is decreased from $719 \pm 9 \text{ ns}$ to $559 \pm 6 \text{ ns}$, assuming only statistical errors.

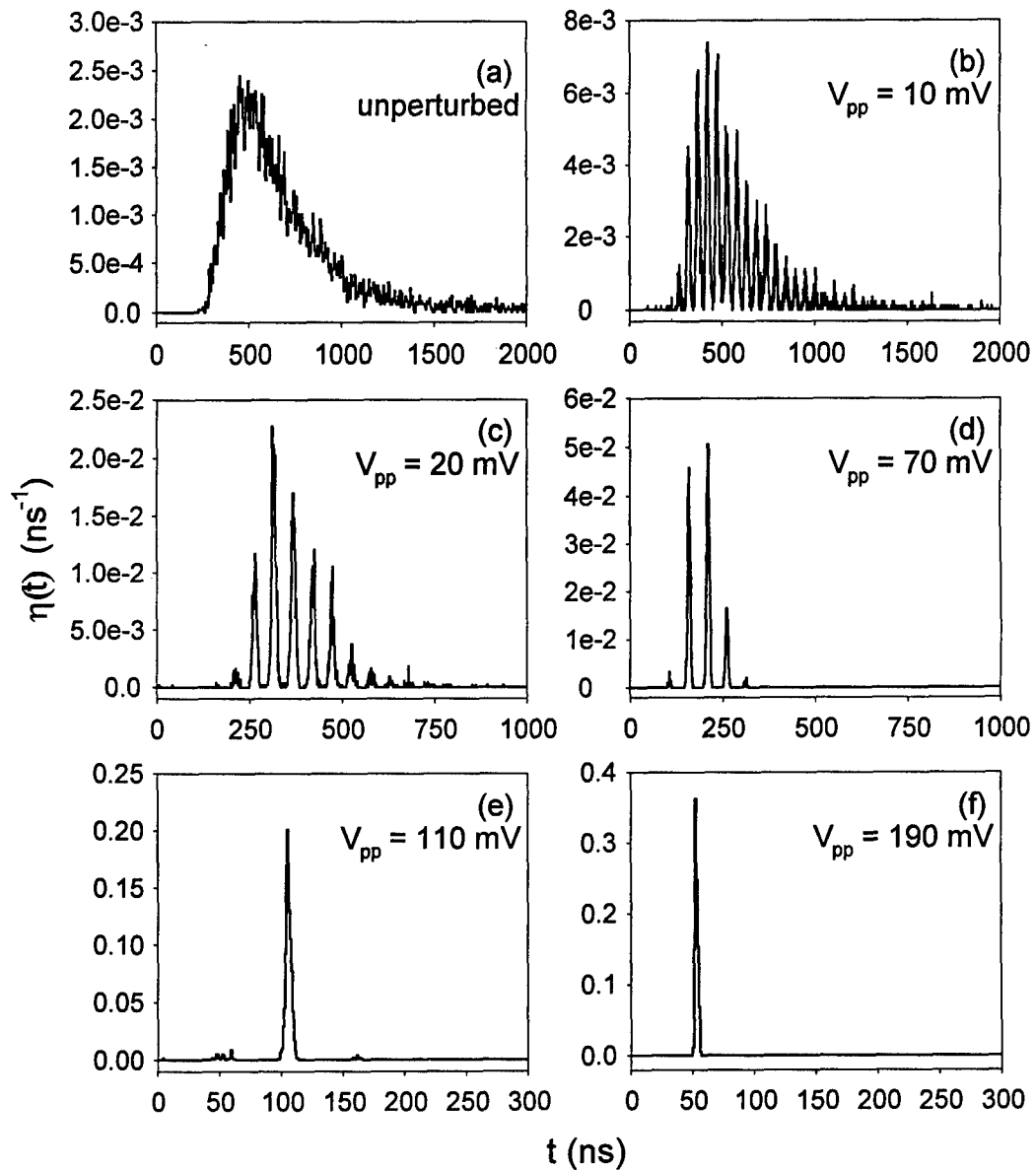


Figure 6.3: Probability distributions $\eta(t)$ for interspike intervals when a 19 MHz modulation is applied for various amplitudes. Weak modulation shifts the distribution and causes a comb to appear with peaks occurring at multiples of the drive period. At sufficiently large amplitudes, $\eta(t)$ is collapsed to a single peak, indicating a regular appearance of dropout events.

The remaining graphs of Fig. 6.3 illustrate the dependence of $\eta(t)$ as the amplitude of the modulation is increased. The mean time τ_{II} is reduced (note the changes in scale) and fewer peaks appear in the distribution. Graphs (e) and (f) show two particularly interesting cases, for which the interspike intervals occur in a narrow region near a single dominant time. In graph (e) this time is 105 ns, corresponding to twice the period of modulation, and in graph (f) it is 53 ns, exactly the period of the modulation. This indicates that the dropouts are occurring at regular intervals, a very different behavior from that of the unperturbed system. I examine these cases carefully in the following section.

6.2.2 Entrainment of dropouts

I have shown that the interspike intervals occur at essentially a single time if the modulation amplitude is sufficiently large, as illustrated in Fig. 6.3e and f. This indicates that the irregular, probabilistic timing of the interspike intervals is converted to a more periodic behavior. This effect is illustrated by the time series shown in Fig. 6.4. As before, graph 6.4a shows the unperturbed case for reference, using the same system parameters as in the previous section. Graph 6.4b shows the case where the interspike intervals occur near 105 ns only (see Fig. 6.3e), clearly demonstrating that the modulation has entrained the power dropout such that one event occurs every two drive cycles. The applied modulation $V_{pp} = 110$ mV corresponds to a current modulation amplitude of 1.76 mA, or 8% of the dc current level. Graph 6.4c illustrates the behavior of the system when the interspike intervals occur only near 53 ns, the period of the modulation. In this case, one dropout appears every drive cycle. For graph 6.4c, $V_{pp} = 190$ mV, corresponding to a current modulation amplitude of 3.04 mA (14% of the dc current level). The frequencies associated with this entrainment are comparable to the relaxation oscillation frequency of the external cavity laser,

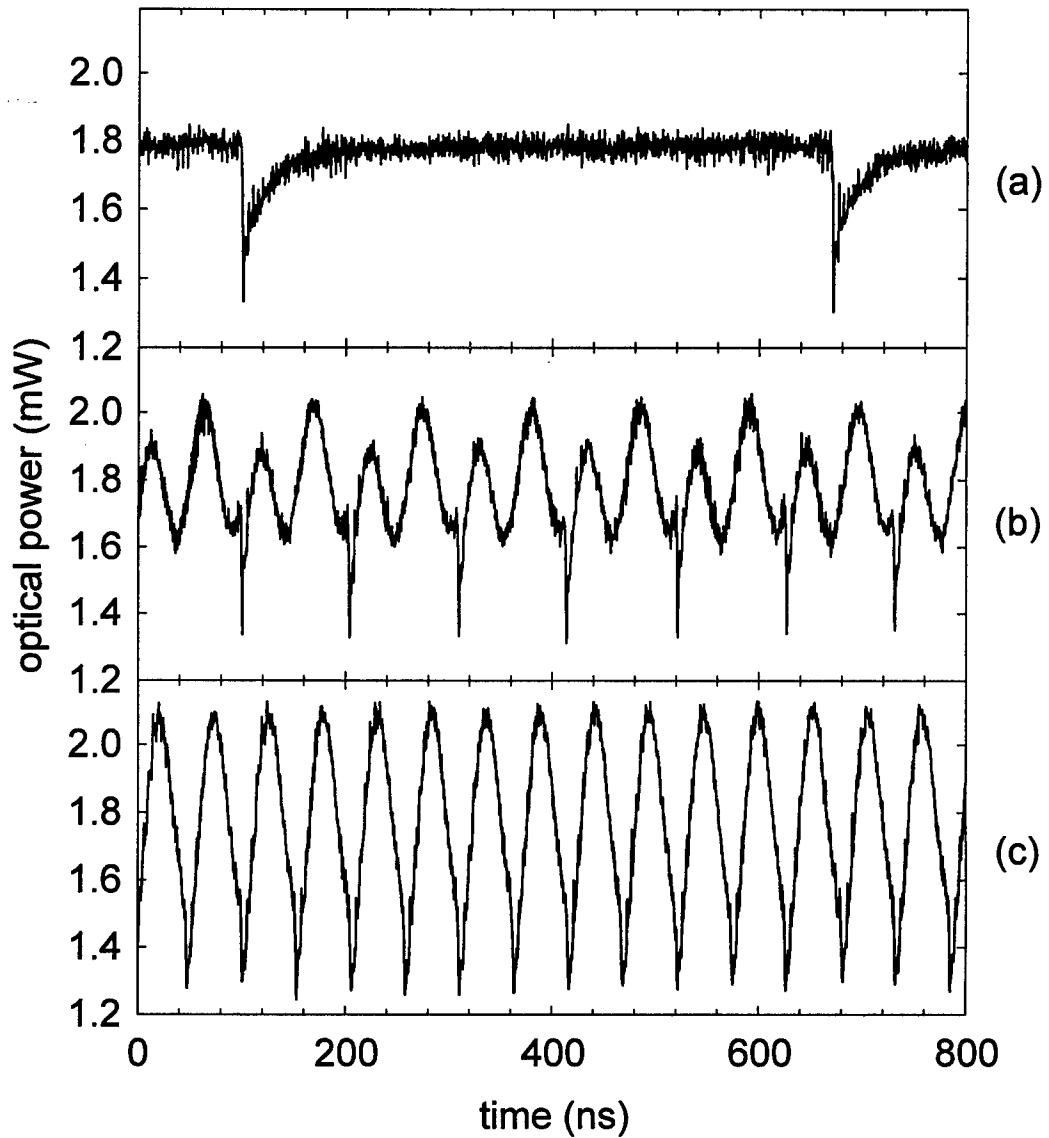


Figure 6.4: Experimental time series of the laser intensity illustrating entrainment of power dropouts. Graph (a) shows dynamics of the unperturbed system, while (b) and (c) illustrate entrained dynamics. The current modulation amplitudes for (b) and (c) are 8% and 14% of the dc level, respectively.

which I calculate from the Henry and Kazarinov model to be 2.5 MHz.

Some understanding of how this entrainment comes about can be gained from a numerical study of the dynamics of the modulated system in phase space. Fig. 6.5 compares one representative simulated dropout event in phase space (a) with four dropouts occurring in sequence when current modulation is included (b) such that the simulated dynamics show one-to-one entrainment. These graphs show that the 19 MHz current modulation restricts the region of phase space in which the dynamics occur. Specifically, the modulation forces the dropout to occur long before the dynamics have reached the neighborhood of the maximum gain mode. The entrained dropouts do *not* all occur at precisely the same point on the ellipse despite the interspike intervals being almost identical, possibly due to the probabilistic quality of dynamics as the system moves along the external cavity modes. The system parameters used in this simulation are $J/J_{th} = 1.02$ and $\kappa = 0.3$. The modulation amplitude in these simulations is 2% of the solitary threshold current value, smaller than that of the experiment, and is included in the equations as a direct modification of the pump term.

It is interesting to note that entrainment of the power dropouts does *not* eliminate the fast pulsing dynamics of the laser, evident from the strong fluctuations still present in the carrier density in Fig. 6.5. This can be seen experimentally by examining the power spectra and noting that strong peaks at multiples of the cavity roundtrip frequency are still present. Fig. 6.6 compares the RF power spectra of the unperturbed system with the two cases for which the dropouts are entrained. Graphs (a)-(c) emphasize the low-frequency response, with a 5 kHz resolution bandwidth and 3 kHz video filtering. In graph (a), the low-frequency noise attributed to the sporadic dropout behavior is apparent from 0 - 100 MHz, and the fundamental cavity resonance frequency at 212 MHz is clearly visible. Graph (b) corresponds to

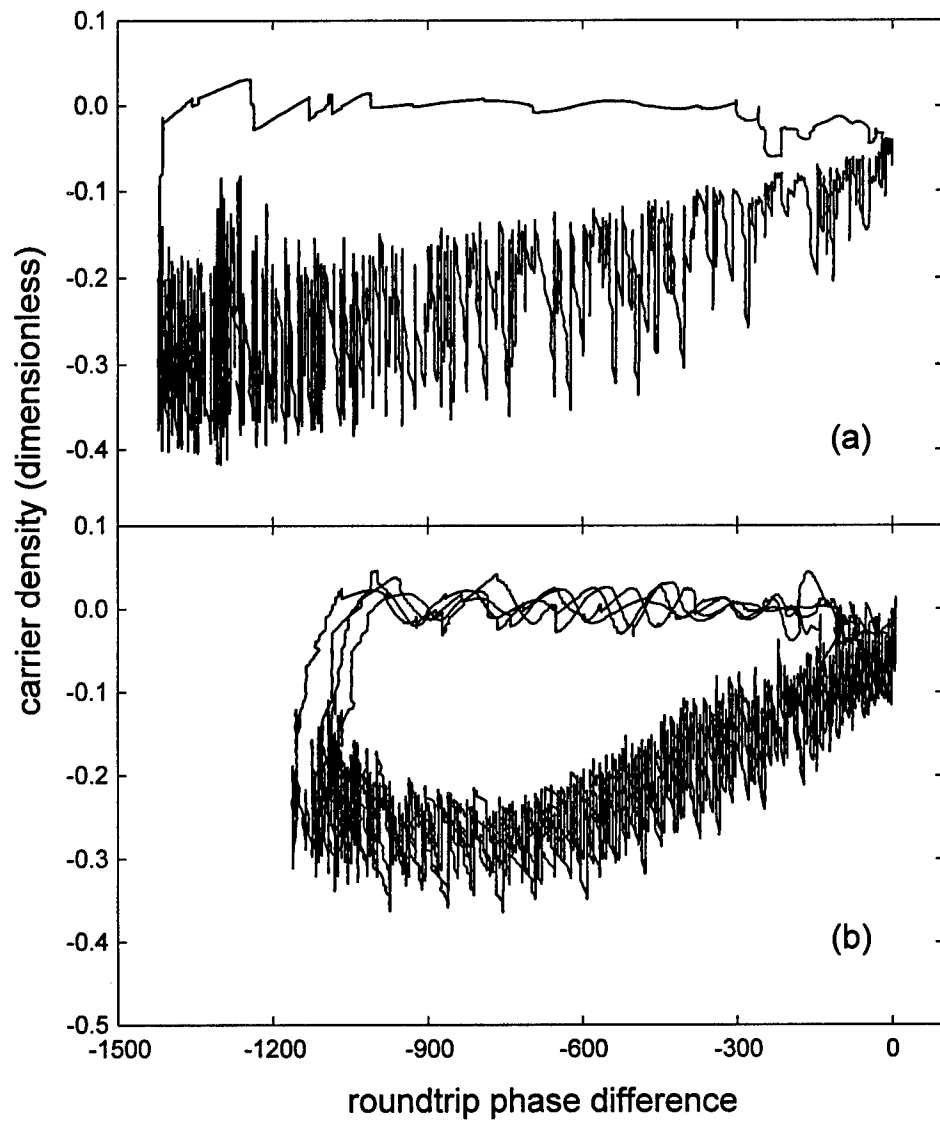


Figure 6.5: Simulated phase space trajectories of the unperturbed (a) and entrained dynamics (b) of the LFF system. Graph (a) shows a single typical dropout event, and (b) shows four dropouts in sequence. The entrained dynamics occupy a limited region of phase space.

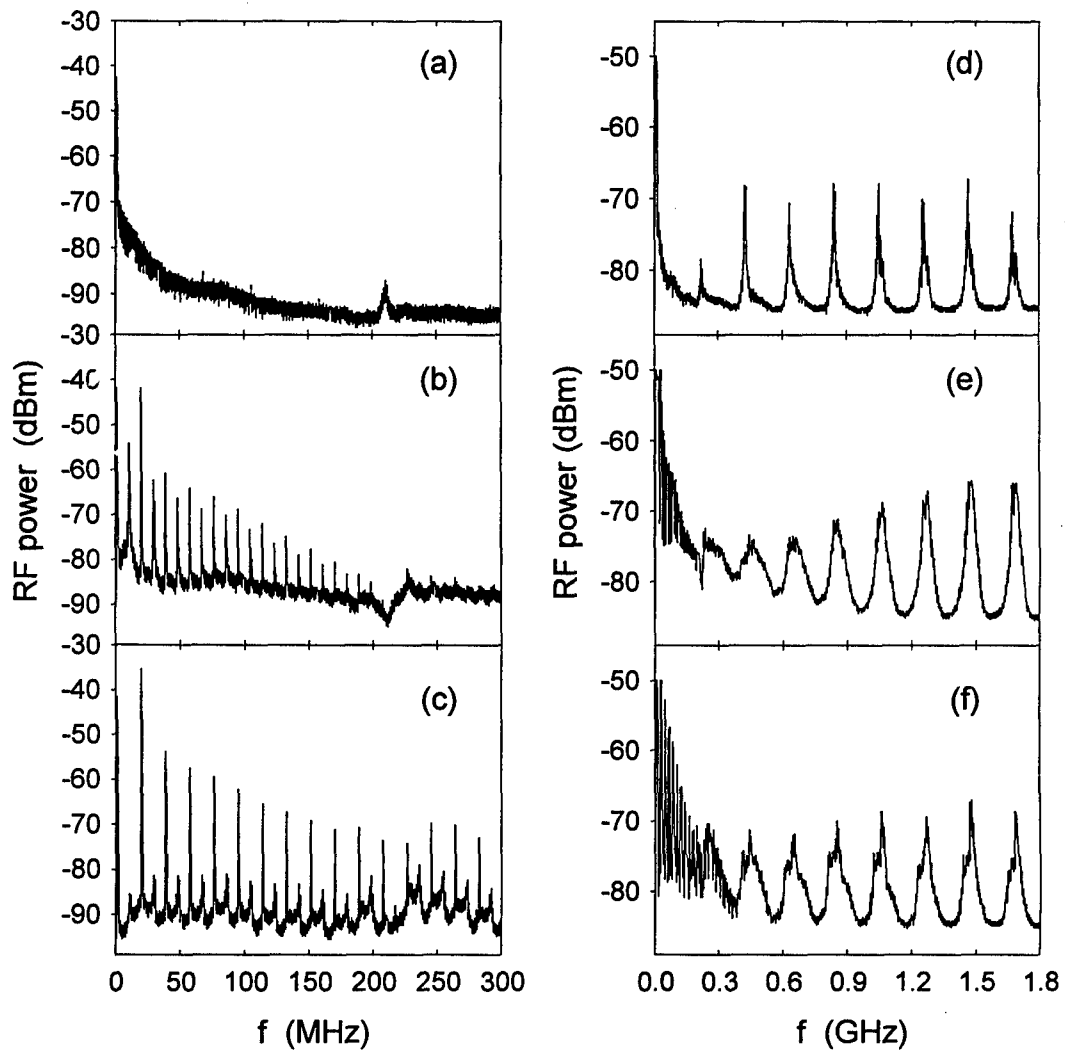


Figure 6.6: Experimental power spectra of the unperturbed and entrained dynamics. Graphs (a) and (d) show the spectra of the unperturbed system, (b) and (e) show 1:2 entrainment, and (c) and (f) show 1:1 entrainment. The entrained dynamics exhibit reduced low-frequency noise, but the high-frequency features are not suppressed.

the conditions of Fig. 6.4b, where one dropout occurs every two drive cycles. The first peak occurs at 9.5 MHz, corresponding to one-half of the drive frequency. Graph (c) is the power spectrum corresponding to the one-to-one entrainment illustrated in Fig. 6.4c. In this case, the first peak occurs at $f = 19$ MHz. Graph (c) also clearly shows that the low-frequency noise is greatly reduced when the dropouts are entrained. Finally, the sequence of graphs (d)-(f) show the same progression as (a)-(c) over the full range of the spectrum analyzer (1.8 GHz). The peaks at the harmonics of the external cavity resonance frequency are significantly broadened but are by no means eliminated, indicating that the fast pulsing dynamics persist in the presence of the 19 MHz modulation.

6.3 High-frequency modulation

In addition to the low-frequency entrainment study, I also investigate the response of the external cavity semiconductor laser system to higher frequency perturbations. As I mentioned at the beginning of this chapter, almost any modulation frequency will cause the dropouts to occur more frequently, that is, τ_{II} decreases. This is illustrated in Fig. 6.7, where I compare representative time series from the (a) unmodulated system and the system when (b) 230 MHz and (c) 120 MHz modulations are added to the pump current. It is apparent that the mean interspike interval is shorter in the presence of the perturbations. However, it also seems that the dynamics of the dropouts may be changed in other ways; note the appearance of regions in graph (c) where the dropouts follow one another closely, sometimes in short bursts. The apparent irregularity of the dropout depths is primarily due to a reduced sampling rate (1 Gs/s) of the oscilloscope used to capture these time series. The laser parameters are: drive current 20.5 mA, $\Delta C/C = 0.147$, and $P/P_1 = 1.96$. The sinusoidal signal is applied such that the current modulation amplitude is about 0.38 mA, or 1.9% of

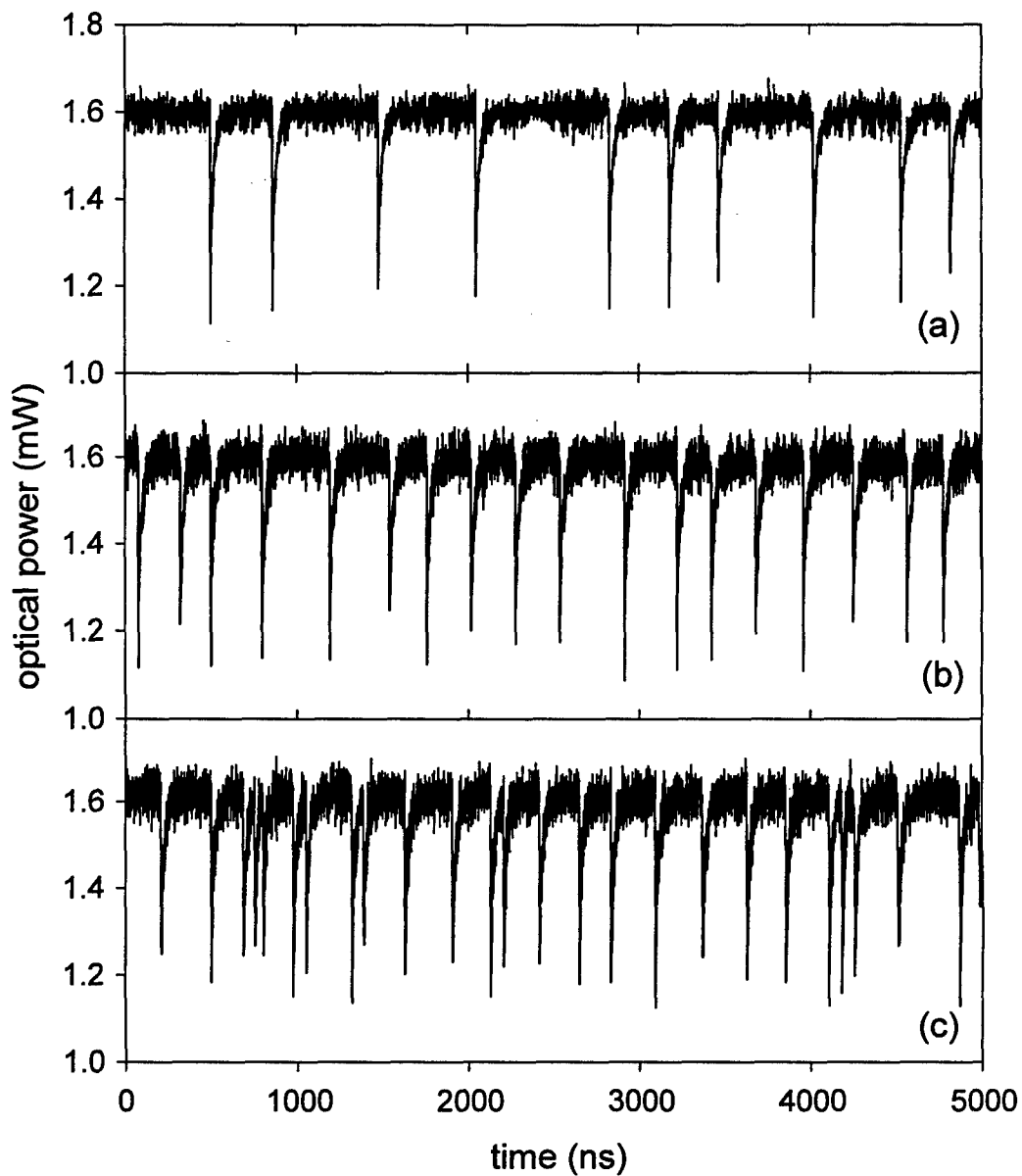


Figure 6.7: Experimental time series of laser intensity comparing the (a) unperturbed system with the system when a 1.9% current modulation is applied at (b) 230 MHz and (c) 120 MHz. The high-frequency modulation increases the average dropout rate, and can induce rapid sequences of dropouts (c).

the dc level.

The probability distributions $\eta(t)$ of the interspike intervals is a sensitive indicator of the presence of high-frequency modulation and altered dynamics, just as it was for the low-frequency case. In Fig. 6.8, I show $\eta(t)$ for several different frequencies while the current modulation amplitude is held constant. The system parameters are the same as for Fig. 6.7. As usual, graph (a) displays $\eta(t)$ for the unperturbed system, and graphs (b) through (f) show the experimentally measured distributions with the modulation applied. Several interesting features are immediately apparent. First, for all cases with modulation except $f = 212$ MHz, the probability distribution develops a comblike appearance, much like Fig. 6.3b, where the spacing between the spikes is equal to the period of the drive. Thus, the power dropouts are forced to occur only at intervals that are integral multiples of the modulation period. I measure these histograms using a 1 ns bin size to provide sufficient resolution. Another interesting feature of these probability combs is that the overall envelope of the distribution develops a second peak at short times (50 - 100 ns) for certain cases, such as graphs (b) and (f). This indicates that the dropouts are likely to appear in rapid succession, the case illustrated by the time series of Fig. 6.7c. Finally, the modulation frequency $f = 212$ MHz (graph 6.8d) leads to a surprising result. It does not appear to affect the distribution at all! The values for τ_{II} are the same within statistical uncertainty (unperturbed $\tau_{II} = 436 \pm 5$ ns, modulated $\tau_{II} = 431 \pm 1.5$ ns) and the shapes of $\eta(t)$ are also almost identical. This phenomenon is as yet unexplained, although it is almost certainly related to the fact that 212 MHz is the fundamental frequency of the external cavity.

A first step in understanding the high-frequency modulation results is to reproduce the observed behavior using numerical simulations. The two simulated time series shown in Fig. 6.9 show the evolution of the output power if the system is

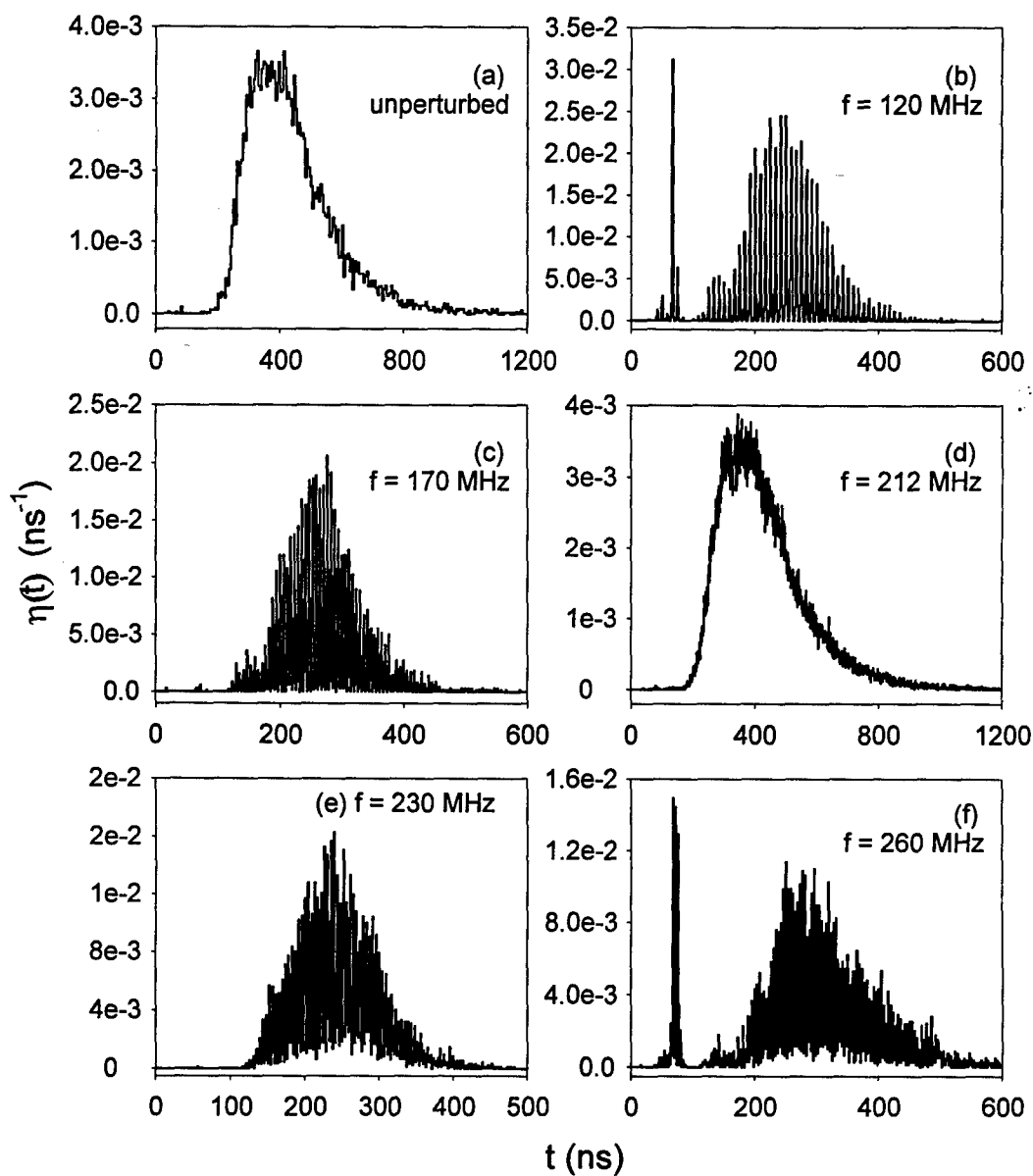


Figure 6.8: Experimental probability distributions $\eta(t)$ of interspike intervals under high-frequency modulation of fixed amplitude (1.9% of dc current) and varying frequency. The modulation induces a comb in $\eta(t)$ except when the frequency corresponds to the external cavity resonance (d). In some cases (b), (f) a feature appears at small interspike times, indicating a significant probability of power dropouts occurring in rapid succession.

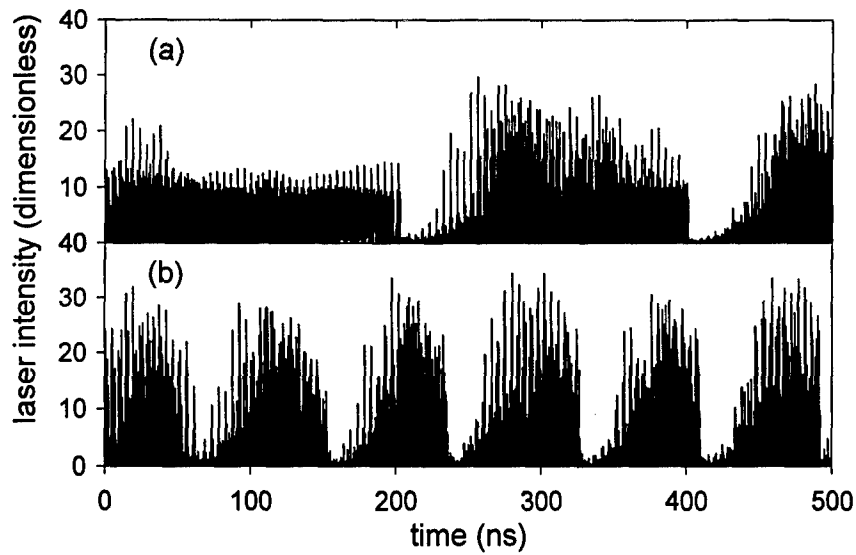


Figure 6.9: Simulated time series of laser intensity showing unperturbed behavior (a) and increased dropout rates when a 230 MHz modulation is applied to the pump current (b).

(a) unperturbed or (b) driven with a 230 MHz modulation. The application of the open-loop signal induces an increased rate of dropouts. The system parameters for these simulations are $J/J_{th} = 1.02$ and $\kappa = 0.4$, and the modulation amplitude is 1% of J_{th} . I note that simulations for which the frequency is set to be 212 MHz shows no qualitative change in the behavior of the dropouts (not shown), also agreeing with experimental findings. Future work in the analysis of the response of the LFF dynamics to open-loop control will be to further extend the Henry and Kazarinov theory to include a time-dependent term representing the external modulation, and thereby calculate $\eta(t)$ for this system.

As with the low-frequency modulation, an examination of the dynamics of Fig. 6.9 in phase space also yields additional insight. Such phase space representations are given in Fig. 6.10, where graph (a) shows the unperturbed dynamics over a period of 500 ns, and graph (b) shows the trajectory when the 230 MHz modulation is added.

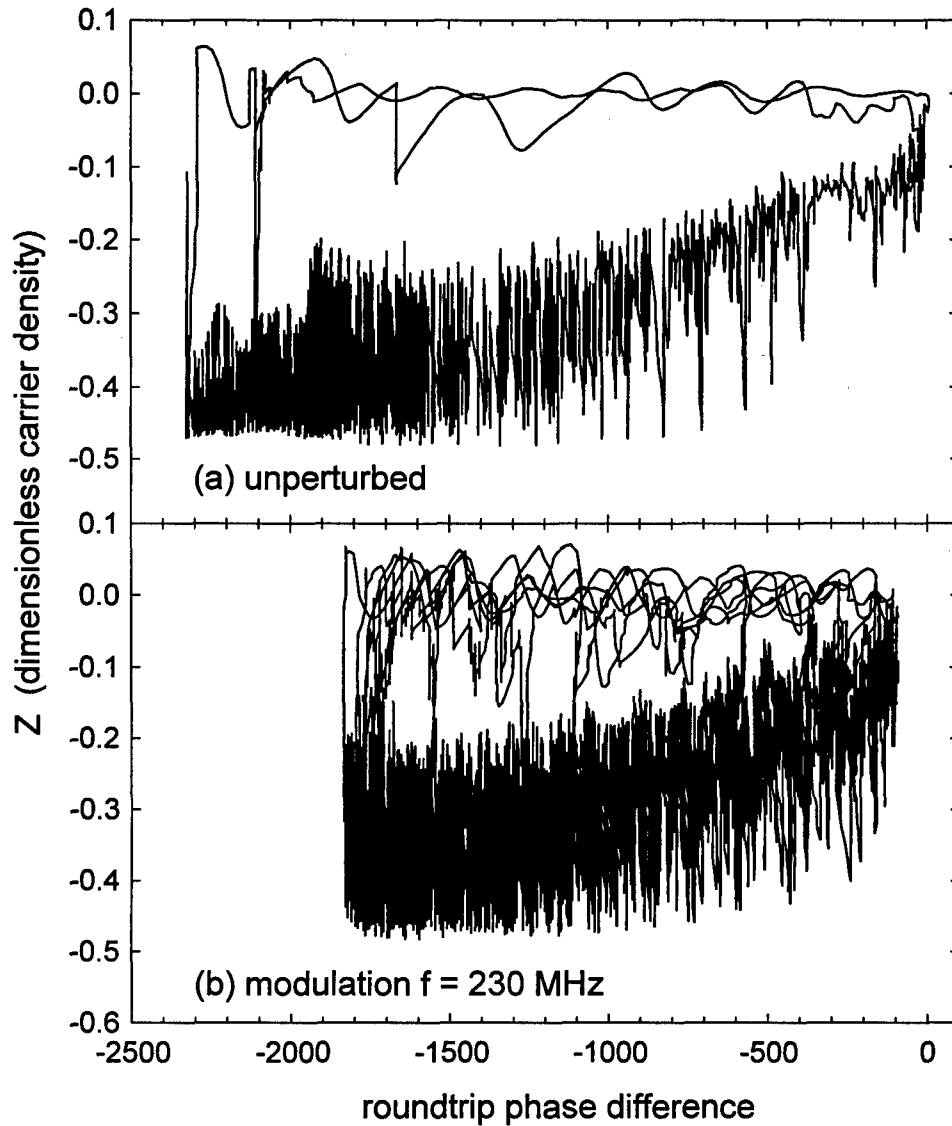


Figure 6.10: Phase space representation of simulated time series from Fig. 6.8. The 230 MHz modulation (b) restricts the region in which the dynamics occur, forcing dropouts to occur before the maximum gain mode is reached and reinjecting the dynamics onto the ellipse before the roundtrip phase difference reaches zero.

The high-frequency modulation limits the phase space regime in which the dynamics take place, similar to the behavior shown in Fig. 6.5 with low-frequency entrainment. There is a subtle difference, however, in that the high-frequency perturbation seems to limit the region of phase space at both large and *small* values of the roundtrip phase difference. That is, it appears that the dynamics are reinjected onto the ellipse before the phase difference goes to zero. Numerical experiments show that this effect is increased at greater drive amplitudes, further decreasing the range. For example, all the phase space dynamics occur between values of -700 and -1400 radians for the roundtrip phase difference if the 230 MHz drive amplitude is increased to 4% of J_{th} . The power dropout events are no longer clearly defined in this regime, as the system rapidly moves on and off the ellipse.

In this chapter I have studied the effects of open-loop control perturbations on the dynamics of LFF. I have shown that a moderately strong 19 MHz modulation applied to the pump current can eliminate the randomness in timing of interspike intervals, collapsing the probability distribution $\eta(t)$. The dropouts can be entrained in 1:1 or 1:2 ratios with the drive, and numerical simulations indicate that the modulation forces the dropout to occur well before the dynamics approach the maximum gain mode. When entrainment occurs, the low-frequency noise usually present in the system is greatly reduced. If the modulation is not strong enough to induce entrainment, $\eta(t)$ is still a sensitive indicator of the presence of the modulation, showing that the interspike intervals will occur at integral multiples of the drive period. Weak high-frequency modulation has a similar effect on $\eta(t)$, generating a comb in the distribution, as well as restricting the area in phase space in which the dynamics occur. However, there remain unexplained effects of the high-frequency modulation, such as the appearance of closely-spaced dropouts in some cases and the disappearance of the comb in $\eta(t)$ when the modulation frequency exactly corresponds to the external

cavity resonance frequency.

It is instructive to consider why no modulation frequencies were able to suppress the power dropout events. Much of the difficulty may be due to the complexities inherent to the system. For example, the external cavity semiconductor laser is very high-dimensional, in contrast with laser systems in which open-loop control produces entrainment of an orbit, such as the CO₂ laser [65, 148]. In addition, the role of spontaneous emission is very important in semiconductor lasers, but its influence is not fully understood in this system. Another observation is that success or failure of open-loop control is known to be highly dependent on the specific form of the dynamical system [67]; it may be that the injection current, while easily accessible, is the wrong variable to perturb. From observation of the dynamics on the attractor, the instability occurs rapidly along the direction of the carrier density. The instability may be suppressed more effectively by perturbing a different variable such as the phase of the slowly-varying electric field, which could be accomplished by varying the effective cavity length using an electro-optic modulator. This concludes my investigation of open-loop control, and in the next chapter I present some brief results describing my preliminary attempts at feedback control of a steady state of the external cavity semiconductor laser.

Chapter 7

Attempts to Stabilize an Unstable Steady State of an External-Cavity Semiconductor Laser

This chapter presents my attempts to stabilize the LFF system using a true closed-loop feedback signal, in contrast with the open-loop perturbations used in the previous chapter. I use a high-pass filter control protocol, using the laser intensity as the measured system variable and the pump current as the accessible control parameter. This method is designed to stabilize an unstable steady state (USS), a desirable behavior that decreases noise and improves the laser's coherence properties. This experiment is at the forefront of high-speed control, representing an attempt to control an instability that is orders of magnitude faster than that of the 10 MHz diode resonator, the fastest chaotic system controlled by feedback to date. It is also a much more complex system, and it is not clear what the most relevant timescales will be. Specifically, the falling edge of the power dropout (duration ~ 1 ns) may be the most important, but it is also conceivable that successful control may have to address the ultrafast pulsing dynamics, increasing the frequency scale to several GHz.

In this chapter I explain the high-pass filter feedback protocol, and show how it can be interpreted as a limiting case of ETDAS control of unstable periodic orbits. I then illustrate how this technique can be implemented in the laser system. Experimental results show that the feedback affects the system by changing the shape of individual power dropouts and modifying the probability distribution of the interspike intervals, but it is unsuccessful at stabilizing USS's. I present experimental data for the probability distributions, as well as time series illustrating how the dropout

shape is altered by the feedback. I conclude by discussing possible reasons for the ineffectiveness of the control and methods that may improve the results.

7.1 High-pass filter control

I apply high-pass filter control to attempt to stabilize one of the many stationary solutions possessed by the external cavity laser system. Stabilization of USS's is discussed in Chapter 2 using the example of the inverted pendulum, and several control protocols are reviewed there as well. I choose the control protocol for which the feedback signal is identical in form to a single-pole high-pass filter, described by Eq. 2.17. Restating the general form of that equation here, this technique prescribes the continuous adjustment of an accessible system parameter p by $\delta p(t)$ where $\delta p(t)$ evolves according to

$$\frac{d}{dt}\delta p(t) = -\gamma \frac{d\xi(t)}{dt} - \omega_o \delta p(t), \quad (7.1)$$

where $\xi(t)$ is a measured dynamical variable of the system, γ is the feedback gain, and ω_o corresponds to the corner frequency of the filter. This method is well-suited to high-speed operation, it can be implemented very easily, and has successfully stabilized an USS of a chaotic electronic circuit [45]. It also has an advantage over the derivative control technique (Eq. 2.16) in that it is not as susceptible to high-frequency noise.

It is easy to understand the logic of this method. If the measured system variable $\xi(t)$ is constant, as it must be for an unstable steady state, $\partial\xi/\partial t = 0$ and thus $\delta p(t)$ goes to zero. When the system begins to move off of the USS, the time derivative of $\xi(t)$ becomes nonzero and thus the feedback grows. This idea can be expressed in the frequency domain as well, and I motivate this approach by considering the relationship between high-pass filter control and ETDAS, the continuous feedback method for stabilizing unstable periodic *orbits*, described in Chapter 3.

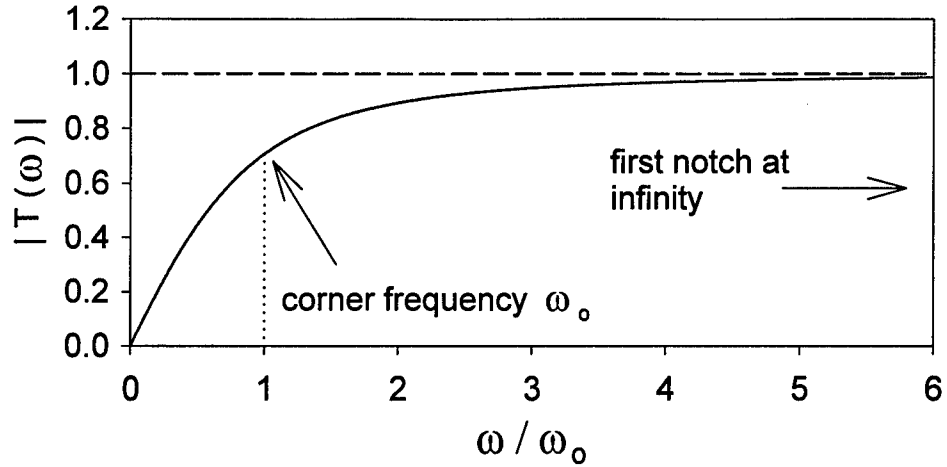


Figure 7.1: Transfer function of the high-pass filter. The corner frequency is the point at which the response of the filter has fallen off by 3 dB. This is equivalent to the ETDAS transfer function with the first notch at infinity.

To understand this relationship, recall the frequency-domain characteristics of ETDAS as described by its transfer function $T(f)$. This is described by Eq. 3.5 and illustrated in Fig. 3.3. The first notch in the transfer function at a nonzero frequency occurs at $f^* = 1/\tau$ where τ is the period of the unstable periodic orbit. If this notch were located at a very high frequency (much higher than any frequencies present in the system), the effective transfer function would then appear as in Fig. 7.1, which is equivalent to a high-pass filter. This can be accomplished by taking the limit $\tau \rightarrow 0$ while letting $R \rightarrow 1$. This relationship can be derived mathematically by first noting that ETDAS may be expressed recursively [20], i.e.

$$\begin{aligned}
 \delta p(t) &= -\gamma \left[\xi(t) - (1-R) \sum_{k=1}^{\infty} R^{k-1} \xi(t-k\tau) \right] \\
 &= -\gamma [\xi(t) - \xi(t-\tau)] + R\delta p(t-\tau).
 \end{aligned} \tag{7.2}$$

The next step is to subtract $\delta p(t-\tau)$ from both sides of the equation and divide by

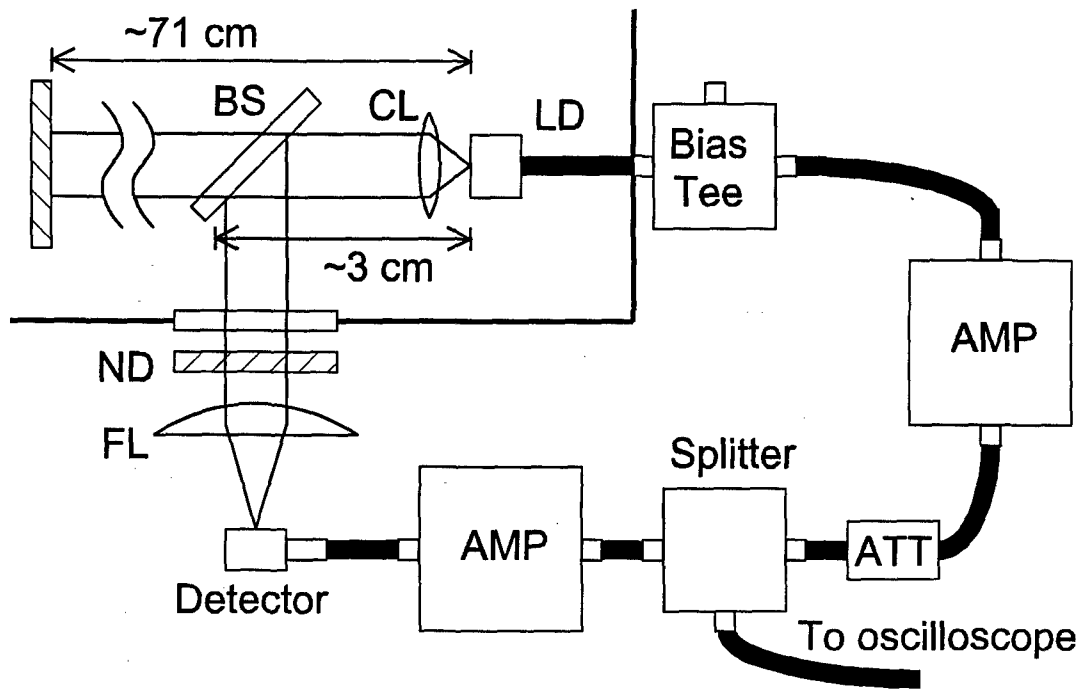


Figure 7.2: Experimental layout for implementation of high-pass filter control in the external cavity semiconductor laser system.

τ to obtain

$$\frac{\delta p(t) - \delta p(t - \tau)}{\tau} = -\gamma \frac{[\xi(t) - \xi(t - \tau)]}{\tau} + \frac{1}{\tau} (R - 1) \delta p(t - \tau). \quad (7.3)$$

Shifting time forward by τ and simultaneously taking the limits $\tau \rightarrow 0$ and $R \rightarrow 1$ with $\omega_o = (R - 1) / \tau$ held finite, Eq. 7.3 becomes

$$\frac{d}{dt} \delta p(t) = -\gamma \frac{d\xi(t)}{dt} + \omega_o \delta p(t). \quad (7.4)$$

This is identical to Eq. 7.1, and thus high-pass filter feedback control may be understood as a limiting case of ETDAS.

One very desirable feature of high-pass filter control is that it extraordinarily simple to implement experimentally. In this experiment, the measured system variable is the laser intensity emerging from the semiconductor chip and the feedback

is applied to the injection current. One configuration for this process is illustrated in Fig. 7.2, where organization of the feedback loop is designed to minimize control loop latency. The beam from the laser diode (LD) is collimated (CL), and sampled by the beamsplitter (BS) that directs 30% of the incident power out of the aluminum box through a glass plate. The beam passes through a neutral density filter (ND) with an optical density of 0.8 which prevents damage to the detector, after which a focussing lens (FL) directs the beam onto the New Focus 1537-LF photoreceiver. The photocurrent is converted to a voltage by a transimpedance amplifier and ac-coupled, all within the photoreceiver unit. This is the point at which the high-pass filtering is performed. The voltage is then amplified (AMP), attenuated (ATT), or inverted as desired before it is injected into the RF port of the bias-tee, thus feeding back to the laser current. The amplifiers (B&H Electronics type AC5120HL) are inverting, with a bandwidth from 2 kHz - 5 GHz and a gain of 20 dB each. The attenuators (JFW Inc. type 50HF-SMA) have a bandwidth of dc - 18 GHz and a variety of fixed values available (1 - 20 dB). The splitter (Mini-Circuits ZFRSC-42, bandwidth dc - 4.2 GHz) is used to sample the signal. All signals propagate through SMA connectors and short lengths of RG-174 flexible coaxial cable not exceeding five inches. I estimate that this feedback system has a total control loop latency of 3 - 4 ns, based on propagation speeds in electronic components and the path length of the loop.

7.2 Experimental effects of high-pass filter feedback

As stated in the introduction to this chapter, I find that high-pass filter control in this implementation is not successful at stabilizing an USS nor at suppressing power dropout events. When control is turned on (by simply connecting the cable to the bias-tee), the dropouts continue to occur at an equal or faster average rate and drop

to approximately the same depth. The feedback does affect the system, however, by changing the shape of individual power dropouts, illustrated in Fig. 7.3. Graph (a) shows a typical dropout of the unperturbed system. Graphs (b)-(d) illustrate the effects as the feedback gain is increased, going from a minimal change (b) to a ringing effect (d). The ringing becomes stronger as the feedback increases, and eventually goes into continuous oscillations at sufficiently high gains (e) (note the change in scale). The laser parameters are: drive current 19 mA, relative threshold reduction $\Delta C/C = 0.15$, and $P/P_1 = 1.46$.

To calculate the feedback response as a function of the optical power reflected from the beamsplitter, I account for the neutral density filter, conversion gain of the photoreceiver, and the amplifiers and attenuators present in the loop. The most convenient quantity to calculate is the voltage applied at the bias-tee as a function of the optical power reflected from the beamsplitter. This avoids the complications of frequency-dependent coupling of the applied voltage into the current, described in the previous chapter. It is important to remember that *fluctuations* in the optical power are the relevant quantities, since the high-pass filter action ignores changes that are slower than the 10 kHz cutoff of the ac-coupled photodetector. With that in mind, the conversion gains associated with the time series shown in Fig. 7.3 are 114, 181, 228, and 360 mV/mW for graphs (b), (c), (d), and (e), respectively, and are assumed not to be frequency-dependent.

The sign of the gain in Fig. 7.3 is chosen such that decreasing optical power results in increasing pump current. There is no *a priori* reason that this should be the correct sign to use, however, and therefore I test the opposite sign as well. I find that this case lengthens significantly the duration of the dropouts, suggesting that this is indeed the wrong choice of sign. This behavior is illustrated in Fig. 7.4, where graph (a) shows a single dropout of the unperturbed system, and graph (b) shows

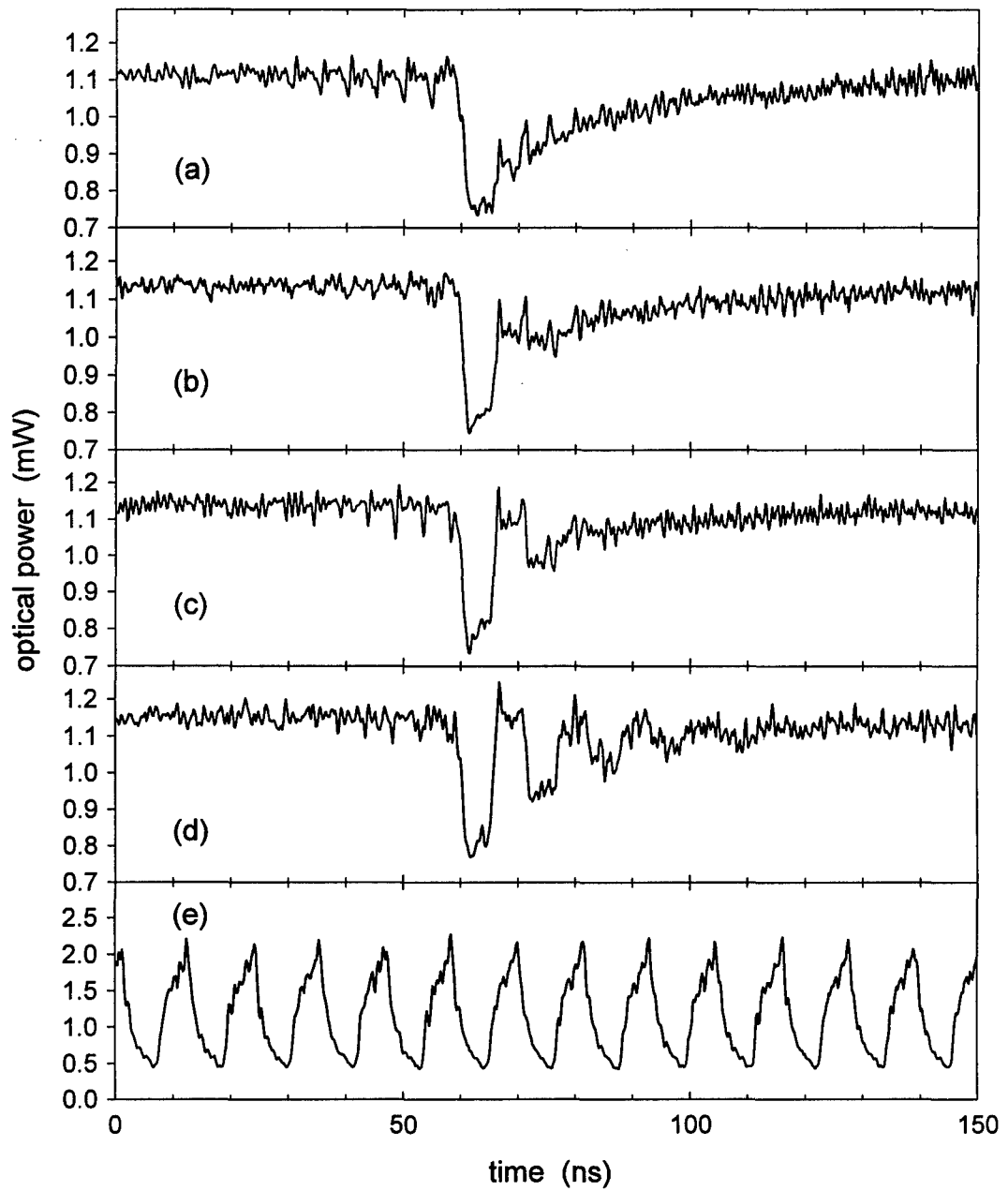


Figure 7.3: Experimental time series of laser intensity with high-pass filter feedback. The shape of the dropout is dependent on the feedback gain.

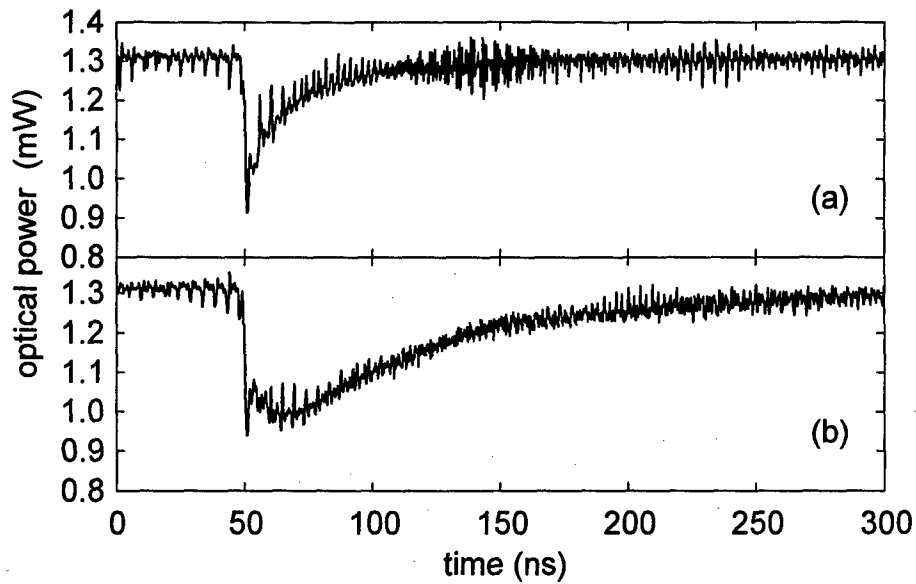


Figure 7.4: The effect of feedback with the wrong sign of the gain on power dropout shape. The dropout when (b) feedback is applied has a much longer duration, compared with the (a) unperturbed dropout.

the result when the feedback is applied. The magnitude of the conversion gain is 228 mV/mW, the drive current is 20 mA, $\Delta C/C = 0.16$, and $P/P_1 = 1.93$.

I experimentally measure probability distributions $\eta(t)$ of the interspike intervals for the system, to quantify the effect of feedback on the long-term behavior of the system. This data is presented in Fig. 7.5, where graph (a) shows $\eta(t)$ for the unperturbed system, and graphs (b) - (d) are with feedback, with the same gains as the corresponding letters in Fig. 7.3. The graphs show that the feedback changes $\eta(t)$ little, only shifting the distribution somewhat toward shorter interspike intervals. The mean time of the unperturbed system is $\tau_{II} = 1050 \pm 20$ ns, and decreases to $\tau_{II} = 888 \pm 15$ ns in graph (d), assuming only statistical errors. For this data set, the drive current is 21 mA, $\Delta C/C = 0.15$, and $P/P_1 = 1.93$.

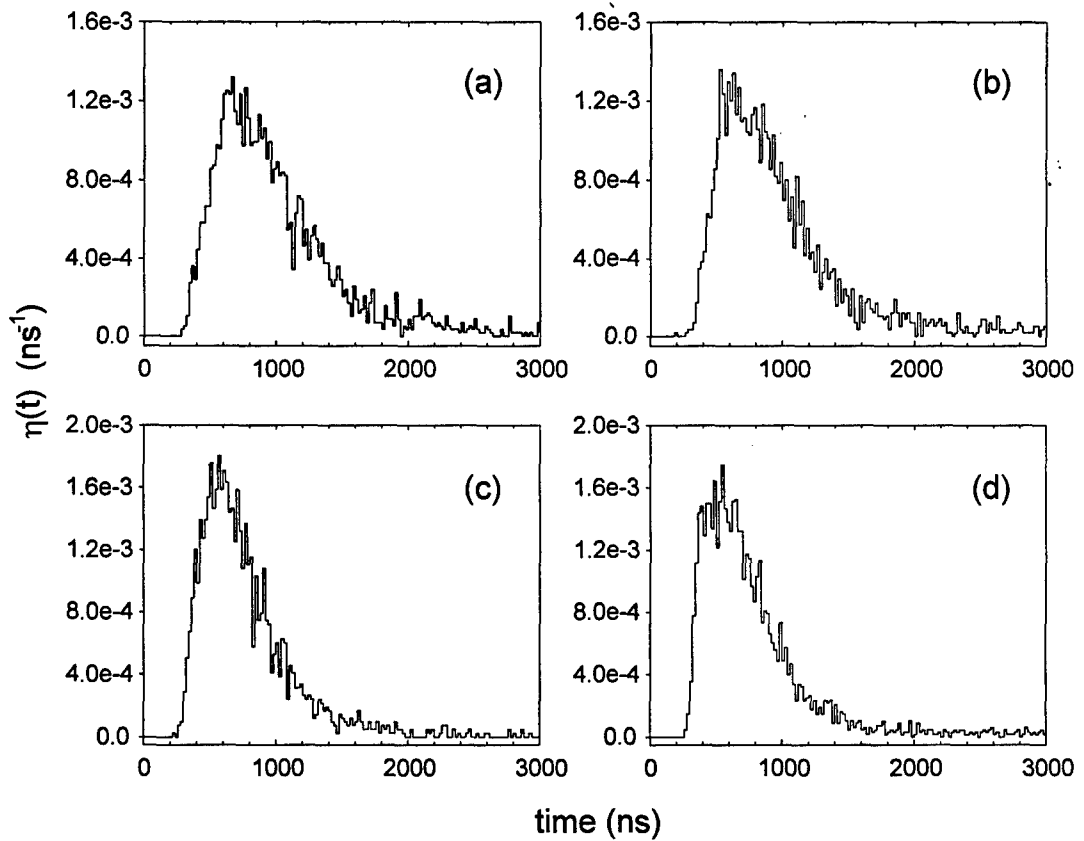


Figure 7.5: Experimentally measured probability distributions $\eta(t)$ of the interspike intervals when high-pass filter feedback is introduced. The unperturbed dynamics are represented in graph (a).

7.3 Discussion

To conclude this chapter, I consider possible reasons for the ineffectiveness of this implementation of high-pass filter control and discuss improvements by which it may be more effective. The high-speed, high-dimensional LFF dynamics are certainly much more complex than those of previously controlled systems, and the stochastic effects may also be a destabilizing influence. It is not surprising that these complications make control difficult, especially given the speed of the dynamics. However, it is encouraging that the feedback scheme is capable of changing the dropout shapes, suggesting that improved implementations may have more success. For example, it is likely that latency remains a problem in the current implementation, despite my efforts to minimize it. From the shape of the dropouts in Fig. 7.3, it appears that a few nanoseconds elapse between the falling edge of the dropout and first visible sign of the feedback being applied, which is consistent with the control loop latency. To decrease the latency, it may be necessary to reconfigure the experiment, placing the detection and feedback electronics inside a larger aluminum box to minimize the path length. Ideally, the electronics could be amassed into a single custom-built design, eliminating the need for multiple amplifiers and cable connections. Other improvements may also enhance performance of the control. The frequency dependence of the coupling of the feedback signal into the laser may be a source of problems. Taking a lesson from the electronic implementation of ETDAS, an appropriately designed predistortion filter could compensate for this effect. In addition, it may also be that the fast pulsing dynamics need to be taken into account, perhaps carefully adjusting the timing of the loop such that the feedback pulse arrives in conjunction with an optical pulse in the cavity.

This chapter has shown the effects of high-pass filter control on the dynamics of

an external cavity semiconductor laser. In the concluding chapter that follows, I will review all the major results of this thesis, and consider future work to be done.

Chapter 8

Conclusion and Future Directions

To draw this dissertation to a close, I reflect on how my research contributes to the fields of physics and nonlinear dynamics, review the major results of this thesis, and consider extensions of this project. The primary theme of this thesis is control of instabilities and chaos in systems that display temporal instabilities on fast timescales. My research encompasses two such systems, possessing instabilities among the fastest that have been investigated experimentally in a nonlinear dynamics context to date. My goals in this work are to better understand the dynamics of these systems, to develop and demonstrate new control techniques that are suitable for application to fast dynamics, and to increase the understanding of the practical issues involved in such control.

This work grows from foundations in the fields of dynamical systems and control theory, as discussed in the introductory chapters. The subfield of controlling chaos became very visible and important in 1990 following the work of Ott, Grebogi, and Yorke [8], who showed how chaotic systems may be controlled by taking advantage of the unstable dynamics inherent to the system, such as unstable steady states and unstable periodic orbits. In my introduction I illustrate this concept in the simplest of nonlinear systems, a damped pendulum. In my consideration of different control techniques, I review the Ott, Grebogi, and Yorke technique, as well as a variety of other feedback algorithms that have been proposed and demonstrated in various low-speed systems. I emphasize the issues that arise in controlling fast systems and consider how existing control techniques may be adapted to address such concerns, particularly those of latency through the control loop and accurate sampling of the

system at discrete times. An important point to remember is that *continuous* control algorithms minimize these difficulties and are therefore better suited for control in fast systems. All the control techniques studied in this thesis are continuous in nature. I also point out that open-loop control techniques do not suffer problems with latency at all, and are thus good candidates for high-speed control applications as well.

Following this introductory material, I develop a new feedback control technique for stabilizing unstable periodic orbits, ETDAS, which is an extension of a scheme proposed by Pyragas [23]. It generates a feedback signal based on difference of the current state of a dynamical variable of the chaotic system and an infinite series of past values of that variable. The time domain characteristics of ETDAS and a linear stability analysis technique give insight into the mechanisms of time-delay control. I also examine ETDAS in the frequency domain and identify that its transfer function has notches at integral multiples of the characteristic frequency of the orbit to be controlled, a feature that allows the feedback to vanish when an unstable periodic orbit is stabilized. Thus, ETDAS is a technique that is true to the Ott, Grebogi, and Yorke concept of stabilizing unstable dynamics inherent to the system.

Turning to experimental considerations, I describe the necessary components for a real implementation of ETDAS, noting that an all-optical version using the reflected field from a Fabry-Pérot interferometer is possible. I then provide a detailed description and layout of an electronic implementation that addresses practical considerations such as latency and fidelity of signal reproduction, balanced with low cost and ease of construction. In this version of ETDAS it is crucial to compensate for frequency-dependent attenuation in the cable that produces the time delay, in order to accurately reproduce the ETDAS form.

I then apply this form of ETDAS to a chaotic diode resonator circuit driven at 10.1 MHz, and obtain the important result of successful stabilization of period-1 and

period-4 orbits. These controlled orbits are identified as unstable periodic orbits of the unperturbed system by demonstrating that the feedback becomes very small when the orbits are stabilized. Examination of first-return maps confirms this as well, as the stabilized orbits lie on the attractor of the unperturbed system. In addition, ETDAS is demonstrated to be superior to Pyragas's scheme in that it allows for stabilization of orbits over a broader range of system parameters, including values of the bifurcation parameter for which control was previously not attainable. Furthermore, it is more effective in the presence of large control-loop latency, suggesting that ETDAS may be a good technique in even faster systems for which significant latencies may be unavoidable. These experimental results are in good agreement with theoretical predictions.

With the conclusion of the investigation of ETDAS control of the diode resonator, I next investigate the external cavity semiconductor laser system and the instability of low-frequency fluctuations. New measurements are made of the probability distribution of interspike intervals to help understand the laser dynamics. This study is valuable due to the currently incomplete understanding of the complex LFF behavior. For example, Sano [110] and van Tartwijk *et al.* [39] characterize LFF as deterministic antimode dynamics, but this model offers little understanding of the long-term behavior or the role of stochastic forces. I instead derive an approximate closed-form theoretical expression for the probability distribution of interspike intervals $\eta(t)$, based on a first-passage time analysis of the Henry and Kazarinov theory [108]. This theory models the LFF dynamics as a stochastically-driven overdamped particle in a well, where the well is formed by the maximum gain mode and a power dropout occurs when the particle escapes over a potential barrier. The results provides reasonable agreement with experimental measurements in some cases, under an interpretation that accounts empirically for a reinjection time following a dropout

event. However, in other cases the theory is qualitatively incorrect, failing to predict the appearance of structure in $\eta(t)$ which may be evidence of additional deterministic dynamics in the system.

Following the fundamental investigation of LFF, I apply control perturbations to the system beginning with open-loop control in the form of a 19 MHz sinusoidal modulation of the drive current. This represents an investigation of control in an extremely complex, high-dimensional system, extending the current understanding of controlling chaos. I discover that the power dropouts can be entrained to the drive frequency in 1:1 and 1:2 ratios when the modulation amplitude is $\gtrsim 8\%$ of the dc injection current. This is a significant alteration of the dynamics, since the interspike intervals are usually distributed randomly in time. Forcing the dropouts to become regularly-spaced also reduces the low-frequency noise in the system, a potentially important result for some applications.. In addition, I find that $\eta(t)$ is very sensitive to the presence of the 19 MHz perturbation even when it is too weak to entrain the dropouts, which may be connected with stochastic resonance phenomena. In this case, the interspike intervals are somewhat irregular, but only occur at intervals that are integral multiples of the drive period. At higher drive frequencies, the distribution $\eta(t)$ again shows that dropouts occur preferentially at times that are multiples of the drive period, although no entrainment is found. The modulation also can induce new dynamics in some cases, in the form of short, rapid bursts of dropouts. Curiously, there is no apparent effect on $\eta(t)$ if the frequency is set at the resonance frequency of the external cavity.

My last experiment is a preliminary effort at applying high-pass filter feedback control to the laser system as it undergoes LFF, in an attempt to stabilize one of the stationary solutions of the system. This feedback method may be interpreted as a limiting case of ETDAS. I use the optical power as the measured system variable,

and injection current as the accessible control parameter. The feedback changes the shape of the individual power dropouts but is unsuccessful at stabilizing the system.

The experiments described in this thesis lead the way to many further investigations. With the successful proof-of-principle demonstration of ETDAS, it remains to be seen if the technique can stabilize orbits in laser systems. This experiment may best be tried in a laser system other than one exhibiting LFF, where UPO's may be more obviously present and noise not such an important factor. The all-optical implementation of ETDAS has yet to be tried in an experimental system, although it has been considered theoretically by other researchers [46, 47]. In further attempts at applying feedback control to the LFF system, there are several ways to improve the high-pass filter control, as described at the end of Chapter 7. These efforts are focused primarily on technical improvements to the construction of the control loop, decreasing its latency and accounting for frequency-dependent distortion of the feedback signal.

There also remains a sizeable amount of work to be done in understanding the LFF system, its dynamics, and its response to control perturbations. On the theoretical front, it is an open question if the first-passage time description of $\eta(t)$ based on the Henry and Kazarinov theory can be improved, perhaps by incorporating a stochastic element to the reinjection process or constructing a different potential well that may predict some of the structure in $\eta(t)$ observed at high powers. Other work to be done with this model is to find a way to incorporate the sinusoidal modulation, to better understand the comblike probability distribution. In addition, the unexplained experimental results of this thesis may prompt further investigation, perhaps leading to a better understanding of the system. The unexpected lack of effect due to modulation at the cavity frequency remains to be explained. In addition, the sensitive response of $\eta(t)$ to even weak modulation at other frequencies may be of

interest to the stochastic resonance community.

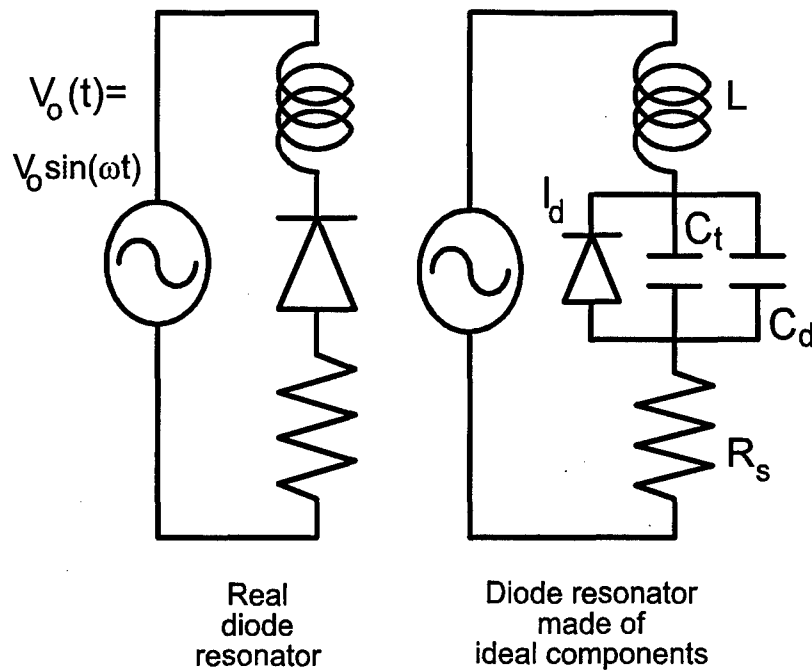


Figure A.1: Schematic of the diode resonator and its model using ideal components.

Appendix A

The Diode Resonator

This Appendix contains the derivation of the circuit equations of the diode resonator used in Chapter 4 (Eqs. 4.1 and 4.2). They are derived from a standard circuit analysis in which the system is treated as a collection of ideal components, in a form delineated by Newell *et al.* [156]. I also derive the dimensionless form of the equations used in the numerical and theoretical computations. Finally, I will describe how I determine the model parameters from the real system.

A.1 Circuit model

The basic equations for the diode resonator can be obtained through standard circuit analysis and the application of Kirchoff's Laws. The model treats the real circuit as a collection of ideal components as shown schematically in Fig. A.1. The resistor R_s and the inductor L account for the total reactance and inductance of the circuit, respectively. The rectifier diode is modeled as the parallel combination of a nonlinear resistor and two nonlinear capacitors C_d and C_t [157]. This model is well suited for rectifier diodes, such as the type 1N4007 used in my resonator [158]. Other types of diodes are more accurately described by different models [24, 28, 29, 30].

The voltage drops around the circuit lead to the equation

$$V_0(t) = L \frac{dI}{dt} + V_d + IR_s \quad (\text{A.1})$$

where $V_0(t) = V_0 \sin(\omega t)$ is the sinusoidal drive voltage, I is the total current flowing through the circuit, and V_d is the voltage drop across the diode. This gives the differential equation for the current. To derive an equation for the diode voltage drop, consider the currents I_{C_d} and I_{C_t} that flow through the parallel nonlinear capacitances C_d and C_t , respectively. The sum $I_{C_d} + I_{C_t}$ is equal to $I - I_d$ by conservation of current, where I_d is the portion of the total current flowing through the nonlinear resistor. This leads to

$$\frac{dV_d}{dt} = \frac{(I - I_d)}{(C_d + C_t)}. \quad (\text{A.2})$$

An expression for I_d can be found by treating it as an ideal diode whose voltage-to-current characteristics is described by the Shockley formula

$$I_d = I_s [\exp(eV_d/nk_B T) - 1], \quad (\text{A.3})$$

where I_s is the reverse-bias current, $e/k_B T$ is the thermal voltage, and n accounts for carrier recombination in the depletion zone.

Expressions for the capacitances C_d and C_t are given by the following equations. The voltage-dependent capacitor C_t accounts for the junction capacitance; its form is given by

$$C_t = \begin{cases} C_b(1 - V_d/V_J)^{-m} & V_d < V_J/2 \\ C_b(b_1 + mV_d/V_J)/b_2 & V_d \geq V_J/2 \end{cases}, \quad (\text{A.4})$$

where C_b is the zero-bias junction capacitance, $V_J = 0.6$ V is the junction potential, m quantifies the variation of the doping concentration across the junction, and $b_1 = (1 - m)/2$ and $b_2 = 2^{-(m+1)}$ ensures that C_t is continuous.

The second voltage-dependent capacitor C_d accounts for the diffusion capacitance arising from the finite response time of carriers to a changing field. Its form is given by

$$C_d = C_o \exp(eV_d/nkT), \quad (\text{A.5})$$

where C_o is the zero-bias diffusion capacitance.

A.1.1 Dimensionless form

The differential equations describing the diode resonator may be written as

$$\begin{aligned} \frac{dI}{dt} &= \left(\frac{1}{L}\right) [-V_d - IR_s + V_0(t)], \\ \frac{dV_d}{dt} &= \frac{I - I_d}{C_d + C_t}. \end{aligned} \quad (\text{A.6})$$

It is convenient to convert these equations into dimensionless form, for ease in numerical study. This form is given by

$$\begin{aligned} \frac{d\mathcal{I}}{d\Upsilon} &= -\mathcal{V} - \frac{\mathcal{I}}{\beta} + V_1 \sin(\Upsilon), \\ \frac{d\mathcal{V}}{d\Upsilon} &= G(\mathcal{I}, \mathcal{V}), \end{aligned} \quad (\text{A.7})$$

where

$$G(\mathcal{I}, \mathcal{V}) = \frac{I - \Gamma(e^{\alpha\mathcal{V}} - 1)}{c_1 [e^{\alpha\mathcal{V}} + c_2(1 - \mathcal{V})^{-m}]} \text{ if } \mathcal{V} < \frac{1}{2}, \quad (\text{A.8})$$

$$G(\mathcal{I}, \mathcal{V}) = \frac{I - \Gamma(e^{\alpha\mathcal{V}} - 1)}{c_1 \left[e^{\alpha\mathcal{V}} + c_2 \frac{(b_1 + m\mathcal{V})}{b_2} \right]} \text{ if } \mathcal{V} \geq \frac{1}{2}.$$

These dimensionless expressions for the diode resonator are obtained by means of the following transformations: $\mathcal{I} = (\omega L/V_J)I$, $\mathcal{V} = V_d/V_J$, $V_1 = V_0/V_J$, $\alpha = eV_J/nk\Upsilon$, $\beta = \omega L/R_s$, $\Gamma = \beta I_s R_s/V_J$, $c_1 = R_s \beta \omega C_0$, $c_2 = C_b/C_0$, and $\Upsilon = \omega t$.

A.2 Measurement of real circuit parameters

Valid parameter values for the circuit are required if the model is to accurately characterize the dynamics of the system. I determine these values by measuring several of the circuit characteristics. First, I remove the 1N4007 diode from the circuit and measure its I-V curve. The Shockley formula (Eq. A.3) describes this curve, and thus can be used to determine the parameters I_s and n . I use a Marquardt-Levenberg curve fitting algorithm (supplied with the SigmaPlot for Windows software) to find the parameter values. Reasonable agreement between the measured and predicted behavior is found with $I_s = 8.8$ nA and $n = 1.79$. These values represent the best fit to the forward-biased portion of the I-V curve. The junction voltage $V_J = 0.6$ V, as measured from the I-V curve.

The ac characteristics of the diode resonator are determined by measuring its response to a weak sinusoidal modulation with a dc offset. Specifically, I measure $I(t)$ when the resonator is driven by a voltage $V_o(t) = V_{dc} + \delta V \sin \omega t$ as a function of ω for $-4 \text{ V} \leq V_{dc} \leq 0.5 \text{ V}$ and $\delta V \simeq 890 \mu\text{V}$. The frequency response of the resonator displays a resonance due to the combined action of the inductor, capacitors, and resistors. I calculate this resonance curve by assuming a system response to the drive of the form

$$V_d = V_d^0 + \frac{1}{2}V_d' e^{-i\omega t} + \frac{1}{2}V_d'^* e^{i\omega t}, \quad (\text{A.9})$$

$$I = I^0 + \frac{1}{2}I'e^{-i\omega t} + \frac{1}{2}I'^*e^{i\omega t},$$

where the superscripts ⁰ and ' denote a dc and ac component, respectively, and the * indicates a complex conjugate. Inserting Eqs. A.9 into Eqs. A.6 and retaining only the oscillatory terms of the form $e^{-i\omega t}$, the resulting equations are

$$\begin{aligned} V_0 &= R_s I' - i\omega L I' + V'_d, \\ -i\omega V'_d C &= \frac{I'}{2} - I_s \kappa \frac{V'_d}{2} e^{\kappa V_d^0}, \end{aligned} \quad (\text{A.10})$$

where $\kappa \equiv e/nkT$ and $C = C_d + C_t$. These equations may be solved for I' , yielding the response function of the circuit

$$I' = \frac{V_0 (\kappa I_s e^{\kappa V_d^0} - i\omega C)}{(1 + R_s \kappa I_s e^{\kappa V_d^0} - \omega^2 LC) - i(\omega R_s C + \omega L \kappa I_s e^{\kappa V_d^0})}. \quad (\text{A.11})$$

It can be seen from Eq. A.11 that the frequency response of the system will display a resonance, and that the shape of the curve will depend on the dc value of the drive because of the $e^{\kappa V_d^0}$ terms. I collect a family of curves at several dc voltages ($-4 \text{ V} \leq V_{dc} \leq 0.5 \text{ V}$), and again use the curve-fitter to determine the remaining parameter values. This task can be simplified somewhat by recognizing that the $e^{\kappa V_d^0}$ terms become very small if V_{dc} is large and negative. This also causes the diffusion capacitance C_d to be very small, so that C can be approximated as the junction capacitance C_t , thereby helping to isolate its component parameters C_b and m . Similarly, C_d is large compared to C_b when V_{dc} becomes positive, thus C_o can be isolated.

Despite these simplifications, the parameter fits change somewhat over the range of V_{dc} . This may be a result of saturation of the inductor as the higher currents, an effect not accounted for in this model. I therefore select from the range of fits the parameters which yield the best agreement with the experimental bifurcation

Physical parameters	
I_s	8.8 nA
n	1.79
R_s	245 Ω
L	25 μ H
V_J	0.6 V
m	0.33
C_0	0.2 pF
C_b	17 pF
Dimensionless values	
α	12.89
β	6.41
Γ	2.30×10^{-5}
c_1	0.02
c_2	85

Table A.1: Parameters for the diode resonator model

diagram of the unperturbed diode resonator, particularly with regard to the location of events such as bifurcations, periodic windows, and the onset of chaos. These best overall values are listed in the table below.

Appendix B

The Lang-Kobayashi Equations

This appendix contains the derivation of the Lang-Kobayashi equations [36] that I use in Chapters 5 through 7. I begin by establishing the connection with semiclassical laser theory, deriving the wave equation from Maxwell's equations and explaining the complications that make a quantum mechanical description of the semiconductor medium difficult. I then apply phenomenological considerations to derive rate equations for the electric field and the carrier density. Finally, I show how the rate equations can be expressed in a dimensionless form that is convenient for computational use.

There is currently no standard notation for these equations; indeed there is a bewildering variety of different (but equivalent) forms and notations. I choose to derive the version of the equations used by Mork *et al.* [159, 124] because this form is the basis for the dimensionless equations studied by Alsing *et al.* [135].

B.1 Derivation of the equations

B.1.1 Semiclassical foundations

The semiclassical semiconductor laser equations treat the electric field classically, and therefore I begin with Maxwell's equations in a macroscopic medium [129], given in MKS units as

$$\nabla \times \mathcal{E} = -\frac{\partial \mathcal{B}}{\partial t}, \quad (\text{B.1})$$

$$\nabla \times \mathcal{H} = \mathcal{J} + \frac{\partial \mathcal{D}}{\partial t}, \quad (\text{B.2})$$

$$\nabla \cdot \mathcal{D} = \rho_f, \quad (\text{B.3})$$

$$\nabla \cdot \mathcal{B} = 0, \quad (\text{B.4})$$

where \mathcal{E} is the electric field, \mathcal{B} is the magnetic induction, \mathcal{H} is the magnetic field, \mathcal{J} is the density of free currents, \mathcal{D} is the displacement, and ρ_f is the density of free charges. The fields \mathcal{E} and \mathcal{H} propagating in a medium give rise to the displacement and magnetic induction, and this interaction is described by the constitutive relations (B.5, B.6) and Ohm's Law (B.7), given for a nonmagnetic dielectric medium as

$$\mathcal{D} = \epsilon_0 \mathcal{E} + \mathcal{P}, \quad (\text{B.5})$$

$$\mathcal{B} = \mu_0 \mathcal{H}, \quad (\text{B.6})$$

$$\mathcal{J} = \sigma \mathcal{E}, \quad (\text{B.7})$$

where \mathcal{P} is the induced electric polarization density, σ is the conductivity of the medium, and ϵ_0 and μ_0 are the permittivity and permeability of free space, respectively. The quantities ϵ_0 and μ_0 are related by $\epsilon_0 \mu_0 = 1/c^2$, where c is the speed of light.

Manipulation of these equations leads to the wave equation by the following process. I take the curl of Eq. B.1 and substitute using Eqs. B.2, B.6 to obtain

$$\nabla \times \nabla \times \mathcal{E} = \mu_0 \frac{\partial}{\partial t} \left(\mathcal{J} + \frac{\partial \mathcal{D}}{\partial t} \right). \quad (\text{B.8})$$

Next, I express \mathcal{J} and \mathcal{D} in terms of \mathcal{P} and \mathcal{E} using Eqs. B.5, B.7 to find

$$\nabla \times \nabla \times \mathcal{E} = -\mu_0 \sigma \frac{\partial \mathcal{E}}{\partial t} - \mu_0 \epsilon_0 \frac{\partial^2 \mathcal{E}}{\partial t^2} - \mu_0 \frac{\partial^2 \mathcal{P}}{\partial t^2}, \quad (\text{B.9})$$

and the right hand side can be simplified with the vector relationship

$$\nabla \times \nabla \times \mathcal{E} = \nabla (\nabla \cdot \mathcal{E}) - \nabla^2 \mathcal{E}. \quad (\text{B.10})$$

The $\nabla \cdot \mathcal{E}$ term in Eq. B.10 is taken to be zero, which assumes no free charges ($\rho_f = 0$) and neglects the dielectric discontinuities that do occur in many diode lasers. The

wave equation is then

$$\nabla^2 \mathcal{E} - \frac{\sigma}{\epsilon_0 c^2} \frac{\partial \mathcal{E}}{\partial t} - \frac{1}{c^2} \frac{\partial^2 \mathcal{E}}{\partial t^2} = \frac{1}{\epsilon_0 c^2} \frac{\partial^2 \mathcal{P}}{\partial t^2}. \quad (\text{B.11})$$

where the constants have been rewritten using $\epsilon_0 \mu_0 = 1/c^2$.

In the usual semiclassical treatment, the polarization density \mathcal{P} is calculated quantum mechanically through its connection with the dipole-moment operator $\hat{\mathbf{p}}$ by [160]

$$\mathcal{P} = \text{Tr}(\hat{\rho} \hat{\mathbf{p}}), \quad (\text{B.12})$$

where $\hat{\rho}$ is the density-matrix operator and the sum is over all energy states in the medium. Using the dipole approximation, the evolution of the density operator is described by [161]

$$\frac{d}{dt} \hat{\rho} = \frac{1}{i\hbar} [\hat{H}_o - \hat{\mathbf{p}} \cdot \mathcal{E}, \hat{\rho}] - \frac{1}{2} (\hat{\gamma} \hat{\rho} + \hat{\rho} \hat{\gamma}) + \hat{\Lambda}, \quad (\text{B.13})$$

where \hat{H}_o is the unperturbed Hamiltonian of the semiconductor medium, $\hat{\gamma}$ is the decay operator that accounts for *all* decay mechanisms, and $\hat{\Lambda}$ takes into account carrier generation in the active region due to external pumping.

This formalism is not generally used for the semiconductor laser, however, because a realistic analysis is very complicated. The unperturbed Hamiltonian \hat{H}_o requires detailed knowledge of the band structure and density of states for the conduction and valence bands. Furthermore, the intraband decay processes that must be included in the decay operator $\hat{\gamma}$ are not well-understood [117]. Therefore, a phenomenological approach is commonly used for the description of the semiconductor medium, and has proven to be very successful. The main assumptions of this approach are that the optical gain and the refractive index of the semiconductor medium vary linearly with the carrier density. A variety of equivalent forms and notations have sprung up; I follow the notation of Mork [159].

B.1.2 Phenomenological description

I Fourier transform the wave equation B.11 to convert the time derivatives to products, using

$$E_\omega(\mathbf{r}) = \int_{-\infty}^{\infty} \mathcal{E}(\mathbf{r}, t) e^{-i\omega t} dt, \quad (\text{B.14})$$

$$P_\omega(\mathbf{r}) = \int_{-\infty}^{\infty} \mathcal{P}(\mathbf{r}, t) e^{-i\omega t} dt, \quad (\text{B.15})$$

where $\mathbf{r} = (x, y, z)$. Next, a susceptibility χ is defined that relates the complex mode amplitudes $E_\omega(\mathbf{r})$ and $P_\omega(\mathbf{r})$ via

$$P_\omega(\mathbf{r}) = \epsilon_o \chi_\omega(\mathbf{r}) E_\omega(\mathbf{r}), \quad (\text{B.16})$$

which assumes that the polarization adiabatically follows the electric field. For simplicity, I assume the field propagates in the z -direction and is linearly polarized in the transverse (x, y) plane. Inserting Eqs. B.14 - B.16, the wave equation B.11 becomes

$$\left[\nabla^2 + \frac{\omega^2}{c^2} \epsilon_\omega(\mathbf{r}) \right] E_\omega(\mathbf{r}) = 0, \quad (\text{B.17})$$

where I have defined

$$\epsilon_\omega(\mathbf{r}) = 1 + \chi_\omega(\mathbf{r}) - i \frac{\sigma(\mathbf{r})}{\epsilon_o \omega}, \quad (\text{B.18})$$

which contains the interaction of the electric field with the semiconductor medium.

Next, I account for the transverse structure of the lasing mode as follows. Assume that Eq. B.17 is separable, that is, $E_\omega(\mathbf{r}) = E_\omega(z) \phi_o(x, y)$, and furthermore that $\phi_o(x, y)$ is a fundamental single transverse mode that satisfies [130, 118]

$$\left[\left(\frac{\partial^2}{\partial x^2} + \frac{\partial^2}{\partial y^2} \right) + \frac{\omega^2}{c^2} \epsilon_\omega(\mathbf{r}) \right] \phi_o(x, y) = k^2(z) \phi_o(x, y). \quad (\text{B.19})$$

Then, the equation for $E_\omega(z)$ is

$$\left[\frac{\partial^2}{\partial z^2} + k^2(z) \right] E_\omega(z) = 0, \quad (\text{B.20})$$

using the normalization $\int \int \phi_o \phi_o^* dy dx = 1$, and introducing the complex longitudinal wave number $k(z)$.

For a Fabry-Pérot laser, the wave number k is independent of z , and is taken to have the form [130]

$$k(\omega, N) = \frac{\omega}{c} n'(\omega, N) + i \frac{1}{2} [g(\omega, N) - a_i], \quad (\text{B.21})$$

where N is the average carrier density of the active region, n' is the part of the real refractive index, a_i is the internal loss per unit length, and g is the modal gain representing the difference of the stimulated emission and stimulated absorption per unit length. The carrier density is a fundamental variable of the system; I will derive its rate equation later. Eventually, I will perform a Taylor expansion of the system about a stationary value, and therefore will require the partial derivatives of $k(\omega, N)$. Defining the effective group refractive index $n_g = n' + \omega (\partial n' / \partial \omega)$ and the group velocity $v_g = c/n_g$, the derivatives are

$$\frac{\partial k}{\partial \omega} = \frac{1}{v_g} + i \frac{1}{2} \frac{\partial g}{\partial \omega}, \quad (\text{B.22})$$

$$\frac{\partial k}{\partial N} = i \frac{1}{2} (1 + i\alpha) \frac{\partial g}{\partial N}. \quad (\text{B.23})$$

The term α in Eq. B.23 is the *linewidth enhancement factor* [134]. It can be expressed as

$$\alpha = -\frac{2\omega (\partial n' / \partial N)}{c (\partial g / \partial N)}, \quad (\text{B.24})$$

$$= \frac{(\partial n' / \partial N)}{(\partial n'' / \partial N)}, \quad (\text{B.25})$$

where the quantities n' and n'' in Eq. B.25 are the real and imaginary parts of the *complex* refractive index $n_c \equiv n' - in''$, with $k \equiv \omega n_c / c$. Nonzero values of α lead to the phase-amplitude coupling that is characteristic of semiconductor laser dynamics.

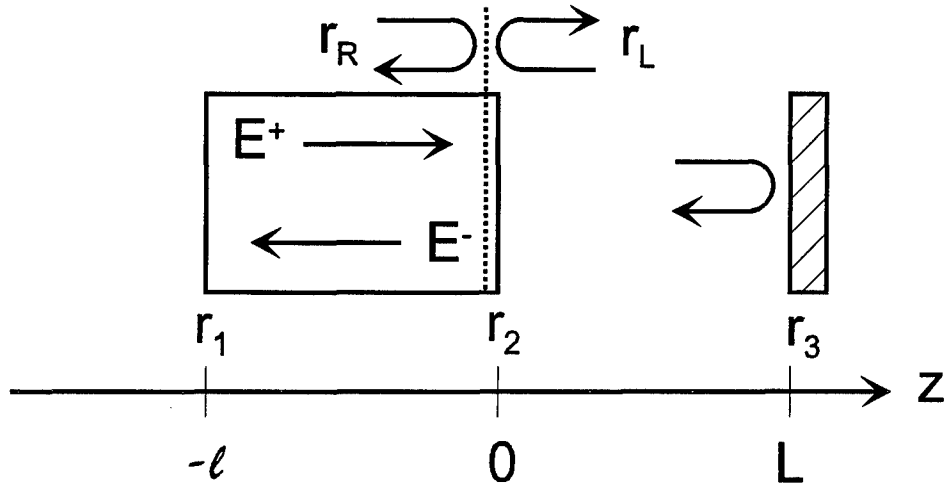


Figure B.1: Schematic of a semiconductor laser with external feedback. The rectangle between $z = -\ell$ and $z = 0$ represents a Fabry-Perot laser diode with facet reflectivities of r_1 and r_2 . The external cavity is formed by a flat mirror of reflectivity r_3 located at $z = L$. Effective reflectivities r_R and r_L are defined for right and leftgoing fields E^+ and E^- .

B.1.3 Rate equation for electric field

I now have derived a wave equation (B.20) and a complex wavevector k (B.21) that accounts for the interaction of the electric field with the semiconductor medium. They can be used to obtain a rate equation for the slowly-varying amplitude of the electric field. The process will be to determine boundary conditions in terms of effective reflectivities, which give a condition for oscillation. I will then expand one of these conditions about a fixed operating point (ω_s, N_s) , and transform the resulting equation into a dynamic equation for the slowly-varying complex envelope function of the electric field. An equation for the carrier density is also derived.

The first step is to decompose $E_\omega(z) = E_\omega^+(z) + E_\omega^-(z)$, the right and left travelling components illustrated in Fig. B.1. The boundary condition at the left facet ($z = -\ell$) is simply that $E_\omega^+(-\ell) = r_1 E_\omega^-(-\ell)$, which may also be expressed at a

reference plane just inside the *right* facet at $z = 0$ (the dotted line in the figure). This transformed boundary condition is derived in Ref. [130] as

$$E_{\omega}^{+}(0) = r_L(\omega, N) E_{\omega}^{-}(0). \quad (\text{B.26})$$

where the effective reflectivity of the leftgoing field $r_L(\omega, N)$ is

$$r_L(\omega, N) = r_1 \exp[-2ik(\omega, N)\ell]. \quad (\text{B.27})$$

Similarly,

$$E_{\omega}^{-}(0) = r_R(\omega) E_{\omega}^{+}(0), \quad (\text{B.28})$$

where $r_R(\omega)$ is the effective reflectivity of the rightgoing field. The Lang-Kobayashi model assumes weak feedback, meaning that only one reflection from the external mirror at $z = L$ contributes significantly. This is reasonable if r_3 is small or if the right facet has an antireflection coating. The form of r_R in such circumstances is [162, 163]

$$r_R(\omega) = r_2 + (1 - r_2^2) r_3 e^{-i\omega\tau}, \quad (\text{B.29})$$

where τ is the roundtrip time in the external cavity, given by $2L/c$. Note that r_3 could be described in a frequency dependent manner if the distant reflector were a grating.

The boundary conditions (B.26, B.28) provide a condition for sustained laser oscillations. Assuming operation at some stationary solution (ω_s, N_s) yields

$$r_L(\omega_s, N_s) r_R(\omega_s) = 1. \quad (\text{B.30a})$$

By eliminating the external cavity (equivalent to setting $r_R = r_2$), this equation determines the lasing frequencies supported by the *solitary* laser cavity. The imaginary part of the exponential in r_L must be a multiple of 2π . leading to

$$\omega_m = m \frac{\pi c}{n(\omega_m, N_{th}) \ell}, \quad (\text{B.31})$$

where m is an integer and ω_m is the m th longitudinal mode of the solitary laser cavity.

To obtain a rate equation for the field, I again use Eq. B.26, but now perform a Taylor expansion of the exponential for (ω, N) near (ω_s, N_s) . Rewriting Eq. B.26 as

$$\frac{1}{r_L(\omega, N)} E_\omega^+(0) = E_\omega^-(0), \quad (\text{B.32})$$

the effective reflectivity is expanded as

$$\begin{aligned} \frac{1}{r_L(\omega, N)} &= \frac{1}{r_1} \exp[2ik(\omega, N)l], \\ &\simeq \frac{1}{r_1} \exp[2ik(\omega_s, N_s)l + 2i\Delta k l], \\ &\simeq \frac{1}{r_1} [1 + 2i\Delta k l] \exp[2ik(\omega_s, N_s)l]. \end{aligned} \quad (\text{B.33})$$

Recalling Eqs. B.21 - B.23,

$$\begin{aligned} 2\Delta k l &= 2l \left[(\omega - \omega_s) \frac{\partial k}{\partial \omega} + (N - N_s) \frac{\partial k}{\partial N} \right], \\ &= \tau_{in} \left[\left(1 + i\frac{1}{2}G_\omega \right) (\omega - \omega_s) + i\frac{1}{2}(1 + i\alpha) G_N (N - N_s) \right], \end{aligned} \quad (\text{B.34})$$

where the roundtrip time inside the solitary laser cavity $\tau_{in} = 2l/v_g$ and the gain per unit time $G = v_g g$, with partial derivatives $G_\omega = \partial G/\partial \omega$ and $G_N = \partial G/\partial N$. Upon insertion of Eqs. B.33, B.34 into Eq. B.32, I find

$$i\omega E_\omega^+(0) - i\omega_s E_\omega^+(0) = \frac{1}{2} C G_N (N - N_s) E_\omega^+(0) + f_D [r_L E_\omega^-(0) - E_\omega^+(0)], \quad (\text{B.35})$$

where $C \equiv (1 + i\alpha) / (1 + i\frac{1}{2}G_\omega)$ and $f_D = 1 / [\tau_{in} (1 + i\frac{1}{2}G_\omega)]$. The terms C , G_N , f_D , and r_L are all evaluated at (ω_s, N_s) . To convert Eq. B.35 into a rate equation, I introduce the complex envelope functions of the electric field at the reference plane, given as

$$A^\pm(t) e^{i\omega_s t} = \frac{1}{2\pi} \int_0^\infty E_\omega^\pm(0) e^{i\omega t} d\omega. \quad (\text{B.36})$$

These functions are related to the real electric fields by

$$\mathcal{E}^\pm(0, t) = A^\pm(t)e^{i\omega_s t} + \text{complex conjugate.} \quad (\text{B.37})$$

Multiplying Eq. B.35 by $\exp(i\omega t)$, the first term on the right-hand side may be rewritten

$$i\omega E_\omega^+(0) e^{i\omega t} = \frac{d}{dt} (E_\omega^+(0) e^{i\omega t}), \quad (\text{B.38})$$

so that when I integrate and apply Eq. B.36 the dynamic equation

$$\frac{d}{dt} A^+(t) = \frac{1}{2} C G_N (N - N_s) A^+(t) + f_D [r_L A^-(t) - A^+(t)], \quad (\text{B.39})$$

is obtained.

I next relate $A^-(t)$ to $A^+(t)$, which is given as the convolution

$$\begin{aligned} A^-(t) &= \varrho(t) \otimes A^+(t), \\ &= \int_{-\infty}^{\infty} \varrho(t') A^+(t - t') dt', \end{aligned} \quad (\text{B.40})$$

where the response function $\varrho(t)e^{i\omega_s t}$ is given by

$$\varrho(t)e^{i\omega_s t} = \frac{1}{2\pi} \int_{-\infty}^{\infty} r_R(\omega) e^{i\omega t} d\omega. \quad (\text{B.41})$$

From Eqs. B.40, B.41 I find

$$A^-(t) = r_2 A^+(t) + r_3 (1 - r_2^2) e^{-i\omega\tau} A^+(t - \tau). \quad (\text{B.42})$$

I insert this formula into Eq. B.39 and choose the solitary laser threshold conditions (ω_o, N_{th}) as the stationary point (ω_s, N_s) . For the solitary laser, $r_L = 1/r_2$ and G_ω is assumed to be zero, corresponding to the laser oscillating near the gain peak. The rate equation thus becomes

$$\frac{d}{dt} A^+(t) = \frac{1}{2} (1 + i\alpha) G_N (N - N_{th}) A^+(t) + \frac{\kappa}{\tau_{in}} e^{-i\omega_o t} A^+(t - \tau), \quad (\text{B.43})$$

where the κ is the relative feedback level, given as

$$\kappa = \frac{r_3(1 - r_2^2)}{r_2}. \quad (\text{B.44})$$

To express the electric field in a form that will be convenient for deriving the carrier rate equation, $A^+(t)$ is converted to a new complex field variable $E(t)$, normalized such that *total photon number in the active region* $I(t)$ is given by

$$I(t) = V_c |E(t)|^2, \quad (\text{B.45})$$

where V_c is the volume of the active region. The final rate equation for the complex field variable is then

$$\frac{d}{dt} E(t) = \frac{1}{2} (1 + i\alpha) G_N (N - N_{th}) E(t) + \frac{\kappa}{\tau_{in}} e^{-i\omega_o \tau} E(t - \tau). \quad (\text{B.46})$$

B.1.4 Rate equation for carrier density

To complete the rate equation description of the semiconductor laser, an equation for the carrier density N is required. The usual expression for N is given by [131]

$$\frac{d}{dt} N(t) = J - R(N) - \frac{G(\omega_s, N) I(t)}{V_c}, \quad (\text{B.47})$$

where J represents the carrier density rate injected into the active region by the pumping current, and $R(N)$ gives the rate of spontaneous recombinations per second. Agrawal [117] states that a “reasonably suitable form” for $R(N)$ is given by $R(N) = AN + BN^2 + CN^3$, which incorporates spontaneous radiative recombination effects as well as Auger recombination. A simpler form for $R(N)$ is used in the Lang-Kobayashi equations,

$$R(N) = \frac{N}{\tau_s}, \quad (\text{B.48})$$

where τ_s is the carrier lifetime. The gain rate $G(\omega_s, N)$ in Eq. B.50 is expressed by Mork [124] as $G(N) = G_N(N - N_o)$, where $G_N = (\partial G / \partial N)_{th}$ is the differential gain

Parameter	Symbol	Value
Photon lifetime	τ_p	4.5 ps
Carrier lifetime	τ_s	700 ps
Internal cavity roundtrip time	τ_{in}	3.9 ps
External cavity roundtrip time	τ	4.7 ns
Linewidth enhancement parameter	α	5
Differential gain	G_N	$2.6 \times 10^{-6} \text{ cm}^3/\text{s}$
Threshold carrier density	N_{th}	$1.5 \times 10^{18} \text{ cm}^{-3}$

Table B.1: Parameter values for the Lang-Kobayashi equations

evaluated for the carrier density at solitary laser threshold, and N_o is a constant (usually the carrier density at transparency). Again assuming operation near threshold, it is convenient to write $G(N)$ as

$$\begin{aligned}
 G(N) &= G(N_{th}) + G_N(N - N_{th}) \\
 &= \frac{1}{\tau_p} + G_N(N - N_{th})
 \end{aligned}
 \tag{B.49}$$

where τ_p is the photon lifetime. By substituting Eqs. B.48, B.49 for $R(N)$ and $G(N)$ and applying Eq. B.45, I obtain the carrier density rate equation

$$\frac{d}{dt}N(t) = J - \frac{N}{\tau_s} - \left[\frac{1}{\tau_p} + G_N(N - N_{th}) \right] |E|^2.
 \tag{B.50}$$

Equations B.46 and B.50 together are known as the Lang-Kobayashi equations.

In numerical simulations, I use parameter values as listed in Table B.1. These values are based on papers by Simpson *et al.* [35, 164], who have studied SDL-5301-G1 lasers. These lasers have essentially the same characteristics as the SDL-5401-G1 model I use in the experiments of this thesis.

B.2 Dimensionless form

The Lang-Kobayashi equations in the regime of LFF are “stiff,” owing to the large-amplitude picosecond pulses the system exhibits. It is therefore advantageous to use

a dimensionless form for computational work. Alsing *et al.* [135] have derived such a form, which I have used for my numerical results in Chapters 5 through 7. I review here the transformations by which these equations are obtained.

To transform Equations B.46 and B.50 I use the new dimensionless variables

$$Y \equiv \sqrt{\frac{\tau_s G_N}{2}} E, \quad (\text{B.51})$$

$$Z \equiv \left(\frac{\tau_p G_N}{2} \right) (N - N_{th}), \quad (\text{B.52})$$

$$s \equiv \frac{t}{\tau_p}, \quad (\text{B.53})$$

and new parameters

$$P \equiv \frac{\tau_p G_N N_{th}}{2} \left(\frac{J}{J_{th}} - 1 \right), \quad (\text{B.54})$$

$$J_{th} \equiv \frac{N_{th}}{\tau_s}, \quad (\text{B.55})$$

$$\eta \equiv \kappa \frac{\tau_p}{\tau_{in}}, \quad (\text{B.56})$$

$$T = \frac{\tau_s}{\tau_p} \quad (\text{B.57})$$

$$\theta \equiv \frac{\tau}{\tau_p}, \quad (\text{B.58})$$

$$\Omega \equiv \omega_o \tau_p. \quad (\text{B.59})$$

In terms of these new dimensionless quantities, the Lang-Kobayashi equations are expressed as

$$\frac{dY}{ds} = (1 + i\alpha) ZY + \eta e^{-i\Omega\theta} Y (s - \theta), \quad (\text{B.60})$$

$$T \frac{dZ}{ds} = P - Z - (1 + 2Z) |Y|^2, \quad (\text{B.61})$$

with Y becoming the dimensionless electric field and Z representing the carrier number deviation from the threshold value.

Appendix C

The Henry and Kazarinov Theory and First-Passage Time Problems

This appendix contains mathematical details of the first-passage time problem, following the development given in Ref. [146]. I also present the derivation of the approximate solution for the mean interspike intervals and probability distribution, based on Henry and Kazarinov's theory as discussed in Chapter 5.

C.1 The first-passage time problem

The first-passage time (FPT) problem is one of a special class of problems relating to systems in which the underlying processes can be described in stochastic terms (*e.g.* spontaneous emission). The usual formulation of the problem involves establishing two possible regions in which a random variable may reside. The FPT is defined as the time \mathbf{T} that elapses before the variable is driven from its initial region to the other for the first time. The dynamics of such a system is often expressed by a Langevin force equation

$$\frac{dX(t)}{dt} = a(X, t) + d^{\frac{1}{2}}(X, t) f(t), \quad (\text{C.1})$$

where $X(t)$ is the random variable, a is called the drift function, and d is called the diffusion function. The term $f(t)$ is taken to be a Gaussian white-noise process. It is well-established (see Refs. [165, 166, 167], for example) that the density function $P(n, t; n')$ of the random variable $X(t)$ evolves according to the forward Fokker-Planck equation

$$\frac{\partial}{\partial t} P(n, t; n') = -\frac{\partial}{\partial n} [a(X, t) P(n, t; n')] + \frac{1}{2} \frac{\partial^2}{\partial n^2} [d(X, t) P(n, t; n')], \quad (\text{C.2})$$

assuming that $f(t)$ obeys

$$\langle f(t) \rangle = 0, \quad (\text{C.3})$$

$$\langle f(t) f(u) \rangle = \delta(t - u). \quad (\text{C.4})$$

The probability density $P(n, t; n')$ is defined such that $P(n, t; n') dn$ is the probability that $X(t)$ lies between n and $n + dn$, given that the initial value of $X(0) = n'$. The density $P(n, t; n')$ is related to the FPT probability density as follows: let $P_1(n', t)$ be the probability that X is still in its initial region at time t , assuming n' was the initial location. The FPT probability density $\zeta(n', t)$ is then defined such that $\zeta(n', t) dt$ is the probability that \mathbf{T} lies between t and $t + dt$, and is related to $P_1(n', t)$ by

$$\zeta(n', t) = -\frac{dP_1(n', t)}{dt}. \quad (\text{C.5})$$

It is possible in theory to determine the FPT probability from this equation by solving Eq. C.2. However, this may be a very difficult task, and it is more convenient to seek a solution by a slightly different approach.

I consider instead the *integral* FPT probability density $\psi(n', t)$, which describes the likelihood that the FPT is less than t given the usual initial condition. To be definite, let X be constrained to lie between 0 and A , where the first passage occurs when X reaches A . I then define a transition probability $W(n, dt; n')$ that describes the probability that the system moves from n' to between n and $n + dn$ in a time dt . The position $n + dn$ is then taken as a new initial condition. This may be mathematically expressed as

$$\psi(n', t + dt) = \int_0^A W(n, dt; n') \psi(n, t) dn. \quad (\text{C.6})$$

Next, $\psi(n, t)$ is expanded about n'

$$\psi(n, t) \simeq \psi(n', t) + \frac{\partial \psi(n', t)}{\partial n'} (n - n') + \frac{1}{2} \frac{\partial^2 \psi(n', t)}{\partial n'^2} (n - n')^2 + \dots \quad (\text{C.7})$$

and inserted into Eq. C.6 to find

$$\begin{aligned}\psi(n', t + dt) \simeq & \psi(n', t) \int_0^A W(n, dt; n') dn \\ & + \frac{\partial \psi(n', t)}{\partial n'} \int_0^A (n - n') W(n, dt; n') dn \\ & + \frac{1}{2} \frac{\partial^2 \psi(n', t)}{\partial n'^2} \int_0^A (n - n')^2 W(n, dt; n') dn + \dots\end{aligned}\quad (\text{C.8})$$

Since $\int_0^A W(n', dt; n) dn = 1$, I subtract $\psi(n', t)$ from Eq. C.8, divide by dt , and take the limit as $dt \rightarrow 0$ to find

$$\frac{\partial \psi(n', t)}{\partial t} = a_1(n') \frac{\partial \psi(n', t)}{\partial n'} + \frac{a_2(n')}{2} \frac{\partial^2 \psi(n', t)}{\partial n'^2}, \quad (\text{C.9})$$

where $a_j(n')$ is the “ j^{th} infinitesimal transition moment” defined as

$$a_j(n') \equiv \lim_{dt \rightarrow 0} \frac{1}{dt} \int_0^A (n - n')^j W(n, dt; n') dn. \quad (\text{C.10})$$

Boundary conditions are then established for Eq. C.9. First, $\psi(A, t) = 1$ since the FPT occurs if $n' = A$. Also, $\partial \psi(0, t) / \partial n' = 0$ if the system cannot venture beyond $n < 0$ (it is a “reflecting barrier” [146]).

The next step in the derivation is to define the j^{th} moment of the first-passage time starting from n' as

$$\mu_j(n') = \int_0^\infty t^j \frac{\partial \psi(n', t)}{\partial t} dt. \quad (\text{C.11})$$

One particularly useful feature of the moments of the FPT is that they are related recursively. To derive the equations that relate them, differentiate Eq. C.9 with respect to time, multiply by t^j , and change the order of differentiations to find

$$t^j \frac{\partial^2 \psi(n', t)}{\partial t^2} = a_1(n') \frac{\partial}{\partial n'} t^j \frac{\partial \psi(n', t)}{\partial t} + \frac{a_2(n')}{2} \frac{\partial^2}{\partial n'^2} t^j \frac{\partial \psi(n', t)}{\partial t}, \quad (\text{C.12})$$

which upon integration over all time yields

$$\frac{a_2(n')}{2} \frac{\partial^2 \mu_1(n')}{\partial n'^2} + a_1(n') \frac{\partial \mu_1(n')}{\partial n'} = -1, \quad (\text{C.13})$$

$$\frac{a_2(n')}{2} \frac{\partial^2 \mu_j(n')}{\partial n'^2} + a_1(n') \frac{\partial \mu_j(n')}{\partial n'} = -j \mu_{j-1}(n'), \quad (\text{C.14})$$

where Eq. C.14 is valid for $j \geq 2$. These relationships are used to derive an approximate analytical result for the system described by the Henry and Kazarinov theory.

C.2 Approximate solution for Henry and Kazarinov model

To find an approximate solution for the FPT probability distribution for the Henry and Kazarinov model will require two steps. I first make a series of approximations to solve Eq. C.13, deriving an expression for the mean FPT. Subsequently, I use the recursive relationship to deduce the form of the probability distribution for the FPT.

To begin, I restate the Langevin force equation derived by Henry and Kazarinov (Eq. 5.27)

$$\dot{n} = -\frac{\partial U}{\partial n} + F(t), \quad (\text{C.15})$$

where n represents fluctuations in the carrier density away from the dominant mode, and $U(n)$ and $F(t)$ are described by

$$U(n) = \gamma \left(\frac{n^2}{2} - \frac{n^3}{3n_o} \right), \quad (\text{C.16})$$

$$\langle F(t) F(t') \rangle = 2D\delta(t-t'). \quad (\text{C.17})$$

The barrier of the potential function $U(n)$ is located at n_o , at a height of $\gamma n_o/6$. The theoretical form of D is given by Eq. 5.30, but can also be estimated from experimental data. To formulate the FPT problem, it is assumed that the system begins in the potential well at $n = 0$ and a power dropout occurs when the system is forced past the barrier at n_o .

For this system, the a_j coefficients given by Eq. C.10 are simply $a_1(n) = -\partial U/\partial n \equiv A$, and $a_2(n) = 2D$ (see Ref. [146], p. 374), where I have now dropped the prime from n . The coefficient a_2 is a constant and does not depend on n . The

calculation of the mean FPT begins by noting that the first moment of the integral first passage time μ_1 is exactly the average first passage time $\langle T \rangle$. Introducing the new variable $v \equiv \partial \langle T \rangle / \partial n$, Eq. C.13 leads to

$$\frac{\partial v}{\partial n} + \frac{A}{D}v = -\frac{1}{D}, \quad (\text{C.18})$$

which is solved using an integrating factor

$$\beta(n) = \exp \left[\int_{-\infty}^n \frac{A(m)}{D} dm \right] = \exp \left[\frac{-U(n)}{D} \right]. \quad (\text{C.19})$$

Here, m is merely a dummy variable for integration. Using Eq. C.19, the integral expression for $v(n)$ is

$$v(n) = -\frac{\exp \left[\frac{U(n)}{D} \right]}{D} \int_{-\infty}^n \exp \left[\frac{U(m)}{D} \right] dm, \quad (\text{C.20})$$

leading to

$$\langle T(n) \rangle = -\frac{1}{D} \int_{-\infty}^n dm \exp \left[\frac{U(m)}{D} \right] \int_{-\infty}^m dm' \exp \left[-\frac{U(m')}{D} \right] + C_2. \quad (\text{C.21})$$

To solve for the constant C_2 , I use the condition that the FPT must be zero if the system is already at the barrier, *i.e.* $T(n_o) = 0$. With this condition, Eq. C.21 becomes

$$\langle T(n) \rangle = \frac{1}{D} \int_n^{n_o} dm \exp \left[\frac{U(m)}{D} \right] \int_{-\infty}^m dm' \exp \left[-\frac{U(m')}{D} \right], \quad (\text{C.22})$$

with the implicit assumption that $n < n_o$. I assume in the rest of this derivation that the initial condition for n is that it starts at the bottom of the potential well at $n = 0$.

To solve Eq. C.22, I now begin making suitable approximations to its integrals. First, consider the integral $\int_{-\infty}^m dm' \exp [-U(m')/D]$. The exponential is largest near $n = 0$, and therefore I Taylor expand the potential about the origin to simplify the

exponent, finding

$$U(n) = U(0) + n \frac{\partial U}{\partial n} + \frac{1}{2!} n^2 \frac{\partial^2 U}{\partial n^2} + O(n^3) \simeq \frac{\gamma}{2} n^2, \quad (\text{C.23})$$

where the derivatives are evaluated at the origin. If $U(n_o)/D \simeq -\gamma n_o^2/2D \gg 1$, the function inside the integral will have fallen to zero well before the barrier is reached, so the integral will remain nearly constant for $n \gtrsim \sqrt{2D/\gamma}$.

I now consider the remaining integral in Eq. C.22, $\int_n^{n_o} dm \exp[U(m)/D]$. The exponential in this integral dominates when $n \approx n_o$ and $n \leq -n_o$. However, it is multiplied by the previous integral, which is approximately constant near $n = n_o$ but is essentially zero at $n \leq -n_o$. It is therefore permissible to perform a Taylor expansion of the potential about the peak of the barrier, resulting in

$$\begin{aligned} U(n) &= U(n_o) + (n - n_o) \frac{\partial U}{\partial n} + \frac{(n - n_o)^2}{2!} \frac{\partial^2 U}{\partial n^2} + O(n^3) \\ &\simeq \frac{\gamma n_o}{6D} - \frac{\gamma (n - n_o)^2}{2D}. \end{aligned} \quad (\text{C.24})$$

With these approximations, Eq. C.22 can be rewritten as

$$\langle \mathbf{T}(n) \rangle = \frac{1}{D} \int_n^{n_o} dm \exp \left[\frac{\gamma n_o}{6D} \right] \exp \left[-\frac{\gamma (m - n_o)^2}{2D} \right] \int_{-\infty}^{\infty} dm' \exp \left[-\frac{\gamma m'^2}{2D} \right], \quad (\text{C.25})$$

where I have changed the upper limit of the final integral from m to ∞ , which is reasonable since the value of the integral is nearly constant over the region where $\exp[-\gamma(m - n_o)^2/2D]$ is significant. The resulting definite integral has a good closed-form solution $\int_{-\infty}^{\infty} dm' \exp[-\gamma m'^2/2D] = \sqrt{2\pi D/\gamma}$, and thus the expression for $\langle \mathbf{T}(n) \rangle$ is

$$\langle \mathbf{T}(n) \rangle \simeq \sqrt{\frac{2\pi}{\gamma D}} \exp \left[\frac{U(n_o)}{D} \right] \int_n^{n_o} dm \exp \left[-\frac{\gamma (m - n_o)^2}{2D} \right]. \quad (\text{C.26})$$

The remaining integral can be solved approximately by demanding that the initial position of the system is far from the barrier at n_o relative to $\gamma/2D$, that is,

$m \ll n_o - \sqrt{2D/\gamma}$. Then the integral becomes independent of m , and I change the limits so that $\int_n^{n_o} dm \simeq \frac{1}{2} \int_{-\infty}^{\infty} dm$. This Gaussian integral has an exact closed-form solution, $\frac{1}{2} \int_{-\infty}^{\infty} dm \exp[-\gamma(m-n)^2/2D] = \sqrt{\pi D/2\gamma}$, and the approximate analytical solution for the average FPT is

$$\langle \mathbf{T}(n) \rangle \simeq \frac{\pi}{\gamma} \exp \left[\frac{U(n_o)}{D} \right], \quad (\text{C.27})$$

which is the form given in Eq. 5.33. I emphasize that this solution is only valid if the system is initially far from the barrier. This will be true if the initial location is at the bottom of the well ($n = 0$) and the diffusion coefficient D is small.

I use Eq. C.27 in conjunction with Eq. C.14 for the higher-order moments of the integral FPT to determine the form of the full FPT probability distribution. Recall that the higher-order moments obey

$$D \frac{\partial^2 \mu_j}{\partial n^2} + A \frac{\partial \mu_j}{\partial n} = -j \mu_{j-1}, \quad (\text{C.28})$$

which is valid for $j \geq 2$. However, Eq. C.27 shows that $\mu_1 = \langle \mathbf{T} \rangle$ is approximately constant. Therefore, the higher-order moments can be found using the same analysis by which I determined the mean time, with the result that each successive moment μ_j depends on the previous one with a factor of $j \langle \mathbf{T} \rangle$, giving

$$\begin{aligned} \mu_2 &= 2 \langle \mathbf{T} \rangle \frac{\pi}{\gamma} \exp \left[\frac{U(n_o)}{D} \right] = 2 \langle \mathbf{T} \rangle^2, \\ \mu_3 &= 3 \cdot 2 \langle \mathbf{T} \rangle^2 \frac{\pi}{\gamma} \exp \left[\frac{U(n_o)}{D} \right] = 3! \langle \mathbf{T} \rangle^3, \\ \mu_j &= j! \langle \mathbf{T} \rangle^j. \end{aligned} \quad (\text{C.29})$$

The moments given by Eq. C.29 are of the exact form that is expected for an exponentially decaying FPT probability distribution $\zeta(n, t)$. Assuming proper normalization, this form must be

$$\zeta(t) = \frac{1}{\langle \mathbf{T} \rangle} \exp \left(-\frac{t}{\langle \mathbf{T} \rangle} \right), \quad (\text{C.30})$$

which has moments that can be calculated using integration by parts as

$$\mu_j = j! \langle \mathbf{T} \rangle^j, \quad (\text{C.31})$$

and this is the same as Eq. C.29.

To summarize the analytical results, the mean first passage time $\langle \mathbf{T} \rangle$ is approximately constant of n , and the FPT probability distribution $\zeta(t)$ is simply a decaying exponential that depends only on $\langle \mathbf{T} \rangle$. The forms of these solutions are

$$\langle \mathbf{T} \rangle \simeq \frac{\pi}{\gamma} \exp \left[\frac{U(n_o)}{D} \right], \quad (\text{C.32})$$

$$\zeta(t) = \frac{1}{\langle \mathbf{T} \rangle} \exp \left(-\frac{t}{\langle \mathbf{T} \rangle} \right), \quad (\text{C.33})$$

which are valid only if $n_o \gg \sqrt{2D/\gamma}$, assuming that the system starts near the bottom of the potential well at $n = 0$.

Bibliography

- [1] Poincaré, H. *The Foundations of Science*. Vol. 3, *Science and Method*. Translated by George Bruce Halsted. New York: The Science Press, 1929, p. 397-398.
- [2] Lorenz, E. N. Deterministic non-periodic flow. *J. Atmos. Sci.*, 20:130-41, 1963.
- [3] Haken, H. *Light*. Vol. 2, *Laser light dynamics*. Amsterdam: North-Holland Physics Publishing, 1985, Section 8.3.
- [4] Bergé, Pierre, Yves Pomeau, and Christian Vidal. *Order within chaos: Towards a deterministic approach to turbulence*. Translated by Laurette Tuckerman. Paris, France: Hermann, and New York: John Wiley & Sons, 1984.
- [5] Ogata, K. *Modern Control Engineering*. 2d ed. New Jersey: Prentice Hall, 1990.
- [6] Sontag, E. D. *Mathematical Control Theory*. Texts in Applied Mathematics, F. John, J. E. Marsden, L. Sirovich, M. Golubitsky, and W. Jäger, eds. New York: Springer-Verlag, 1990.
- [7] Dyson, Freeman J. *Infinite in All Directions*. New York: Harper & Row, 1988, p. 183.
- [8] Ott, Edward, Celso Grebogi, and James A. Yorke. Controlling Chaos. *Phys. Rev. Lett.* 64:1196-1199, 1990.
- [9] Grebogi, Celso, Edward Ott, and James A. Yorke. Unstable periodic orbits and the dimensions of multifractal chaotic attractors. *Phys. Rev. A*, 37:1711-1724, 1988.
- [10] Ott, Edward, and Mark Spano. Controlling Chaos. *Physics Today* 48:34-40, 1995, and references therein.
- [11] Bishop, S. R., and Daolin Xu. Control of chaos in noisy flows. *Phys. Rev. E* 54:3204-3210, 1996.
- [12] Yumin, Liaw, and Tung Picheng. Controlling chaos via state feedback cancellation under a noisy environment. *Phys. Lett. A* 211:350-356, 1996.
- [13] Christini, David J., and James A. Collins. Controlling Nonchaotic Neuronal Noise Using Chaos Control Techniques. *Phys. Rev. Lett.* 75:2782-2785, 1995.

- [14] Tamaševičius, A., and A. Cenys. Synchronizing hyperchaos with a single variable. *Phys. Rev. E* 55:297-299, 1997.
- [15] Colet, P., R. Roy, and K. Weisenfeld. Controlling hyperchaos in a multimode laser model. *Phys. Rev. E* 50:3453-3457, 1994.
- [16] Christini, David J., James A. Collins, and Paul S. Linsay. Experimental control of high-dimensional chaos: The driven double pendulum. *Phys. Rev. E* 54:4824-4827, 1996.
- [17] Bleich, M. E., D. Hochheiser, J. V. Moloney, and J. E. S. Socolar. Controlling extended systems with spatially filtered time-delayed feedback. *Phys. Rev. E* 55:2119-2126, 1997.
- [18] Martin, R., A. J. Scroggie, G.-L. Oppo, and W. J. Firth. Stabilization, Selection and Tracking of Unstable Patterns by Fourier Space Techniques. *Phys. Rev. Lett.* 77:4007-4010, 1996.
- [19] Johnson, G. A., M. Löcher, and E. R. Hunt. Stabilized spatiotemporal waves in a convectively unstable open flow system: couple diode resonators. *Phys. Rev. E* 51:R1625-1628, 1995.
- [20] Socolar, J. E. S., D. W. Sukow and D. J. Gauthier. Stabilizing unstable periodic orbits in fast dynamical systems. *Phys. Rev. E* 50:3245-3248, 1994.
- [21] Sukow, David W., Michael E. Bleich, Daniel J. Gauthier, and Joshua E. S. Socolar. Controlling chaos in a fast diode resonator using extended time-delay autosynchronization: experimental observations and theoretical analysis. To appear in *Chaos* 7, 1997.
- [22] Romeiras, Filipe J., Celso Grebogi, Edward Ott, and W.P. Dayawansa. Controlling chaotic dynamical systems. *Physica D* 58:165-192, 1992.
- [23] Pyragas, K. Continuous control of chaos by self-controlling feedback. *Phys. Lett. A* 170:421-428, 1992.
- [24] Linsay, Paul S. Period Doubling and Chaotic Behavior in a Driven Anharmonic Oscillator. *Phys. Rev. Lett.* 47:1349-1352, 1981.
- [25] Pérez, José, and Carson Jeffries. Direct observation of a tangent bifurcation in a nonlinear oscillator. *Phys. Lett.* 92A:82-84, 1982.

- [26] Jeffries, Carson, and José Pérez. Observation of a Pomeau-Manneville intermittent route to chaos in a nonlinear oscillator. *Phys. Rev. A* 26:2117-2122, 1982.
- [27] Hilborn, R. Quantitative Measurement of the Parameter Dependence of the Onset of a Crisis in a Driven Nonlinear Oscillator. *Phys. Rev. A* 31:378-382, 1985.
- [28] Testa, James, José Pérez, and Carson Jeffries. Evidence for Universal Chaotic Behavior of a Driven Nonlinear Oscillator. *Phys. Rev. Lett.* 48:714-717, 1982.
- [29] Rollins, R. W., and E. R. Hunt. Exactly Solvable Model of a Physical System Exhibiting Universal Chaotic Behavior. *Phys. Rev. Lett.* 49:1295-1298, 1982.
- [30] Hunt, E. R., and R. W. Rollins. Exactly solvable model of a physical system exhibiting multidimensional chaotic behavior. *Phys. Rev. A* 29:1000-1001, 1984.
- [31] Su, Z., R. W. Rollins, and E. R. Hunt. Simulation and characterization of strange attractors in driven diode resonator systems. *Phys. Rev. A* 40:2698-2705, 1989.
- [32] Gauthier, Daniel J., David W. Sukow, Hope M. Concannon, and Joshua E. S. Socolar. Stabilizing unstable periodic orbits in a fast diode resonator using continuous time-delay autosynchronization. *Phys. Rev. E* 50:2343-2346, 1994.
- [33] Petermann, Klaus. External Optical Feedback Phenomena in Semiconductor Lasers. *IEEE J. Sel. Top. Quantum Electron.* 1:480-489, 1995, and references therein.
- [34] van Tartwijk, G. H. M., and D. Lenstra. Semiconductor lasers with optical injection and feedback. *Quantum Semiclass. Opt.* 7:87-143, 1995, and references therein.
- [35] Liu, Jia-Ming, and T. B. Simpson. Four-Wave Mixing and Optical Modulation in a Semiconductor Laser. *IEEE J. of Quant. Elec.* 30:957-965, 1994.
- [36] Lang, Roy, and Kohroh Kobayashi. External Optical Feedback Effects on Semiconductor Injection Laser Properties. *IEEE J. of Quant. Elec.* QE-16:347-355, 1980.
- [37] Risch, Ch., and C. Voumard. Self-pulsation in the output intensity and spectrum of GaAs-AlGaAs cw diode lasers coupled to a frequency-selective external optical cavity. *J. Appl. Phys.* 48:2083-2085, 1977.

- [38] Hohl, Angela, H. J. C. van der Linden, and Rajarshi Roy. Determinism and stochasticity of power-dropout events in semiconductor lasers with optical feedback. *Opt. Lett.* 20:2396-2398, 1995.
- [39] van Tartwijk, G. H. M., A. M. Levine, and D. Lenstra. Sisyphus Effect in Semiconductor Lasers with Optical Feedback. *IEEE J. Sel. Top. in Quant. Elec.* 1:466-472, 1995.
- [40] Fischer, I., G. H. M van Tartwijk, A. M. Levine, W. Elsässer, E. Göbel, and D. Lenstra. Fast Pulsing and Chaotic Itinerancy with a Drift in the Coherence Collapse of Semiconductor Lasers. *Phys. Rev. Lett.* 76:220-223, 1996.
- [41] Tsukamoto, Takayuki, Maki Tachikawa, Toshiki Sugawara, and Tadao Shimuzu. Locking of a passive Q-switched chaotic laser system to a small external modulation. *Phys. Rev. A* 52:1561-1569, 1995.
- [42] Liu, Yun, Noriyuki Kikuchi, and Junji Ohtsubo. Controlling dynamical behavior of a semiconductor laser with external optical feedback. *Phys. Rev. E* 51:R2697-2700, 1995.
- [43] Colet, Pere, and Y. Braiman. Control of chaos in multimode solid state lasers by the use of small periodic perturbations. *Phys. Rev. E* 53:200-206, 1996.
- [44] Newell, T. C., A. Gavrielides, V. Kovanis, D. Sukow, T. Erneux, and S. A. Glasgow. Unfolding the period two bifurcation in a fiber laser pumped with two modulation tones. *Phys. Rev. E* 56:1-9, 1997.
- [45] Chang, Austin, G. Martin Hall, and Daniel J. Gauthier. Stabilizing unstable steady states using extended time-delay autosynchronization (preprint).
- [46] Lu, W., and R. G. Harrison. Controlling chaos using continuous interference feedback: proposal for all optical devices. *Opt. Comm.* 109:457-461, 1994.
- [47] Simmendinger, C., and O. Hess. Controlling delay-induced chaotic behavior of a semiconductor laser with optical feedback. *Phys. Lett. A* 216:97-105, 1996.
- [48] Sussmann, H. J., ed. *Nonlinear Controllability and Optimal Control*. Monographs and textbooks in pure and applied mathematics. New York: Marcel Dekker, Inc, 1990.
- [49] Aström, K. J., C. C. Goodwin, and P. R. Kumar, eds. *Adaptive Control, Filtering, and Signal Processing*. The IMA Volumes in Mathematics and its Applications. New York: Springer-Verlag, 1995, and references therein.

- [50] Chen, Han-Fu, and Lei Guo. *Identification and Stochastic Adaptive Control*. Systems & Control: Foundations & Applications. Boston: Birkhäuser, 1991.
- [51] Francis, Bruce A., and Pramod P. Khargonekar, eds. *Robust Control Theory*. The IMA Volumes in Mathematics and its Applications. New York: Springer-Verlag, 1995.
- [52] Kushner, Harold J. *Weak Convergence Methods and Singularly Perturbed Stochastic Control and Filtering Problems*. Systems & Control: Foundations & Applications. Boston: Birkhäuser, 1990.
- [53] Kolmanovskii, V. B., and L. E. Shaĭhet. *Control of Systems with Aftereffect*. Translations of Mathematical Monographs. Rhode Island: American Mathematical Society, 1996.
- [54] Graef, John R., and Jack K. Hale, eds. *Oscillation and Dynamics in Delay Equations: Proceedings of an AMS Special Session held January 16-19, 1991*. Contemporary Mathematics. Rhode Island: American Mathematical Society, 1991.
- [55] Wiener, Joseph, and Jack K. Hale, eds. *Ordinary and delay differential equations*. Pitman Research Notes in Mathematics Series. New York: John Wiley and Sons, Inc., 1992.
- [56] Giacomelli, Giovanni, and Antonio Politi. Relationship between Delayed and Spatially Extended Dynamical Systems. *Phys. Rev. Lett.* 76:2686-2689, 1996.
- [57] Wangersky, P. J., and W. J. Cunningham. Time lag in prey-predator population models. *Ecology*, 38:136-139, 1957.
- [58] Shvitra, D. I. On some specific features of behavior of a generalized Hutchinson equation. *Differentsial'nye Uravneniya Primenen* 29:135-145, 1981.
- [59] Delgado-Restituto, M., and A. Rodriguez-Vasquez. A CMOS Monolithic Chua's Circuit. *J. Circuits Syst. Comput.* 3:2-9, 1993.
- [60] Cuomo, K. M., and A. V. Oppenheim. Circuit implementation of synchronized chaos with applications to communication. *Phys. Rev. Lett.* 71:65-68, 1993.
- [61] Hayes, Scott, Celso Grebogi, Edward Ott, and Andrea Mark. Experimental Control of Chaos for Communication. *Phys. Rev. Lett.* 73:1781-1784, 1994.

- [62] Pecora, Louis M., and Thomas L. Carroll. Synchronization in Chaotic Systems. *Phys. Rev. Lett.* 64:821-824, 1990.
- [63] Schiff, S. J., K. Jerger, D. H. Duong, T. Chang, M. L. Spano, and W. L. Ditto. Controlling Chaos in the Brain. *Nature* 370:615-620, 1994.
- [64] In the nomenclature of modern control engineering, a control protocol that stabilizes a system about a state that is inherently part of the system is called a regulator control scheme.
- [65] Ciofini, M., R. Meucci, and F.T. Arecchi. Experimental control of chaos in a laser. *Phys. Rev. E* 52:94-97, 1995, and references therein.
- [66] Mettin, R., and T. Kurz. Optimized periodic control of chaotic systems. *Phys. Lett. A* 206:331-339, 1995, and references therein.
- [67] Mettin, Robert, Alfred Hübler, Alexander Scheeline, and Werner Lauterborn. Parametric entrainment control of chaotic systems. *Phys. Rev. E* 51:4065-4075, 1995.
- [68] See, for example, Strang, Gilbert. *Linear Algebra and its Applications*. 3rd ed. San Diego: Harcourt Brace Jovanovich, 1988.
- [69] Brockett, R. W. "Asymptotic stability and feedback stabilization" In *Differential Geometric Control Theory*, ed. R. W. Brockett, R. S. Millman, and H. J. Sussman, 181-191. Boston: Birkhäuser, 1983.
- [70] Abed, Eyad H., and Jyun-Horng Fu. Local feedback stabilization and bifurcation control, I. Hopf bifurcation. *Syst. & Control Lett* 7:11-17, 1986.
- [71] Abed, Eyad H., and Jyun-Horng Fu. Local feedback stabilization and bifurcation control, I. Stationary bifurcation. *Syst. & Control Lett* 8:467-473, 1987
- [72] A system ergodically explores the neighborhoods of the infinite number of unstable states when it is chaotic. Targeting techniques can be used to direct the system to the desired state.
- [73] Typically, Modern Control Engineers use a different, but equivalent, method for expressing the perturbations. For example, it is common to find the perturbations expressed as $\delta p_i = p_i - \bar{p} = -\mathbf{K}^T [\mathbf{z}_i - \mathbf{z}_*(\bar{p})]$ where \mathbf{K}^T is a $1 \times m$ feedback matrix.

- [74] Ditto, W. L., S. N. Rauseo, and M. L. Spano. Experimental Control of Chaos. *Phys. Rev. Lett.* 65:3211-3214, 1990.
- [75] Hunt, E. R. Stabilizing High-Period Orbits in a Chaotic System: The Diode Resonator. *Phys. Rev. Lett.* 67:1953-1956, 1991.
- [76] Peng, B., V. Petrov, and K. Showalter. Controlling Chemical Chaos. *J. Phys. Chem.* 95:4957-4959, 1991.
- [77] Carr, T. W., and I. B. Schwartz. Controlling unstable steady states using system parameter variation and control duration. *Phys. Rev. E* 50:3410-3415, 1995.
- [78] Carr, T. W., and I. B. Schwartz. Controlling the unstable steady state in a multimode laser. *Phys. Rev. E* 51:5109-5111, 1995.
- [79] Qu, Zhilin., Gang Hu, and Benkun Ma. Controlling Chaos via continuous feedback. *Phys. Lett. A* 178:265-270, 1993.
- [80] Bielawski, S., M. Bouazaoui, D. Derozier, and P. Glorieux. Stabilization and characterization of unstable steady states in a laser. *Phys. Rev. A* 47:3276-3279, 1993.
- [81] Johnson, Gregg A., and Earle R. Hunt. Derivative Control of the Steady State in Chua's Circuit Driven in the Chaotic Region. *IEEE Trans. Circuits Sys.* 40:833-834, 1993.
- [82] Parmananda, P., and M. Eisworth. Stabilizing Unstable Fixed Points Using Derivative Control. *J. Phys. Chem.* 100:16568-16570, 1996.
- [83] Pyragas, K., and A. Tamaševičius. Experimental control of chaos by delayed self-controlling feedback. *Phys. Lett. A* 180:99-102, 1993.
- [84] Namajūnas, A., K. Pyragas, A. Tamaševičius. Stabilization of an unstable steady state in a Mackey-Glass system. *Phys. Lett. A* 204:255-262, 1995.
- [85] Bielawski, S., D. Derozier, and P. Glorieux. Controlling unstable periodic orbits by a delayed continuous feedback. *Phys. Rev. E* 49:R971-974, 1994.
- [86] Pierre, Th., G. Bonhomme, and A. Atipo. Controlling the chaotic regime of nonlinear ionization waves using the time-delay autosynchronization method. *Phys. Rev. Lett.* 76:2290-2293, 1996.

- [87] Hikihara, T., and T. Kawagoshi. An experimental study on stabilization of unstable periodic motion in magneto-elastic chaos. *Phys. Lett. A* 211:29-36, 1996.
- [88] Ye, M., D. W. Peterman, and P. E. Wigen. Controlling chaos in thin YIG films with a time-delayed method. *Phys. Lett. A* 203:23-28, 1995.
- [89] Schöll, E., and K. Pyragas. Tunable Semiconductor Oscillator Based on Self-Control of Chaos in the Dynamic Hall Effect. *Europhys. Lett.* 24:159-164, 1993.
- [90] Lourenço, C., and A. Babloyantz. Control of Chaos in Networks with Delay: A Model for Synchronization of Cortical Tissue. *Neural Comp.* 6:1141-1154, 1994.
- [91] Pyragas, K. Control of chaos via extended delay feedback. *Phys. Lett. A* 206:323-330, 1995.
- [92] A map-based version of ETDAS was proposed independently by Abed, E. H., H. O. Wang, and R. C. Chen. Stabilization of period doubling bifurcations and implications for control of chaos. *Physica D* 70:154-164, 1994.
- [93] Socolar, J. E. S. and M. E. Bleich. Private communication.
- [94] Bleich, M. E., and J. E. S. Socolar. Stability of periodic orbits controlled by time-delay feedback. *Phys. Lett. A* 210:87-94, 1996.
- [95] Bleich, Michael Edward. "Controlling Chaos with Time-Delay Feedback." Ph.D. diss., Duke University, 1997.
- [96] Lega, J., J. V. Moloney, and A. C. Newell. Swift-Hohenberg equation for lasers. *Phys. Rev. Lett.* 73:2978-2981, 1994.
- [97] Lega, J., J. V. Moloney, and A. C. Newell. Universal description of laser dynamics near threshold. *Physica D*, 83:478-498, 1995.
- [98] Just, W., T. Bernard, M. Ostheimer, E. Reibold, and H. Benner. Mechanism of Time-Delayed Feedback Control. *Phys. Rev. Lett.* 78:203-206, 1997.
- [99] Flake, G. W., G.-Z. Chen, Y.-C. Lee, and H. H. Chen. In *Advances in Neural Information Processing Systems 6*, edited by J. D. Cowan, G. Tesauro, and J. Alspector. New York: Morgan Publishers, 1994.
- [100] Born, M., and E. Wolf. *Principles of Optics*. 6th Ed. New York: Pergamon Press, 1980, Sec. 7.6.1.

- [101] Analog Devices, One Technology Way, P.O. Box 9106, Norwood, MA 02062-9106.
- [102] Press-n-Peel film #100PNPR, Techniks, Inc., P.O. Box 463, Ringoes, NJ 08551.
- [103] Andrew Corporation, 10500 W. 153rd Street, Orland Park, IL 60462.
- [104] Hewlett-Packard, 3000 Hanover St., Palo Alto, CA 94304-1185.
- [105] Kay Elemetrics Corp., 12 Maple Ave., P.O. Box 2025, Pine Brook, NJ 07058-2025.
- [106] Tektronix, Inc., 26600 SW Parkway, P.O. Box 1000, Wilsonville, OR 97070-1000.
- [107] Press, William H., Brian P. Flannery, Saul A. Teukolsky, and William T. Vetterling. *Numerical Recipes in C: The Art of Scientific Computing*. Cambridge: Cambridge University Press, 1988.
- [108] Henry, Charles H. and Rudolf F. Kazarinov. Instability of Semiconductor Lasers Due to Optical Feedback from Distant Reflectors. *IEEE J. of Quant. Elec.* QE-22:294-301, 1986.
- [109] Sacher, J., W. Elsässer, and E. O. Göbel. Intermittency in the coherence collapse of a semiconductor laser with external feedback. *Phys. Rev. Lett.* 63:2224-2227, 1989.
- [110] Sano, Takuya. Antimode dynamics and chaotic itinerancy in the coherence collapse of semiconductor lasers with optical feedback. *Phys. Rev. A* 50:2719-2726, 1994.
- [111] Hall, R. N., G. H. Fenner, J. D. Kingsley, T. J. Soltys, and R. D. Carlson. Coherent Light Emission from GaAs Junctions. *Phys. Rev. Lett.* 9:366-368, 1962.
- [112] Holonyak, Jr., Nick, and S. F. Bevacqua. Coherent (Visible) Light Emission from Ga(As_{1-x}P_x) Junctions. *Appl. Phys. Lett.* 1:82-83, 1962.
- [113] Nathan, Marshall I., William P. Dumke, Gerald Burns, Frederick H. Hill, Jr., and Gordon Lasher. Stimulated Emission of Radiation from GaAs p-n Junctions. *Appl. Phys. Lett.* 1:62-63, 1962.

- [114] Quist, T. M., R. H. Rediker, R. J. Keyes, W. E. Krag, B. Lax, A. L. McWorther, and H. J. Zeiger. Semiconductor Maser of GaAs. *Appl. Phys. Lett.* 1:91-92, 1962.
- [115] Haken, H. Analogy between higher instabilities in fluids and lasers. *Phys. Lett. A* 53A:77-78, 1975.
- [116] Arecchi, F. T., G. L. Lippi, G. P. Puccioni, and J. R. Tredicce. In *Coherence and Quantum Optics*. Edited by L. Mandel and E. Wolf. New York: Plenum, 1984.
- [117] Agrawal, G. P., and N. K. Dutta. *Long-wavelength semiconductor lasers*. New York: Van Nostrand Reinhold Company, 1986, and references therein.
- [118] Henry, C. H. Theory of spontaneous emission noise in open resonators and its application to lasers and optical amplifiers. *J. Lightwave Technol.* LT-4:288-297, 1986.
- [119] Fleming, M. W., and A. Mooradian. Spectral characteristics of external-cavity controlled lasers. *IEEE J. of Quant. Elec.* QE-17:144-59, 1981.
- [120] Goldberg, L., H. F. Taylor, A. Dandridge, J. F. Weller, and R. O. Miles. Spectral characteristics of semiconductor lasers with optical feedback. *IEEE J. of Quant. Elec.* QE-18:555-564, 1982.
- [121] Favre, F., D. Le Guen, and J. C. Simon. Optical feedback effects upon laser diode oscillation field spectrum. *IEEE J. of Quant. Elec.* QE-18:1712-1718, 1982.
- [122] Sacher, Joachim, Dieter Baums, Peter Panknin, Wolfgang Elsässer, and Ernst O. Göbel. Intensity instabilities of semiconductor lasers under current modulation, external light injection, and delayed feedback. *Phys. Rev. A* 45:1893-1905, 1992.
- [123] Lenstra, D., M. van Vaalen, and B. Jaskorzyńska. On the theory of a single-mode laser with weak optical feedback. *Physica B-C* 125C:255-264, 1984.
- [124] Mork, Jesper, Bjarne Tromborg, and Peter L. Christiansen. Bistability and Low-Frequency Fluctuations in Semiconductor Lasers with Optical Feedback: A Theoretical Analysis. *IEEE J. of Quant. Elec.* 24:123-132, 1988.
- [125] Özizmir, E., A. M. Levine, G. H. M. van Tartwijk, and D. Lenstra. Power spectrum of a bistable external-cavity diode laser. *Opt. Lett.* 17:1073-1075, 1992.

- [126] Lenstra, Daan. Statistical theory of the multistable external-feedback laser. *Opt. Comm.* 81:209-214, 1991.
- [127] Lenstra, D., B. H. Verbeek, and A. J. den Boef. Coherence collapse in single-mode semiconductor lasers due to optical feedback. *IEEE J. of Quant. Elec.* QE-21:674-679, 1985.
- [128] Olesen, Henning, Jens Henrik Osmundsen, and Bjarne Tromborg. Nonlinear Dynamics and Spectral Behavior for an External Cavity Laser. *IEEE J. of Quant. Elec.* QE-22:762-773, 1986.
- [129] Jackson, J. D. *Classical Electrodynamics*, 2nd ed. New York: John Wiley & Sons, 1975.
- [130] Tromborg, Bjarne, Henning Olesen, Xing Pan, and Shigeru Saito. Transmission Line Description of Optical Feedback and Injection Locking for Fabry-Perot and DFB Lasers. *IEEE J. of Quant. Elec.* QE-23:1875-1889, 1987.
- [131] Yamada, M. Transverse and longitudinal mode control in semiconductor injection lasers. *IEEE J. of Quant. Elec.* QE-19:1365-1380, 1983.
- [132] Bogatov, A. P., P. G. Eliseev, and B. N. Sverdlov. Anomalous interaction of spectral modes in a semiconductor laser. *IEEE J. of Quant. Elec.* QE-11:510-515, 1975.
- [133] Homar, M., J. V. Moloney, and M. San Miguel. Travelling wave model of a multimode Fabry-Perot laser in free running and external cavity configurations. *IEEE J. of Quant. Elec.* QE-32:553-566, 1996.
- [134] Henry, C. H. Theory of the linewidth of semiconductor lasers. *IEEE J. of Quant. Elec.* QE-18:259-264, 1982.
- [135] Alsing, P. M., V. Kovanis, A. Gavrielides, and T. Erneux. Lang and Kobayashi phase equation. *Phys. Rev. A* 53:4429-4434, 1996.
- [136] Tromborg, B., J. H. Osmundsen, and H. Oleson. Stability analysis for a semiconductor laser in an external cavity. *IEEE J. of Quant. Elec.* QE-20:1023-1032, 1984.
- [137] Acket, G. A., D. Lenstra, A. J. den Boef, and B. H. Verbeek. The influence of feedback intensity on longitudinal mode properties and optical noise in index-guided semiconductor lasers. *IEEE J. of Quant. Elec.* QE-20:1163-1169, 1984.

- [138] Mork, J., B. Tromborg, and J. Mark. Chaos in semiconductor lasers with optical feedback: theory and experiment. *IEEE J. of Quant. Elec.* QE-28:93-108, 1992.
- [139] Cohen, J. S., R. R. Drenten, and B. H. Verbeek. The effect of optical feedback on the relaxation oscillation in semiconductor lasers. *IEEE J. of Quant. Elec.* QE-24:1989-1995, 1988.
- [140] Spectra Diode Labs, Inc., 80 Rose Orchard Way, San Jose, CA 95134-1365.
- [141] Wieman, Carl E., and Leo Hollberg. Using diode lasers for atomic physics. *Rev. Sci. Instrum.* 62:1-20, 1991.
- [142] Concannon, Hope M. "Two-Photon Raman Gain in a Laser Driven Potassium Vapor." Ph.D. diss., Duke University, 1996.
- [143] Lax, M. Fluctuations from the nonequilibrium steady state. *Rev. Mod. Phys.* 32:25-64, 1960.
- [144] Temkin, H., N. A. Olsson, J. H. Abeles, R. A. Logan and M. B. Panish. Reflection noise in index-guided InGaAsP lasers. *IEEE J. of Quant. Elec.* QE-22:286-293, 1986.
- [145] Gillespie, Daniel T. The mathematics of Brownian motion and Johnson noise. *Am. J. Phys.* 64:225-240, 1996.
- [146] Weiss, G. H. "First Passage Time Problems in Chemical Physics." In *Stochastic Processes in Chemical Physics: The Master Equation*, ed. Irwin Oppenheim, Kurt E. Shuler, and George H. Weiss, 361-378. Cambridge, Massachusetts: The MIT Press, 1977.
- [147] Mork, J., M. Semkow, and B. Tromborg. Measurement and theory of mode hopping in external cavity lasers. *Electron. Lett.* 26:609-610, 1990.
- [148] Meucci, M., W. Gadowski, M. Ciofini, and F. T. Arecchi. Experimental control of chaos by means of weak parametric perturbations. *Phys. Rev. E* 49:R2528-2531, 1994.
- [149] Liu, Y., N. Kikuchi, and J. Ohtsubo. Controlling dynamical behavior of a semiconductor laser with external optical feedback. *Phys. Rev. E* 51:R2697-2700, 1995, and references therein.
- [150] Moss, F., D. Pierson, and D. O'Gorman. Stochastic resonance: tutorial and update. *Int. J. of Bif. and Chaos* 4:1383-1397, 1994.

- [151] Wiesenfeld, K., and F. Moss. Stochastic resonance and the benefits of noise: from ice ages to crayfish and SQUIDS. *Nature* 373:33-36, 1995.
- [152] Sukow, David W. "Shifting of bifurcation points in a drive Nd fiber laser by subharmonic perturbations." Kirtland AFB, NM: Phillips Laboratory, 1995.
- [153] Arimoto, Akira, Masahiro Ojima, Naoki Chinone, Akio Oishi, Toshihoko Gotoh, and Nobutaka Ohnuki. Optimum conditions for the high frequency noise reduction method in optical videodisc players. *Applied Optics* 25:1398-1403, 1986.
- [154] Ryan, Andrew T., Govind P. Agrawal, George R. Gray, and Edward C. Gage. Optical-feedback-induced chaos and its control in semiconductor lasers. *IEEE J. of Quant. Elec.* QE-30:668-679, 1994.
- [155] Stubkjaer, K. E. and M. B. Small. Noise properties of semiconductor lasers due to optical feedback. *IEEE J. of Quant. Elec.* QE-20:472-478, 1984. *IEEE J. of Quant. Elec.* QE-20:472-478, 1984.
- [156] Newell, T. C., P. M. Alsing, A. Gavrielides, and V. Kovanis. Synchronization of chaotic resonators based on control theory. *Phys. Rev. E* 51:2963-2973, 1995.
- [157] Antognetti, Paolo, and Giuseppe Massobrio, eds. *Semiconductor Device Modeling with SPICE*. New York: McGraw-Hill, 1988.
- [158] Hunt, E. R., J. Testa, J. Pérez, and C. Jeffries. Comment on a driven nonlinear oscillator (and reply). *Phys. Rev. Lett.* 49:1054-1055, 1982.
- [159] Mork, Jesper. "Nonlinear Dynamics and Stochastic Behavior of Semiconductor Lasers with Optical Feedback." Ph.D. diss., Technical University of Denmark, 1988.
- [160] Yariv, Amnon. *Quantum Electronics*, 3rd ed. New York: John Wiley & Sons, 1989.
- [161] Sargent, Murray, Marian O. Scully, and Willis E. Lamb, Jr. *Laser Physics*. Massachusetts: Addison-Wesley Publishing Company, 1974.
- [162] Olsson, A., and C. L. Tang. Coherent optical interference effects in external-cavity semiconductor lasers. *IEEE J. of Quant. Elec.* QE-17:1320-1323, 1981.
- [163] Osmundsen, J. H., and N. Gade. Influence of optical feedback on laser frequency

- spectrum and threshold conditions. *IEEE J. of Quant. Elec.* QE-19:465-469, 1983.
- [164] Simpson, T. B., J. M. Liu, A. Gavrielides, V. Kovanis, and P. M. Alsing. Period-doubling cascades and chaos in a semiconductor laser with optical injection. *Phys. Rev. A* 51:4181-4185, 1995.
- [165] Chandrasekhar, S. Stochastic Problems in Physics and Astronomy. *Rev. Mod. Phys.* 15:1-89, 1943.
- [166] Pathria, R. K. *Statistical Mechanics*, 2nd ed. Oxford: Butterworth-Heinemann, 1996.
- [167] Reif, F. *Fundamentals of statistical and thermal physics*. New York: McGraw-Hill Book Company, 1965.

Biography

David W. Sukow, 



graduated second in his class from River Falls High School in 1987. Remaining true to his Scandinavian roots, he attended Gustavus Adolphus College in St. Peter, Minnesota in the fall of 1987 as a National Merit Scholar. He was inducted into Phi Beta Kappa at Gustavus in 1991, the same year he graduated with high honors and a Bachelor of Arts in Physics. By now thoroughly familiar with the small midwestern town milieu, he crossed the Mason-Dixon line in 1991 and chose to pursue physics at Duke University in Durham, North Carolina as a Townes Graduate Fellow. Under the supervision of Dr. Daniel J. Gauthier, he earned his Master of Arts in 1994. In the summer of 1995 he worked at the Phillips Laboratories in Albuquerque, New Mexico as an AFOSR Graduate Summer Research Associate. In his years at Duke he managed to retain his liberal arts interests, training sporadically in modern dance and ballet. These interests proved particularly fortuitous, since it was in ballet class that he met Gretchen Smith, who married him on October 27, 1996. He received his Ph.D. in June 1997. He will return to Albuquerque as a National Research Council Postdoctoral Research Associate.

LIST OF PUBLICATIONS

'Statistics of power-dropout events in semiconductor lasers with delayed optical feedback,' D. W. Sukow and D. J. Gauthier, submitted to *Phys. Rev. A Rapid Communications*.

'Controlling chaos in a fast diode resonator using extended time-delay autosynchro-

nization: experimental observations and theoretical analysis,' D. W. Sukow, M. E. Bleich, D. J. Gauthier, and J. E. S. Socolar, *Chaos*, 7, 1997 (invited paper for Focus Issue on control and synchronization of chaos).

'Unfolding of the period two bifurcation in a fiber laser pumped with two modulation tones,' T. C. Newell, A. Gavrielides, V. Kovanis, D. Sukow, T. Erneux and S. A. Glasgow, *Phys. Rev. E*, 56:1-9, 1997.

'Regulation and entrainment of power-dropout events in external cavity semiconductor lasers,' D. W. Sukow and D. J. Gauthier, *Quantum Electronics and Laser Science Conference*, OSA Technical Digest Series 12:181-182, 1997.

'Controlling chaos and instabilities in fast optical systems,' D. J. Gauthier and D. W. Sukow, *LEOS newsletter*, 10:15-17, 1996.

'Controlling chaos in fast optical systems,' D. J. Gauthier and D. W. Sukow, LEOS '95 IEEE Lasers and Electro-Optics Society 1995 Annual Meeting, Conference Proceedings, 1:32-33, 1995.

'Stabilizing unstable periodic orbits in fast dynamical systems,' J. E. S. Socolar, D. W. Sukow, and D. J. Gauthier, *Phys. Rev. E*, 50:3245-3248, 1994.

'Stabilizing unstable periodic orbits in a fast diode resonator using continuous time-delay autosynchronization,' D. J. Gauthier, D. W. Sukow, H. M. Concannon, and J. E. S. Socolar, *Phys. Rev. E*, 50:2343-2346, 1994.

LIST OF PRESENTATIONS

'Entrainment of power-dropout events in external cavity semiconductor lasers,' D. W. Sukow and D. J. Gauthier, contributed poster at the Quantum Electronics and Laser Science Conference (QELS '97), Baltimore, Maryland, May 1997.

'Regulation of power-dropout events in an external cavity semiconductor laser under current modulation,' D. W. Sukow and D. J. Gauthier, contributed poster at Dynamics Days '97, Scottsdale, Arizona, January 1997.

'Controlling chaos under 100 ns,' D. W. Sukow and H. M. Concannon, contributed poster at Dynamics Days, Durham, North Carolina, January 1994.